EVALUATION OF A MICROWAVE RADIATIVE TRANSFER MODEL FOR CALCULATING SATELLITE BRIGHTNESS TEMPERATURE

by

SIMONETTA D THOMPSON
B.S. University of Central Florida, 2002

A thesis submitted in partial fulfillment of the requirements
for the degree of Master of Science
in the Department of Electrical and Computer Engineering
in the College of Engineering and Computer Science
at the University of Central Florida
Orlando, Florida

Fall Term
2004

ABSTRACT

Remote sensing is the process of gathering and analyzing information about the earth's ocean, land and atmosphere using electromagnetic "wireless" techniques. Mathematical models, known as Radiative Transfer Models (RTM), are developed to calculate the observed radiance (brightness temperature) seen by the remote sensor. The RTM calculated brightness temperature is a function of fourteen environmental parameters, including atmospheric profiles of temperature, pressure and moisture, sea surface temperature, and cloud liquid water. Input parameters to the RTM model include data from NOAA Centers for Environmental Prediction (NCEP), Reynolds weekly Sea Surface Temperature and National Ocean Data Center (NODC) WOA98 Ocean Salinity and special sensor microwave/imager (SSM/I) cloud liquid water. The calculated brightness temperatures are compared to collocated measurements from the WindSat satellite. The objective of this thesis is to fine tune the RadTb model, using simultaneous environmental parameters and measured brightness temperature from the well-calibrated WindSat radiometer. The model will be evaluated at four microwave frequencies (6.8 GHz, 10.7 GHz, 18.7 GHz, and 37.0 GHz) looking off- nadir for global radiance measurement.

ACKNOWLEDGEMENTS

I would like to thank the Almighty God for his many blessings and my parents' for their continual support and encouragement over the years, while doing my studies.

I would also like to express my sincere gratitude to those who have supported me in completing this thesis research. I am greatly indebted to my advisor and committee chair Dr. Linwood Jones, who brought me on his group to work on this project. The completion of this thesis is greatly due to his stimulating advice and suggestions given while doing research and writing this thesis. Additional thanks to Dr. Josko Zec, Jun Park and Liang Hong for their help and valuable suggestions.

Last but not least, my committee members including Dr. Takis Kasparis and Dr. Michael Haralambous for their time.

TABLE OF CONTENTS

LIST OF FIGURES

LIST OF TABLES

CHAPTER ONE: INTRODUCTION

1.1 Background of Microwave Remote Sensing

Remote sensing is the science of detecting and acquiring geophysical information from objects and media without making physical contact. Because of the great distances involved, remote sensing usually involves electromagnetic (EM) techniques. EM radiances over a wide range of wavelengths, from radio frequencies to beyond visible light, contain geophysical information of the Earth's ocean, land, ice and atmosphere. The interpretation of these signals is the science of remote sensing, which have applications in many areas of physical sciences. Remote sensing can be classified into two types, active and passive. Active remote sensing involves the transmission of EM energy (or uses natural radiation from the sun), and depends upon the scatter of EM waves from objects or surfaces. On the other hand, passive remote sensing depends upon the measurement of natural blackbody radiance emitted from physical media.

The first application of remote sensing began in the mid-eighteenth century, when the camera was used to obtain photographic imagery. The development of remote sensing science

began with aid of balloons and kites, and progressively made its way of using airplanes and then satellites. Aerial photography was a success in providing information about the earth, but it had limitations in the presence of bad weather conditions, such as fog, clouds and rain and at low light conditions. A more suitable technique for earth observations, in the presence of clouds and rain and at night, is the application of microwave sensors. Active microwave systems (Radar) were developed during World War II to detect and track moving objects such as ships and later, planes. For the past three decades, both active and passive microwave observations from satellites provide information about the Earth's surface for topographical mapping, military operations, agricultural purposes as well aiding in the study of the environment, which include meteorology, oceanography, hydrology, and glaciology.

This thesis research deals with remote sensing from satellites using passive microwave techniques. The microwave radiance, also known as brightness temperature, Tb, is measured using an instrument called a microwave radiometer. Mathematical models, known as Radiative Transfer Models (RTM) are developed to account for the radiance collected by the radiometer antenna. The theory of radiative transfer is essential to interpret the emitted radiance/brightness measurement to infer the physical properties of the media that produced them.

For purposes of assessing global climate change, it is important to provide consistent multi-decadal time series of geophysical measurements from satellite microwave remote sensors to assess subtle changes in the earth's environment. Absolute calibration of a radiometric instrument is important to prevent errors in the measured brightness temperature; therefore, it is necessary to inter-calibrate the radiometric brightness temperatures to remove instrumental

effects (radiometric biases) from the geophysical measurements time series. To assist in this process, radiative transfer models can be used to interpret brightness temperature from radiometers with different characteristics. Radiometers operate at different viewing geometries (incidence angles) and different frequencies, both of which affect the measured brightness temperature. Given knowledge of the atmosphere and surface environmental parameters and the radiometer characteristics, RTM's can be used to normalize measured brightness temperatures to a common reference for comparison.

Over oceans, a microwave radiative transfer model named RadTb is used by the Central Florida Remote Sensing Laboratory (CFRSL) in their passive microwave research. RadTb, built on the RTM developed by Wisler and Hollinger [1], is driven by fourteen environmental measurements of the ocean and atmosphere and three radiometric parameters. The RadTb model was previously evaluated by comparison with satellite radiometer measurements for the nadir-viewing geometry [2]. These comparisons were made with collocated, simultaneous brightness temperatures, Tb, at three microwave frequencies from the Topex/Poseidon Microwave Radiometer (TMR). It was found that the calculated brightness temperature using RadTb agreed well with the brightness temperature measurements of the TMR except for a "small offset" (bias) in the absolute brightness temperature. Further, this evaluation of RadTb also showed that there are four significant environmental parameters that affect the brightness temperature, namely: wind speed, water vapor, cloud liquid water and sea surface temperature.

The objective of this thesis is to evaluate the RadTb model, using simultaneous measurement of environmental parameters and measured Tb's from the well-calibrated WindSat

imaging radiometer. The WindSat obtains global brightness temperature images of the ocean surface (off-nadir in a conical scan) using four microwave frequencies (6.8 GHz, 10.7 GHz, 18.7 GHz and 37.0 GHz) and vertical and horizontal polarizations. This research characterizes the accuracy of the RadTb calculations through statistical comparisons with the WindSat radiometer as a function of frequency, polarization and atmospheric and surface environmental parameters.

The topics discussed in this thesis, include the discussion of: the fundamental concepts of microwave remote sensing in this chapter; satellite microwave radiometers used in this investigation in Chapter 2; investigation of the systematic error in the RadTb model and the radiative transfer model tuning is described in Chapter 3; and results and evaluations are presented in Chapter 4. Finally, conclusions and recommendations for future studies are presented in Chapter 5.

1.2 Fundamental Concepts of Microwave Remote Sensing

1.2.1 Blackbody Radiation

Based on the principles of thermodynamics, all matter above temperatures of zero Kelvin both absorb and emit EM energy simultaneously. A medium which perfectly absorbs and emits energy is called a blackbody. The relationship between the spectral flux density of energy

emitted from a blackbody, temperature and wavelength is described by Planck's law [3]:

$$S(\lambda) = \frac{2\pi hc^2}{\lambda^5} \frac{1}{e^{ch/\lambda kT} - 1} \qquad (1\text{-}1)$$

where, $S(\lambda)$ = spectral radiance per wavelength band in Watts per unit area per incremental wavelength ($W*cm^{-2}*\mu m^{-1}$)

h = Planck's constant = 6.6253×10^{-34}, joule/sec

k = Boltzmann's constant = 1.38×10^{-23}, joule/Kelvin

c = the speed of light in a vacuum = 3.0×10^8 m/s

T = physical temperature of black body in Kelvin

λ = observing wavelength

In the microwave region, the Rayleigh-Jean law can be used to approximate the blackbody radiation described by Planck's law. For the Rayleigh-Jean law to be applicable $ch/\lambda << kT$, which means that this law is applicable for frequencies less than 100 GHz. The spectral emittance is given by:

$$S(\lambda) = \frac{2\pi ckT}{\lambda^4} \qquad (1\text{-}2)$$

On a log-log plot, the spectral emittance appears as a straight line as described by the Rayleigh-Jeans Law:

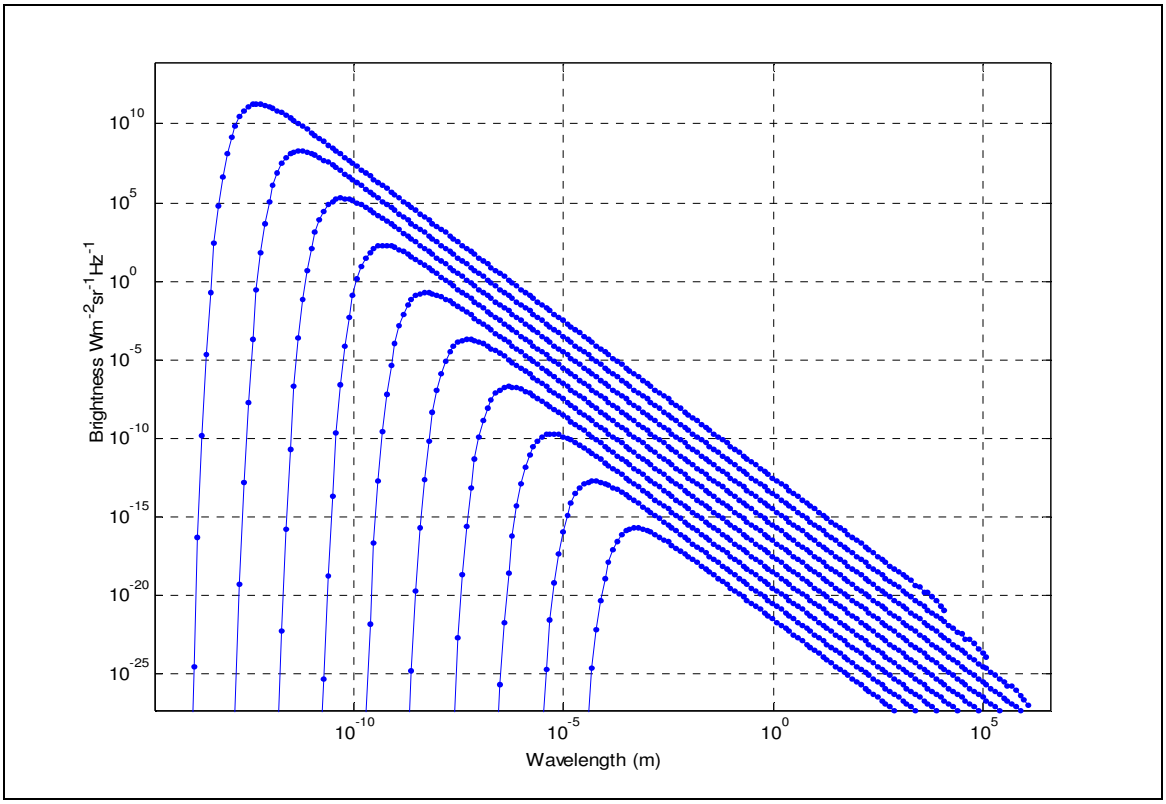

Figure 1: Planck's Blackbody Radiation

1.2.2 Emissivity

The emissivity coefficient relates how efficiently energy is radiated from a physical media in comparison to a perfect blackbody. The emissivity factor varies with the media's electric (permittivity) and magnetic (permeability) properties, which typically changes with wavelength (EM frequency). For example, the 10-12 μm (micron) infrared band is the most suitable one for the determination of surface temperatures by space remote sensing for cloud-free

conditions, since it is situated in the atmospheric window and the relative emissivity of surfaces (land, water and ice) in this wavelength interval is comparatively stable and close to unity [4].

Infrared radiometry provides good resolution of environmental observance such as sea surface temperature. However, infrared measurements are obscured by the presence of clouds. At any given time, approximately 40% of the earth is covered with clouds. Microwave remote sensing is a valuable way of measuring environmental changes as it is relatively insensitive to atmospheric conditions, such as clouds and water vapor, and microwave radiometers are able to measure blackbody emissions day or night and nearly independent of weather conditions.

When observing a blackbody, the power collected by a microwave radiometer antenna is directly proportional to its physical temperature (T_{phys}) and the receiver bandwidth:

$$P_{blackbody} = kT_{phys}Bandwidth \tag{1-3}$$

Thus, the physical temperature may be derived from the radiometer received power measurement.

For a non-blackbody media, the corresponding derived microwave brightness temperature, T_b, is equivalent to the emissivity of the media times its physical temperature:

$$T_b = \varepsilon * T_{phys} \tag{1-4}$$

Non-blackbodies, sometimes called grey-bodies, have emissivities varying between zero and one. The emissivity value can be determined by considering the propagation of EM energy at the interface between two media. When a free propagating EM wave encounters the interface between two media having different electric (or magnetic) properties, it experiences a change in

characteristic impedance, which is determined by the local permittivity (ε) and permeability (μ). For a slightly lossy dielectric medium, the intrinsic impedance of the medium [5] can be derived according to equation:

$$\eta = \sqrt{\mu / \varepsilon_c}\ , \text{ ohms} \qquad (1\text{-}5)$$

where ε_c is the complex permittivity also referred to as the complex dielectric constant.

As an EM wave travels from one medium to another, it is reflected and/or transmitted depending on changes in the characteristic impedance, η. The diagram below illustrates the reflection and transmission of a plane wave at the air/ocean boundary. The incidence angle is the angle between the propagation direction and the perpendicular to the water surface. According to Snell's law, the angles of incidence and reflection (θ_1) are equal and the angle of refraction (θ_2) is calculated.

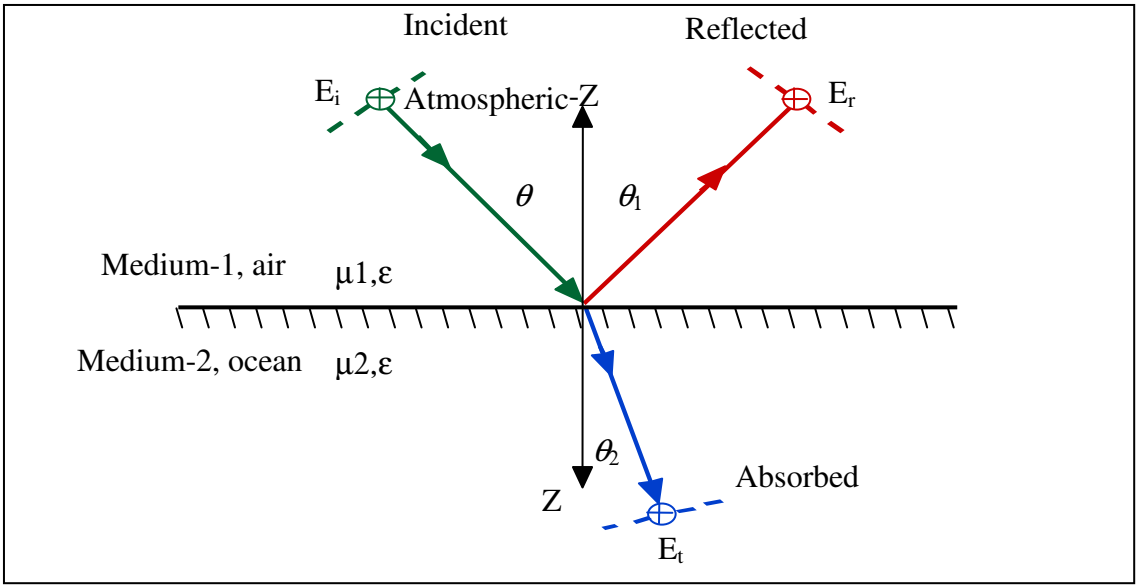

Figure 2: Plane waves reflection and transmission at the air/ocean interface.

A portion of the wave is reflected in the specular direction into the original medium, while the remainder is transmitted across the interface and is absorbed by the bulk media [5]. The voltage reflection coefficient, $\boldsymbol{\rho}$, is a function of the incidence angle and polarization of the EM wave and the change in the characteristic impedances between the two media. For smooth surfaces, the Fresnel power reflection coefficients, $\boldsymbol{\Gamma}$, between air and water for horizontal and vertical polarized incident waves are [5]:

$$\Gamma_{V-pol} = \left|\rho_{v-pol}\right|^2 = \left|\frac{\varepsilon_2 \cos\theta_1 - \sqrt{\mu_2\varepsilon_2 - \sin^2\theta_1}}{\varepsilon_2 \cos\theta_1 + \sqrt{\mu_2\varepsilon_2 - \sin^2\theta_1}}\right|^2 \qquad (1\text{-}6)$$

$$\Gamma_{H-pol} = \left|\rho_{H-pol}\right|^2 = \left|\frac{\mu_2 \cos\theta_1 - \sqrt{\mu_2\varepsilon_2 - \sin^2\theta_1}}{\mu_2 \cos\theta_1 + \sqrt{\mu_2\varepsilon_2 - \sin^2\theta_1}}\right|^2 \qquad (1\text{-}7)$$

A plot of the magnitude of the Fresnel voltage reflection coefficient of water versus incidence angle is shown in Figure 3. The horizontal polarized reflection coefficient increases with incidence angle, while the vertical polarized reflection coefficients decrease with incidence angle. At the Brewster angle ($\theta = 83°$), a null reflection is present for the vertical polarization. Also, note at normal incidence, ($\theta = 0°$), the reflection coefficients for vertical and horizontal polarizations are equal.

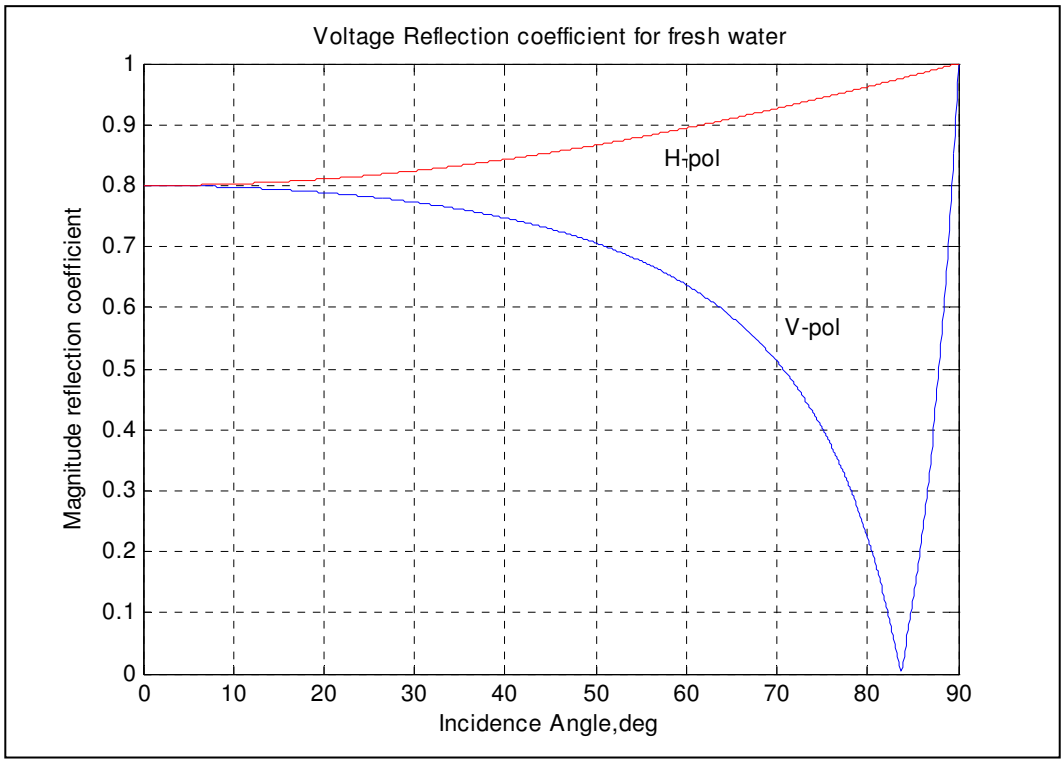

Figure 3: Magnitude of voltage reflection coefficient of water (y-axis) versus incidence angle in deg. Note 83° is the Brewster angle.

1.3 Microwave Interaction in Atmosphere

1.3.1 Dielectric Constant of Sea Water

The dielectric constant of seawater determines its impedance properties, which govern the reflectivity and emissivity at the ocean/air interface. For seawater, the dielectric constant is complex (real and imaginary parts) and is a function of physical parameters (sea surface temperature and salinity) and the frequency of the EM wave. The behavior of the dielectric constant is modeled by the Debye equation [6]:

$$\varepsilon_{s\omega} = \varepsilon_{s\omega\infty} + \frac{(\varepsilon_{s\omega 0} - \varepsilon_{s\omega\infty})}{1 + j2\pi f \tau_{s\omega}} \qquad (1\text{-}8)$$

$\varepsilon_{s\omega\infty}$ = magnitude of the high-frequency relative dielectric constant = 4.9 from [7], dimensionless

$\varepsilon_{s\omega 0}$ = static dielectric constant of saline water is a function of temperature from [8] , dimensionless

f = EM wave frequency, Hz

$\tau_{s\omega}$ = relaxation time of sea water is a function of temperature and salinity, s

Salinity is the measure of the concentration of salt (grams) in a kilogram of saltwater (parts per thousand).

The real part of the relative dielectric constant is:

$$\varepsilon'_{s\omega} = \varepsilon_{s\omega\infty} + \frac{(\varepsilon_{s\omega 0} - \varepsilon_{s\omega\infty})}{1 + (2\pi f \tau_{s\omega})^2} \tag{1-9}$$

and the imaginary part is:

$$\varepsilon''_{s\omega} = \frac{2\pi f \tau_{s\omega}(\varepsilon_{s\omega 0} - \varepsilon_{s\omega\infty})}{1 + (2\pi f \tau_{s\omega})^2} + \frac{\sigma_1}{2\pi\varepsilon_0 f} \tag{1-10}$$

σ_1 = ionic conductivity is a function of temperature and salinity

Knowing the dielectric constant of the two media allows the reflectivity properties to be determined as described by equations (1-6) and (1-7), which is used in calculating the emissivity and reflectivity of the ocean.

1.3.2 Ocean Surface Emission and Reflection

At the air/ocean interface, some of the microwave energy is transmitted across the boundary and the remainder reflects back into the media in which it is propagating. This is illustrated in figure 2 for a wave traveling in air toward the water, and the reflected sky brightness emission occurs at the ocean surface.

Further, this process is reciprocal so that a similar figure applies to a wave propagating in water toward the air. Internal in seawater, the microwave emission is blackbody, but because of the change in impedance, there is a reflection at the water/air interface. Snell's law and the Fresnel voltage reflection coefficient determine the reflection in the specular direction relative to

the incident wave; and the emissivity is the percentage of the blackbody emission (power) that crosses through this boundary.

Ocean physical properties, sea surface temperature and salinity, affect its emissivity through changes in the complex dielectric constant. Also, surface winds cause the generation of small ocean waves that roughens the surface; and this results in diffuse scattering that increases the Fresnel power reflection coefficient (Γ), which in turn affects the emissivity. Also, larger breaking waves cause foam, which is approximately a blackbody to microwaves, which increases the surface emissivity. Both the roughness and fractional foam coverage are strongly dependent on the interaction of the wind and seawater. By the conservation of energy, the transmission coefficient of energy from the seawater into the atmosphere is the emissivity, which is equal to $(1-\Gamma)$, where Γ includes specular and diffuse reflection as well as the fractional foam cover reductions in the overall reflectivity.

1.4 Microwave Interaction in Atmosphere

The interaction of microwaves with the earth's atmosphere is dominated by absorption and emission by gas molecules of water vapor, oxygen, and cloud liquid water and precipitation.

1.4.1 Water Vapor Absorption

In the atmosphere, microwaves under-go resonant absorption (and emission) at certain

wavelengths due to the quantum energy states of the water vapor molecule. Thus, the presence of water vapor in the atmosphere causes an increase in the brightness measured by a microwave radiometer. The strength of the microwave emission depends upon the total number of water vapor molecules along the propagation path through the atmosphere and their ambient pressure. At higher altitudes, the number of molecules per unit volume (density) decreases; but the decrease of pressure reduces the bandwidth of water vapor emission (absorption), which increases the strength of the absorption at the peak of the resonance line. The water vapor absorption coefficient, shown for sea level pressure in figure 4, is calculated as a function of altitude using the Van Vleck-Weisskopf model as modified by Gross [9]. The peak of emission due to water vapor is concentrated at the 22.2 GHz and 183.3 GHz.

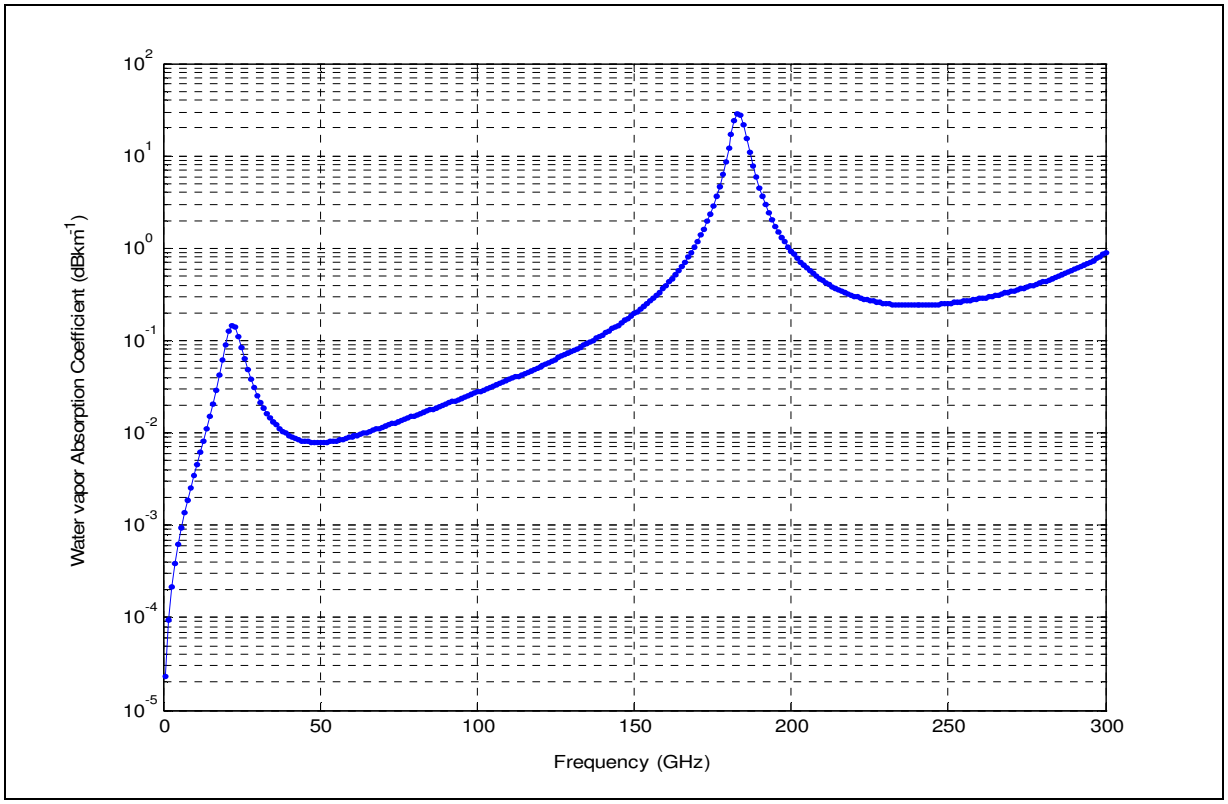

Figure 4: Calculated water vapor absorption at sea level pressure.

1.4.2 Oxygen Absorption

The second main contributor to atmosphere microwave absorption (and emission) is molecular oxygen. The significant absorption bands for oxygen consist of a cluster of resonant lines in the 50 to 70 GHz region of the microwave spectrum and a second harmonic absorption line at 118.75 GHz [10]. Like water vapor, the absorption is proportional to the number of oxygen molecules along the propagation path through the atmosphere, which varies with altitude

according to the pressure level in the atmosphere. An increase in altitude causes a decrease in pressure, which results in a decrease in the amount of oxygen present in the atmosphere; but the absorption line bandwidth narrows and becomes stronger at the resonant frequency [11]. The intensity of the absorption is due to the following; the number of absorbing oxygen molecules per unit volume (gas density), the temperature and pressure of the gas, and the molecular transitions (allowed quantum energy states) for the oxygen molecule.

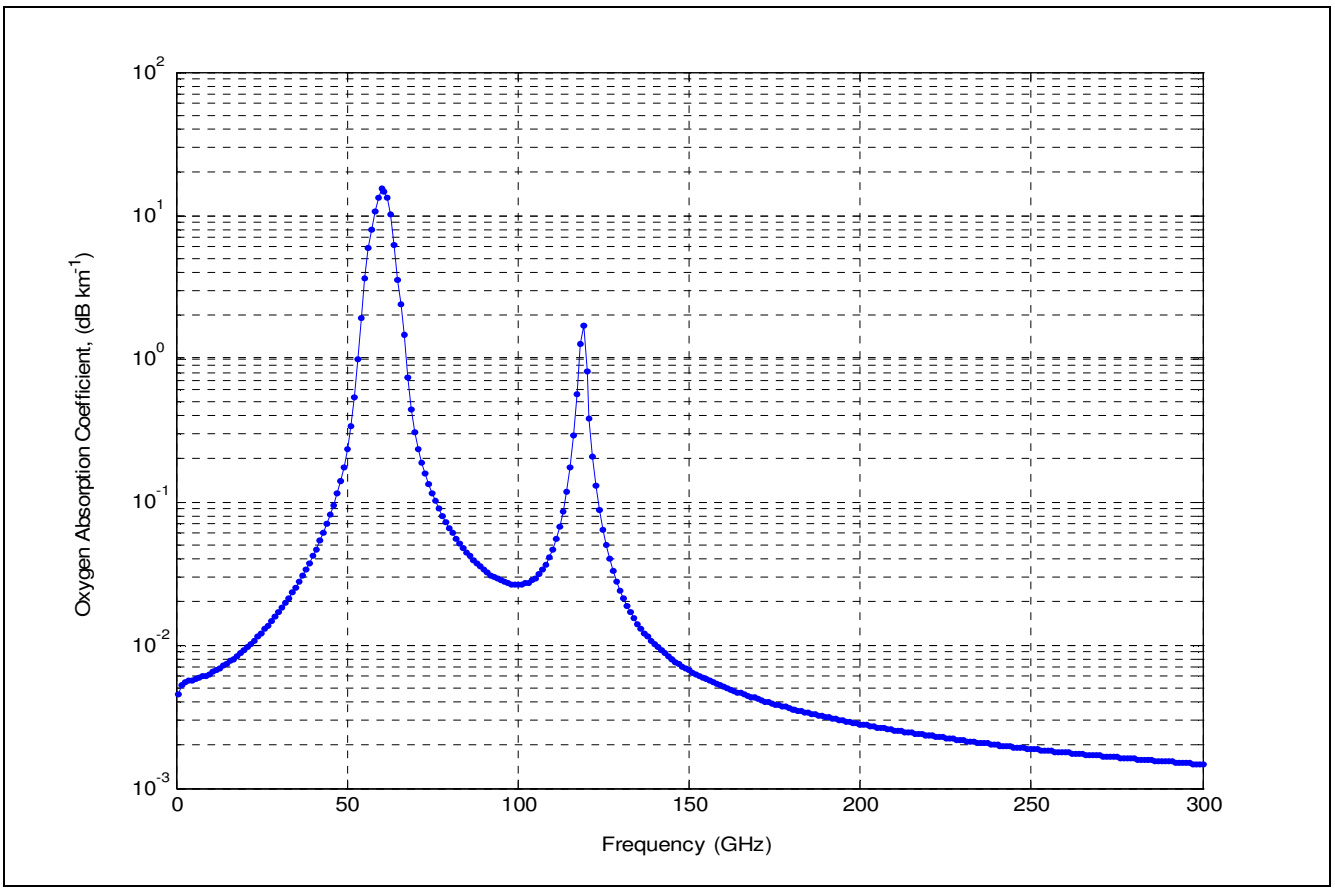

Figure 5: Calculated water vapor at sea level conditions.

1.4.3 Cloud Liquid Water Absorption

For microwave frequencies > 10 GHz, propagation in the atmosphere is also affected by clouds. Clouds consist of small liquid water droplets of condensed water vapor above the surface of the Earth. Solar absorption of visible light at the earth's surface causes the air at the ground surface to be heated through conduction. When a parcel of air rises, it expands as the atmospheric pressure decreases with height, and this process (known as an adiabatic expansion) causes the air to cool; and the resulting negative rate of change of the air parcel's temperature with height is referred to as the lapse rate. When water vapor is present and the temperature is right for condensation, a cloud base formation will result and liquid water is carried above the freezing level by the vertical motion of the air. At any given time, about half of the earth is covered with clouds [4].

The interaction of electromagnetic waves with cloud water droplets causes absorption and emission of energy. The amount of energy emission is dependent on the integration of the volume of the cloud particle size distribution, the density of cloud liquid and the dielectric properties of water. This microwave absorption grows approximately as the square of the microwave frequency. Because the cloud liquid water particles are usually less than 100 μm [Elachi], scattering of blackbody emissions does not occur at microwave frequencies (< 100 GHz). For this Rayleigh region, the scattering effect, on both emission is negligible because the diameter of the water droplets is very much smaller than the wavelength of the radiation.

1.4.4 Precipitation

When microwaves encounter precipitation, it causes absorption of energy and if the hydrometeors are large enough, scattering of the propagating EM wave. The absorption and corresponding emission occur simultaneously in a thermodynamic balance; but scattering has the effect of reducing the emission that reaches the top of the atmosphere. Of the different forms of precipitation, such as rain and snow, only the liquid form of precipitation causes absorption (frozen water is mostly transparent). Rain particles are water droplets of 0.5mm or greater; and when rain droplets are larger than 5-6 mm, scattering of energy occurs at the high frequency microwave region, typically > 20 GHz.

1.5 Radiative Transfer Theory

The collection of natural gray-body emission, received by a satellite microwave radiometer viewing the ocean through the Earth's atmosphere, is illustrated conceptually in figure 6. Because each source of brightness temperature is wide-band Gaussian noise, the radiometer simply collects the total power i.e., the sum of the three components. To interpret the radiometer measurements, the theory of radiative transfer must be applied to model the emissions (brightness temperature) from various sources, which are:

1. The ocean brightness temperature propagated upwards through a slightly absorbing atmosphere to the antenna.

2. The sum of the cosmic background radiation and the downward-welling brightness temperature of the atmosphere propagated down to the ocean surface and then reflected and transmitted upwards to the antenna.
3. Direct upwelling emission of the brightness temperature of the atmosphere to the antenna.

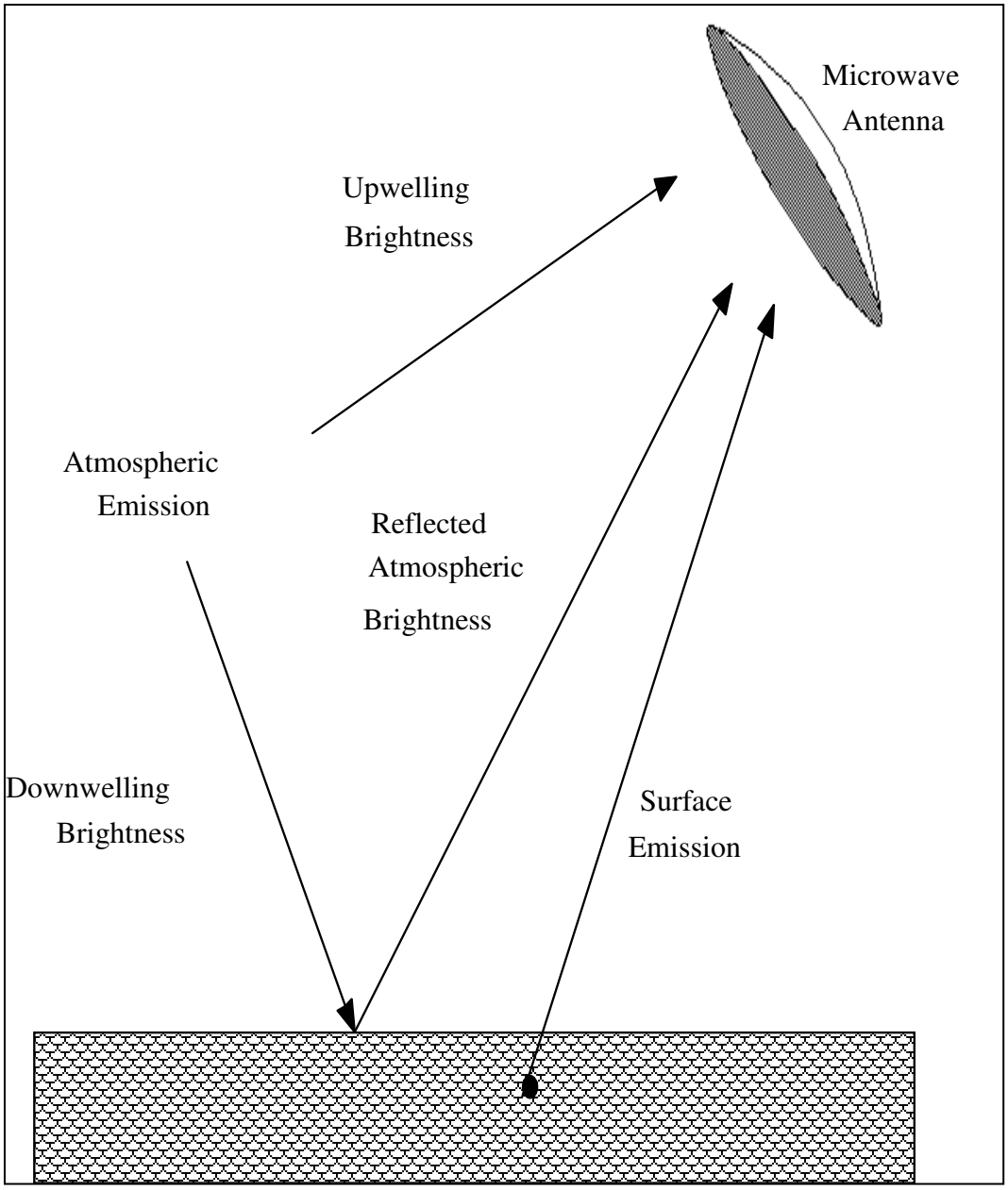

Figure 6: Satellite microwave radiative transfer concept.

All electromagnetic factors contributing to the apparent brightness temperature are a

function of microwave frequency, antenna polarization and incidence angle. Along the propagation path observed from the satellite antenna to the surface, for $\theta \le 70^o$, the path length through the atmosphere is approximated by the height of the atmosphere times the $\sec\theta$. Along this path, knowing the total loss factor of the atmosphere, L_o, affects the Tb seen by the satellite radiometer. The attenuation factor K_a, is the summation of absorption coefficients due to water vapor, oxygen and cloud liquid water. The optical depth (opacity) of the atmosphere is defined by:

$$\tau_o = \int_0^L K_a dz \text{ , Nepers,} \qquad (1\text{-}12)$$

where **z** is the height above the surface. The total loss from the surface to the top of the atmosphere,

$$L_o = e^{-\tau_o} \qquad (1\text{-}13)$$

The down welling brightness temperature,

$$T_{dn} = \sec(\theta)\int_0^\infty K_a(z)T(z)e^{-\tau_o(z)}dz\,, \qquad (1\text{-}14)$$

where $T(z)$ is the atmospheric physical temperature profile, and the integral upper limit is the top of the atmosphere (~ 20 Km). Once the down-welling energy reaches the ocean surface, some of it is absorbed in the ocean while the rest is reflected specularly into the atmosphere. The direct emission of the ocean radiance from the ocean to the atmosphere is:

$$T_b = \varepsilon * SST\,, \qquad (1\text{-}15)$$

where SST is the sea surface temperature

The sky brightness T_{sky}, is:

$$T_{sky}(\theta) = T_{down}(\theta) + T_{ex}(\theta)e^{-\tau_o \sec\theta} \quad (1\text{-}16)$$

T_{ex} is the sum of the cosmic and galactic radiation equal to 2.7K

A portion of the microwave incident on the ocean surface is reflected, T_{refl} towards the atmosphere. The magnitude of the reflected wave is dependent on the emissivity (power reflectivity) of the ocean.

$$T_{refl}(\theta) = \Gamma T_{sky}(\theta) = (1 - \varepsilon) T_{sky}(\theta) \quad (1\text{-}17)$$

The resulting brightness measured by the radiometer is given by the radiative transfer equation:

$$T_{ap}(\theta) = T_{up}(\theta) + T_b e^{-\tau_o \sec\theta} + T_{refl} e^{-\tau_o \sec\theta} \quad (1\text{-}18)$$

The apparent brightness temperature measured over the scene by the satellite antenna is used extensively in the scientific field and civil community. The brightness temperature retrieved from the satellite radiometer must be accurate and precise for useful utilizations. The following chapter describes the SSM/I and Windsat instruments, whose environmental and brightness temperature products are used respectively in this research. Chapter two also discusses the total power radiometer and the calibration techniques used to improve accuracy in measuring brightness temperature at the radiometer antenna.

CHAPTER TWO: SATELLITE MICROWAVE RADIOMETERS

2.1 Satellite Microwave Remote Sensing History

The purpose of this chapter is to describe two satellite microwave radiometer imagers, whose brightness measurements (brightness temperatures and retrieved geophysical products) are used in this thesis. These imagers are the Special Sensor Microwave Imager (SSM/I) and the Microwave Polarimetric Radiometer (WindSat).

2.2 Microwave Radiometry

2.2.1 Total Power Microwave Radiometer

In chapter one, the theory of radiative transfer was used to describe the total apparent brightness temperature incident on a satellite radiometer antenna. This chapter describes the

microwave radiometer system hardware used to measure the apparent brightness temperature. The simplest type of system is the total power radiometer (shown in figure 7) comprises an antenna to capture the incident radiation, a highly sensitive receiver and power detector, and an integrator/dc amplifier output. The noise output power from the antenna (input to the receiver), P_a, is

$$P_a = KT_aB \tag{2-1}$$

where K is Boltzmann's constant, J/K

T_a is the antenna noise temperature, K

B is the noise effective bandwidth of the radiometer receiver, Hz

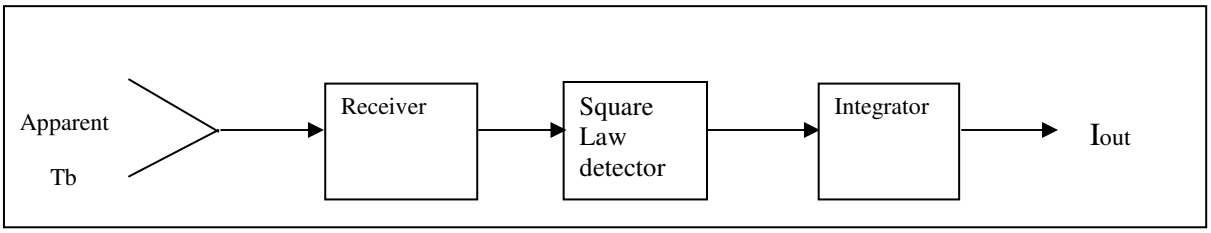

Figure 7: Simplified diagram of a total power radiometer

The antenna is connected to a "noisy" receiver, which generates noise power internally that adds to the noise collected by the antenna; therefore, system has an effective input noise power:

$$P_{sys} = KT_{sys}B \tag{2-2}$$

where

Tsys the system input noise temperature, define as:

$$T_{sys} = T_a + T_{rec} \tag{2-3}$$

T_{rec} is the receiver equivalent input noise temperature, K

The signal is then amplified with a power gain, G, by radio frequency and/or intermediate frequency (IF) amplifiers to produce an output power (average), P_{IF} is:

$$P_{IF} = G * k * T_{sys} * B \tag{2-4}$$

A square law detector is used to detect the mean value of the system output noise power. The average value of the output of the square law detector, $\overline{V_d}$ is:

$$\overline{V_d} = C_d * P_{IF} \tag{2-5}$$

where C_d is the square law detector power sensitivity constant

The signal at the output of the square law detector is then passed through a low pass filter to reduce unwanted ac signal components of the detected voltage, which is equivalent to integrating V_d over some interval of time, τ_{avg}. The integrator dc output voltage component (I_{out}) is proportional to the average system temperature $<T_{sys}>$. The minimum change in T_{sys} that can be reliably detected (i.e., the radiometer measurement precision) is known as the radiometer ΔT. This corresponds to equation (2-6), which defines the sensitivity of the total power radiometer.

$$\Delta T \cong \Delta T_{sys} = \frac{T_{sys}}{\sqrt{B\tau_{avg}}} \tag{2-6}$$

To ensure absolute accuracy of the measured antenna temperature, radiometer system calibration techniques are employed as discussed in the following section.

2.2.2 Radiometric Calibration

Radiometric calibration is the mapping of input apparent brightness temperature, at the radiometer antenna aperture, and the integrator output in terms of volts or digital counts. Since there are other internal sources of noise (e.g., receiver noise) that must be removed from the radiometer output to yield the desired antenna brightness temperature, it is best when radiometer is calibrated directly at the antenna aperture.

This external radiometric calibration can be achieved with at least two blackbody targets of known brightness temperatures placed in front of the antenna aperture. In this manner, the integrator output indication ($I_{\text{out,}}$) is linearly related to the antenna temperature T_a. In the case of the total power radiometers, a hot and cold target are used as the calibration sources and their corresponding measurement according to [2] indicates that:

$$I_{out}^{h} = a(T_{cal}^{h}) + b, \text{ hot target calibration point} \tag{2-7}$$

$$I_{out}^{c} = a(T_{cal}^{c}) + b, \text{ cold target calibration point} \tag{2-8}$$

Solving the above equations for the constants a (receiver gain) and b (integrator offset) provide the radiometer linear transfer function. With good square-law detectors, linearity is not a significant issue as the dynamic range of the radiometer is very small (< 3 dB). The usual practice is to assure that the hot and cold targets bracket the scene brightness temperature.

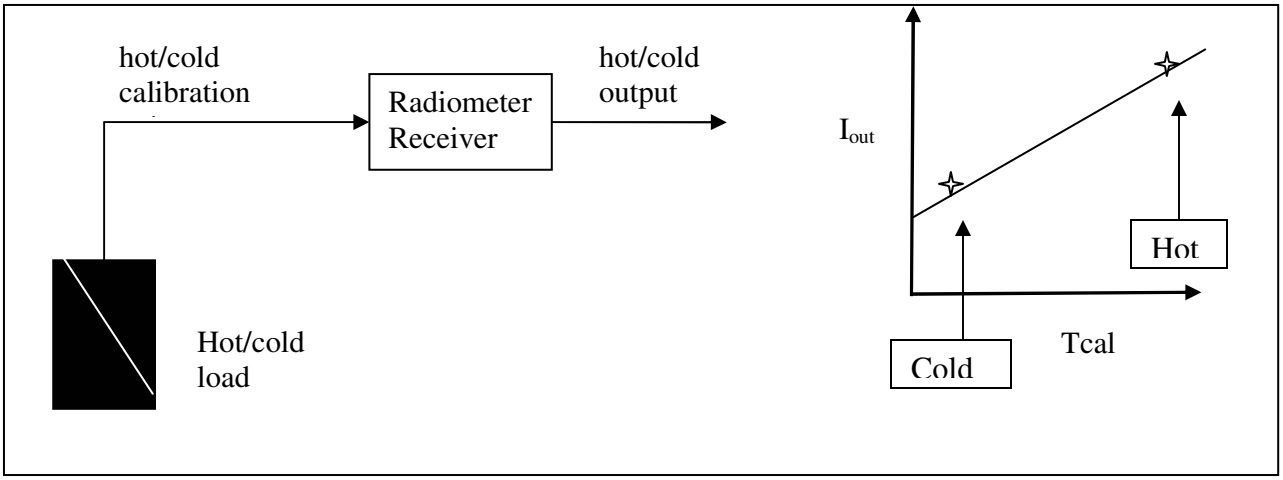

Figure 8: Calibration of a total power radiometer receiver

For space-borne conical scanning microwave imagers the radiometer calibration process uses an ambient temperature blackbody absorber as the warm load and cosmic background radiation at approximately 2.7 K as the cold load. These calibration targets are viewed by the antenna feeds once in each antenna revolution.

2.3 Satellite Microwave Radiometer Imagers

2.3.1 Special Sensor Microwave/Imager (SSM/I)

The Special Sensor Microwave Imager (SSM/I) [12] is a passive microwave sensor that

was first launched June, 1987, onboard the US Air Force Defense Meteorological Satellite Program (DMSP) F8 satellite. Subsequently six SSM/I's have flown on DMSP, and currently three are operating on satellites F-13, F-14 and F-15 [8], which are in circular, sun-synchronous, and near-polar orbits. The SSM/I operates with seven microwave channels and the effective fields of view (EFOV) summarized in table 1. Figure 9 shows SSM/I conical scanning the earth over a ± 51° arc centered on the satellite track, which results in 1394 Km swath width. The SSMI obtains global measurements of water-related geophysical parameters, several of which are relevant to this thesis, namely; water vapor, cloud liquid water, sea-surface wind speed and precipitation. These environmental parameters will be used as input to RadTb in the comparisons described in Chapter 3.

Table 1: SSM/I Channel Characteristics

		Foot Print Size (EFOV)	
Channel Frequency (GHz)	Polarization	Along Track, km	Cross Track, km
19.35	vertical	69	43
19.35	horizontal	69	43
22.235	vertical	60	40
37	vertical	37	28
37	horizontal	37	29
85.5	vertical	15	13
85.5	horizontal	15	13

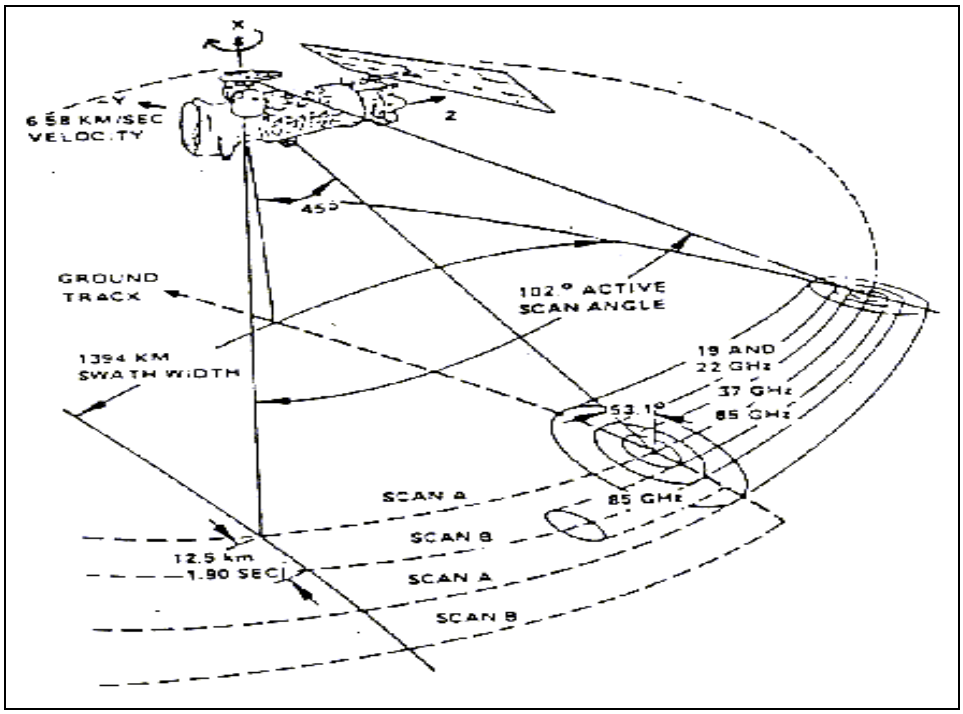

Figure 9: SSM/I scan geometry from [12]

2.3.2 WindSat

WindSat is a satellite polarimetric microwave radiometer, which is used to measure oceanic wind vector from space. It was developed by the Naval Research Laboratory for the U.S. Navy and the National Polar-orbiting Operational Environmental Satellite system (NPOESS) Integrated Program Office (IPO) [13]. WindSat is the main payload of the Coriolis, which is a sun-synchronous weather satellite in a similar orbit as DMSP F-13.

Table 2: Windsat Channel Characteristics

Channel Frequency (GHz)	Polarization
6.8	vertical , horizontal
10.7	vertical, horizontal, ± 45º, left hand circular, right hand circular
18.7	vertical, horizontal, ± 45º, left hand circular, right hand circular
23.8	vertical , horizontal
37	vertical, horizontal, ± 45º, left hand circular, right hand circular

The WindSat has a forward swath coverage of 1025 km with spatial resolution of 25 km. Though Windsat's primary mission is to measure ocean surface wind speed and direction, it also retrieves sea surface temperature, water vapor, cloud liquid water, and rain rate.

Like the SSM/I, WindSat uses offset parabolic antenna to achieve high beam efficiency up to 95% for all frequencies [13]. The WindSat antenna subsystem consist of a 1.8 m offset parabolic reflector, eleven feed horn array along with external warm and cold sky reflector for

calibration purposes as illustrated in figure 10.

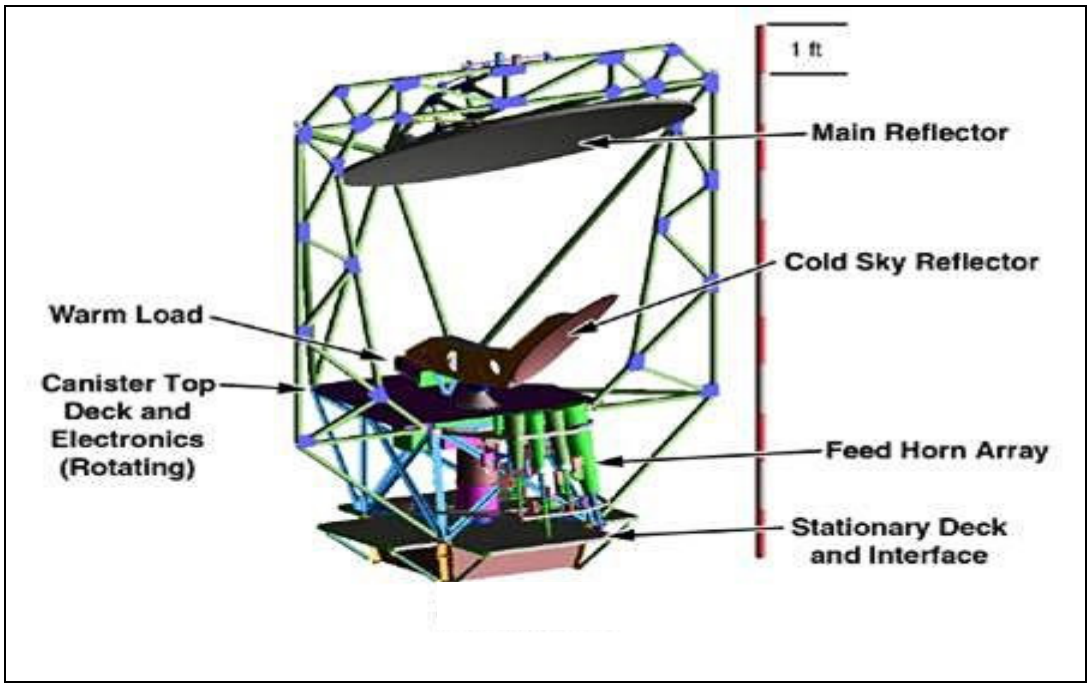

Figure 10: Windsat instrument from [20]

The Windsat radiometer is calibrated once every two seconds, as the feeds rotates about a stationary calibration assembly [21].

For this thesis, only the vertical and horizontal brightness temperature from Windsat will be compared to the corresponding calculations from RadTb. This process is described in Chapter three.

CHAPTER THREE: RADIATIVE TRANSFER MODEL EVALUATION

3.1 Introduction to Methodology of Tb calculation

As described in Chapter 1, the Central Florida Remote Sensing Laboratory uses a microwave radiative transfer model for oceans named RadTb. This model was previously evaluated by comparison with the TMR satellite radiometer [2]; and in this thesis research, when comparing measured Tb's from the WindSat satellite radiometer with corresponding modeled Tb's, results show systematic differences. The objective of this thesis is to characterize these Tb biases as a function of environmental parameters; and this chapter describes the methodology of this investigation.

WindSat was selected for comparison with RadTb model, because it is a wide-swath conical imager that operates over a wide-range of frequencies with excellent absolute accuracy [14, 15]. To effectively compare these modeled and measured Tb, the RTM input environmental parameters must be collocated spatially and temporally. For valid Tb comparisons, corresponding measurements of relevant environmental parameters that vary significantly in space and time (e.g., wind speed, cloud liquid water and precipitation) are provided by SSMI on

the DMSP F-13 satellite, which covers nearly the same measurement swath earlier. The ground track of WindSat (yellow) overlapping SSM/I (blue) is shown in figure 11. It is from these overlapped tracks the modeled Tb is calculated using RadTb. The time between the satellites passes is typically 30 – 40 minutes, so the changes in the geophysical parameters averaged over the 25 Km sensor footprints are fairly insignificant. For other atmospheric environmentals that vary slowly in space and time, a temporal window of ± 1.5 hours about the closest numerical weather analysis time was used for these inputs to RadTb.

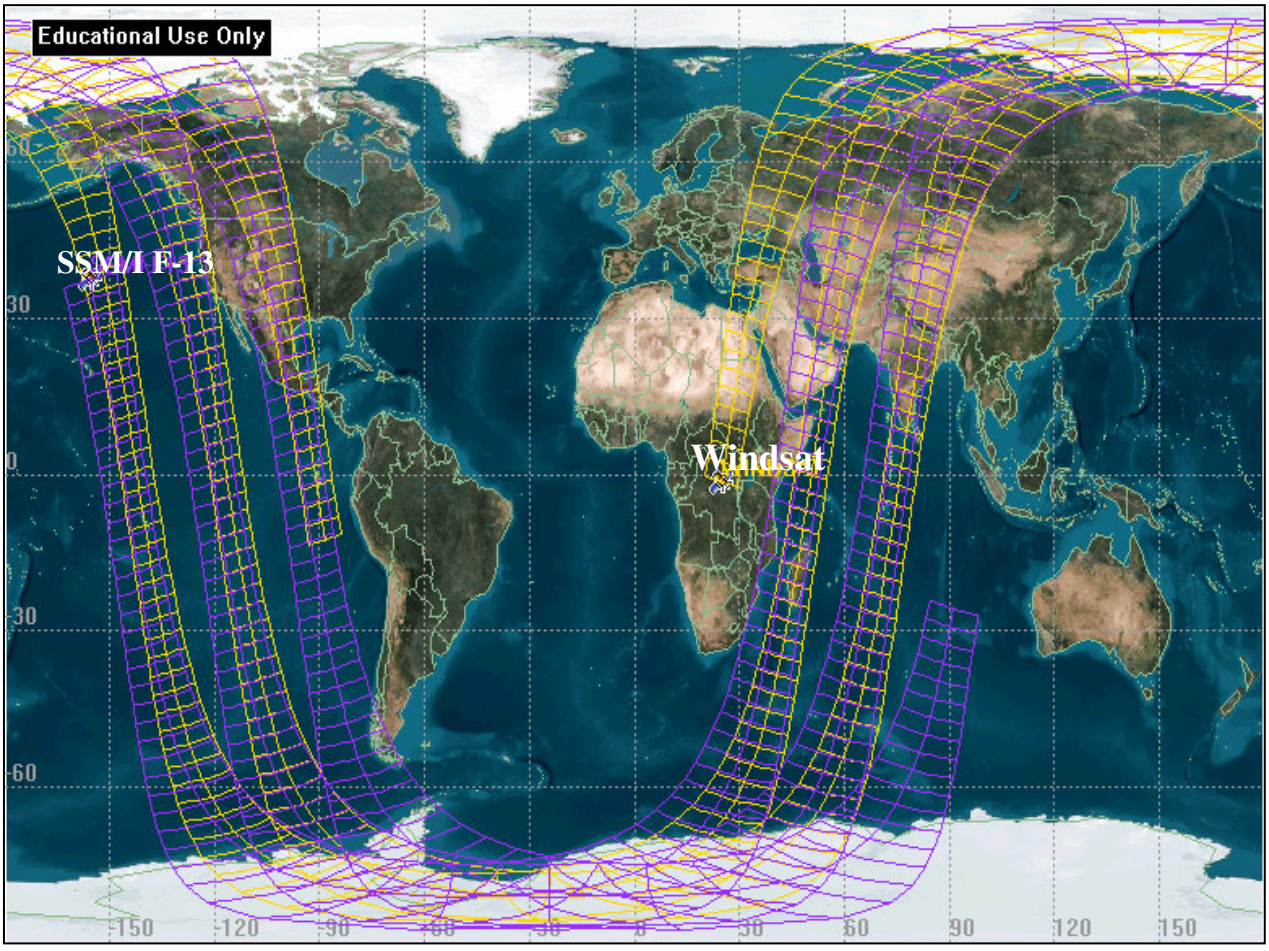

Figure 11: Collocated area of SSM/I DMSP F-13 satellite with Windsat satellite

RadTb uses 14 environmental parameters, which are shown in table 3. The table also shows the sources of these environmental data. A few of the atmospheric parameters, such as the height (top and base) of the cloud and the water vapor mixing ratio above the tropopause are based on typical climatological values.

Table 3: 14 Environmental parameters and their sources

Input Environmental Parameters	Sources
Surface pressure (mb)	NCEP
Surface air temperature (deg C)	NCEP
Air temperature vertical lapse rate (deg C/Km)	NCEP
Surface absolute humidity (gm/m^3)	derived from SSM/I and NCEP products
Columnar density of water vapor (gm/square cm)	SSMI DMSP/F13
Temperature of the tropopause (K)	NCEP
Water vapor mixing ratio above the tropopause =2*10^-6	water vapor climatology
Columnar of cloud liquid water (gm/ cm^2)	SSMI DMSP/F13
Height of cloud base (Km)=1.8	Cloud climatology
Height of cloud top (Km)=0.3	Cloud climatology
Wind speed (m/s)	SSM/I on DMSP F13 satellite
Sea surface temperature (deg C)	Reynold's Sea Surface Temperature Database
Salinity (parts per thousand)	NODC WOA98 Ocean Salinity Database

An overview of the procedure for calculating the Tb using the 14 environmental parameters is presented in figure 12, and a description of the various sources is presented in the following sections of this chapter.

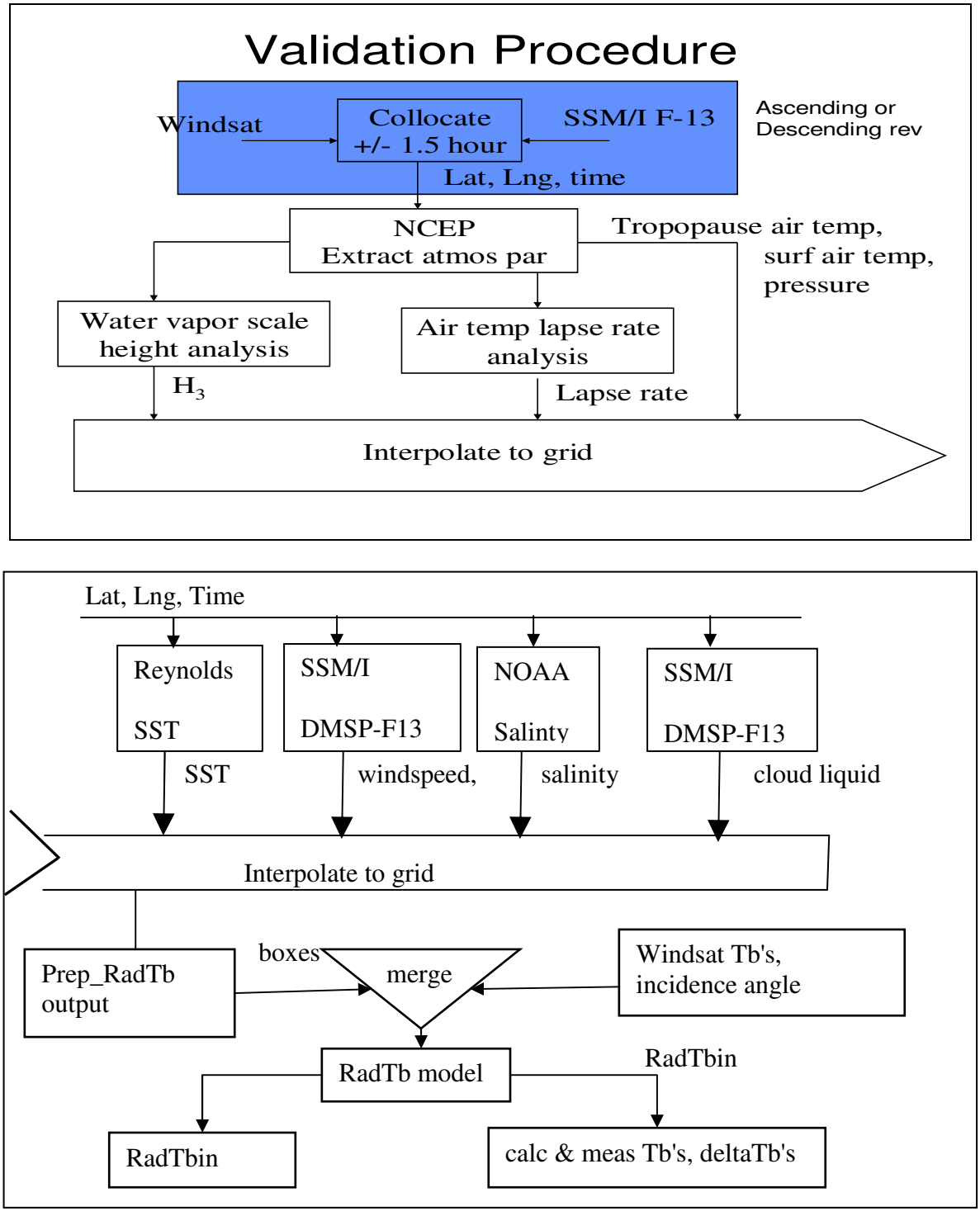

Figure 12: Validation Procedure

3.1.2 SSM/I Geophysical Products

SSMI/I retrievals of geophysical data over oceans include; surface wind speed, integrated "columnar" atmospheric water vapor, integrated cloud liquid water and path average rain rate are derived daily from ascending and descending passes of the DMSP F-13 satellite by Remote Sensing Systems [16]. However, when there is precipitation (rain), these data are flagged and RadTb skips the calculation of the apparent brightness temperature. Because it is very difficult to model rain Tb, these calculations are not included in the RadTb model. Further, because of the transient nature of oceanic rain, the 30 minutes temporal registration between SSM/I and WindSat is not sufficient for "simultaneous" collocations. The SSM/I products available from the Remote Sensing Systems website consist of pre-rendered daily data on a 0.25° grid that are separated into ascending and descending revolutions (half orbits) [16]. These SSM/I products are interpolated to the WindSat measurement locations on a fixed earth grid, 25 km latitude by 25 km longitude.

3.1.3 NCEP

The National Centers for Environmental Prediction (NCEP) numerical weather model reanalysis atmospheric profiles of pressure, temperature and humidity are the environmental parameters used by RadTb. The National Oceanic and Atmospheric Administration's (NOAA) global weather model is used to predict estimates of the atmospheric weather every 6 hours on ~

2.5° latitude by 2.5° longitude grid. There are 17 vertical layers considered for the atmospheric profile [17]. Re-analysis of the weather observations is later performed to improve the atmospheric profile using observations not available for the real-time weather model run. The improved atmospheric parameters (humidity, surface pressure, temperature etc) are then used as input to the RTM.

The relevant atmospheric parameters are derived from the NCEP parameters, interpolated and gridded to 0.25° resolution to that of the geophysical area of the SSM/I pass. These parameters include the derived air temperature lapse rate (ºC/km), which is the linear regression of air temperature with geopotential height. Also, the water vapor scale height (km) was derived using NCEP specific humidity for the first seven layers of atmospheric profile. The derived water vapor scale height is the negative of the slope of natural logarithmic of specific humidity regressed against the geopotential height. After calculating the water vapor scale height, it is used to derive the surface absolute humidity (AHS) by:

$$AHS = 10 * H2OV / H_3 \text{ , gm/m}^3 \qquad (3\text{-}1)$$

where, *H2OV* is the columnar water vapor retrieved by SSM/I

H_3 is the water vapor scale

3.1.4 Reynolds Sea Surface Temperature

Reynolds sea surface temperature is produced on a weekly basis. The global sea surface temperature NCEP product is produced on a 1º grid using in situ and satellite infrared and

microwave SST's [18]. The sea surface temperature is interpolated and applied to produce a 0.25º resolution of an earth grid image. The image in figure 13 shows an improved resolution of the global sea surface temperature. The color bar in figure 13 indicates the variation of SST in Kelvin. Along the equator, sea surface temperature is usually higher and gradually decreases in temperature towards the poles. Water vapor is highly correlated to the variation in sea surface temperature.

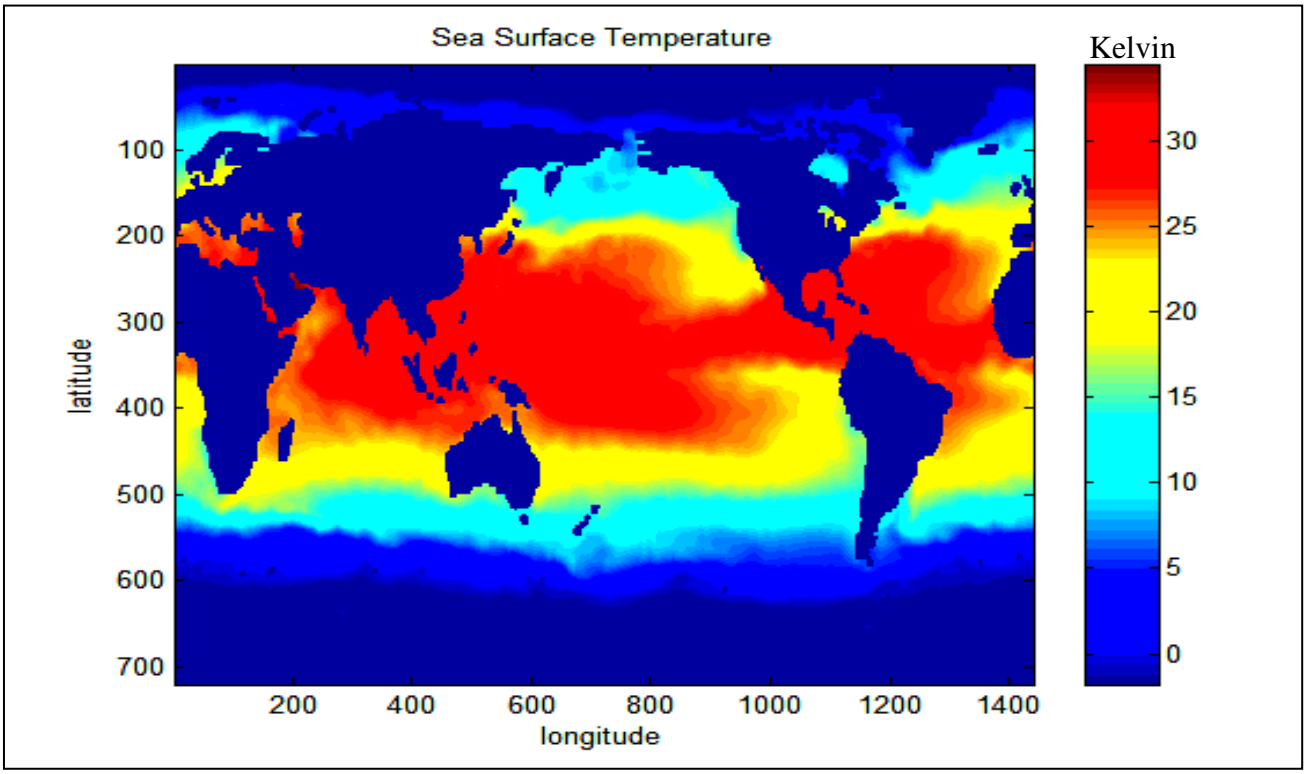

Figure 13: Global sea surface temperatures

3.1.5 Ocean Salinity

Another input parameter to the RTM is ocean salinity. Monthly ocean salinity data is obtained from NOAA National Ocean Data Center (NODC) WOA98 Ocean Salinity climatology [19]. The global coverage of salinity measurements is very sparse as only certain area of the ocean have been sampled by ship borne measurements to determine the sea water salt content. Fortunately, salinity spatial variation is very smooth; so the monthly ocean salinity could be interpolated and gridded to provide the salinity global coverage to a 0.25º grid.

3.1.6 Prep_RadTb

Prep RadTb is the FORTRAN program that prepares an input vector of 14 environmental parameters for the RadTb model. For a collocated area, a user selects a rectangular latitude-longitude box and specifies either an ascending or descending rev to extract and process SSM/I environmental parameters. Prep_RadTb then gathers the necessary NCEP files that are used to generate the relative atmospheric data collocated (space and time) with the SSM/I parameters. The weekly Reynolds SST and monthly salinity databases are also used by the program to extract these ocean parameters.

Prep_RadTb interpolates the geophysical data to the 0.25º by 0.25º resolution earth grid and performs the required unit conversion of input parameters required by RadTb . Prep_RadTb also generates a number of environmental parameters categories (boxes) for wind speed, water

vapor, sea surface temperature and cloud liquid water based on the specified threshold conditions of these four parameters. A 16-column ASCII matrix is the output from Prep RadTb, which includes the pixel longitude and latitude indices with the corresponding 14 environmental parameters.

3.1.7 Windsat Measured Brightness Temperature

The measured Tb data were extracted from the WindSat Sensor Data Record (SDR) provided by the Naval Research Lab (NRL) in Washington DC. This file (SDR) is composed of data records spaced in time for every fourth 37 GHz CP measurement. The SDR is a binary file with FORTRAN 90 structure for each SDR record. The following structures were selected to obtain WindSat's Tb's:

```
real :: Radiometers (16)
real :: BAPTAAngle
real :: Latitude
real :: Longitude
real, dimension(5) :: EIA
integer :: SpinCounter
```

where,

Radiometers is a real array for the brightness temperatures for 6.8 GHz (V,H), 10.7 GHz (V,H,U,F), 18.7 GHz (V,H,U,F), 23.8 GHz (V,H) and 37.0 GHz (V,H,U,F) channels.

BAPTAAngle is the scan position of the feed horns projected through the main antenna reflector (radians)

Latitude and Longitude is the location of the pierce point projected onto the earth (degrees)

EIA is the earth incident angles of the 5-feedhorn frequencies (radians)

SpinCounter is the number of BAPTA spins since the start of the data file.

Multiple revs are extracted to process Tb's, which are collocated with SSM/I's environmental parameter retrievals. These revs are then combined to make a 720 X 1440 earth gridded image of Tb's for dual polarization at each frequency.

3.1.8 Calculated Brightness Temperature

The output matrix from Prep_RadTb program is merged with WindSat data to match the corresponding longitude-latitude indices of the environmental parameters. This procedure ensures that the Windsat measured Tb's for vertical and horizontal polarization are accurately registered to its collocated area. This merged matrix now consists of longitude-latitude indices, 14 environmental parameters with incidence angle, measured vertical Tb's and horizontal Tb's for Windsat frequencies. The matrix is then input to RadTb to calculate the apparent brightness temperature (Tb) for dual polarizations using the specified incidence angle at each frequency. RadTb also calculates the difference of modeled Tb – measured Tb (deltaTb) at each WindSat polarization/frequency. The difference in Tb is then evaluated against input environmental parameters to characterize RadTb model performance relative to actual satellite Tb

measurements.

3.2 Significant Environmental Parameters

For the evaluation of the RadTb model, four environmental factors were analyzed to understand their contribute to the systematic Tb difference (error) produced by the RadTb model. These environmental parameters include: wind speed (WS), water vapor (WV), sea surface temperature (SST) and cloud liquid water (CLW). The dependence of RadTb error with these parameters was observed for three different ranges of threshold levels as specified by Table 4. By this method, observation of the trends of the bias could be examined to assess the Tb error contributed by each parameter.

3.2.1 Threshold environmental boxes

Table 4: Environmental parameters threshold

Four Significant Parameters	Low	Medium	High
Windspeed (m/s)	<= 4	4-8	>=8
Water vapor (g/cm^2)	<=2	2-4	>=4
Sea surface temperature (^oC)	<=10	10-20	>=20
Cloud liquid water (g/cm^2)	<=0.01	0.01-0.02	>=0.02

A combination of the three threshold levels for each environmental condition produces 81 cases. From here on, each threshold combination of environmental factors will be referred to as a 'box'. Out of the 81 boxes, approximately 58 of the boxes had significant points to be used in the analysis. A box such as low WS, low WV, low, medium and high SST and low CLW is referred to as box LLXL, where X is the varied parameter. Combinations of boxes were formed, where one of the environmental factors is varied and the other three were held constant.

3.3 Data Analysis Procedure

The calculated apparent brightness temperature at the aperture of the radiometer antenna is given by the radiative transfer equation:

$$\mathrm{Tap}(sst) = T_{up} + \tau \cdot [\varepsilon \cdot (sst + 273.16)] + \tau(1-\varepsilon)T_{sky} \qquad (3\text{-}2)$$

where τ is the atmospheric transmissivity,

ε is the surface emissivity

1-ε is the surface power reflectivity

As discussed in Chapter 1 and shown in Figure 14, the radiance incident on the radiometer antenna aperture through a slightly absorbing atmosphere comprises the atmosphere upwelling brightness (Tup), down-welling sky brightness reflected off the ocean surface (Trefl) and the direct ocean emission (Tb).

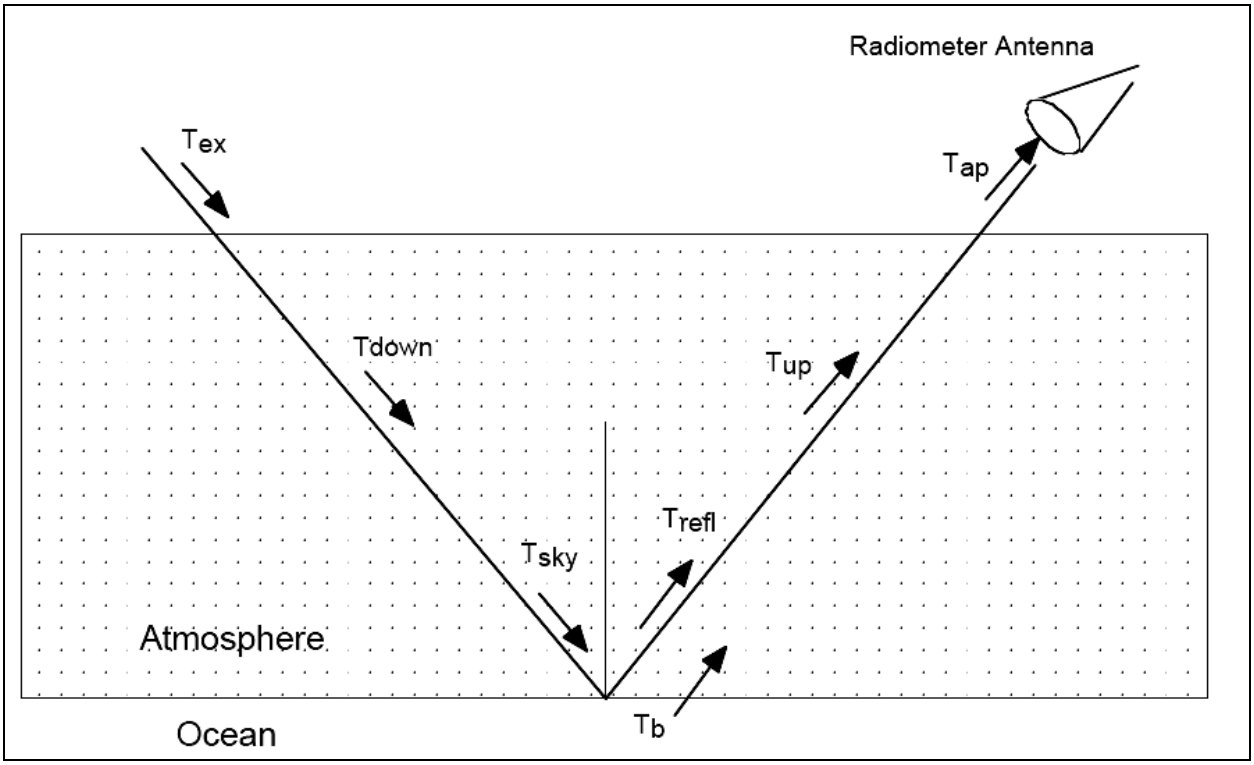

Figure 14: Apparent temperature components as seen by a radiometer

To evaluate RadTb, the preferred approach is to separate the three brightness temperature components and investigate them separately. Of course this is not possible, but at low frequencies, the atmosphere is nearly transparent, which approximately eliminates two components. So our evaluation begins with 6.8 GHz and 10.7 GHz to perform comparisons at the ocean's surface. From the discussion in Chapter 1, it is known that the emissivity varies with the frequency and is affected by salinity, sea surface temperature along with the surface wind speed and its roughening effect on the ocean surface. The emissivity is a function of the seawater dielectric constant via the Fresnel reflection coefficient. Also there is wind speed roughening of

the surface and blackbody emissions from foam caused by breaking waves. In the RadTb model these effects are modeled separately. The wind speed (rough surface) effects are modeled as an additive emissivity term according to an empirical relationship:

Rough Sea Reflection Coefficients (RRO) for dual polarization:

$$RRO_{V-pol} = \Gamma_{v-pol} - \{WS * [0.117 - 2.09\text{E}-03 * \exp(0.0732 * EIA)] * (\sqrt{FQ}) / T\} \quad (3\text{-}3)$$

$$RRO_{H-pol} = \Gamma_{H-pol} - \{WS * [0.115 + (EIA)^2 * 3.8\text{E}-05)] * (\sqrt{FQ}) / T\} \quad (3\text{-}4)$$

The effects of large ocean waves that break forming whitecaps and foam are radiometrically modeled as approximately blackbody emissions from the ocean surface covered with foam. For steady-state conditions on the ocean, these breaking wave effects begin at wind speeds of about 7 m/s and increase monotonically with wind speed. Also, the % of area covered by foam is modeled by an empirical relationship with wind speed. Where the foam occurs, there is high emission (low reflection) from the ocean covered by the "foam patch". The reflection coefficient for foam and the % foam (area) fraction are both empirically derived relationships:

Foam Reflection Coefficients (RFO) for dual polarization:

$$RFO_{v-pol} = 1 - \{(208 + 1.29 * FQ) * [1 - 9.946\text{E}-04 * IE + 3.218\text{E}-05 * (EIA)^2 - 1.187\text{E}-06 * (EIA)^3 + 7\text{E}-20 * (EIA)^{10}] / 288\} \quad (3\text{-}5)$$

$$RFO_{H-pol} = 1 - \{(208 + 1.29 * FQ) * [1 - 1.748\text{E}-03 * EIA - 7.336\text{E}-05 * (EIA)^2 + 1.044\text{E}-07 * (EIA)^3] / 288\} \quad (3\text{-}6)$$

Fraction of Sea Surface Covered with Foam:

$$FOMFR = 7.751\text{E}-06 * WS\text{^}3.321 \quad (3\text{-}7)$$

where, FOMFR = Sea Foam Fraction

Total Ocean Reflection Coefficient (RTOTL) with respect to V- and H-pol

RTOTL=FOMFR*RFO+(1-FOMFR*RRO) (3-8)

The ocean emissivity for a foam covered sea is calculated according to:

$$\varepsilon = 1 - RTOTL \quad (3\text{-}9)$$

An analysis was conducted to investigate the affect varying SST on the emissivity and the resulting deltaTb at the surface. Since the ocean is not a blackbody, the emissivity is less than unity and must be accounted for correctly to determine the oceanic brightness temperature. To evaluate the RadTb calculated direct ocean surface emission, an equivalent WindSat "at the surface" comparison set was created. To accomplish this, the reflected sky and upwelling atmospheric Tb components (and one-way atmospheric transmissivity) were calculated by RadTb and then subtracted from the measured WindSat apparent brightness temperature according to equation (3-13). Based on a worst-case error analysis, the maximum uncertainty in this atmospheric compensation is: ("true correction" - "RadTb estimated")/"true" < 5%.

At the C-band frequency (6.8 GHz), the atmosphere is essentially transparent to the microwaves with very little attenuation. Data for the conditions of low clouds was used to evaluate RadTb model for clear sky (lowest loss) conditions. At the 6.8 GHz, typical values of the reflected and upwelling atmospheric Tb components and the total (one-way) atmospheric transmissivity are: reflected-Tsky (7 K), Tup (4 K), and the transmissivity (0.985). Thus, using RadTb to estimate the "true atmospheric correction", the maximum error introduced is < 0.5 K, which does not significantly influence the deltaTb at the surface results. The surface Tb obtained after removing the reflected sky and upwelling radiance components was cross-checked with

equation (3-12) to validate the surface/ocean Tb calculated measurements. The surface Tb was calculated as follow:

$$T_{sky} = \tau \cdot T_{ex} + T_{down} \text{ , Kelvin} \quad (3\text{-}10)$$

$$T_{refl} = (1-\varepsilon) \cdot T_{sky} \text{ , Kelvin} \quad (3\text{-}11)$$

$$T_b = \varepsilon \cdot (sst + 273.16) \text{ , Kelvin} \quad (3\text{-}12)$$

Measured surface Tb, $Tb_{surfmeas}$ was calculated as

$$Tb_{surfmeas} = \frac{[Tap_{meas} - T_{up} - (T_{refl} * \tau)]}{\tau} \text{, Kelvin} \quad (3\text{-}13)$$

The ideal case of analyzing the surface Tb error was at the LLXL case. Here a specular ocean with clear sky would have been the simplest case to evaluate the error due to emissivity. However, at the LLXL condition, there were not sufficient data points to provide the desired range of SST. So, the LMLXL (low and medium WS, low WV, all ranges of SST and low CLW) conditions were used to develop an empirical deltaTb correction. At each frequency, the vertical and horizontal polarization deltaTb, were averaged over 1º C SST bins to perform a regression analysis (polyfit) of the emissivity error. After establishing the polyfit relation for deltaTb with sea surface temperature, the polyfit coefficients were used to correct the emissivity factor at each frequency in the RadTb model.

After applying the correction for emissivity with SST in RadTb, the brightness temperature was recalculated and the surface deltaTb at 6.8 GHz and 10.7 GHz were re-evaluated for deltaTb at different ranges of wind speed, namely: 0 – 3 m/s, 3 - 4m/s, 4 - 5m/s and

5 - 7m/s. At the 18.7 GHz and 37.0 GHz, the microwaves are respectively sensitive to water vapor absorption and clouds attenuation. The surface deltaTb due to wind speed and water vapor were analyzed at these two frequencies and recorded for future work. Added to this, after applying the correction to the RadTb, the LMLXL correction for emissivity was applied to all cases of environmental boxes to determine how effective the new-RadTb calculates the apparent brightness temperature. The deltaTb's for the total apparent brightness temperature, which includes atmospheric attenuations, was tabulated by various boxes for future work.

To validate the empirical tuning the RadTb model, over a 1,000,000 observations were used at each frequency. A total of 18 days were processed and approximately 200 revs were used to achieve the full range of environmental and atmospheric conditions to be used by the RadTb model. To examine the model error SST, the data were subdivided into 1° bin and histograms of the difference (deltaTb) examined. Each bin consisting of at least 5000 points were averaged to find the mean value and standard deviation of the delta-Tb.

3.4 Data Processing

To validate the evaluation of tuning the RTM model, over a 1,000,000 points were used at each frequency. A total of 18 days were processed and approximately 200 revs were used to retrieve the full range of environmental and atmospheric conditions to be used by the RadTb model. The data was made uniform within two and a half standard deviations of the mean delta-Tb. To find the polyfit relation of deltaTb with varied SST, the distribution of SST is subdivided

in 1º bin to find the average deltaTb of each bin. Bin averaging of SST with deltaTb is applied to achieve a more accurate estimation of the Tb bias per unit bin. Each bin consisting of at least 5000 points is averaged to find the mean bias of the delta-Tb.

3.5 Monte Carlo Simulation

Monte Carlo Simulation was carried out to test the sensitivity of the calculated Tb error when noise is introduced in the input environmental parameters. Having knowledge of the variance of error/noise in the data set, Monte Carlo simulation is used to test the sensitivity of Tb error due to noise in the original data. The uncertainty in Tb error contributed by environmental parameters includes those of wind speed, water vapor, sea surface temperature and cloud liquid water. The simulation included random noise Gaussian distribution about the mean of the data within a specified confidence level. The error introduced in environmental parameters is shown in table 5.

Table 5: Monte Carlo error distribution

Environmental Parameters	STD of mean
Water vapor (gm/square cm)	10% of mean
Cloud liquid water (gm/square cm)	10% of mean
Wind speed (M/sec)	10% of mean
Sea surface temperature (deg C)	1K error of mean

For a given box, 1000 rows were created and the parameters were varied simultaneously with error to ultimately test the sensitivity of the calculated Tb. For each case where the parameter is varied, the standard deviation for the bias was recorded and the root mean square error was determined to see how much of the error is contributed to the original deltaTb standard deviation of the box.

CHAPTER FOUR: RESULTS

4.1 Introduction of Results

Results of the RTM RadTb evaluation are presented in this chapter. The RTM was evaluated globally under varied atmospheric and surface conditions, four radiometer frequencies, and V- and H-polarizations. To perform the analysis, the comparison data set was separated into ascending and descending revs. Following this, these data were further partitioned over four environmental conditions, namely; wind speed, water vapor, sea surface temperature and cloud liquid water; and then comparisons between modeled and measured Tb were performed by frequency and polarization. Preliminary results indicate that there are systematic differences in the Tb between the RadTb model and the WindSat measurements.

At the highest level of comparisons, the calculated RadTb apparent brightness temperatures at the "top of the atmosphere" are directly compared with the corresponding WindSat measurements. As discussed in Chapter three, the delta-Tb is defined as the difference between the RadTb modeled Tb and the WindSat measured Tb. In this comparison, the radiometer is assumed to be the "true apparent brightness temperature" because of its excellent

calibration validation [jones et al WindSat paper IGARSS04]. Further, the random errors caused by the radiometer measurement precision (ΔT) are reduced to zero by the large number of observations averaged.

In this RadTb evaluation, the comparison at lowest frequency channel is the simplest and most reliable because at 6.8 GHz, the atmosphere is almost transparent (transmissivity ~ 98%); so the apparent Tb is mostly due to the sea surface emission. Later in this chapter, the atmospheric emission components are removed and comparisons are performed at the sea surface, the results of which suggest improvements to the RadTb based upon empirical SST corrections to the modeled ocean emissivity. After incorporating these changes, improved RadTb model comparisons of deltaTb's are presented and discussed by frequency and environmental observations.

4.2 Apparent Tb Comparisons

First, results of Tb differences for 6.8 GHz are shown for descending revs and horizontal and vertical polarization in the figure 15 and figure 16 respectively. The gridded image of ocean brightness temperature difference (measured minus modeled) is shown in color with the associated color bar. These images, displayed on a linear Lat./Lng. map projection, are for the collocated area of WindSat and SSMI that occur within ± 1.5 hours of the time for the closest numerical weather analysis.

Overall, the RadTb calculations are greater than the measurements as indicated by

positive delta-Tb (warm colors) that range from approximately - 2 K to + 6 K. Based upon systematic spatial patterns, these differences appear to be related to the varying environmental conditions, which suggest that it is necessary to evaluate RadTb performance as a function of the input surface and atmospheric environmental parameters.

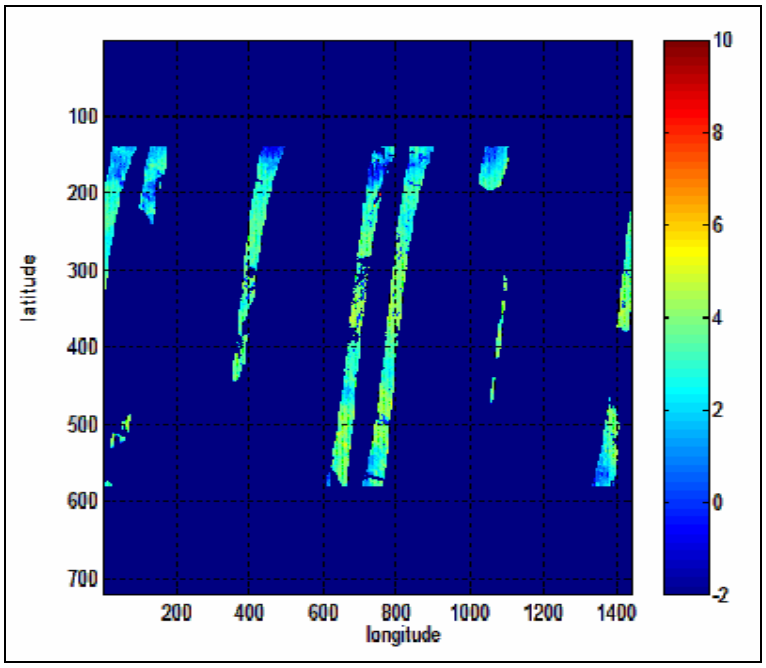

Figure 15: Typical differences of WindSat and RadTb apparent brightness temperatures, deltaTbV in Kelvin, at 6.8 GHz V-pol for descending revs.

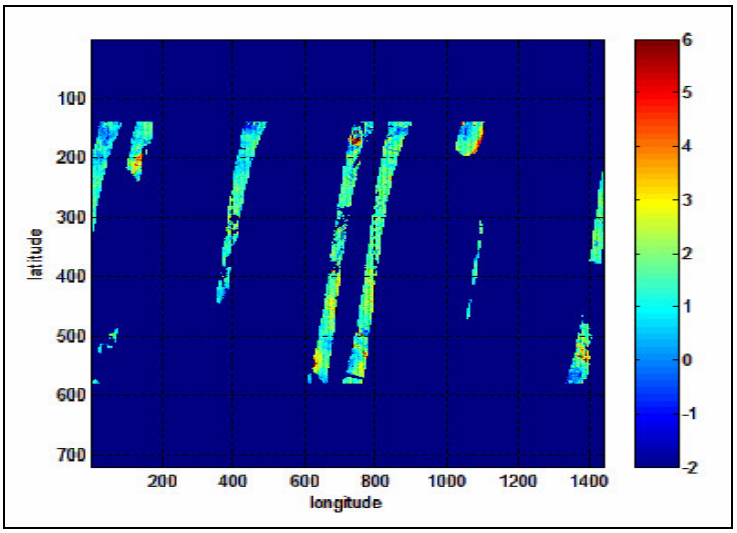

Figure 16: Typical differences of WindSat and RadTb apparent brightness temperatures, DeltaTbH in Kelvin, at 6.8 GHz H-pol for descending revs.

Similar comparisons were performed for the remaining three WindSat radiometer frequencies, and the results are similar to the above except that the Tb differences increase with the WindSat channel frequency. At the 18 GHz and 37 GHz channels, the atmosphere plays an increasingly significant role; so it became useful to separate the direct sea surface emission from the atmospheric components.

4.3 Surface Tb Comparisons

As discussed in Chapter 3, the surface emission (Tb_{sur}) is the product of the sea surface emissivity and the physical temperature (expressed in Kelvin). Thus, the analysis was conducted to investigate the affect varying SST on the emissivity and the resulting delta-Tb_{sur}. Since the ocean is not a blackbody, the emissivity is less than unity and must be accounted for correctly to determine the oceanic brightness temperature. To evaluate the RadTb calculated direct ocean surface emission, an equivalent WindSat "at the surface" comparison set was created. To accomplish this, the reflected sky and upwelling atmospheric Tb components (and one-way atmospheric transmissivity) were calculated by RadTb and then subtracted from the measured WindSat apparent brightness temperature. Based on a worst-case error analysis, the maximum uncertainty in this atmospheric compensation is: ("true correction" – "RadTb estimated")/"true" < 5%. For example, at 6.8 GHz H-polarization, typical values of the reflected and upwelling atmospheric Tb components and the total (one-way) atmospheric transmissivity are: reflected-

Tsky (5 K), Tup (3 K), and the transmissivity (0.985). Thus, using RadTb to estimate the "true atmospheric correction", the maximum error introduced is < 0.5 K, which does not significantly influence the surface deltaTb$_r$ result. The surface deltaTb analysis was performed separately for ascending (asc) and descending (dsc) revs; and, as expected, the results are identical within the expected experimental uncertainty. Further, the calculated surface deltaTb's are only a function of environmental conditions (not space or time), which increases our confidence that results are correct.

For this analysis, the preferred set of environmental conditions are; low wind speed, low water vapor and low cloud conditions. Unfortunately, the number of environmental observations for this set was less than desired to establish reliable Gaussian error statistics; therefore, the L plus M wind speeds (designated LM) were used for the comparisons.

4.3.1 Evaluation versus SST

The evaluation at the surface is presented in figure 17 for 6.8 GHz for (a) horizontal and (b) vertical polarization for the LMLXL environmental conditions (low & med wind speeds, low water vapor, all SST's and low cloud liquid water). For the analysis employed, the surface deltaTb data were first averaged in SST bins of 1° C, and then a least-squares regression analysis (polyfit) performed. If the RadTb model were correct, the surface deltaTb would be independent of SST (i.e., a line with zero slope); but the observed differences increase with SST, which

indicates that RadTb has an emissivity error that is characterized by a second order polynomial in SST. The blue and red curves show the 2nd order regression-fits of the asc and dsc cases respectively. Since the emissivity error is believed to be independent of the direction that the satellite is moving in orbit, the coefficients of the asc and dsc polyfits were averaged separately for each polarization and the resulting correction was applied in RadTb as an additive emissivity term as a function of SST. The averaged ploynominal coefficients are presented in Table 6.

After applying this empirical correction, the revised version of RadTb was used to re-calculate the Tb_{sur} and the reflected sky component; and then the surface deltaTb was re-evaluated. The results at 6.8 GHz are shown in figure 18 for (a) Horizontal and (b) Vertical-polarizations. It is noted that the empirical emissivity correction removes the Tb bias and nearly eliminates the dependence on SST. When asc and dsc results are averaged, the linear regression fit for the combined case is very "flat". Further, the resulting data scatter in the horizontal polarization is slightly greater than that for vertical. Because the reflected sky component is greater for H-pol, the increased scatter is believed to be the result of the residual error in the atmospheric correction.

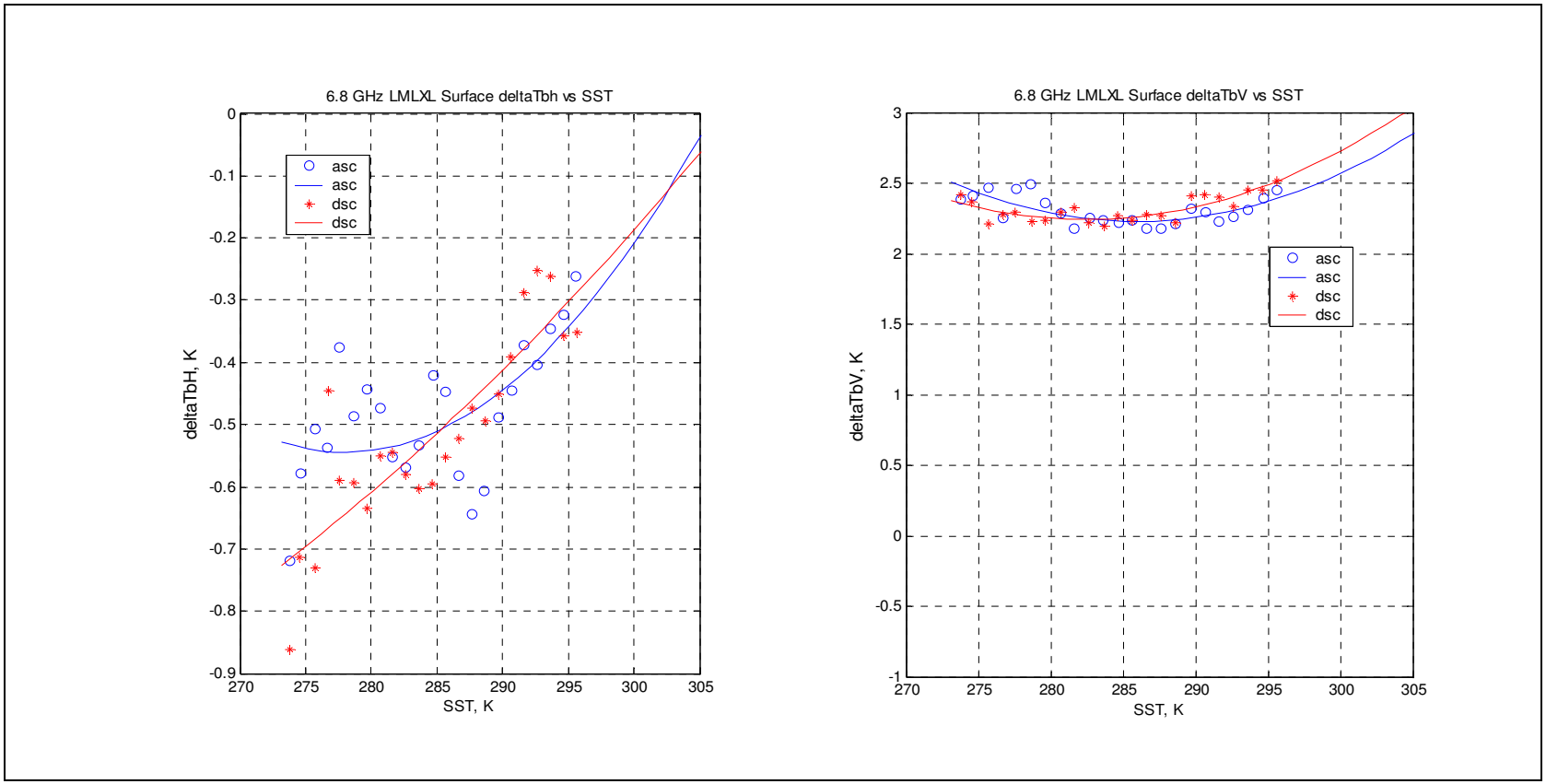

(a) Horizontal polarization (b) Vertical polarization

Figure 17: Modeled minus measured brightness temperature at the ocean surface for original RadTb at 6.8 GHz. Ascending data are blue “o” and descending data are red “+”.

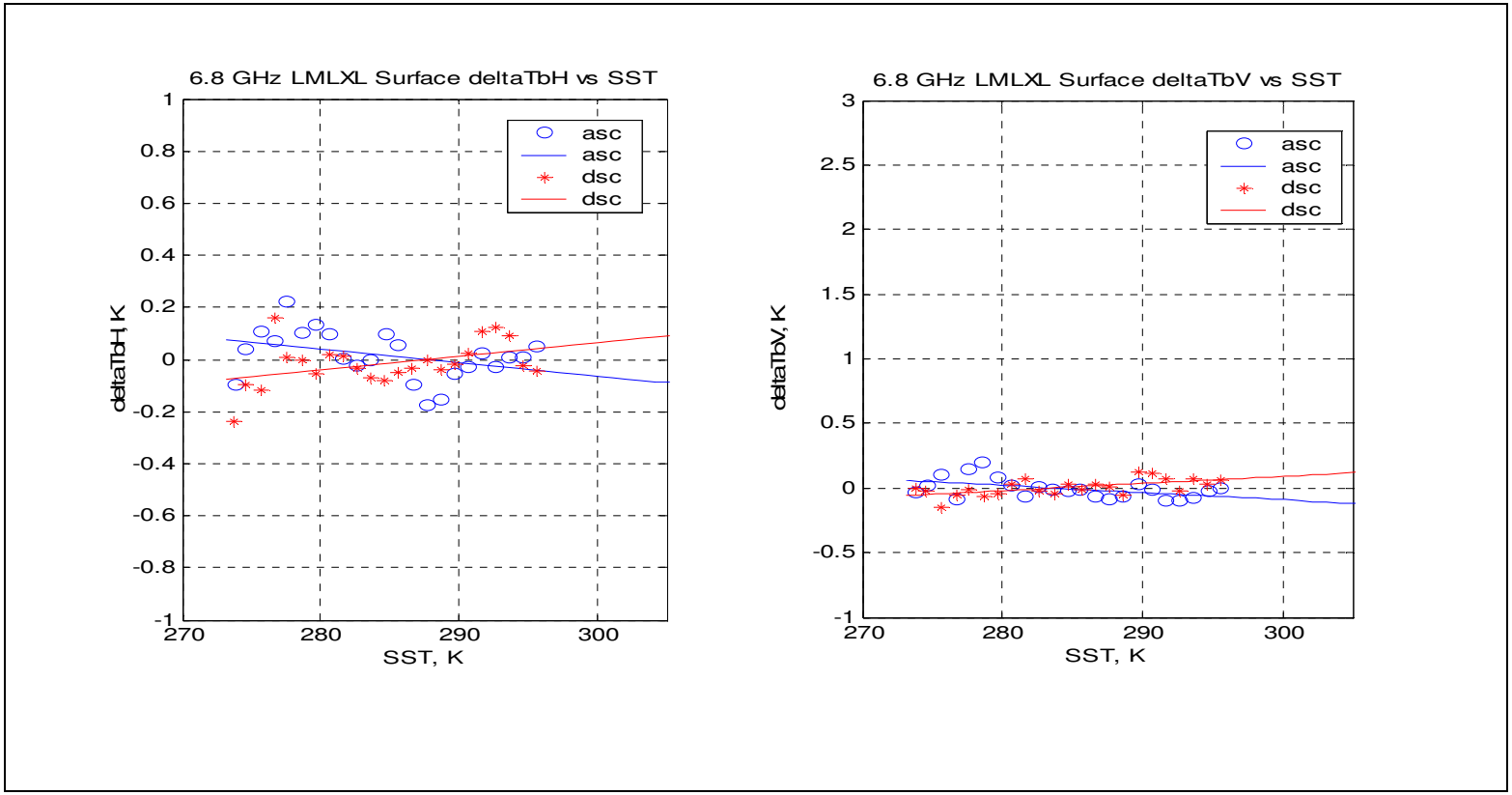

(a) Horizontal polarization (b) Vertical polarization

Figure 18: Modeled minus measured brightness temperature at the ocean surface for revised RadTb at 6.8 GHz. Ascending data are blue “o” and descending data are red “+”.

As previously stated, the scatter plots, shown in figures 17 and 18, use the surface deltaTb averaged in one Centigrade bins of SST. Based upon the central limit theorem, within these SST bins, the comparison differences are approximately Gaussian distributed, which is the result of random errors in the "true" environmental inputs to RadTb. During the data processing, data outside ± 2.5 standard deviations of the delta-Tb mean were removed because they were judged not to be representative of the expected random error statistics. Only the resulting SST bins having a significant number of points to provide reasonable histograms were used, such as shown in figure 19. Furthermore, all difference histograms for binned averages are given in Appendix A.

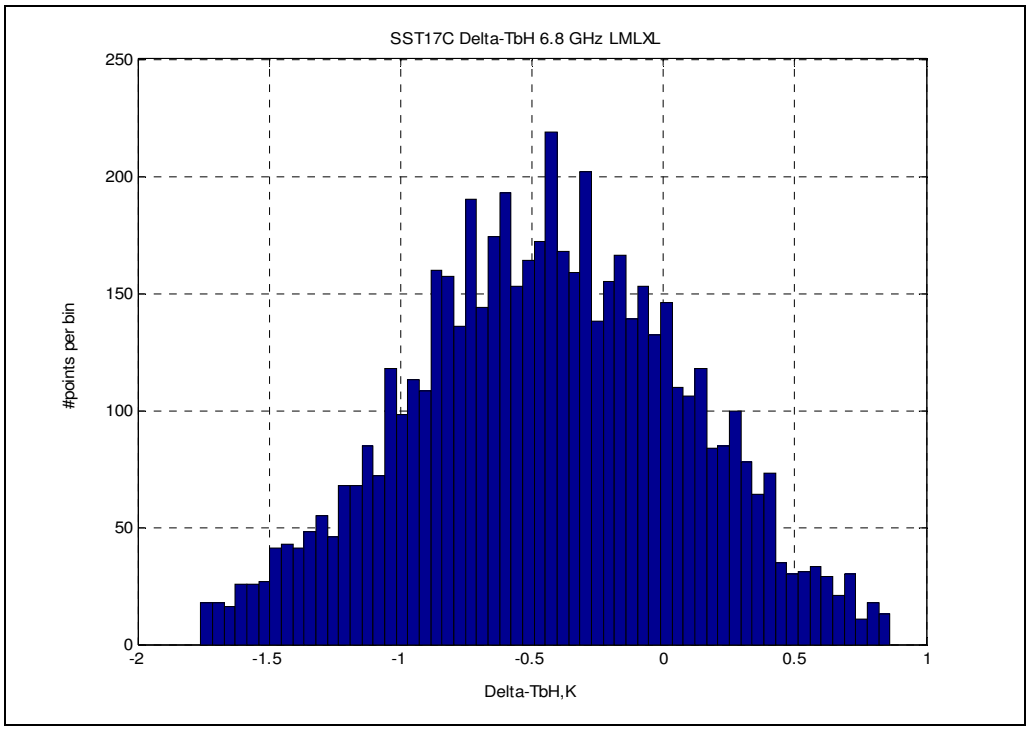

Figure 19: Typical histogram of 6.8 GHz deltaTbH for SST bin: 16 - 17 C for comparisons

before the empirical emissivity adjustment.

The results for 10.7, 18.7 and 37.0 GHz channels are next presented in Figures 20 – 25 for the “before” and “after” cases of adjusting the emissivity factor in RadTb. “Before” results are very similar to those for 6.8 GHz except that the average error for a given SST bin increases with frequency, resulting in a greater correction for the emissivity. Further, at all frequencies, the “after” correction cases are very effective in removing the RadTb biases and the dependence on SST.

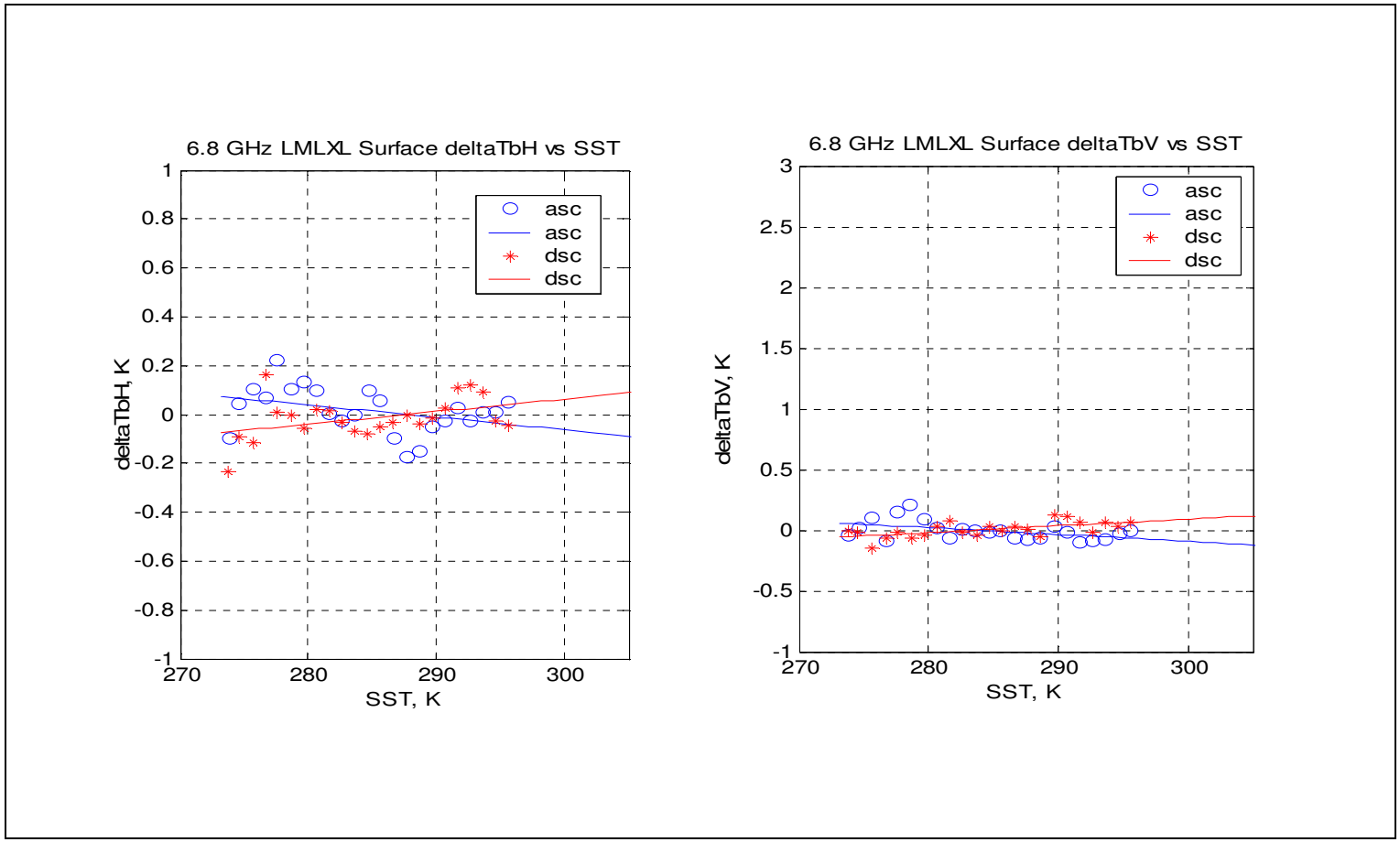

(a) Horizontal polarization (b) Vertical polarization

Figure 20: Modeled minus measured brightness temperature at the ocean surface for original RadTb at 10.7 GHz. Ascending data are blue “o” and descending data are red “+”.

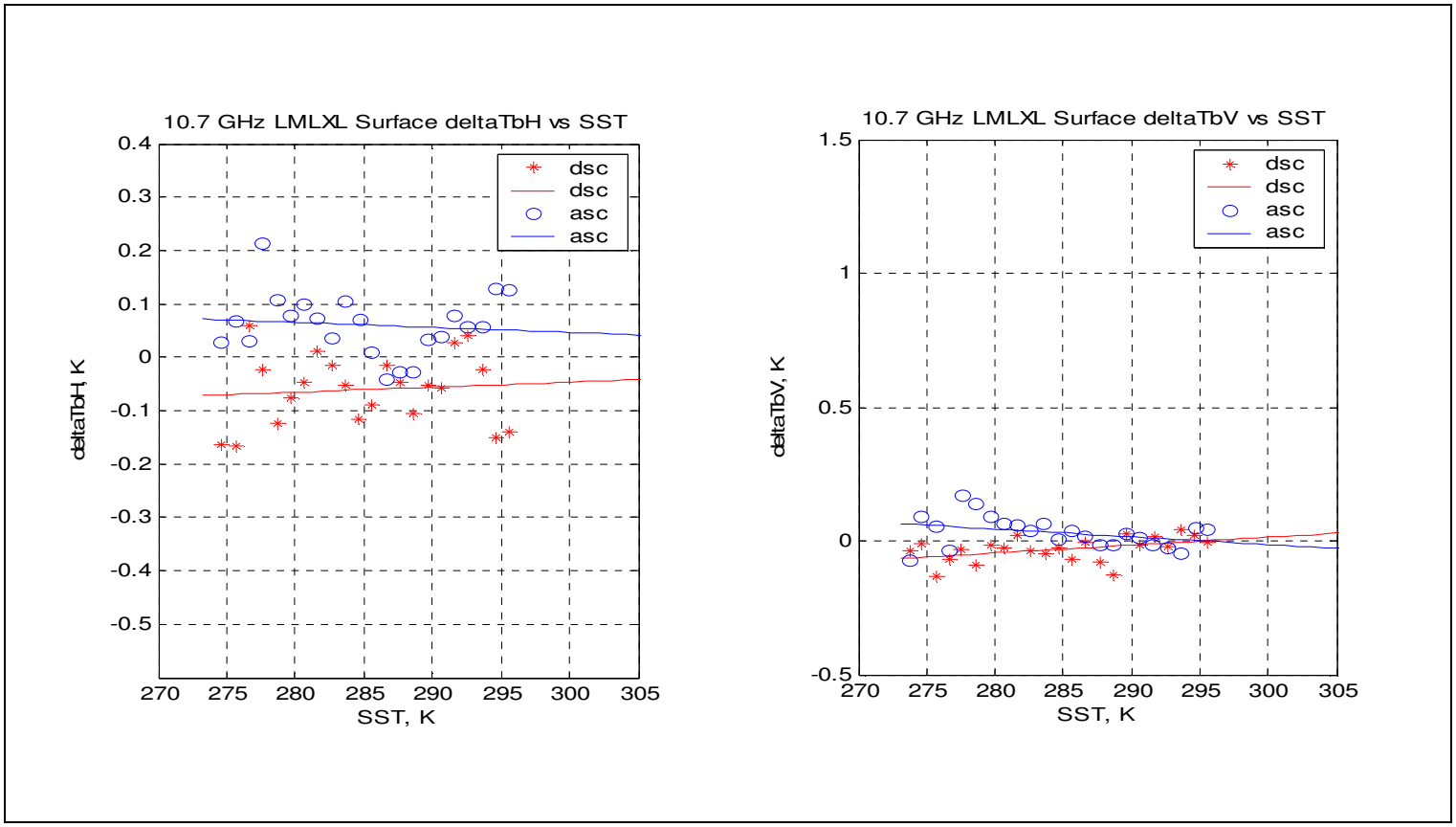

(a) Horizontal polarization (b) Vertical polarization

Figure 21: Modeled minus measured brightness temperature at the ocean surface for revised RadTb at 10.7 GHz. Ascending data are blue “o” and descending data are red “+”.

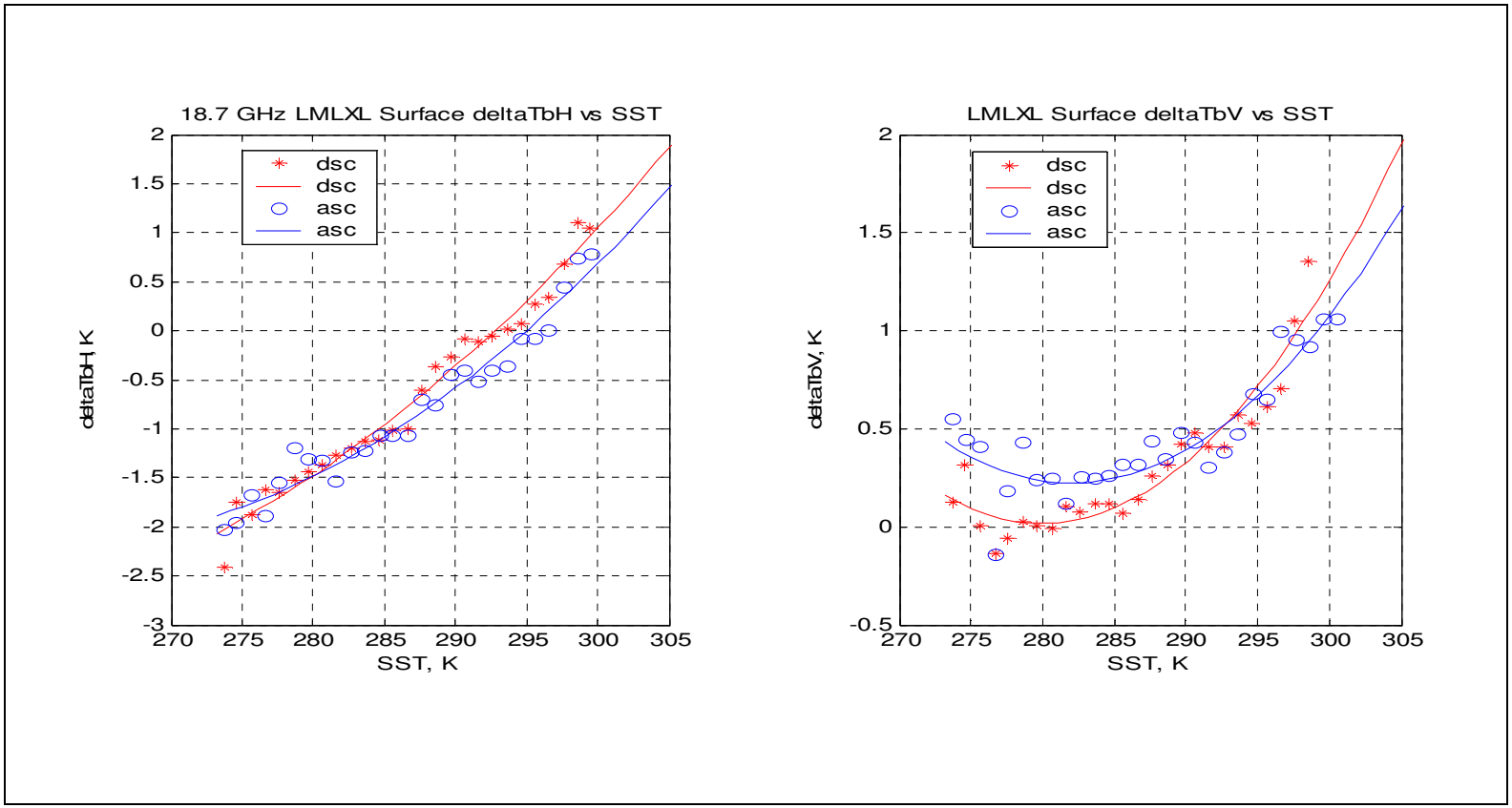

(a) Horizontal polarization (b) Vertical polarization

Figure 22: Modeled minus measured brightness temperature at the ocean surface for original RadTb at 18.7 GHz. Ascending data are blue “o” and descending data are red “+”.

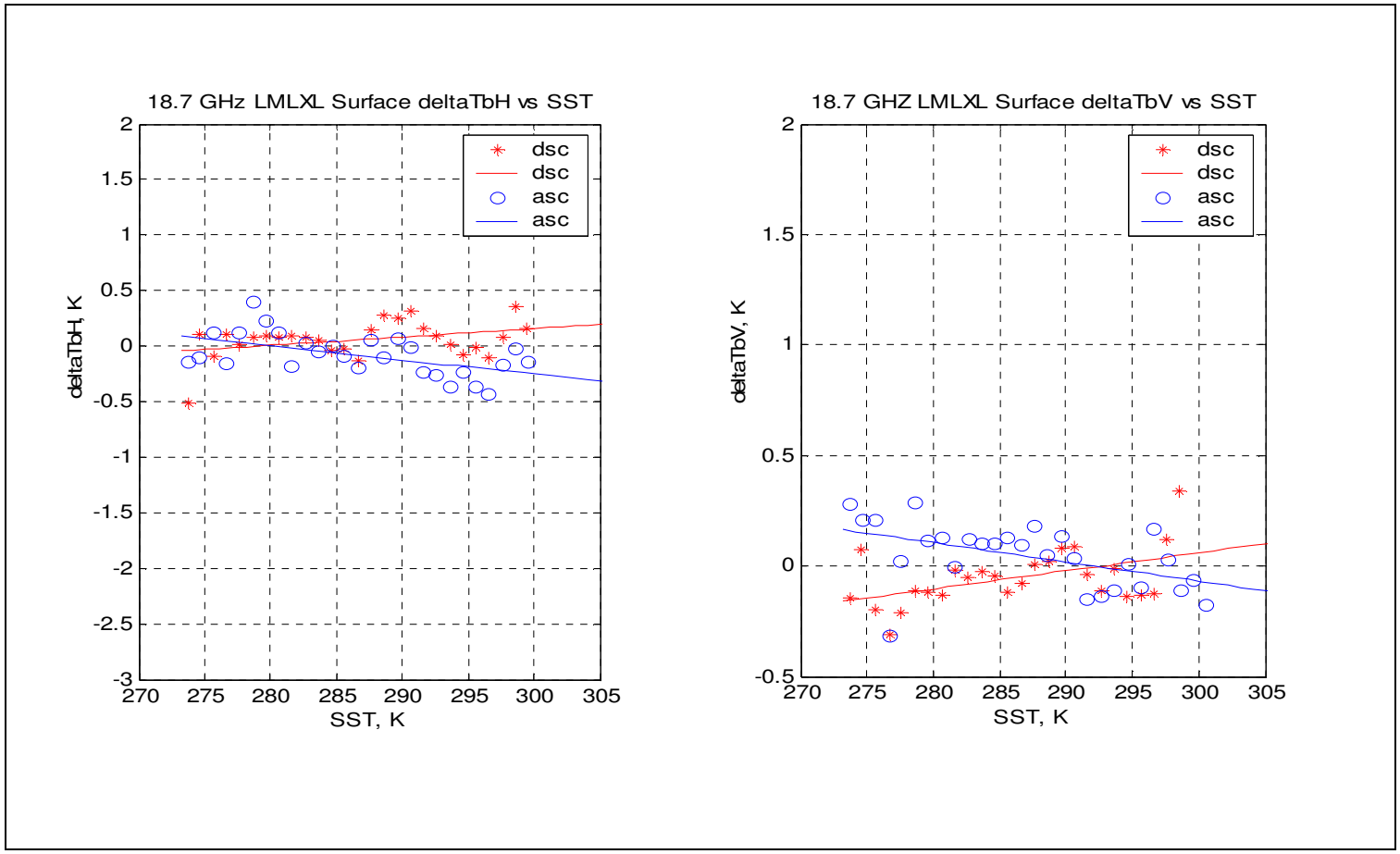

(a) Horizontal polarization (b) Vertical polarization

Figure 23: Modeled minus measured brightness temperature at the ocean surface for revised RadTb at 18.7 GHz. Ascending data are blue “o” and descending data are red “+”.

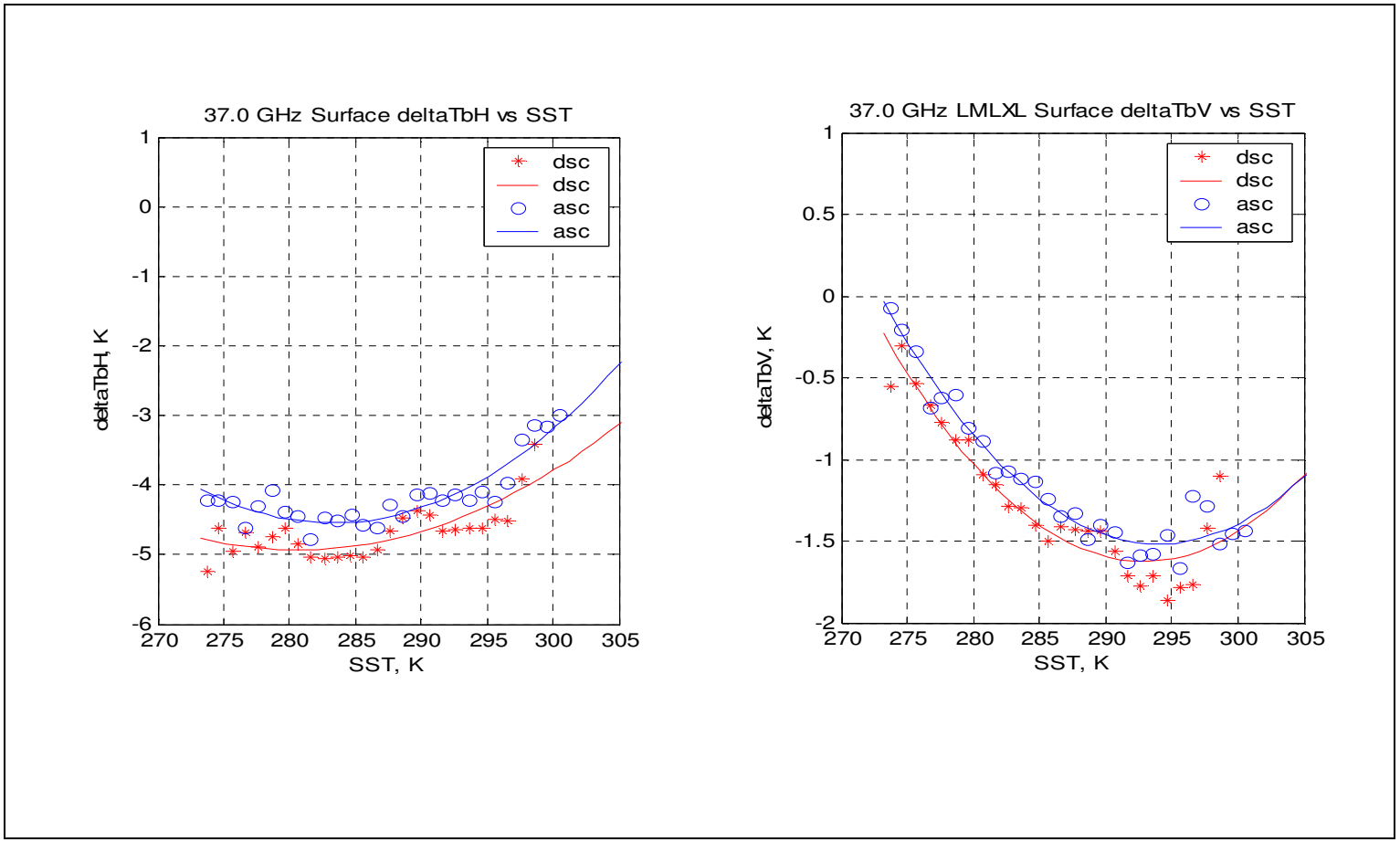

(a) Horizontal polarization (b) Vertical polarization

Figure 24: Modeled minus measured brightness temperature at the ocean surface for original RadTb at 37.0 GHz. Ascending data are blue “o” and descending data are red “+”.

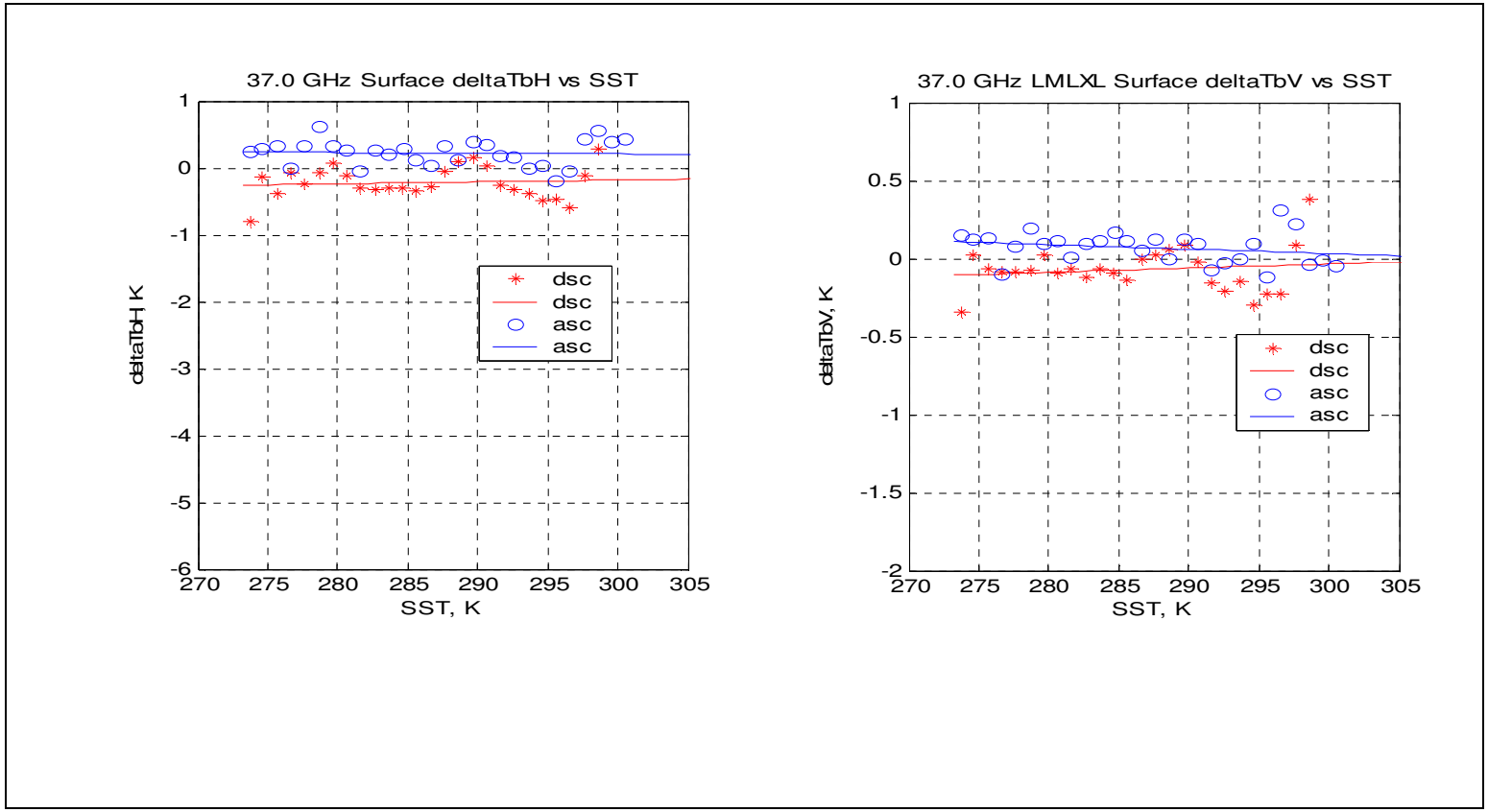

(a) Horizontal polarization (b) Vertical polarization

Figure 25: Modeled minus measured brightness temperature at the ocean surface for revised RadTb at 37.0 GHz. Ascending data are blue “o” and descending data are red “+”.

4.3.2 Evaluation versus Water Vapor

Next the revised RadTb model is evaluated under other possible combinations of environmental parameters, where the water vapor content is varied; and the results are shown in the figures 26 through figures 33 for the combined asc/dsc data sets. In these figures, the delta-Tb_{sur} is plotted versus SST; but there are three different curves: LMLXL (low & med wind speed, low water vapor, all SST's, and low cloud liquid water), LMLMXL (LMLXL + medium water vapor) and LMXXL (LMLMXL + high water vapor). Because water vapor is highly correlated with SST, there are very few occurrences of low water vapor at high SST's; and below ~ 15C all three curves are the same because the water vapor is predominately low. As the water vapor is increased from low to medium to high, the corresponding upper limit for SST increases; and the accuracy of the RadTb performance degrades progressively with radiometer frequency. Also, at each frequency the horizontal polarization has a larger bias in surface deltaTb because the Fresnel reflection coefficient is higher for H-pol, which produces the larger residual error in the atmospheric correction. This trend, of increasing surface deltaTb with increasing water vapor, is probably the result of RadTb slightly over estimating the "true" value of the atmospheric components that should be subtracted from the WindSat measurement to yield the equivalent direct surface emission.

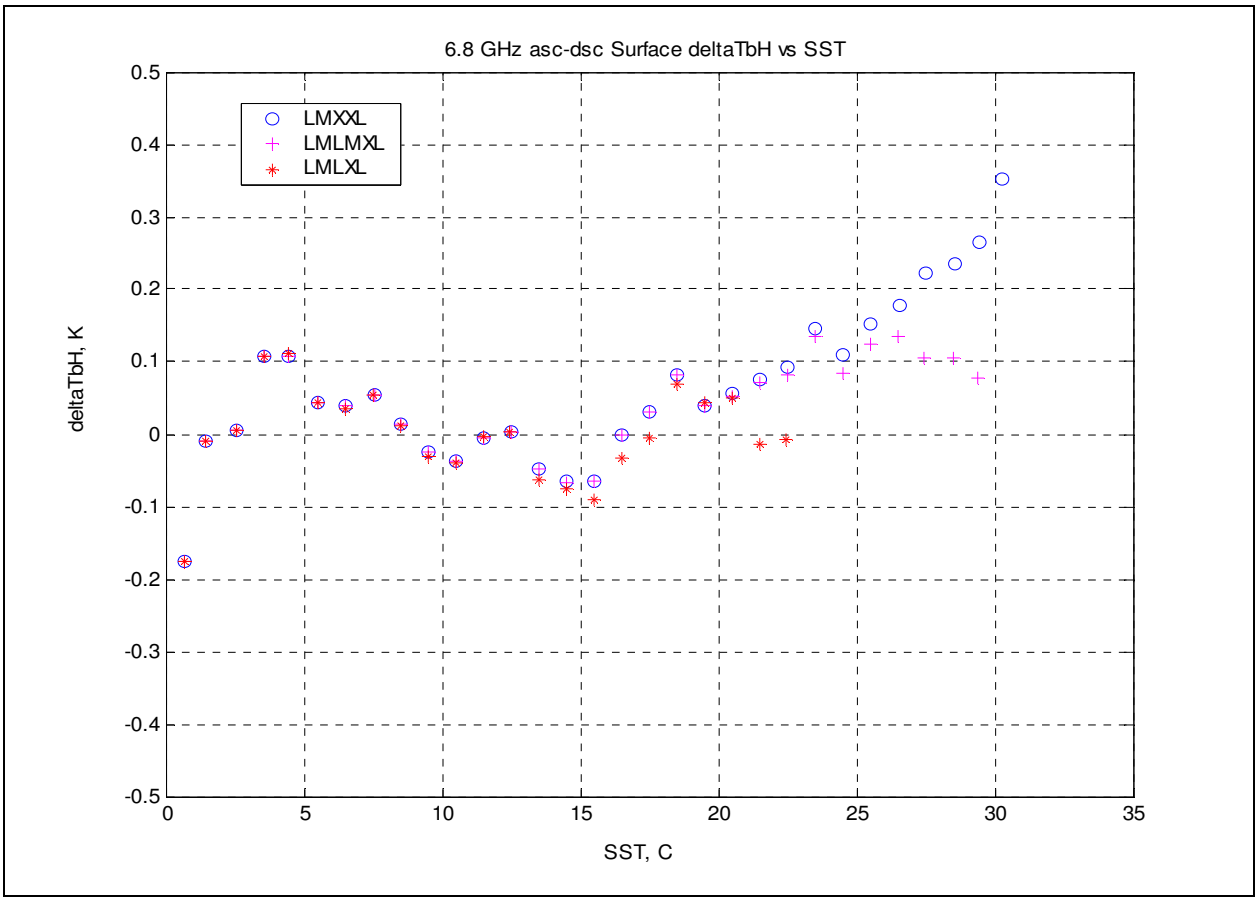

Figure 26: Effect of water vapor on the 6.8 GHz deltaTbH.

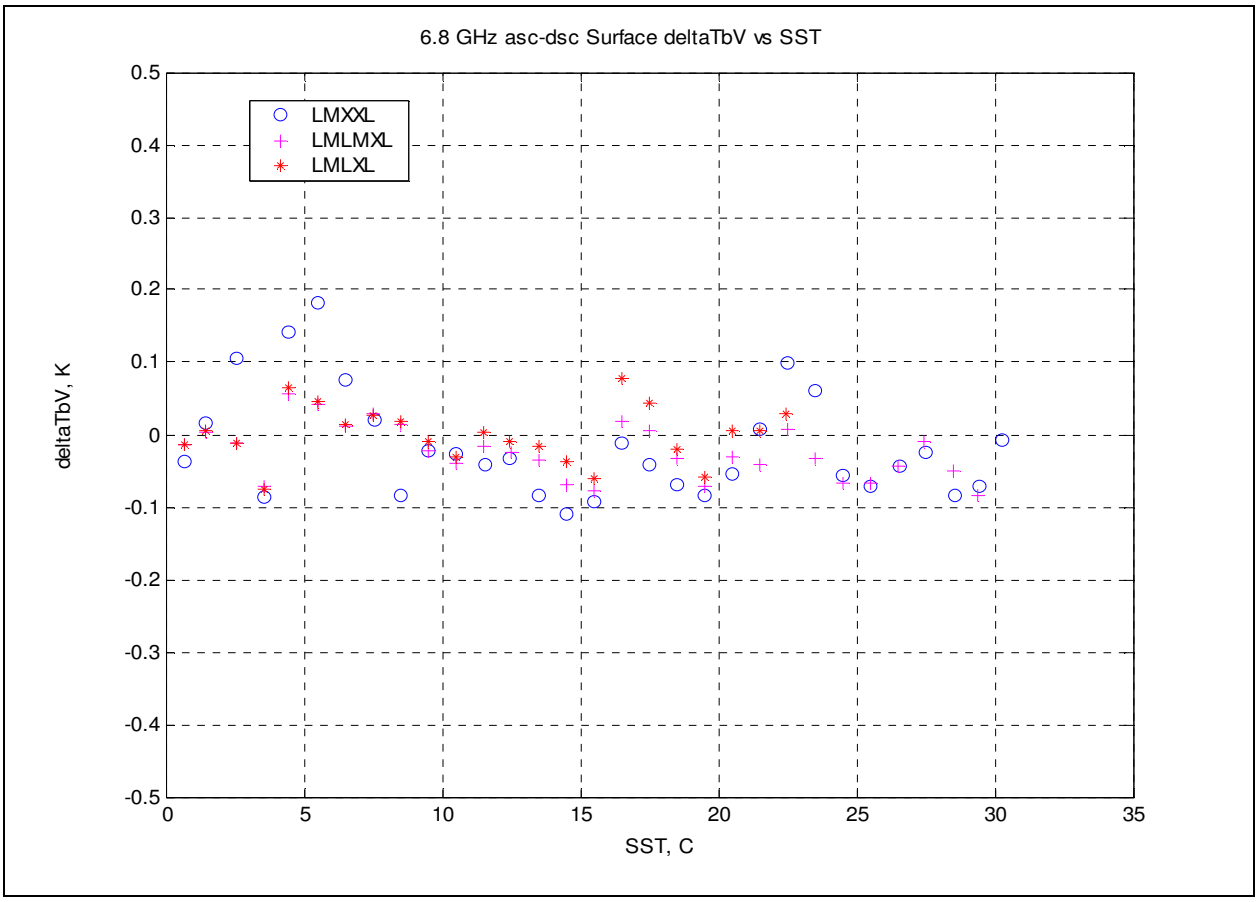

Figure 27: Effect of water vapor on the 6.8 GHz deltaTbV.

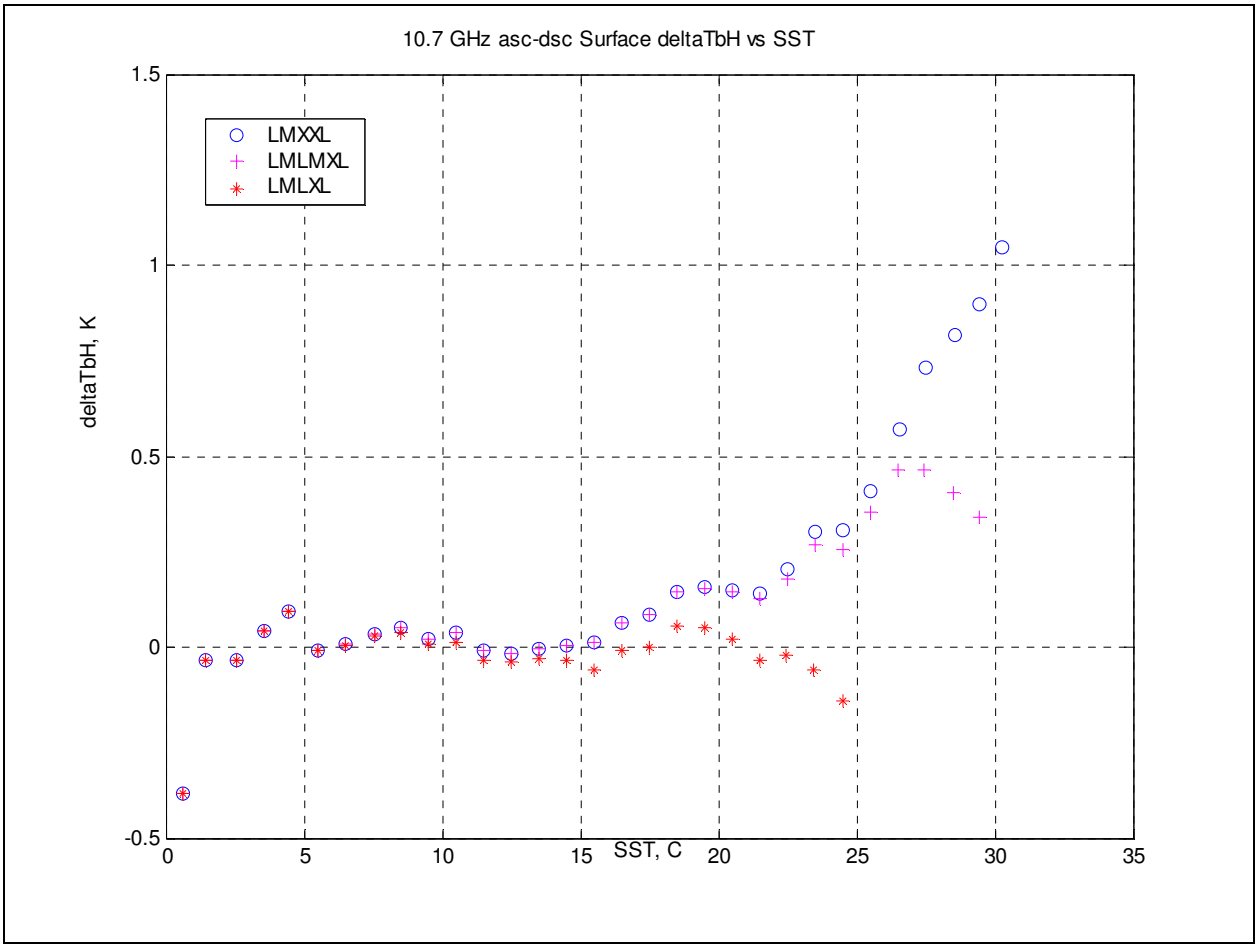

Figure 28: Effect of water vapor on the 10.7 GHz deltaTbH.

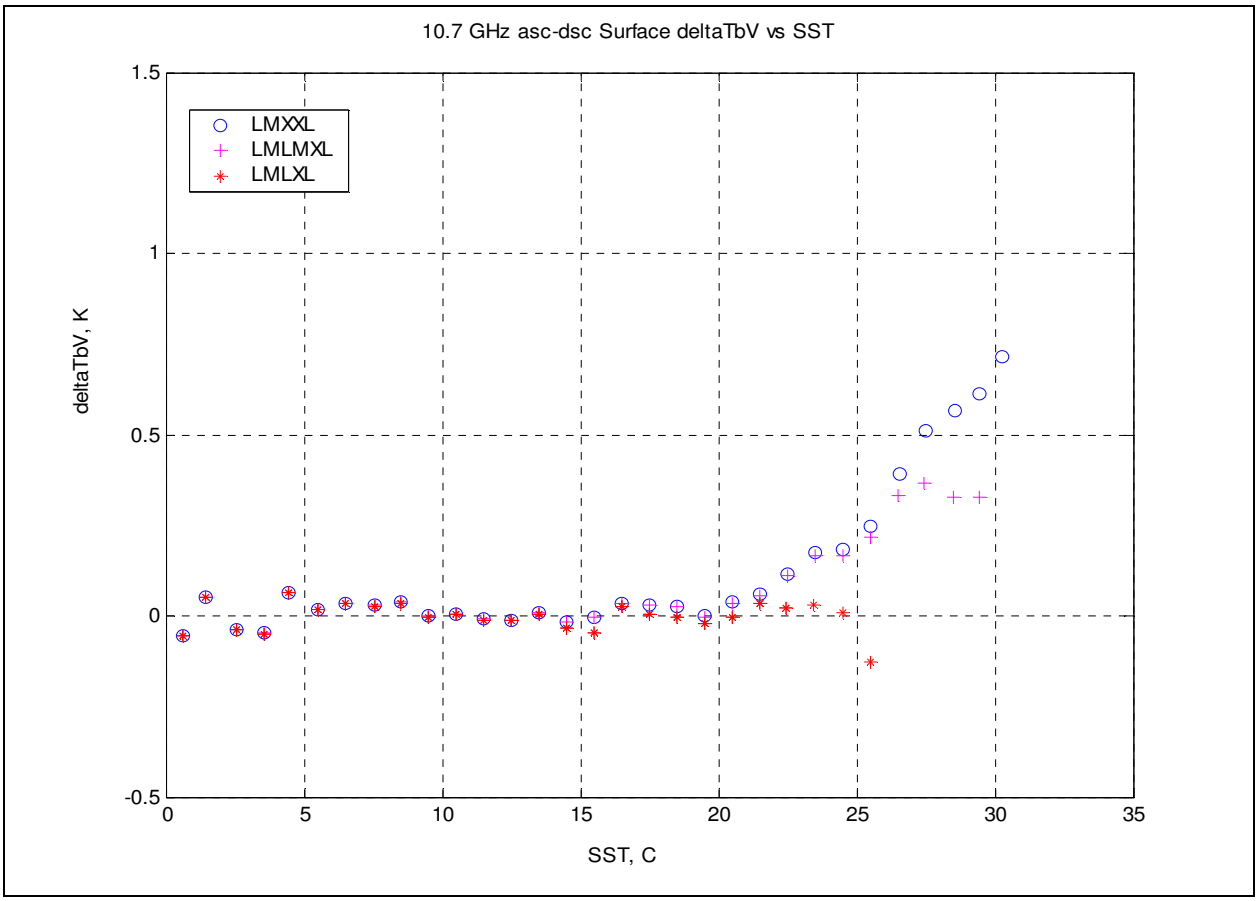

Figure 29: Effect of water vapor on the 10.7 GHz deltaTbV.

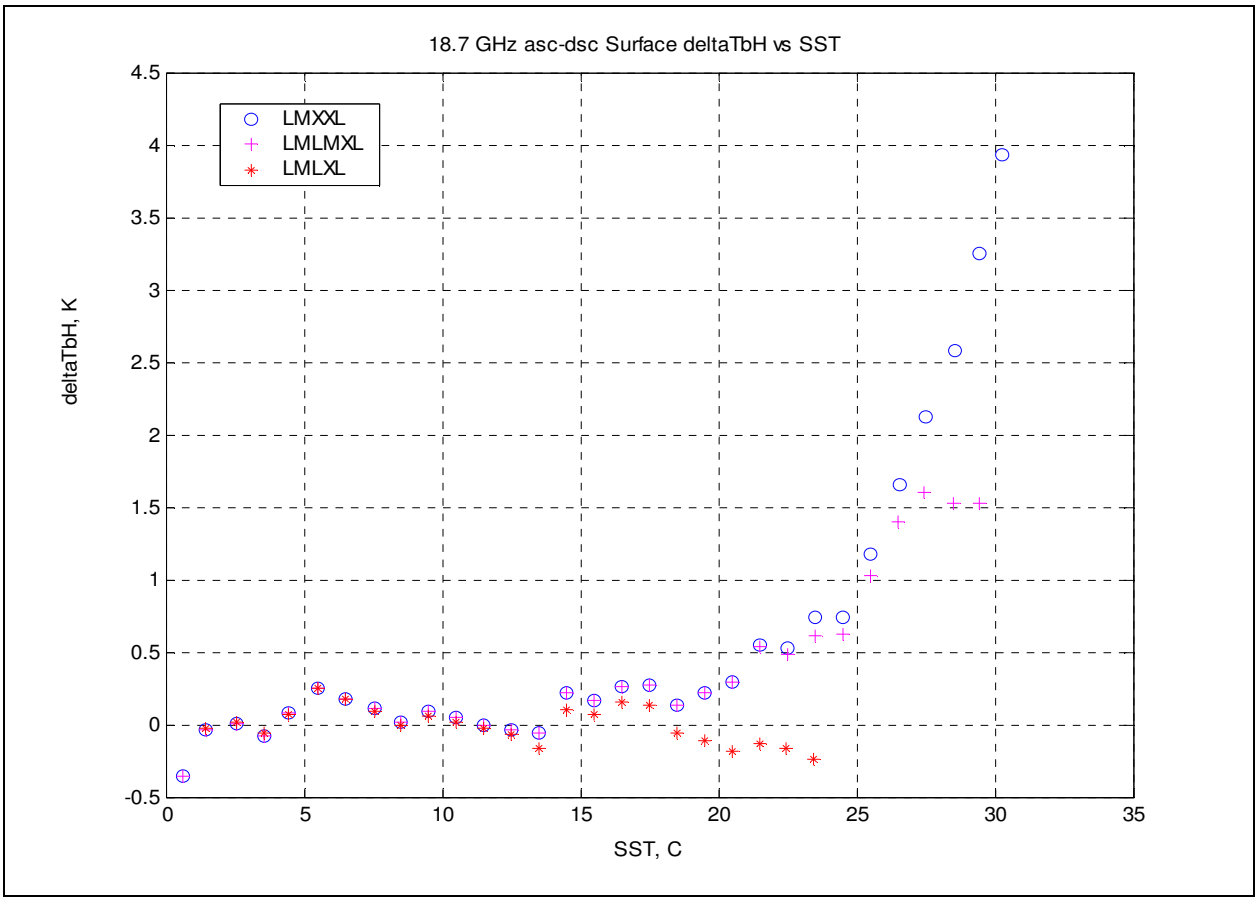

Figure 30: Effect of water vapor on the 18.7 GHz deltaTbH.

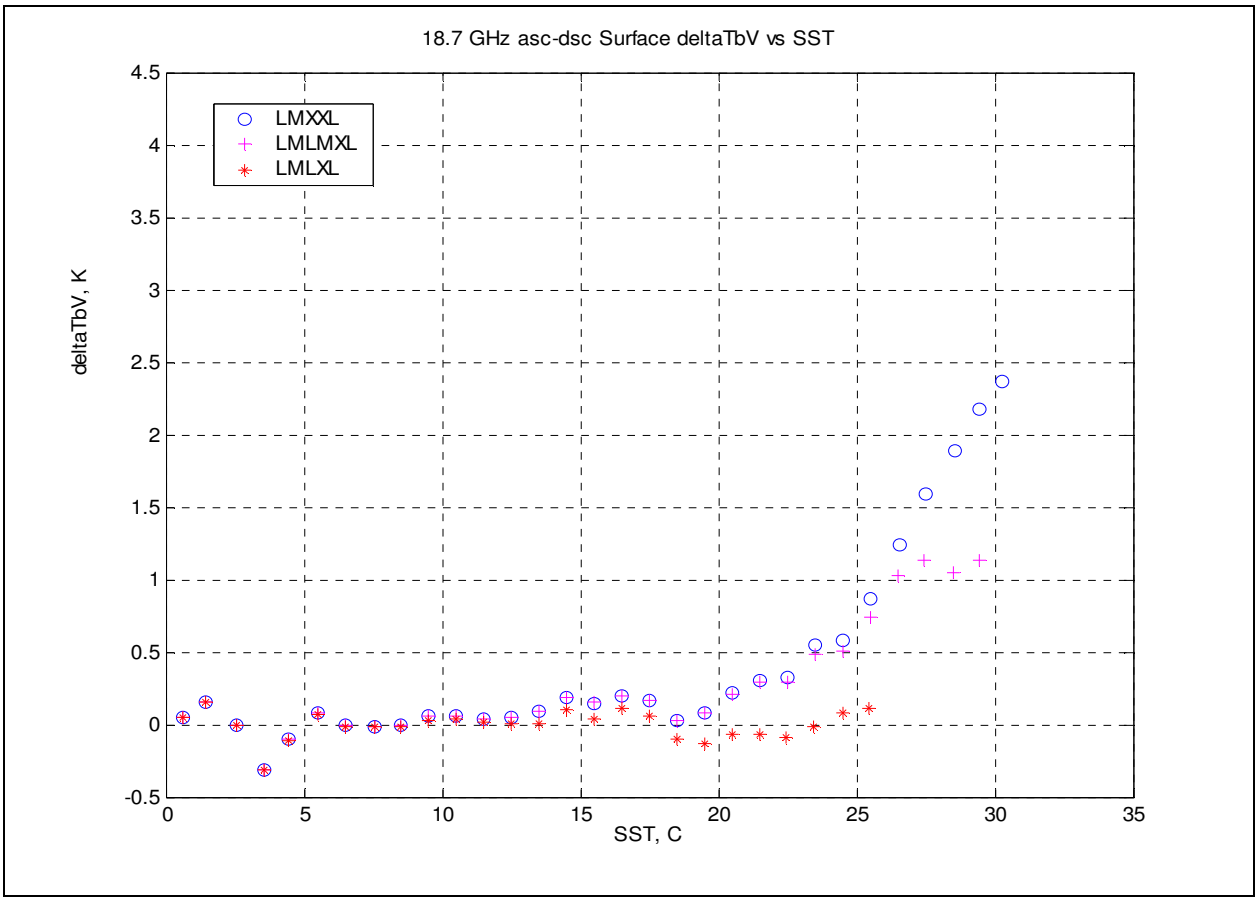

Figure 31: Effect of water vapor on the 18.7 GHz deltaTbV.

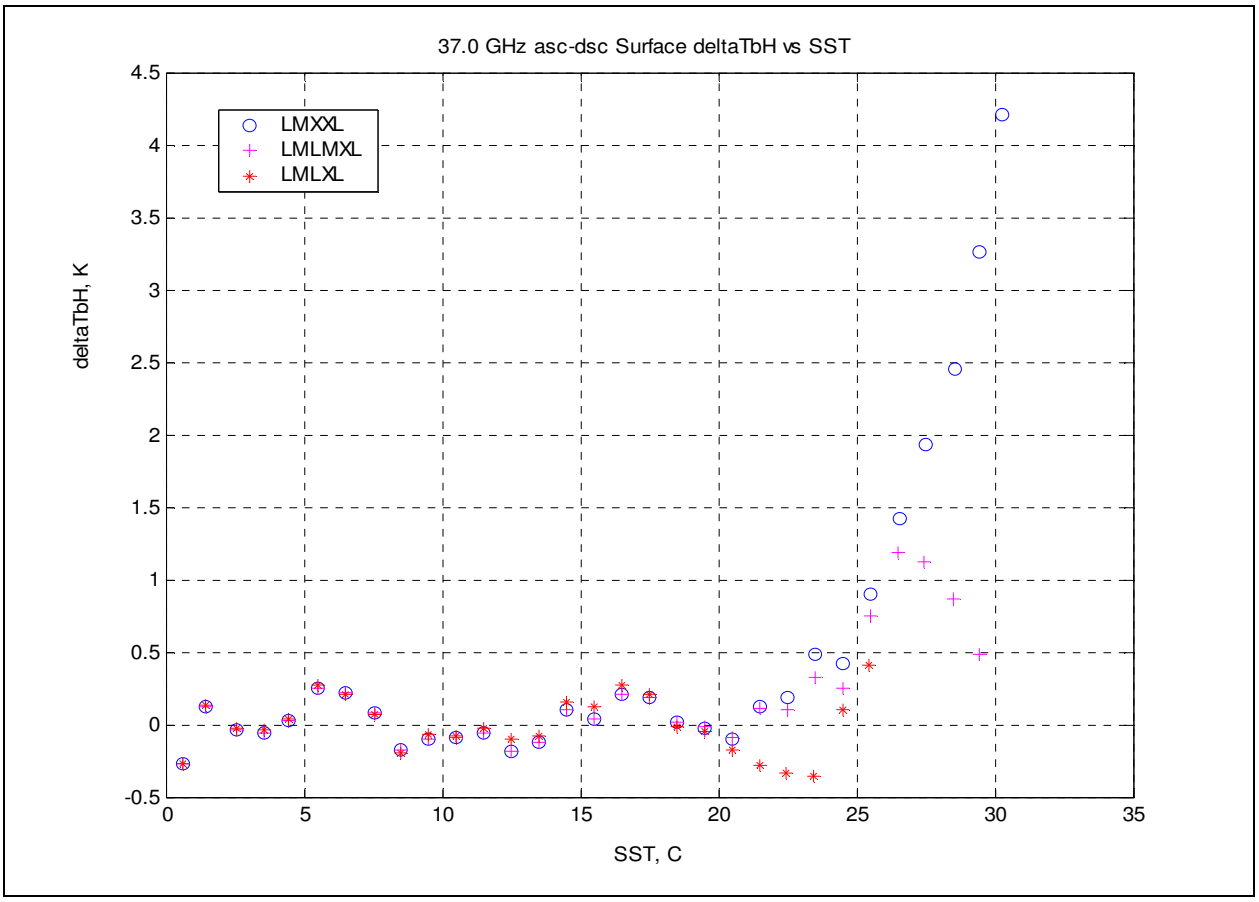

Figure 32: Effect of water vapor on the 37 GHz deltaTbH.

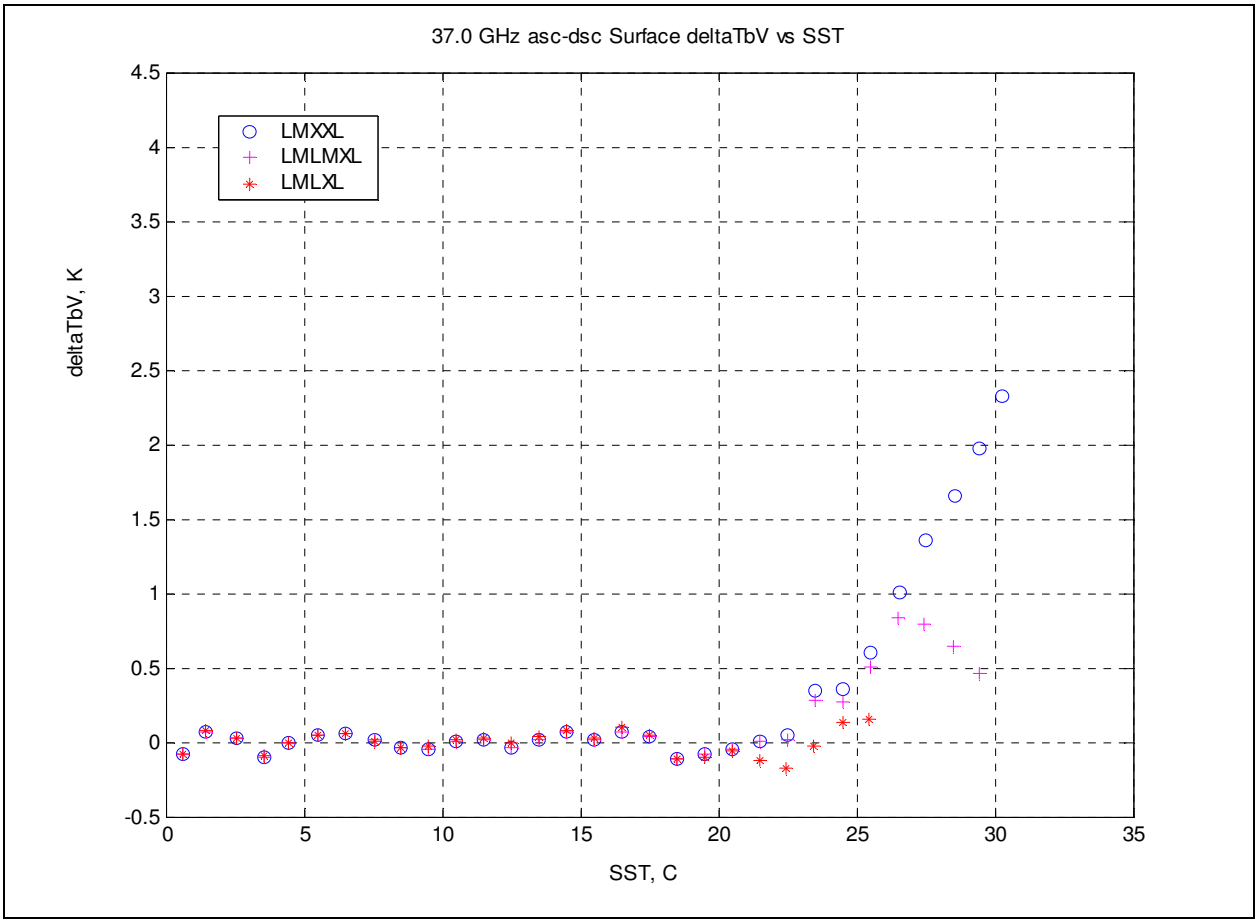

Figure 33: Effect of water vapor on the 37GHz deltaTbV.

4.3.3 Evaluation versus Wind Speed

In RadTb, the wind-roughened ocean surface has increased emissivity, which increases the direct surface emission. This is modeled as an additive "delta-emissivity", which is an empirically derived polynomial of windspeed with coefficients that depend upon the radiometer frequency. This dependence with microwave frequency is weak (approximately square-root) and is polarization dependent (H-pol stronger than V-pol). The delta-emissivity due to wind speed is evaluated for the 6.8 GHz and 10.7 GHz channels because these frequencies are less sensitive to the water vapor and cloud atmospheric correction.

To determine the affect of increasing wind speed on the surface Tb, the LMXXL environmental conditions are used for this analysis. The surface deltaTb is evaluated separately for V- & H-pol, asc and dsc revs and wind speed ranges of: 0 – 3 m/s, 3 – 4 m/s, 4 – 5 m/s, and 5 – 7 m/s. The result of this analysis is given in figures 34 through 41. Overall, the differences between asc and dsc revs are negligible as expected; and the difference between wind speed ranges is small (< 0.5 K). Again H-pol has the largest errors, especially at SST > 17 C (290 K), where the influence of water vapor increases at high SST.

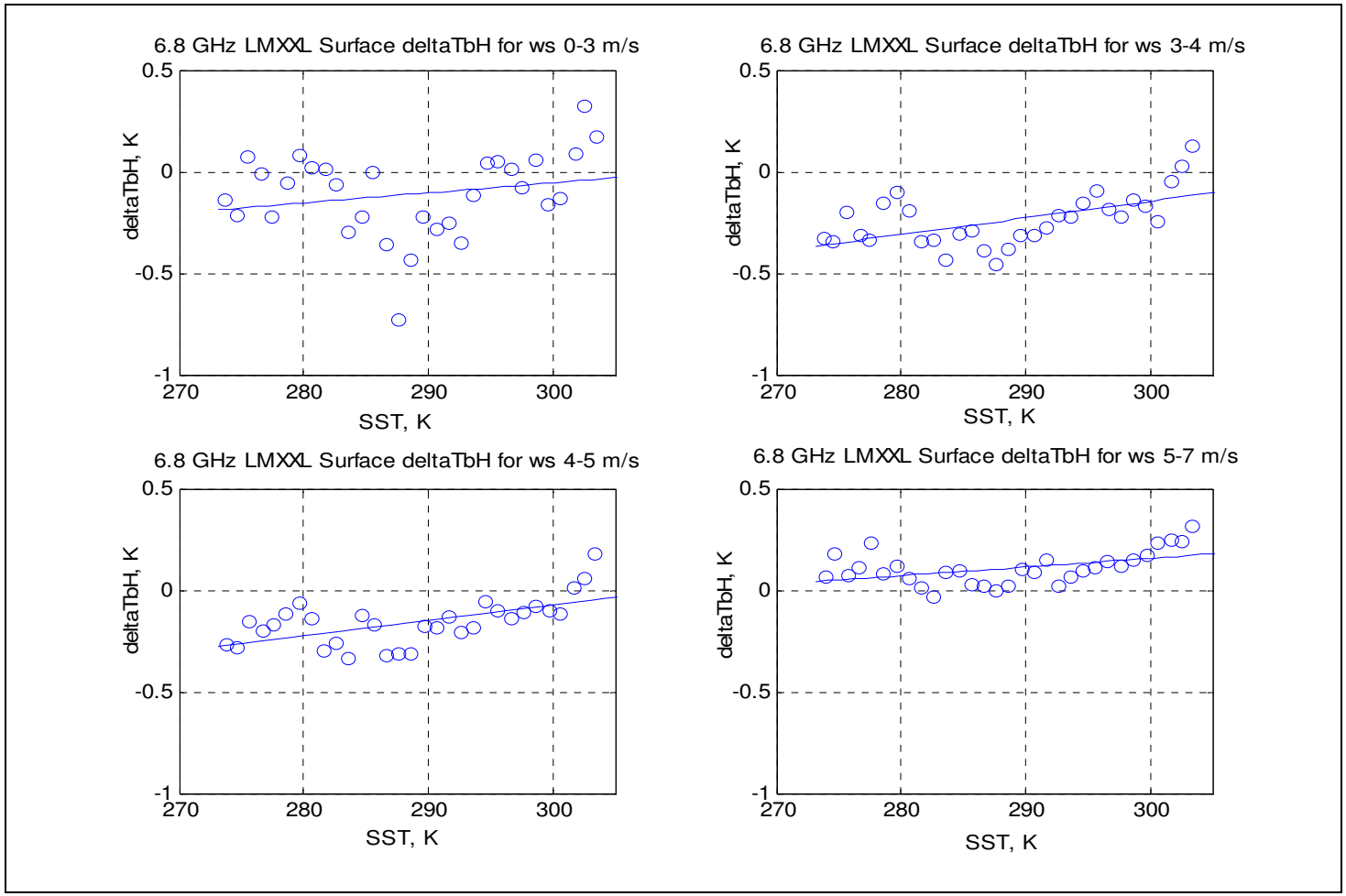

Figure 34**:** 6.8 GHz deltaTbH for ascending revs and different ranges of wind speed.

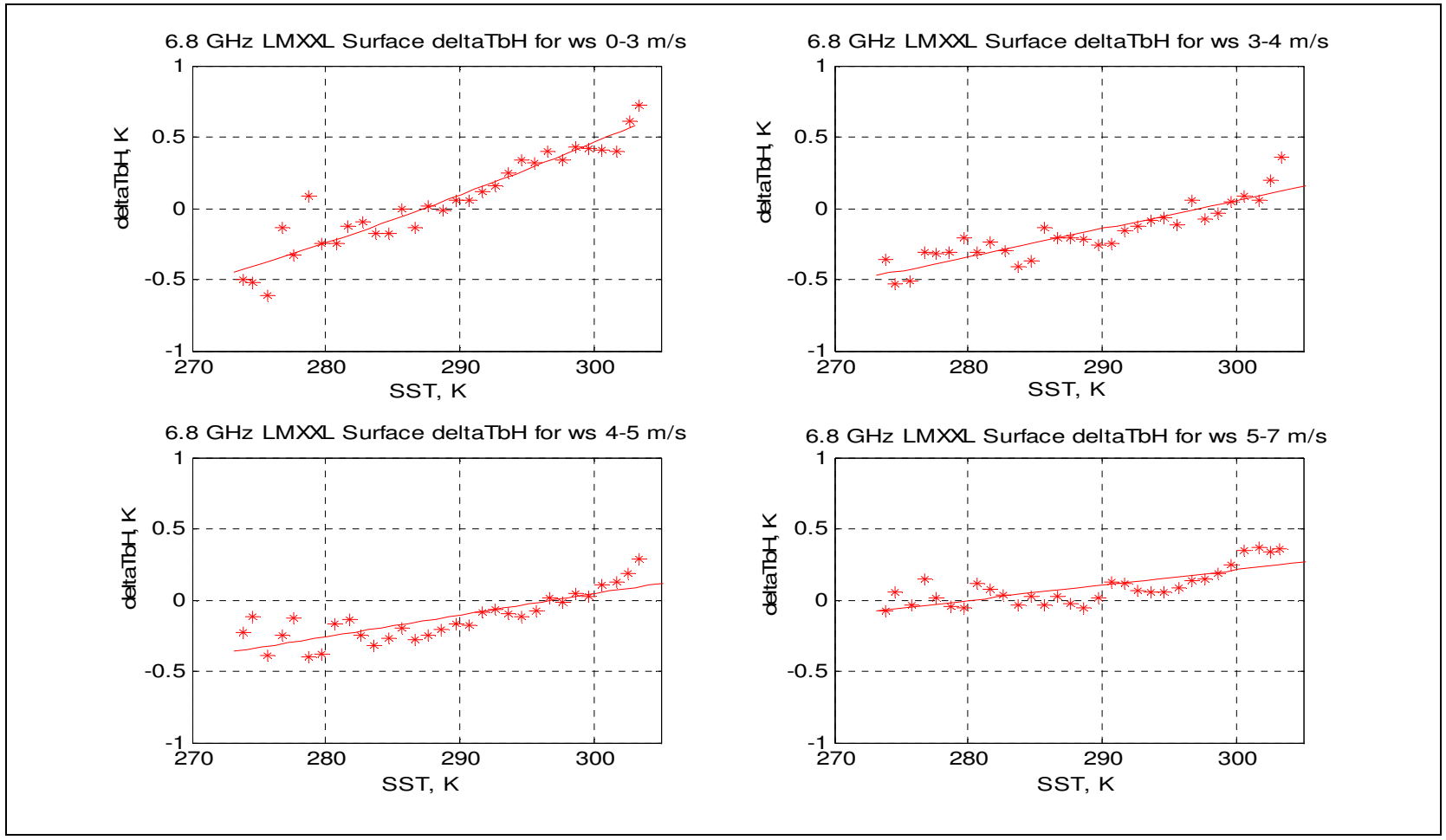

Figure 35: 6.8 GHz deltaTbH for descending revs and different ranges of wind speed.

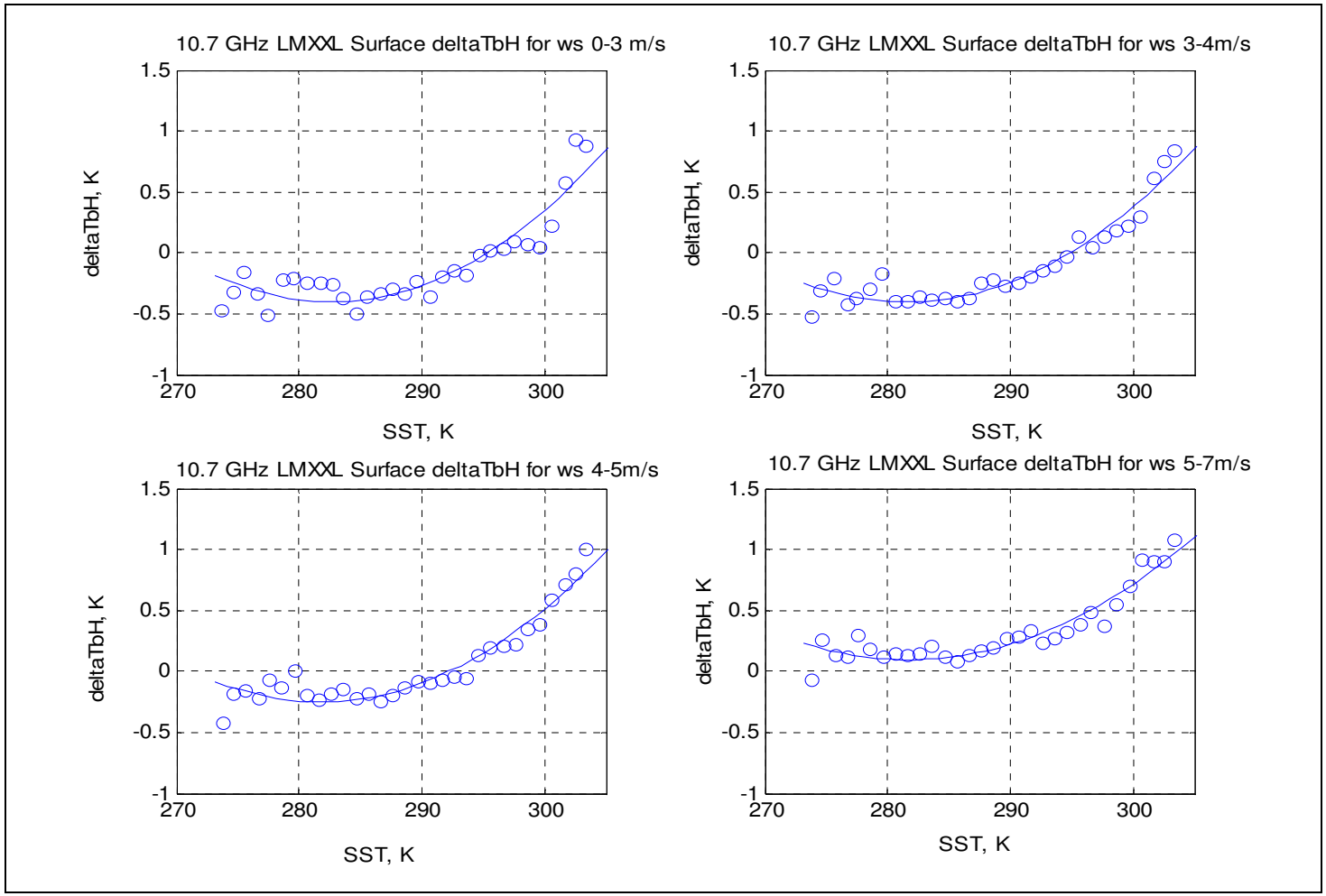

Figure 36: 10.7 GHz deltaTbH for ascending revs and different ranges of wind speed.

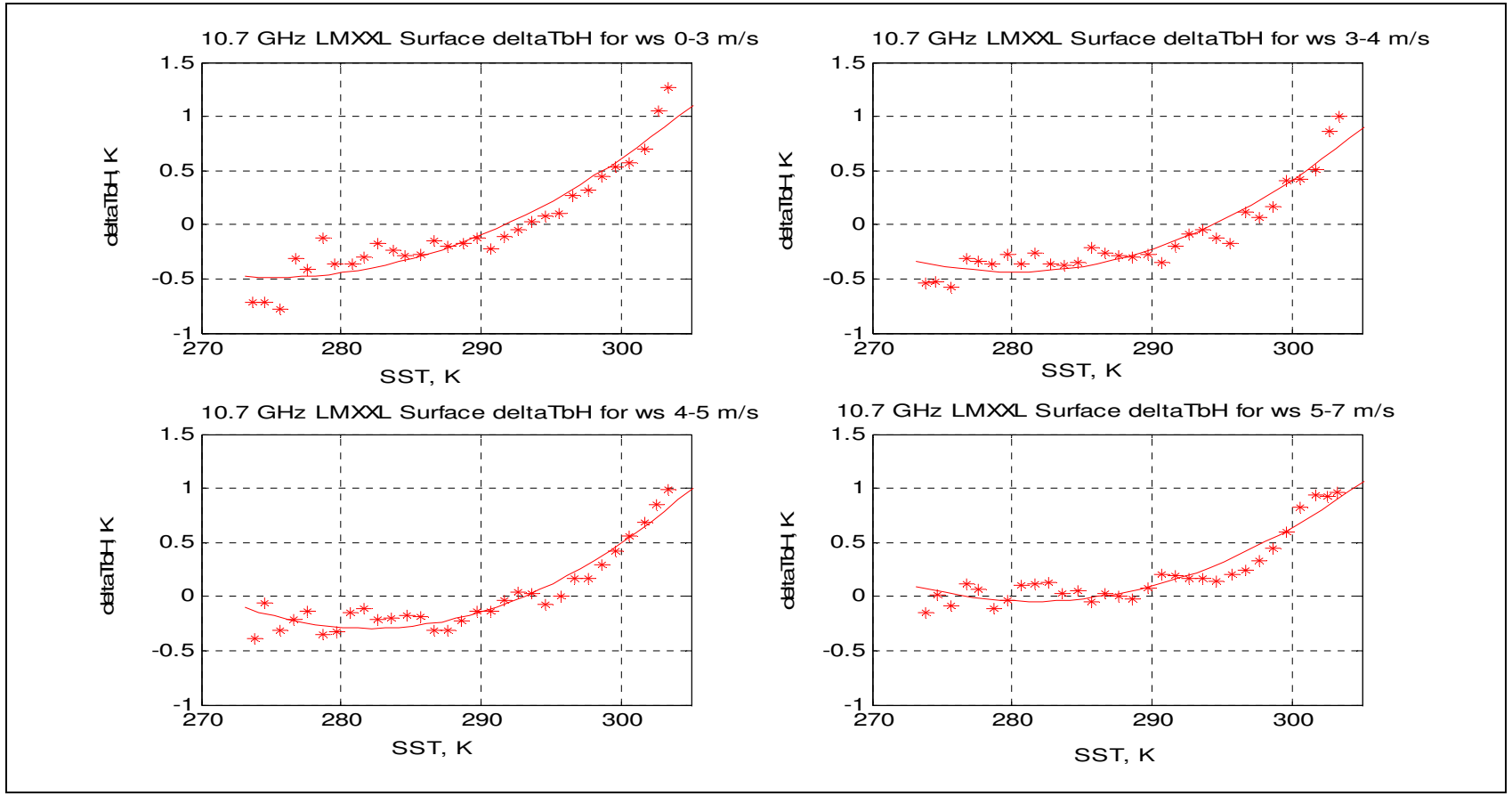

Figure 37: 10.7 GHz deltaTbH for descending revs and different ranges of wind speed.

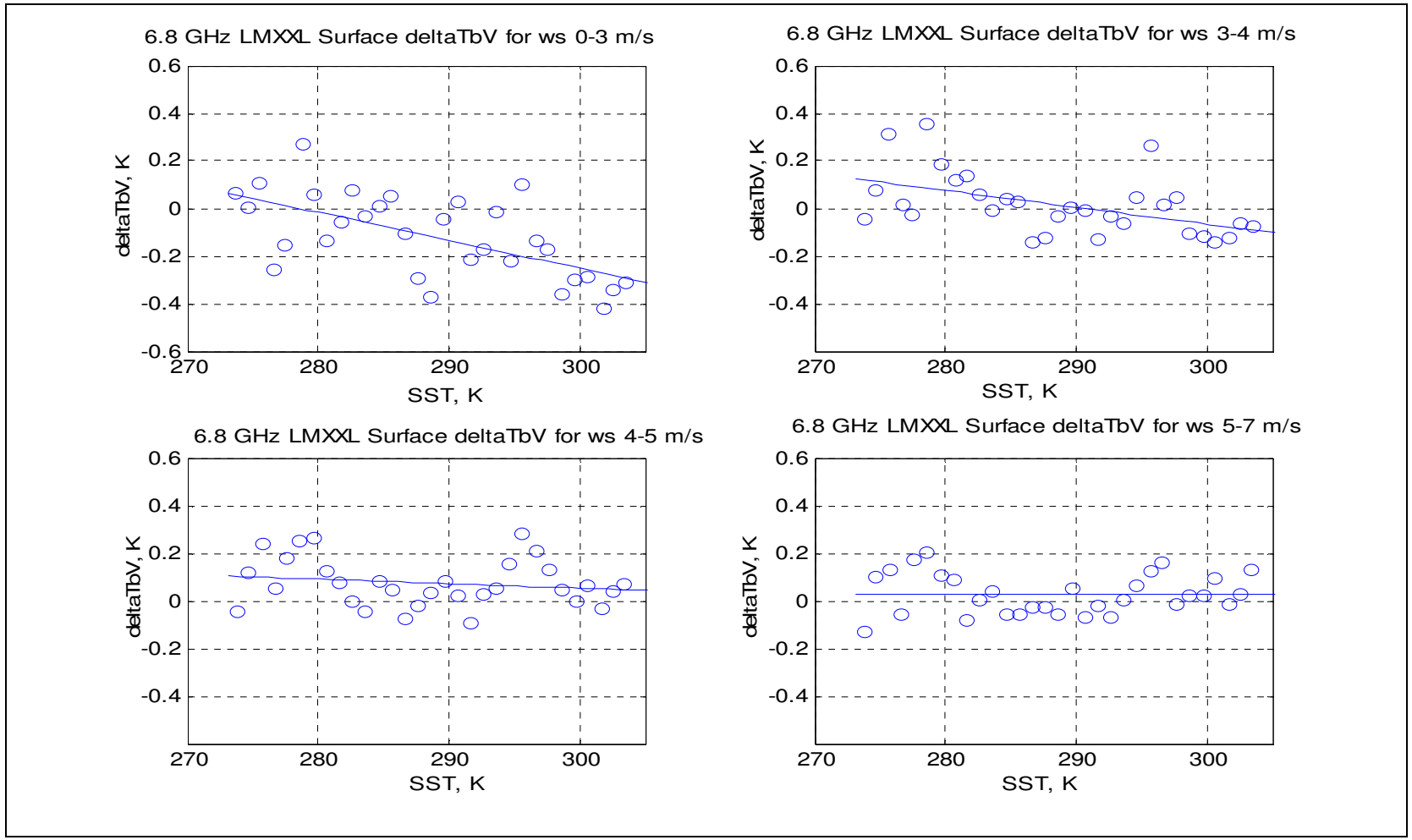

Figure 38: 6.8 GHz deltaTbV for ascending revs and different ranges of wind speed.

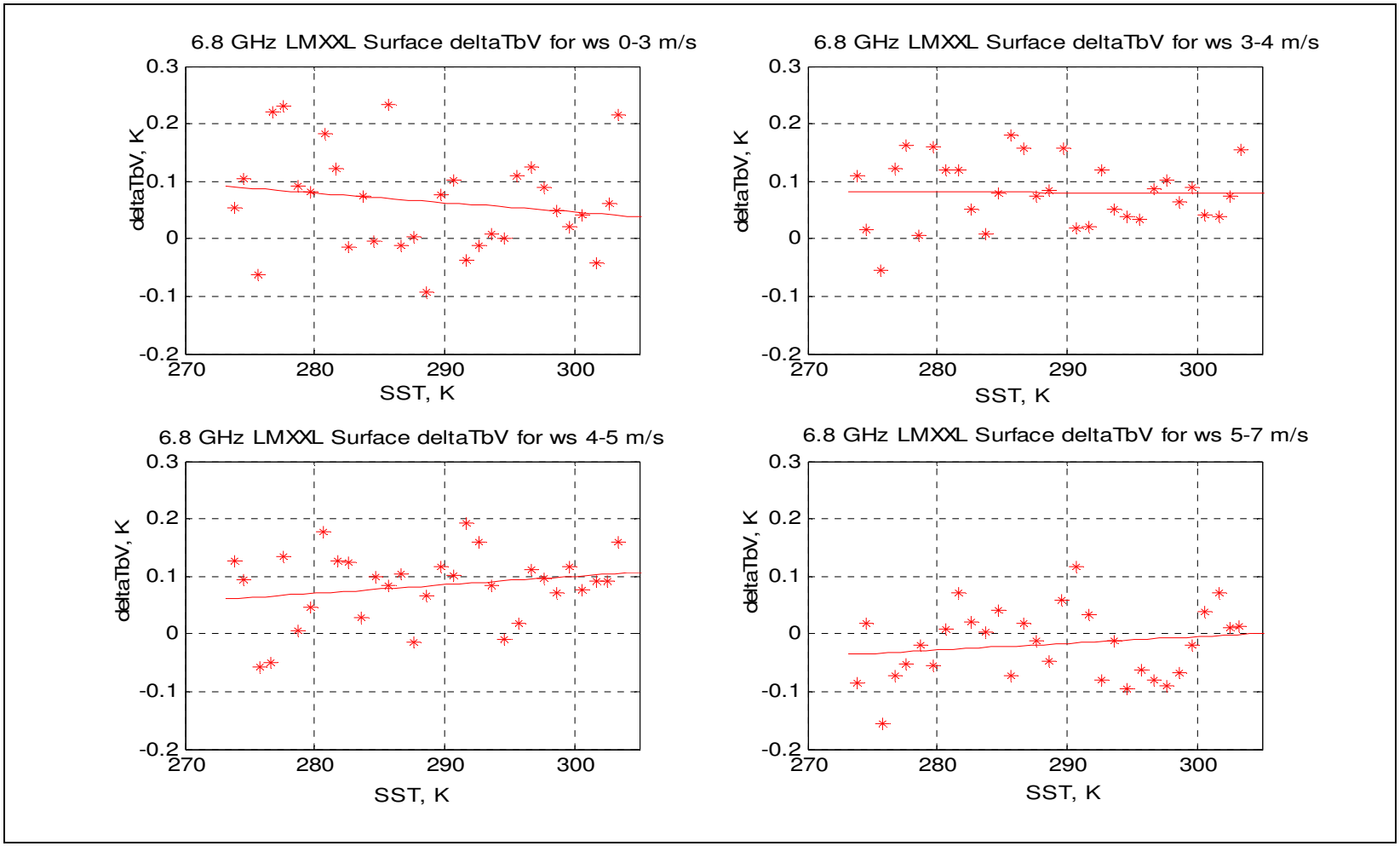

Figure 39: 6.8 GHz deltaTbV for descending revs and different ranges of wind speed.

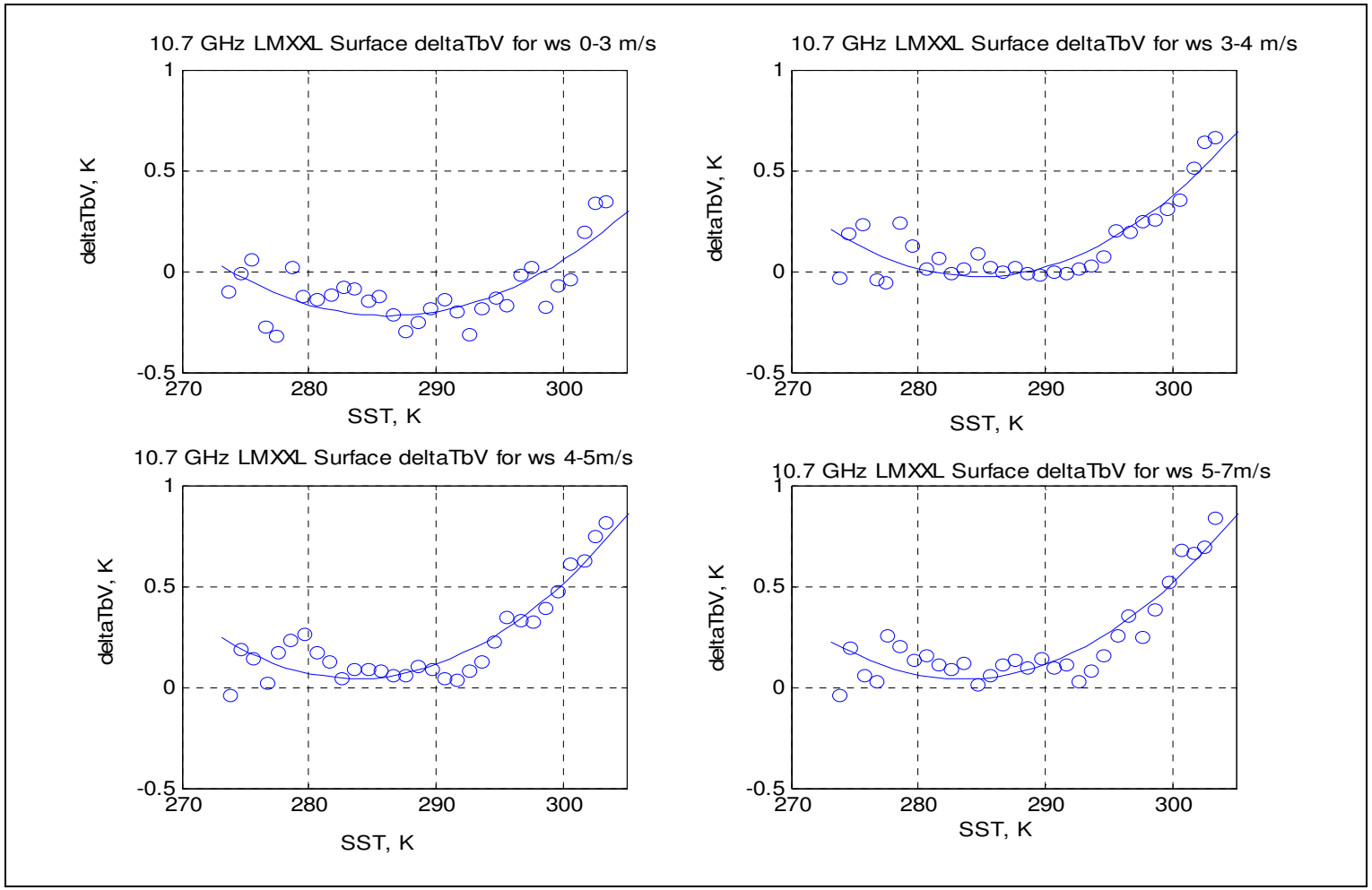

Figure 40: 10.7 GHz deltaTbV for ascending revs and different ranges of wind speed.

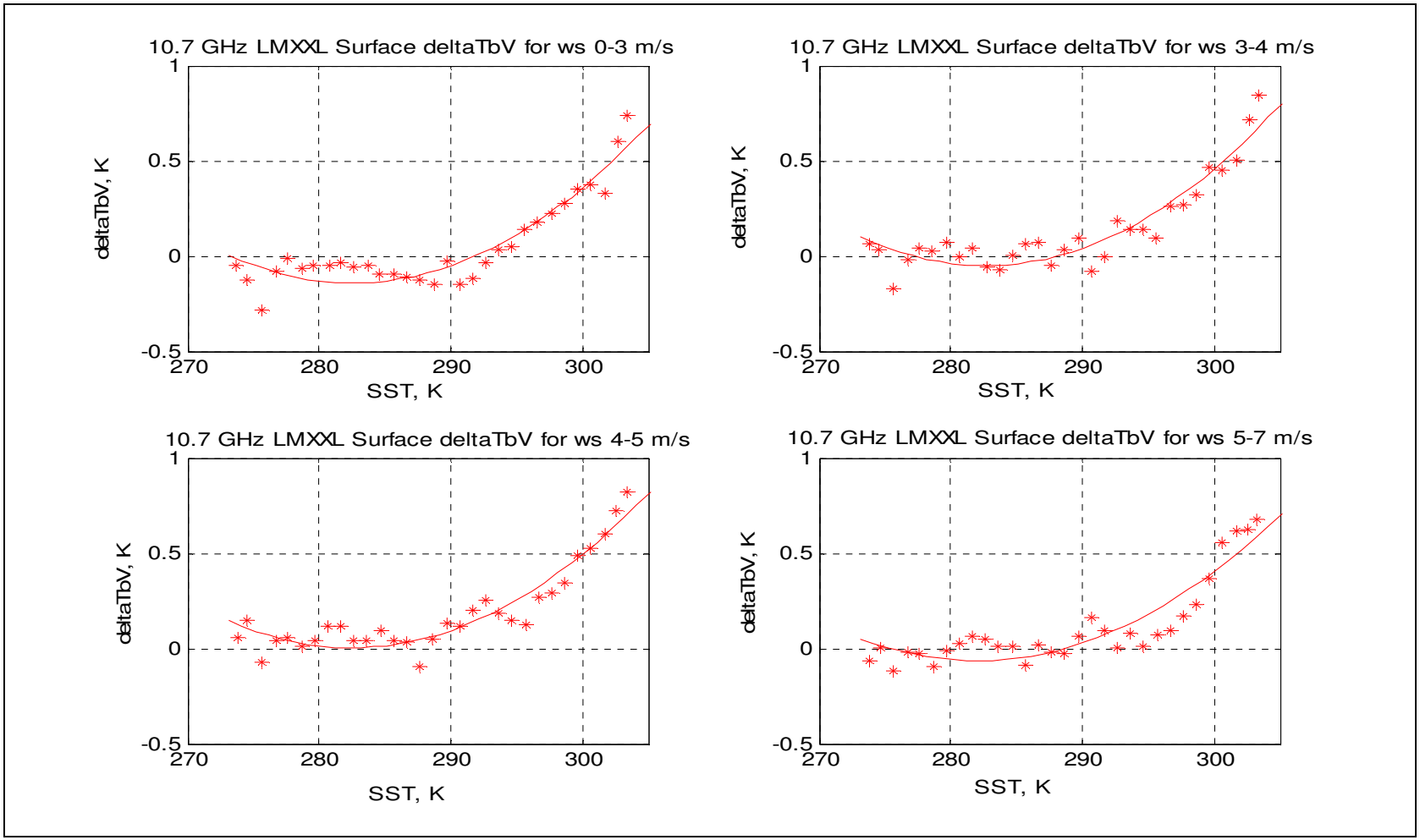

Figure 41: 10.7 GHz deltaTbV for descending revs and different ranges of wind speed.

To determine the accuracy of RadTb for wind speeds > 7 m/s, the LMML (low wind speed), MMML (medium wind speed), and HMML (high wind speed) conditions are used for this analysis. Over these environmental boxes, the average surface deltaTb (and standard deviation) and the corresponding average wind speed is computed, and the results presented in figures 42 through 45. For both H- and V-pol, the surface deltaTb increases for the high wind speed box; but the sign of the error is opposite. For H-pol the error increases with (RadTb > WindSat); but for V-pol the error increases in the negative direction (WindSat > RadTb). Since the atmospheric upwelling brightness is the same for both polarizations, this difference results because of the reflected sky component, which is approximately twice as large at H-pol. This dependence of the RadTb error is much different than that for lower wind speeds where the errors were similar. Wind speeds > 6 - 7 m/s corresponds to the point where breaking waves and foam begin on the ocean; so the RadTb probably does not model this phenomena correctly.

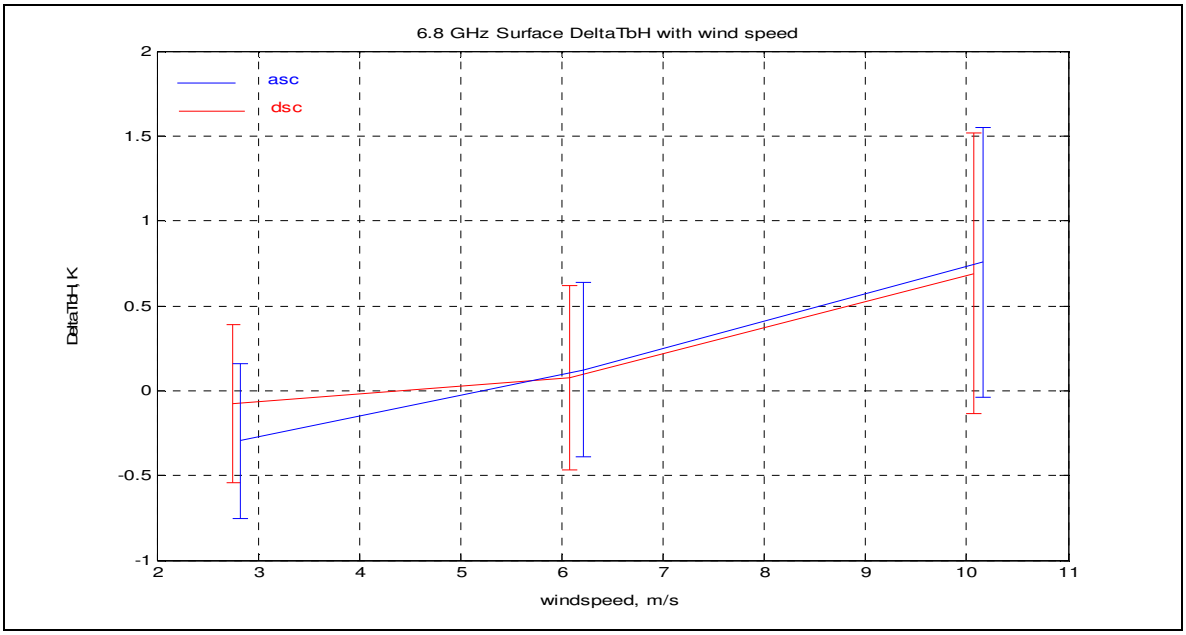

Figure 42: 6.8 GHz deltaTbH for ascending and descending revs.

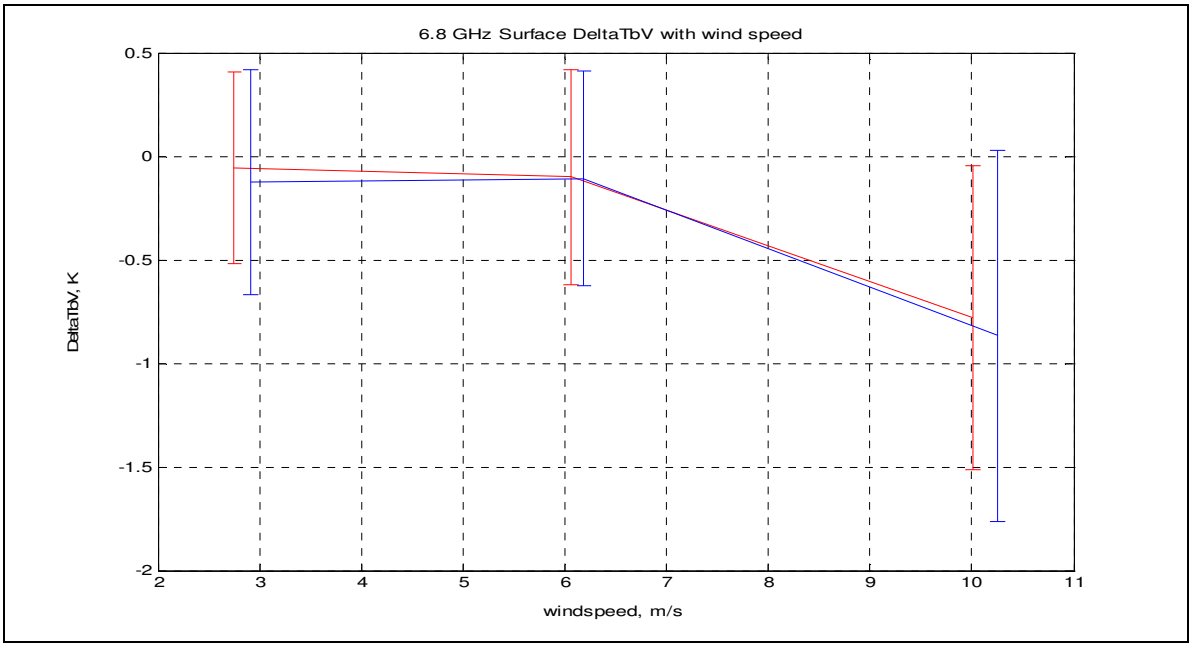

Figure 43: 6.8 GHz deltaTbV for ascending and descending revs.

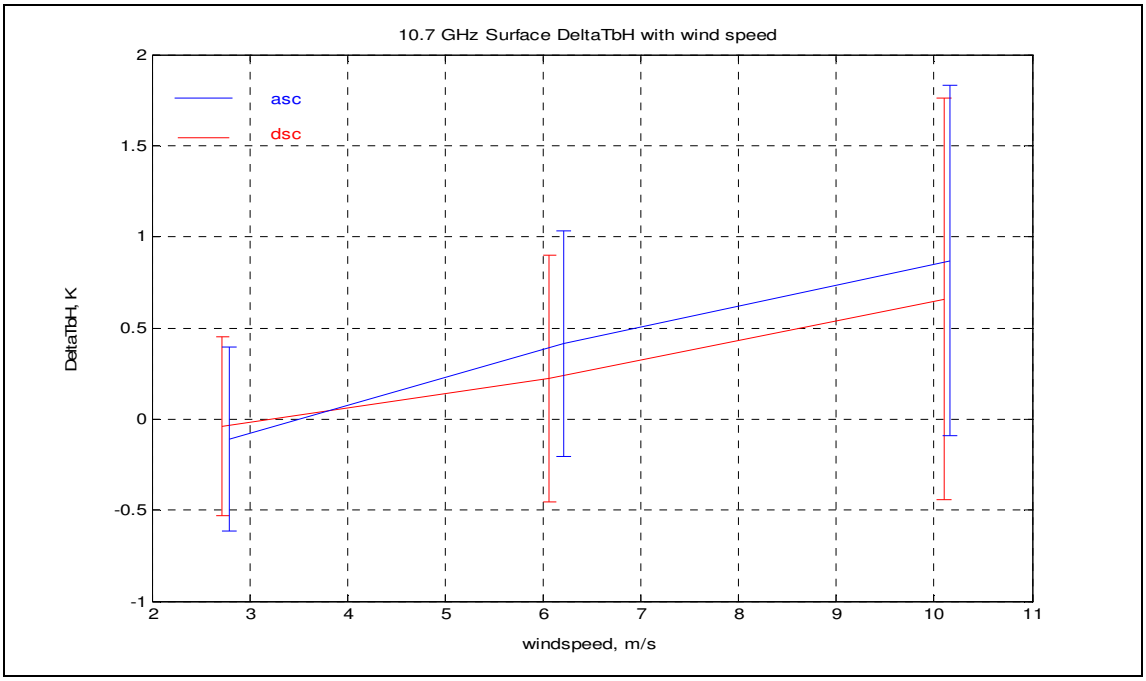

Figure 44: 10.7 GHz deltaTbH for ascending and descending revs.

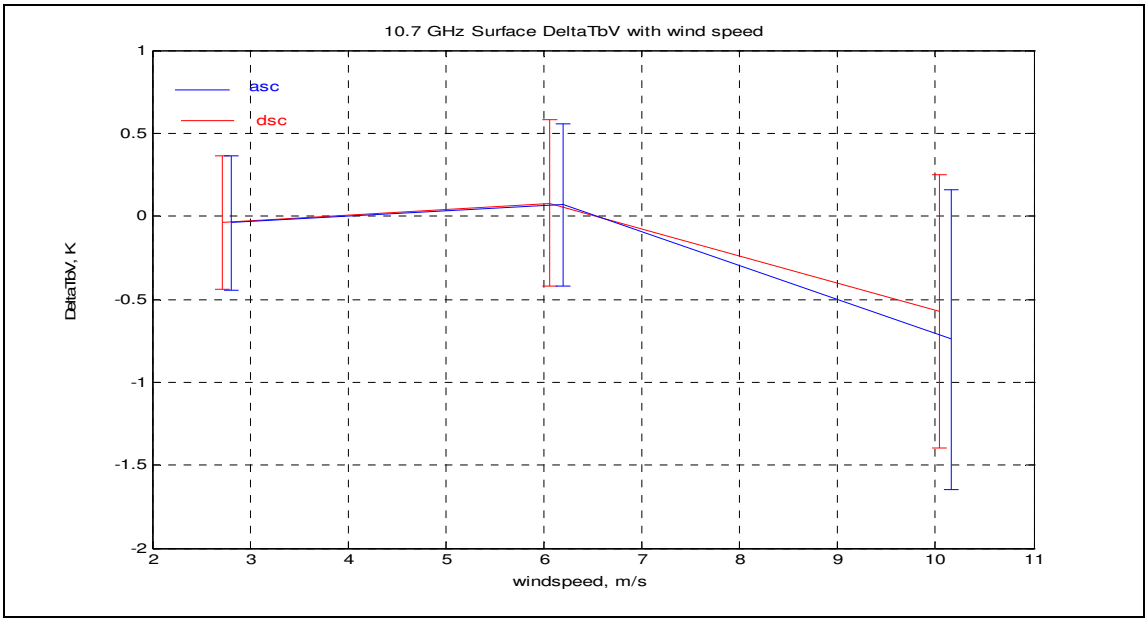

Figure 45: 10.7 GHz deltaTbV for ascending and descending revs.

Even after revising RadTb by incorporating the empirical SST correction, the surface deltaTb results, for all radiometer channels (frequencies and polarizations), still show a significant increase in the error for SST's > 20 C. Further, for the 18.7 GHz and 37.0 GHz channels the errors are greatest because of their increased sensitivity to water vapor. To examine this further, the error dependence on both water vapor and wind speed is analyzed for two cases; SST < 20 C and SST > 20 C. The results of this analysis are shown in figures 46 through 53, where the surface deltaTb is displayed as a color image against the wind speed (x-axis) and the water vapor (y-axis). Clearly, the errors are dependent on water vapor especially for SST > 20 C.

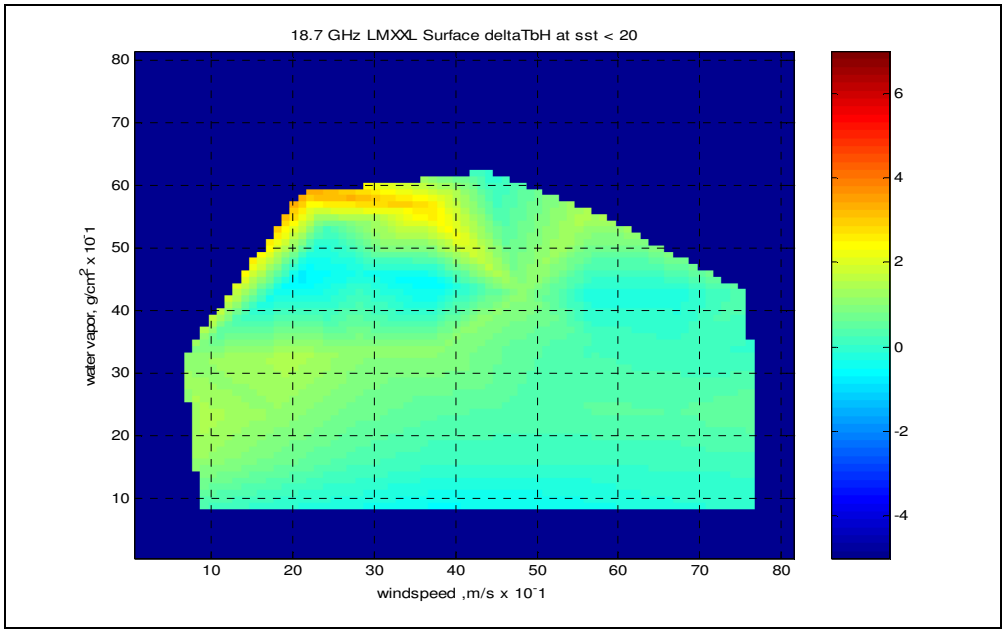

Figure 46: 18.7 GHz DeltaTbH error characterized by water vapor and wind speed for SST<20 C

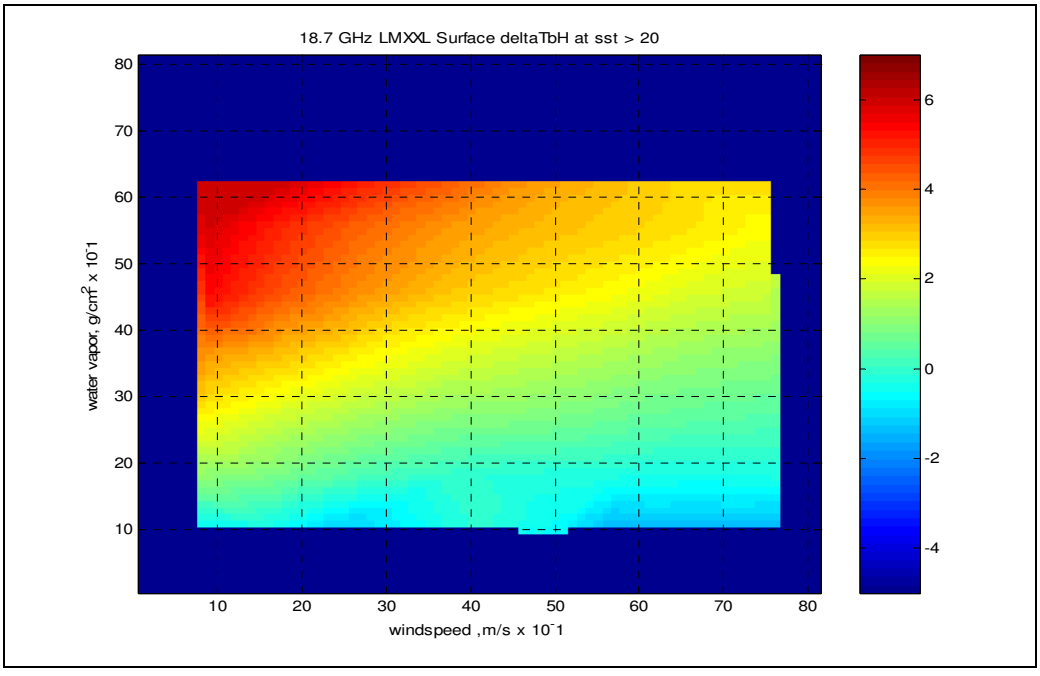

Figure 47: 18.7 GHz DeltaTbH error characterized by water vapor and wind speed for SST>20 C

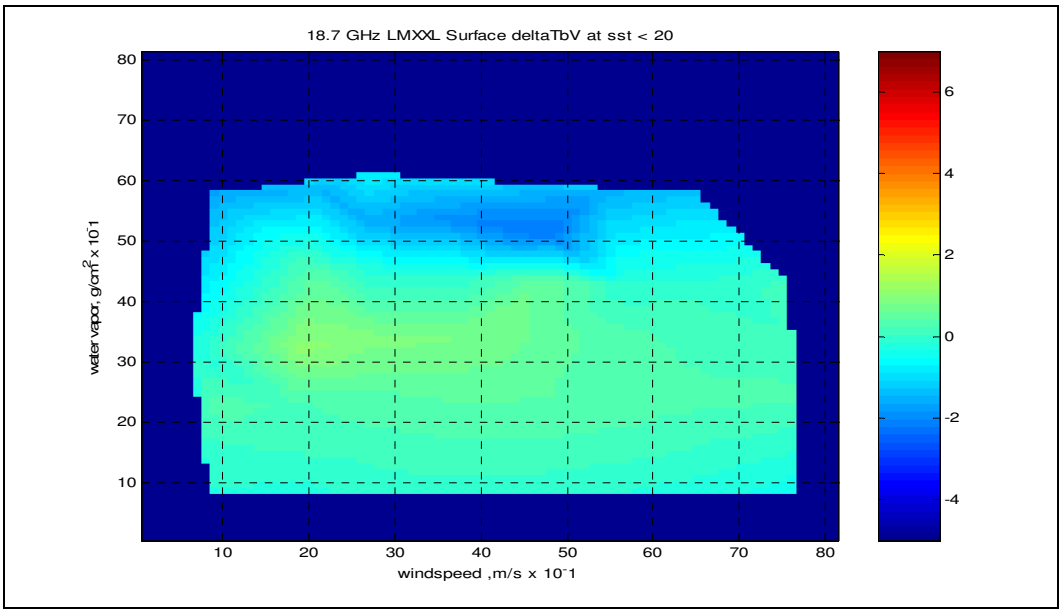

Figure 48: 18.7 GHz DeltaTbV error characterized by water vapor and wind speed for SST<20 C

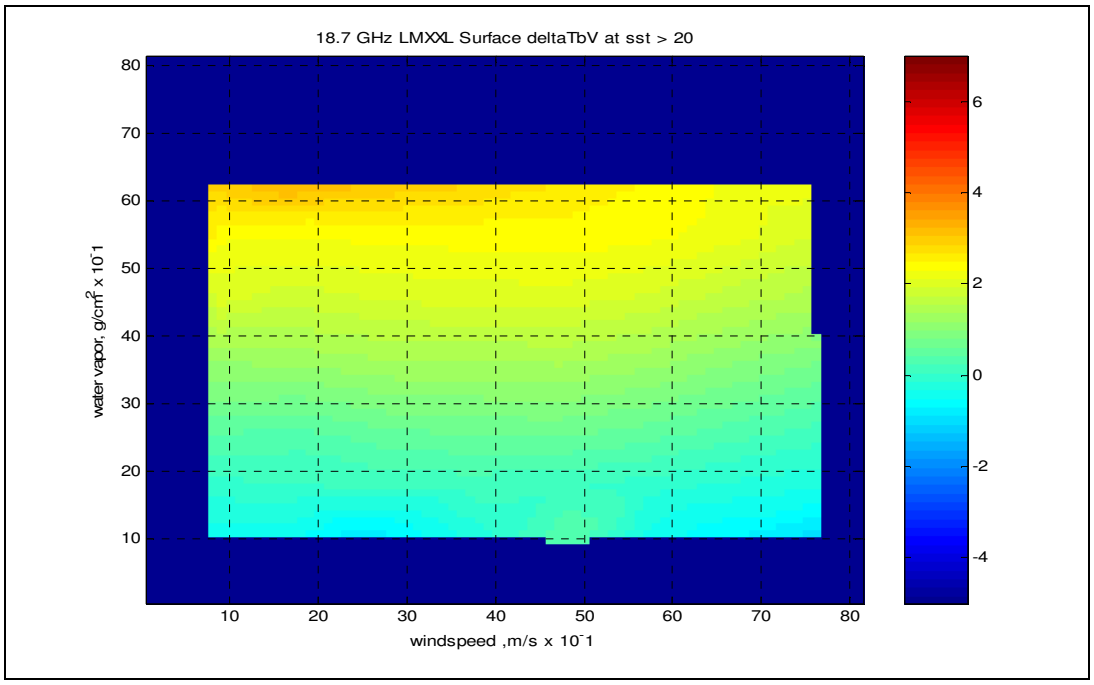

Figure 49: 18.7 GHz DeltaTbV error characterized by water vapor and wind speed for SST>20 C

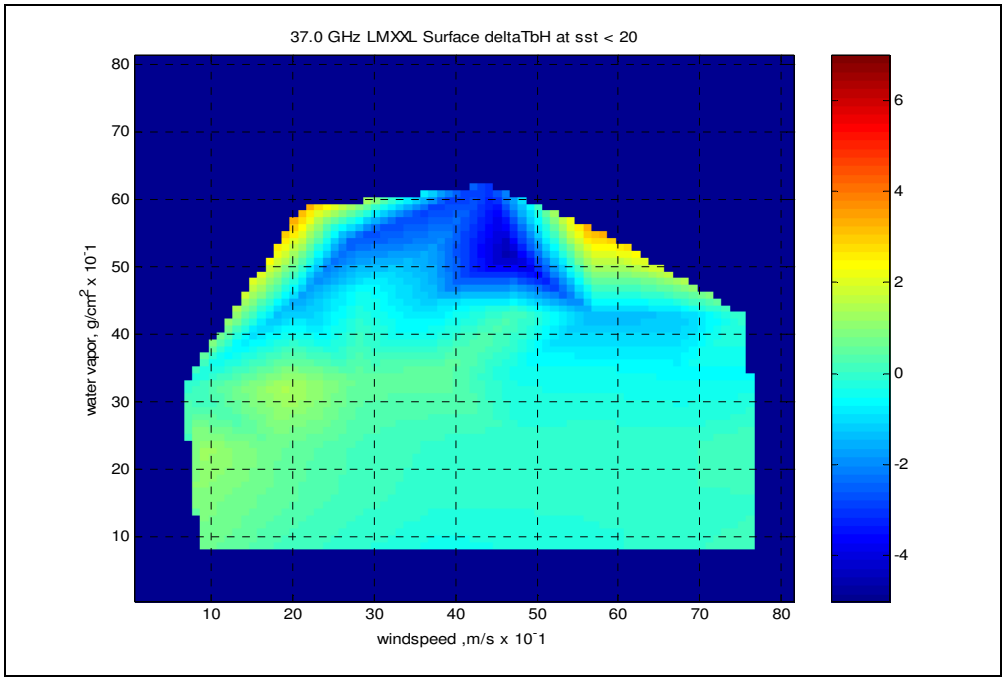

Figure 50: 37.0 GHz DeltaTbH error characterized by water vapor and wind speed for SST<20 C

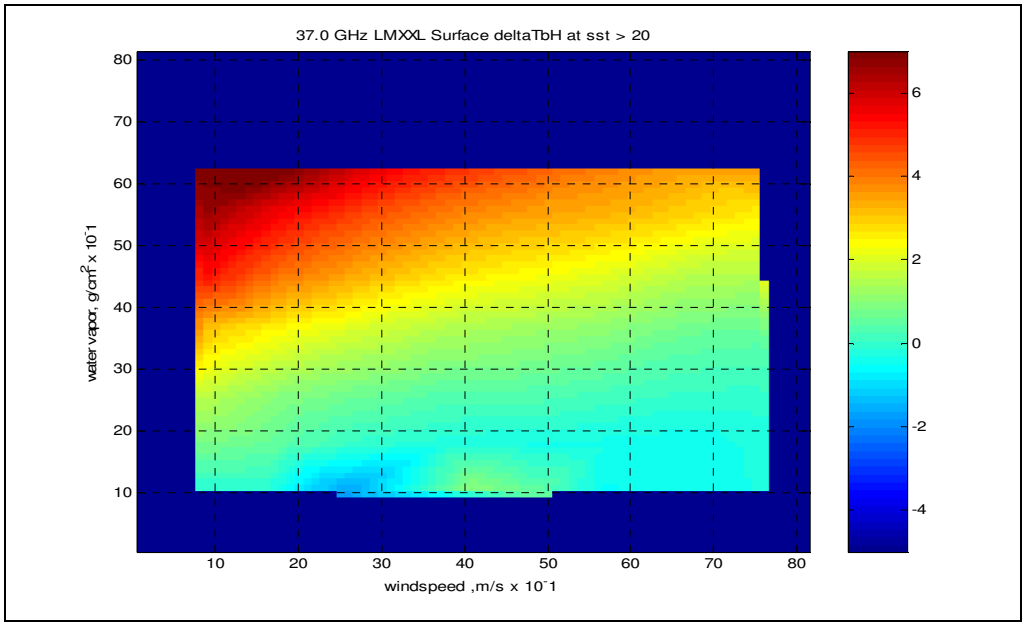

Figure 51: 37.0 GHz DeltaTbH error characterized by water vapor and wind speed for SST>20 C

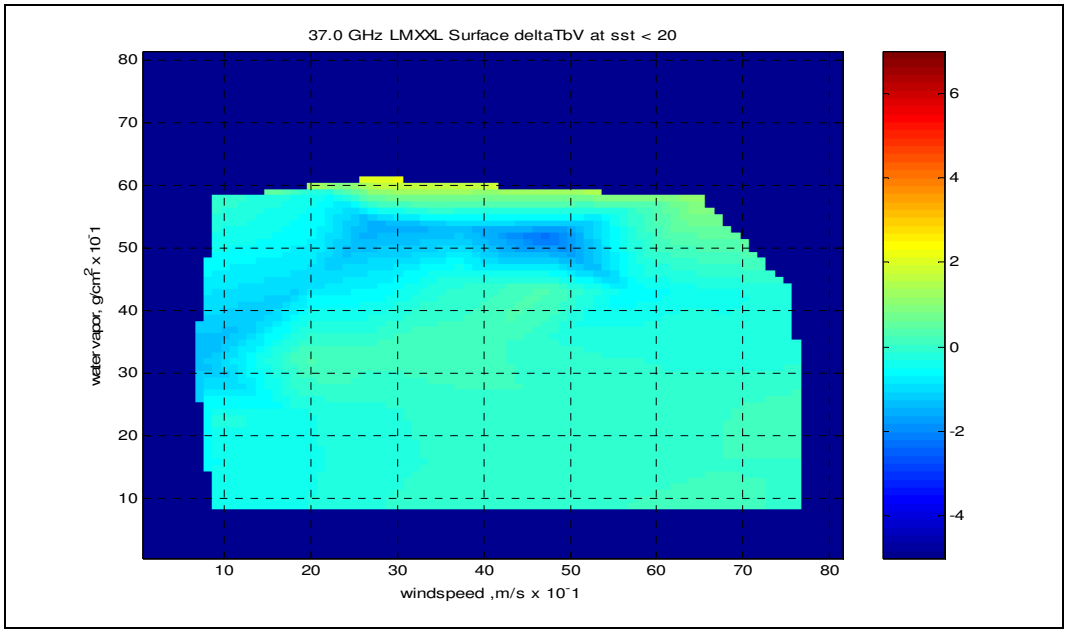

Figure 52: 37.0 GHz DeltaTbV error characterized by water vapor and wind speed for SST<20 C

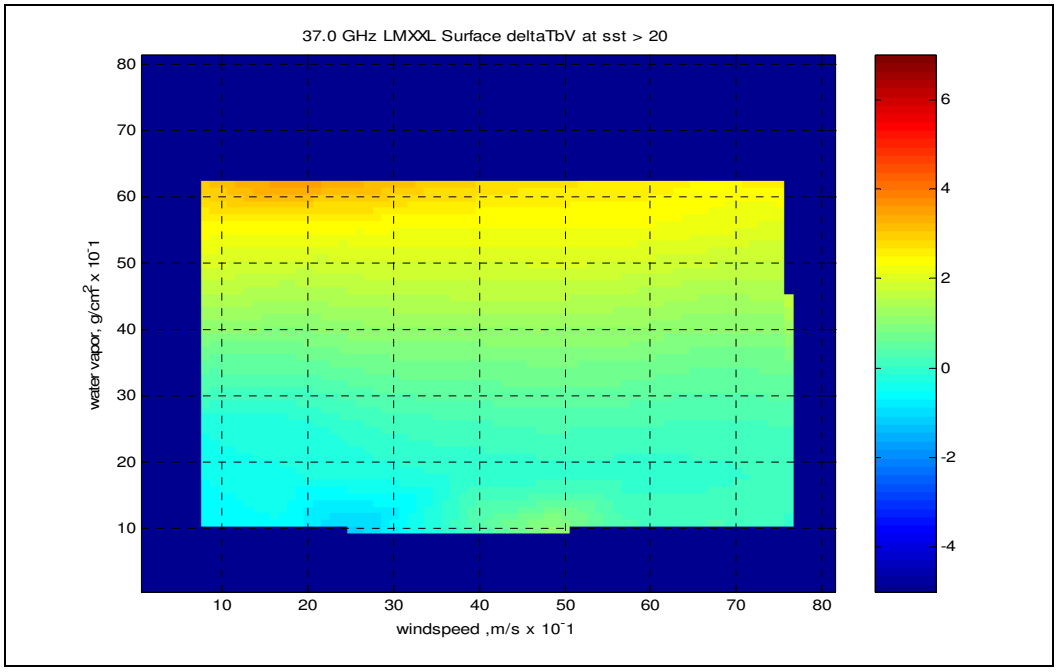

Figure 53: 37.0 GHz DeltaTbV error characterized by water vapor and wind speed for SST>20 C

4.4 Apparent Tb Comparisons

Finally, the overall evaluation of the revised RadTb apparent brightness temperature (at the top of the atmosphere) is performed for all applicable environmental boxes 0 through 80. Of the 81 possible combinations of low, medium and high for the four significant environmental parameters (wind speed, water vapor, SST and cloud liquid water), eleven "null" boxes are not populated with sufficient observations to make meaningful comparisons. The average delta-Tb and corresponding standard deviations are presented in figures 54 through 57; and for the null boxes the square color is dark blue (value = – 7). The x and y axis represents the box number, where box 0 is found in the lower most left hand corner and box 80 is in the uppermost right hand corner. The statistics of each box are now shown in tables 7 through tables 10, which include the mean and standard deviation of the deltaTb and the number of observations in each box.

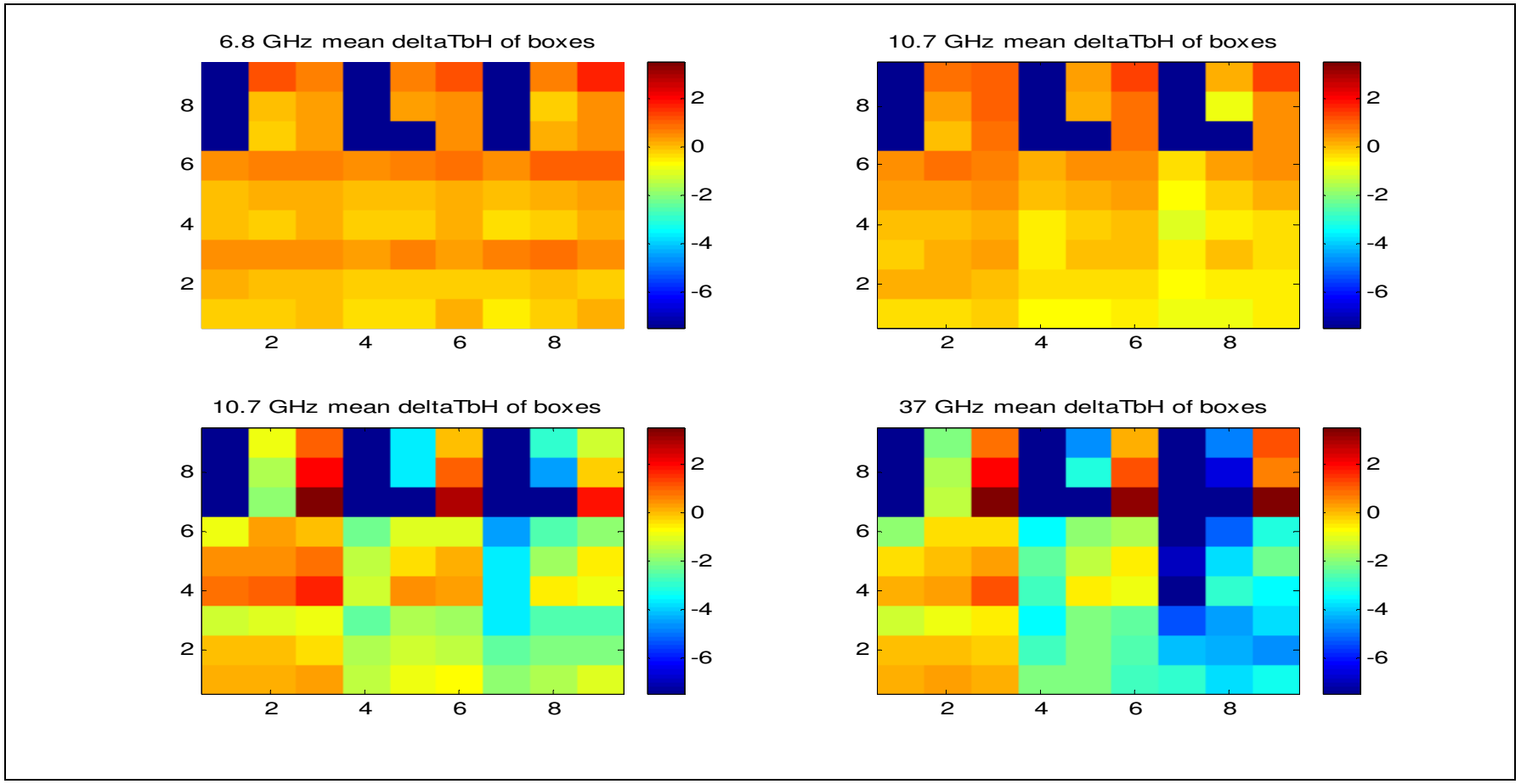

Figure 54: Mean deltaTb (colorbar in Kelvin) of H-pol characterized by environmental boxes. Lower left box is #1 and upper right is #80.

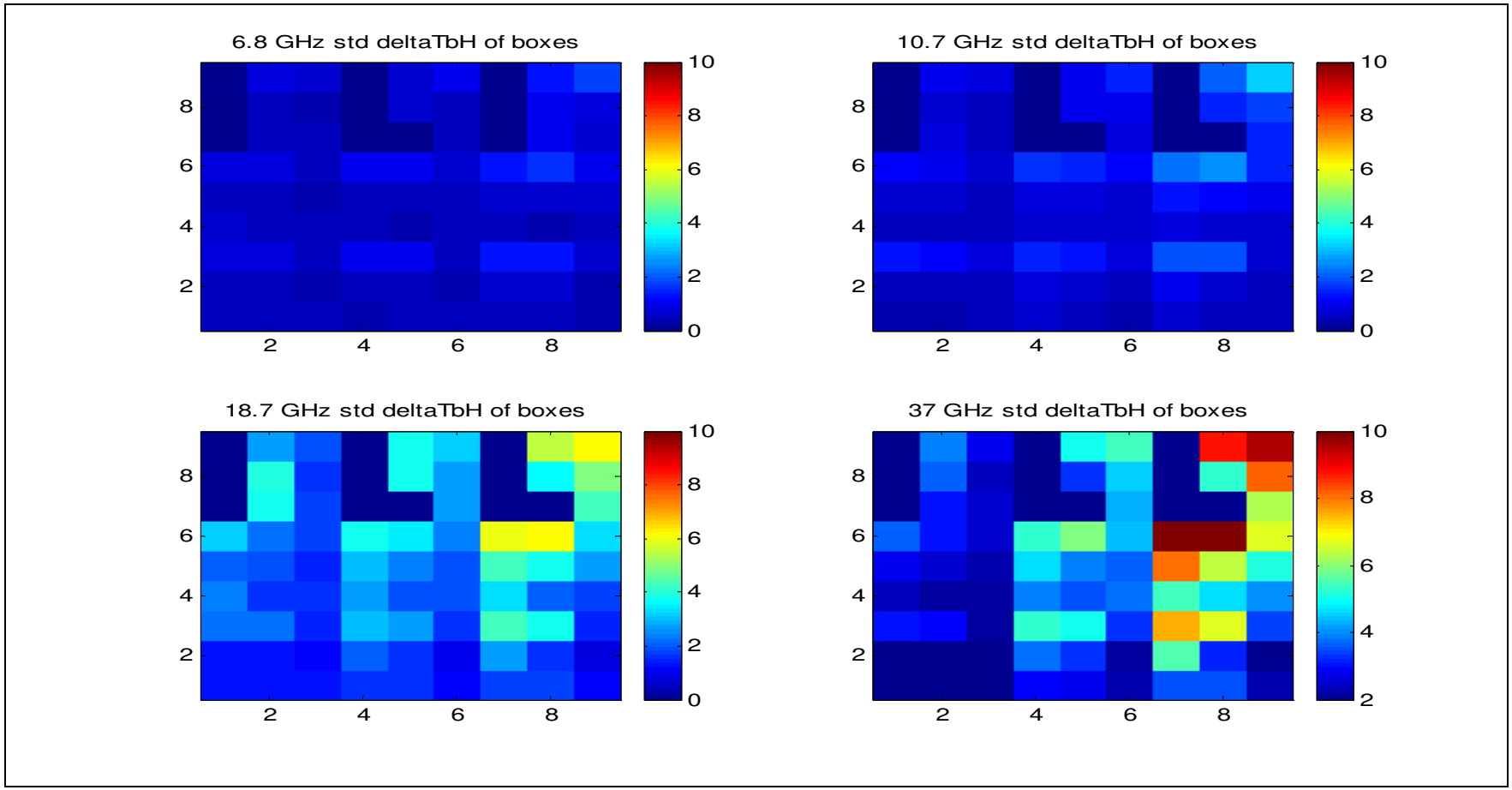

Figure 55: Standard deviation deltaTb (colorbar in Kelvin) of H pol characterized by environmental boxes. Lower left box is #1 and upper right is #80.

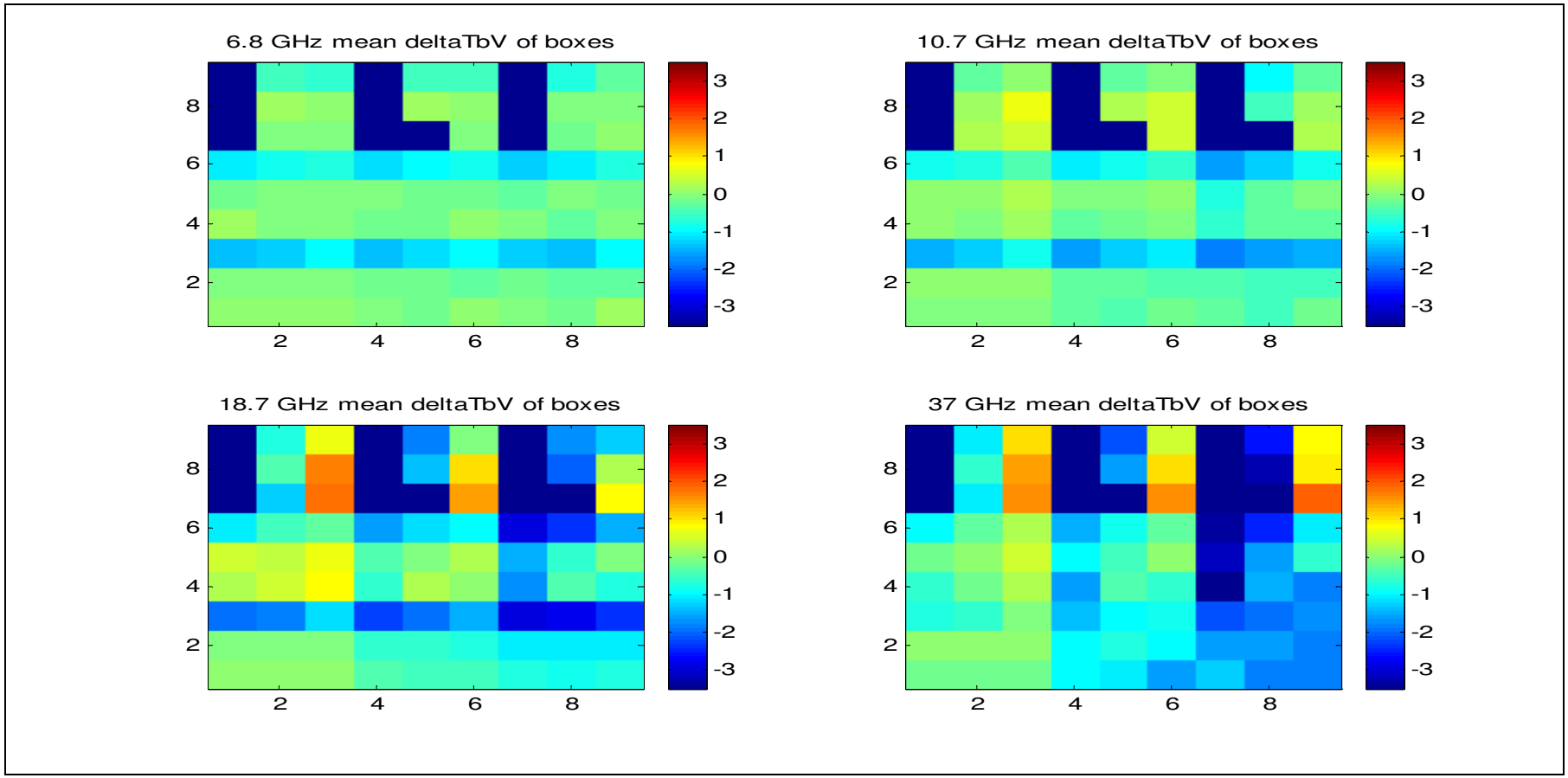

Figure 56: Mean deltaTb (colorbar in Kelvin) of V-pol characterized by environmental boxes.
Lower left box is #1 and upper right is #80.

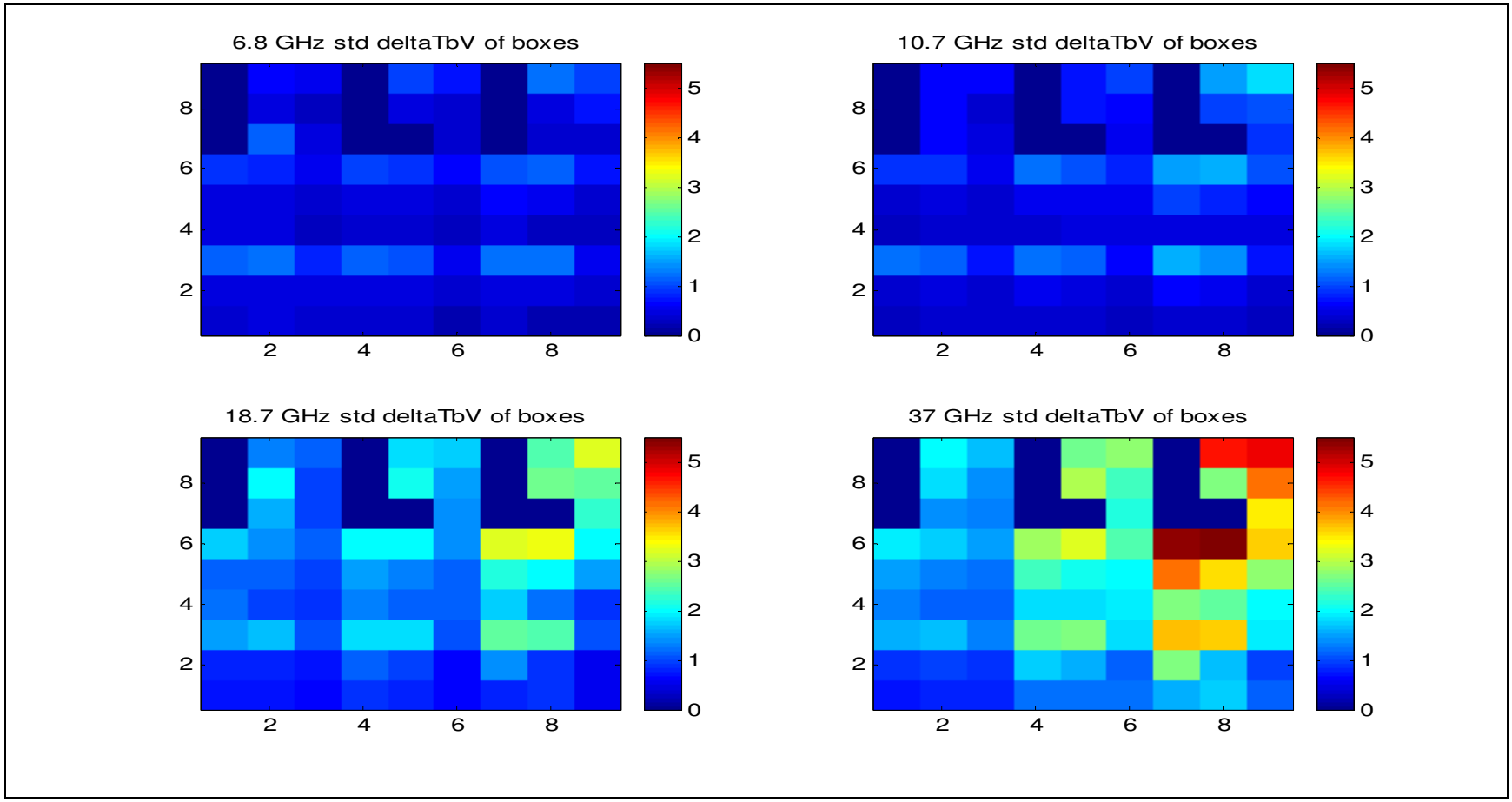

Figure 57: Standard deviation deltaTb (colorbar in Kelvin) of V pol characterized by environmental boxes. Lower left box is #1 and upper right is #8

Table 6: Regression Coefficients for Empirical Emissivity Correction

Frequency	Polarization	Second order polynomial coefficients		
6.8	Horizontal	0.000419	-0.22435	29.36505
	Vertical	0.00164	-0.93223	134.7431
10.7	Horizontal	0.000716	-0.38693	51.93148
	Vertical	0.001162	-0.66184	95.0321
18.7	Horizontal	0.002277	-1.19621	154.9595
	Vertical	0.00287	-1.61277	226.6678
37	Horizontal	0.00395	-2.22994	310.017
	Vertical	0.003506	-2.05766	300.33

The table above lists the second order polynomial coefficients that were used to correct the emissivity factor for dual polarization at 6.8 GHz through 37 GHz.

Table 7: 6.8 GHz statistics

box #	ws	wv	sst	clw	mean TbV	std TbV	# of points in box	mean TbH	std TbH	# of points in box
0	L	L	L	L	0.05	0.37	11368	-0.21	0.47	13015
1	M	L	L	L	-0.01	0.45	45610	0.09	0.53	51556
2	H	L	L	L	-1.34	1.16	176683	0.41	0.88	180074
4	M	M	L	L	-0.16	0.43	1453	0.06	0.53	1594
5	H	M	L	L	-1.01	0.86	4250	0.48	0.91	4410
9	L	L	M	L	0.00	0.45	19322	-0.19	0.49	20909
10	M	L	M	L	-0.01	0.47	62526	0.04	0.49	69098
11	H	L	M	L	-1.25	1.21	116425	0.46	0.85	117151
12	L	M	M	L	-0.09	0.48	5214	-0.17	0.47	5708
13	M	M	M	L	-0.10	0.51	26165	0.10	0.52	28533
14	H	M	M	L	-0.83	0.81	28993	0.72	0.80	31165
18	L	L	H	L	0.02	0.41	7944	-0.10	0.52	9040
19	M	L	H	L	-0.04	0.45	18123	-0.01	0.44	20174
20	H	L	H	L	-0.90	0.80	19559	0.45	0.60	21405
21	L	M	H	L	-0.02	0.34	32791	0.08	0.49	36839

box #	ws	wv	sst	clw	mean TbV	std TbV	# of points in box	mean TbH	std TbH	# of points in box
22	M	M	H	L	-0.05	0.39	95062	0.14	0.43	107261
23	H	M	H	L	-0.75	0.56	73037	0.63	0.58	79567
24	L	H	H	L	-0.08	0.43	32316	0.27	0.53	35917
25	M	H	H	L	0.01	0.34	82393	0.31	0.43	93797
26	H	H	H	L	-0.57	0.54	32900	0.73	0.66	35072
27	L	L	L	M	-0.02	0.39	3886	-0.41	0.46	4217
28	M	L	L	M	-0.20	0.51	12539	-0.12	0.59	13626
29	H	L	L	M	-1.35	1.12	45934	0.32	1.01	46031
31	M	M	L	M	-0.09	0.46	1788	0.05	0.60	1889
32	H	M	L	M	-1.10	1.02	9041	0.41	1.02	9140
36	L	L	M	M	-0.19	0.36	4757	-0.33	0.52	5228
37	M	L	M	M	-0.19	0.49	15322	-0.12	0.55	16466
38	H	L	M	M	-1.19	1.11	30143	0.58	1.04	30119
39	L	M	M	M	-0.18	0.41	2047	-0.19	0.45	2220
40	M	M	M	M	-0.12	0.51	9214	0.04	0.61	10139
41	H	M	M	M	-0.91	0.90	18579	0.74	0.98	19131

box #	ws	wv	sst	clw	mean TbV	std TbV	# of points in box	mean TbH	std TbH	# of points in box
43	M	H	M	M	0.17	0.51	438	0.24	0.63	484
45	L	L	H	M	0.06	0.23	2039	0.07	0.49	2224
46	M	L	H	M	-0.28	0.35	3234	-0.17	0.41	3624
47	H	L	H	M	-0.96	0.56	5413	0.37	0.57	5334
48	L	M	H	M	0.02	0.32	1774	0.12	0.50	1911
49	M	M	H	M	-0.12	0.39	11546	0.22	0.52	12839
50	H	M	H	M	-0.80	0.66	17271	0.75	0.77	18137
51	L	H	H	M	-0.02	0.41	2127	0.42	0.59	2406
52	M	H	H	M	0.00	0.42	9502	0.53	0.58	10553
53	H	H	H	M	-0.49	0.69	9596	1.18	0.97	9831
55	M	L	L	H	-0.16	0.49	2420	-0.14	0.64	2671
56	H	L	L	H	-1.30	1.22	14827	0.58	1.28	14470
58	M	M	L	H	-0.29	0.61	1261	-0.09	0.74	1359
59	H	M	L	H	-1.31	1.05	9808	0.43	1.29	9666
63	L	L	M	H	-0.18	0.25	429	-0.13	0.54	459
64	M	L	M	H	-0.25	0.46	1975	-0.06	0.65	2181

box #	ws	wv	sst	clw	mean TbV	std TbV	# of points in box	mean TbH	std TbH	# of points in box
65	H	L	M	H	-1.32	1.22	7690	0.92	1.38	7221
66	L	M	M	H	-0.24	0.29	532	-0.11	0.44	558
67	M	M	M	H	-0.10	0.53	2649	0.08	0.74	2896
68	H	M	M	H	-1.04	1.12	12964	1.05	1.63	12870
74	H	L	H	H	-0.94	0.53	977	0.44	0.73	1042
76	M	M	H	H	-0.13	0.41	1913	0.28	0.63	2200
77	H	M	H	H	-0.71	0.75	4643	1.09	1.02	4765
79	M	H	H	H	-0.07	0.70	498	0.46	0.87	522
80	H	H	H	H	-0.32	1.00	1112	1.78	1.77	1048

Table 8: 10.7 GHz statistics

box #	ws	wv	sst	clw	mean TbV	std TbV	# of points in box	mean TbH	std TbH	# of points in box
0	L	L	L	L	-0.04	0.32	16716	-0.35	0.46	16612
1	M	L	L	L	0.02	0.41	63087	0.11	0.62	63978
2	H	L	L	L	-1.47	1.22	233242	-0.15	1.27	232475
4	M	M	L	L	0.08	0.42	1850	0.25	0.68	1864
5	H	M	L	L	-0.83	0.94	5307	0.44	1.13	5144
9	L	L	M	L	-0.09	0.36	26269	-0.29	0.46	25881
10	M	L	M	L	0.02	0.45	85186	0.09	0.58	85712
11	H	L	M	L	-1.28	1.20	150071	0.12	1.16	147909
12	L	M	M	L	-0.04	0.39	7404	-0.07	0.49	7238
13	M	M	M	L	0.07	0.48	33913	0.32	0.63	33714
14	H	M	M	L	-0.67	0.87	38437	0.77	1.01	37866
18	L	L	H	L	-0.03	0.37	11404	-0.25	0.47	11292
19	M	L	H	L	0.01	0.40	25179	0.03	0.51	25111
20	H	L	H	L	-0.84	0.74	27636	0.25	0.80	28238
21	L	M	H	L	0.15	0.38	43790	0.16	0.50	43753

box #	ws	wv	sst	clw	mean TbV	std TbV	# of points in box	mean TbH	std TbH	# of points in box
22	M	M	H	L	0.26	0.41	134381	0.42	0.54	134047
23	H	M	H	L	-0.41	0.59	100530	0.67	0.74	100784
24	L	H	H	L	0.50	0.44	49126	0.86	0.57	48810
25	M	H	H	L	0.66	0.38	121163	0.95	0.55	121434
26	H	H	H	L	0.03	0.62	46219	1.05	0.87	44988
27	L	L	L	M	-0.23	0.38	4800	-0.77	0.67	4876
28	M	L	L	M	-0.28	0.57	16397	-0.42	0.82	16384
29	H	L	L	M	-1.60	1.28	60834	-0.48	1.53	59393
31	M	M	L	M	-0.07	0.58	1885	-0.05	0.89	1870
32	H	M	L	M	-1.06	1.27	11758	0.16	1.58	11267
36	L	L	M	M	-0.35	0.39	7094	-0.69	0.54	6790
37	M	L	M	M	-0.27	0.50	21132	-0.32	0.71	21022
38	H	L	M	M	-1.25	1.17	38610	0.05	1.39	37639
39	L	M	M	M	-0.11	0.48	3079	-0.24	0.66	2928
40	M	M	M	M	-0.05	0.55	11957	0.12	0.79	11694
41	H	M	M	M	-0.85	1.11	24348	0.54	1.45	23763

box #	ws	wv	sst	clw	mean TbV	std TbV	# of points in box	mean TbH	std TbH	# of points in box
43	M	H	M	M	0.22	0.76	536	0.23	1.00	531
45	L	L	H	M	-0.11	0.28	2287	-0.50	0.42	2232
46	M	L	H	M	-0.37	0.39	4307	-0.37	0.48	4196
47	H	L	H	M	-0.99	0.67	7265	-0.06	0.79	6996
48	L	M	H	M	-0.03	0.48	2099	-0.09	0.72	2086
49	M	M	H	M	0.09	0.53	14797	0.30	0.78	14716
50	H	M	H	M	-0.63	0.83	23286	0.53	1.10	22853
51	L	H	H	M	0.44	0.56	2992	0.82	0.85	2995
52	M	H	H	M	0.48	0.65	13145	0.92	0.98	13050
53	H	H	H	M	-0.05	0.95	13417	1.27	1.50	12966
55	M	L	L	H	-0.38	0.68	3227	-0.64	1.03	3228
56	H	L	L	H	-1.83	1.55	19596	-0.62	1.99	18773
58	M	M	L	H	-0.67	0.95	1424	-0.77	1.33	1381
59	H	M	L	H	-1.55	1.53	12833	-0.44	2.33	12487
63	L	L	M	H	-0.46	0.37	527	-0.83	0.61	527
64	M	L	M	H	-0.46	0.52	2651	-0.60	0.74	2639

box #	ws	wv	sst	clw	mean TbV	std TbV	# of points in box	mean TbH	std TbH	# of points in box
65	H	L	M	H	-1.62	1.46	9180	-0.07	1.89	8619
67	M	M	M	H	-0.23	0.78	3315	-0.18	1.11	3234
68	H	M	M	H	-1.27	1.63	16343	0.28	2.51	15875
74	H	L	H	H	-1.52	0.77	1490	-0.39	0.70	1433
76	M	M	H	H	-0.05	0.62	2373	0.15	0.98	2368
77	H	M	H	H	-0.80	1.07	6255	0.52	1.49	6039
79	M	H	H	H	0.15	1.09	644	0.47	1.81	651
80	H	H	H	H	-0.28	1.83	1419	1.32	3.21	1399

Table 9: 18.7 GHz statistics

box #	wv	sst	clw	mean TbV	std TbV	# of points in box	mean TbH	std TbH	# of points in box
0	L	L	L	0.10	0.74	16737	0.11	1.25	16676
1	L	L	L	-0.09	0.78	63207	0.01	1.38	62752
2	L	L	L	-1.92	1.54	230720	-1.16	2.21	228802
4	M	L	L	0.44	1.13	1881	0.53	2.12	1874
5	M	L	L	-1.02	1.73	5154	-0.87	3.18	5119
9	L	M	L	0.06	0.69	26412	0.21	1.26	26274
10	L	M	L	-0.01	0.79	85193	-0.06	1.35	84513
11	L	M	L	-1.82	1.67	150819	-1.06	2.20	147697
12	M	M	L	0.49	1.00	7575	0.93	1.66	7309
13	M	M	L	0.39	1.12	34126	0.46	1.89	33268
14	M	M	L	-0.52	1.44	38096	0.31	2.33	37334
18	L	H	L	0.08	0.68	11650	0.32	1.25	11702
19	L	H	L	-0.09	0.75	26091	-0.30	1.16	25500
20	L	H	L	-1.12	1.04	27513	-0.85	1.47	27716
21	M	H	L	0.77	0.92	43941	1.68	1.62	43457

box #	wv	sst	clw	mean TbV	std TbV	# of points in box	mean TbH	std TbH	# of points in box
22	M	H	L	0.69	0.97	134538	0.81	1.55	132857
23	M	H	L	-0.29	1.13	101341	-0.04	1.72	99949
24	H	H	L	1.85	1.01	49454	3.55	1.84	49105
25	H	H	L	1.69	0.98	123392	2.12	1.60	122046
26	H	H	L	0.73	1.19	46135	0.99	1.89	45414
27	L	L	M	-0.42	0.89	4830	-1.35	1.69	4810
28	L	L	M	-0.57	1.12	16241	-1.49	2.05	16076
29	L	L	M	-2.21	1.87	59323	-2.42	3.08	57915
31	M	L	M	-0.39	1.49	1868	-1.45	2.97	1879
32	M	L	M	-1.64	2.06	10567	-2.31	3.82	10424
36	L	M	M	-0.50	0.78	6926	-0.94	1.57	6742
37	L	M	M	-0.56	0.97	20863	-1.29	1.71	20561
38	L	M	M	-1.92	1.82	38968	-1.61	2.74	37442
39	M	M	M	0.30	1.19	3072	0.49	1.99	2908
40	M	M	M	-0.02	1.33	11624	-0.44	2.36	11294

box #	wv	sst	clw	mean TbV	std TbV	# of points in box	mean TbH	std TbH	# of points in box
41	M	M	M	-1.13	2.00	23753	-0.98	3.58	23289
43	H	M	M	-1.34	2.08	515	-3.56	3.90	509
44	H	M	M	-1.85	1.82	705	-3.60	3.80	709
45	L	H	M	-0.51	0.63	2298	-0.71	1.17	2264
46	L	H	M	-0.68	0.67	4246	-1.33	1.09	4189
47	L	H	M	-1.49	1.07	7171	-1.79	1.57	6992
48	M	H	M	0.06	1.18	2116	0.29	2.03	2065
49	M	H	M	0.28	1.16	14491	0.13	1.99	14304
50	M	H	M	-0.91	1.45	22922	-1.03	2.42	22577
51	H	H	M	1.48	1.43	3090	2.85	2.79	3092
52	H	H	M	1.01	1.50	13431	1.09	2.76	13370
53	H	H	M	-0.07	1.79	13568	0.02	3.17	13357
55	L	L	H	-1.06	1.42	3193	-2.42	2.73	3139
56	L	L	H	-2.89	2.50	19258	-3.60	4.36	18498
58	M	L	H	-1.52	2.19	1361	-3.59	4.27	1361
59	M	L	H	-2.92	3.18	12447	-4.50	6.00	12153

box #	wv	sst	clw	mean TbV	std TbV	# of points in box	mean TbH	std TbH	# of points in box
63	L	M	H	-0.79	0.87	546	-1.51	1.79	534
64	L	M	H	-1.03	0.92	2547	-2.17	1.70	2529
65	L	M	H	-2.76	2.45	9384	-2.68	3.81	8704
67	M	M	H	-0.62	2.05	3295	-1.66	3.78	3247
68	M	M	H	-2.36	3.30	16396	-2.67	6.21	16027
74	L	H	H	-2.39	1.05	1475	-2.61	1.42	1460
76	M	H	H	-0.07	1.51	2337	-0.57	2.74	2320
77	M	H	H	-1.45	1.99	6118	-1.90	3.33	5922
79	H	H	H	0.30	2.56	679	-0.19	4.87	673
80	H	H	H	-1.26	3.21	1465	-1.27	6.17	1454

Table 10: 37 GHz statistics

box #	wv	sst	clw	mean TbV	std TbV	# of points in box	mean TbH	std TbH	# of points in box
0	L	L	L	-0.14	0.77	16401	0.17	1.69	16283
1	L	L	L	0.04	0.90	61765	-0.03	2.01	61630
2	L	L	L	-0.76	1.56	227921	-1.22	3.05	224001
4	M	L	L	-0.11	1.48	1870	-0.44	2.78	1846
5	M	L	L	-0.96	1.97	4991	-1.95	3.64	4877
9	L	M	L	-0.16	0.82	26621	0.24	1.59	25861
10	L	M	L	0.07	0.95	83296	-0.01	1.87	82700
11	L	M	L	-0.65	1.69	147051	-0.92	2.97	142878
12	M	M	L	-0.14	1.18	7524	0.38	2.21	7311
13	M	M	L	0.02	1.35	33386	-0.09	2.57	33129
14	M	M	L	-0.22	1.80	37458	-0.32	3.12	36455
18	L	H	L	-0.17	0.82	11480	0.21	1.61	11399
19	L	H	L	0.02	0.94	25759	-0.28	1.69	25397
20	L	H	L	-0.09	1.29	27781	-0.54	2.13	27447
21	M	H	L	0.26	1.15	43582	1.11	2.15	43430

box #	wv	sst	clw	mean TbV	std TbV	# of points in box	mean TbH	std TbH	# of points in box
22	M	H	L	0.44	1.28	134411	0.39	2.26	133548
23	M	H	L	0.22	1.48	100857	-0.31	2.51	99684
24	H	H	L	1.61	1.36	49661	3.50	2.51	49355
25	H	H	L	1.49	1.38	123904	2.01	2.42	122716
26	H	H	L	1.06	1.67	46497	0.81	2.82	45622
27	L	L	M	-0.95	1.26	4681	-2.17	2.88	4736
28	L	L	M	-0.97	1.76	15960	-2.71	3.77	15970
29	L	L	M	-1.35	2.64	58679	-3.44	5.25	57464
31	M	L	M	-0.95	2.35	1866	-2.43	4.73	1862
32	M	L	M	-1.48	2.90	10394	-3.54	5.37	10027
36	L	M	M	-1.01	1.28	6736	-2.03	2.81	6778
37	L	M	M	-0.70	1.63	20754	-2.15	3.29	20596
38	L	M	M	-0.88	2.71	38846	-2.17	5.11	37730
39	M	M	M	-0.34	1.88	3079	-0.55	3.62	2982
40	M	M	M	-0.47	2.08	11492	-1.39	3.96	11270

box #	wv	sst	clw	mean TbV	std TbV	# of points in box	mean TbH	std TbH	# of points in box
41	M	M	M	-0.79	3.18	23978	-1.91	5.92	23237
43	H	M	M	-1.57	2.98	527	-3.06	3.34	421
45	L	H	M	-1.55	1.28	2250	-2.73	2.37	2205
46	L	H	M	-0.98	1.16	4224	-2.68	2.19	4168
47	L	H	M	-0.84	1.85	7255	-2.49	3.29	7056
48	M	H	M	-0.62	1.93	2089	-0.89	3.87	2094
49	M	H	M	0.08	2.01	14442	-0.61	3.74	14272
50	M	H	M	-0.31	2.41	22966	-1.55	4.44	22648
51	H	H	M	1.58	2.22	3116	3.23	4.37	3102
52	H	H	M	1.06	2.38	13649	1.24	4.52	13492
53	H	H	M	0.54	2.79	13798	0.13	5.38	13650
55	L	L	H	-1.64	2.70	3230	-4.21	5.50	3171
56	L	L	H	-2.11	3.76	18969	-5.38	7.50	18435
58	M	L	H	-3.07	4.16	1412	-6.86	8.03	1379
59	M	L	H	-3.38	5.33	12794	-7.55	10.03	12250
63	L	M	H	-1.81	1.74	522	-3.81	3.56	520

box #	wv	sst	clw	mean TbV	std TbV	# of points in box	mean TbH	std TbH	# of points in box
64	L	M	H	-1.58	1.64	2494	-4.26	3.18	2448
65	L	M	H	-1.93	3.69	9101	-4.49	6.71	8632
66	M	M	H	-1.52	2.51	689	-3.03	4.64	673
67	M	M	H	-1.64	3.53	3262	-3.80	6.48	3142
68	M	M	H	-2.51	5.63	16889	-5.24	10.27	16010
74	L	H	H	-1.74	1.91	1479	-3.83	3.43	1466
76	M	H	H	-0.60	2.80	2335	-2.18	5.20	2297
77	M	H	H	-1.02	3.61	6198	-3.05	6.64	6057
79	H	H	H	0.95	4.17	701	0.59	8.14	690
80	H	H	H	0.82	4.89	1521	1.15	9.62	1486

4.5 Monte Carlo Simulation

A Monte Carlo simulation was performed to understand the observed standard deviation of RadTb brightness temperatures for given environmental boxes. This simulation was to test the hypothesis that random error is introduced into the RadTb model output Tb by the input environmental parameters. For this analysis, box LLML was selected for the 10.7 GHz channel; and the standard deviation of the observed histogram of the Tb was determined. Then, the simulation began with the average environmental parameters (14) for box LLML being input to RadTb, and the dual polarized Tb was calculated at the 10.7 GHz. This TbH and TbV calculation became the baseline "zero-error case".

Next, Gaussian random errors were introduced for one parameter at a time while all other (13) input parameters were held at the baseline values; and the Tb's were calculated. For each parameter, the standard deviation of the zero-mean Gaussian noise matched the expected error in the environmental data set (described in Chapter 2). Histograms of these simulated Tb's were produced and found to be Gaussian distributed about the baseline Tb's. After all parameters errors were simulated, it was determined that there were four major environmental parameters (wind speed, water vapor, SST and cloud liquid water) that contributed the major variances.

Results, tabulated in Table 11, demonstrate that the expected random error due to

the four principal input geophysical parameters contributes approximately 89% of the observed Tb standard deviation. These results validate the hypothesis and demonstrate that these four input environmental parameters are the main contributors to the observed standard deviation of the WindSat 10.7 GHz Tb's.

Table 11: Monte Carlo Simulation for LLML box at 10.7 GHz

	Horizontal Brightness Temperature Standard Deviation	Vertical Brightness Temperature Standard Deviation
WindSat Measured 10.7 GHz LLML Baseline	0.9 K	0.6 K
Simulated WS std	0.6 K	0.1 K
Simulated WV std	0.2 K	0.1 K
Simulated SST std	0.2 K	0.4 K
Simulated CLW std	0.3 K	0.1 K
RMS of 4 environmental parameters	0.8 K	0.5 K

CHAPTER FIVE: CONCLUSION

The intent of this thesis was to evaluate the systematic biases produced by the RTM, RadTb, over a wide range of environmental conditions. RadTb was assessed for off-nadir global viewing at four frequencies for dual polarized brightness temperature. The validation of the RTM evaluation as discussed in chapter three was carried out using 14 environmental parameters to generate calculated brightness temperature. This was followed by statistical comparison of calculated and measured brightness temperature at collocated area of SSM/I DMSP F13 and Windsat.

The comparison data set was divided into ranges of four significant environmental parameters to properly analyze the contribution of brightness temperature error due to wind speed, water vapor, sea surface temperature and cloud liquid water. Under a low cloud, rain free condition, RadTb was evaluated at the ocean surface. It was seen that the systematic Tb error was produced in part by the emissivity, which was not correctly accounting for the brightness temperature at different ranges of sea surface temperature. As a result, an adjustment was made to the emissivity factor in the RadTb model for the observed frequencies with respect to vertical and horizontal polarizations.

The emissivity corrections held at all frequencies shows improve calculated Tb's, especially noticeable at the 6.8 and 10.7 GHZ. The 18.7 and 37.0 GHz calculated

brightness temperatures were also improved, but high water vapor contributed to error in the calculated Tb at sea surface temperature above 20^{o}C. This observance signifies that the RadTb model needs to be improved to handle the water vapor parameter better for calculated brightness temperatures. The RTM evaluation also shows that high wind speed skews the calculated Tb results. Further evaluation of the RTM validates the four analyzed significant environmental parameters are the main cause for Tb error. The Monte Carlo Simulation verified that error introduced to the 'true geophysical parameters' influences systematic Tb error produced by RadTb.

The correction for the emissivity factor in RadTb improves the modeled ocean brightness temperatures. However, additional steps need to be taken to correct the calculated brightness temperature error due to wind speed, water vapor and cloud liquid water.

APPENDIX A: SST BINS

6.8 GHZ Ascending

At the 6.8 GHz, the following horizontal and vertical ascending deltaTb bins with respect to SST were used to generate the polyfit coefficients values for the emissivity correction factor. The deltaTb bins for the before and after correction of the emissivity had similar deltaTb distribution per bins. The following bins shown for 6.8 GHz – 37.0 GHz are the result after the emissivity correction in the RadTb program.

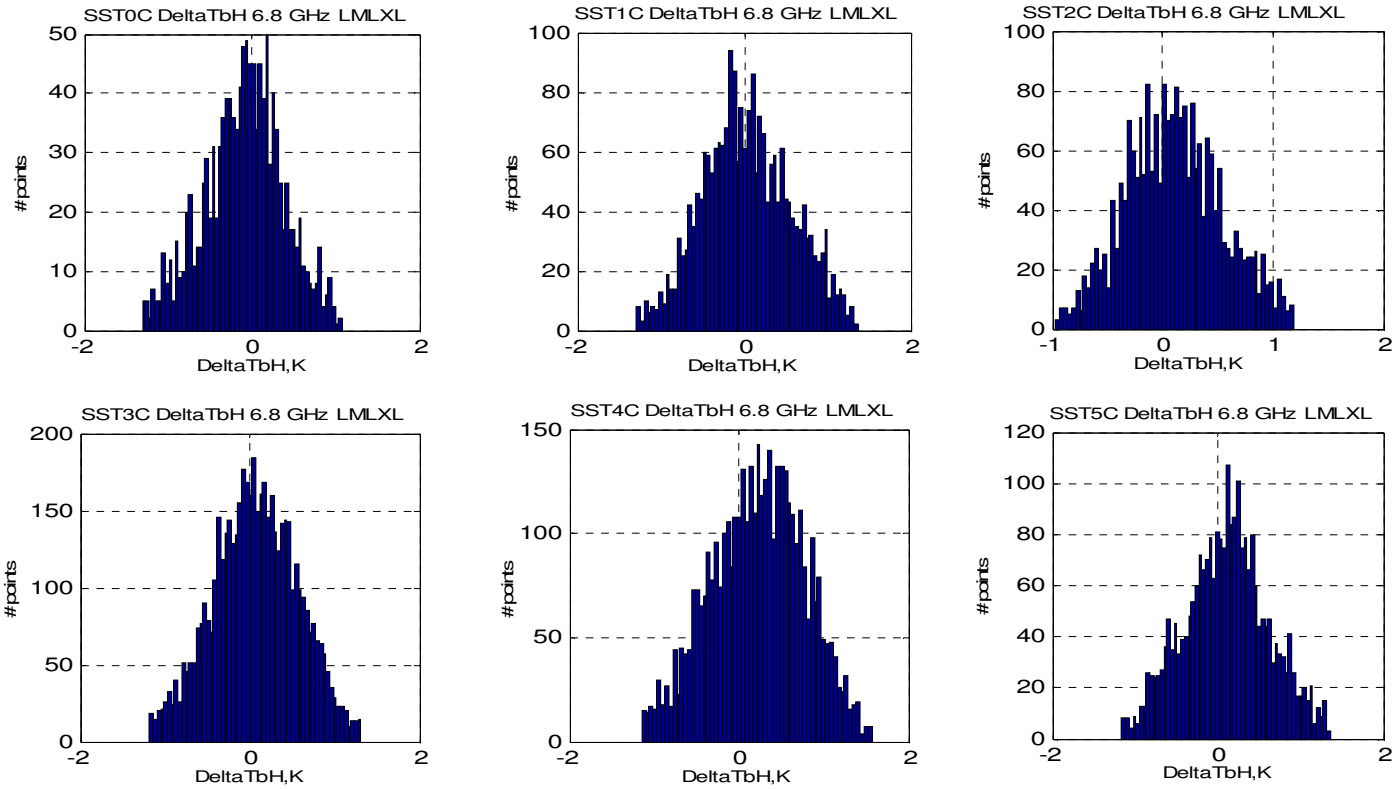
SST0C DeltaTbH 6.8 GHz LMLXL
#points
DeltaTbH,K
SST1C DeltaTbH 6.8 GHz LMLXL
#points
DeltaTbH,K
SST2C DeltaTbH 6.8 GHz LMLXL
#points
DeltaTbH,K
SST3C DeltaTbH 6.8 GHz LMLXL
#points
DeltaTbH,K
SST4C DeltaTbH 6.8 GHz LMLXL
#points
DeltaTbH,K
SST5C DeltaTbH 6.8 GHz LMLXL
#points
DeltaTbH,K

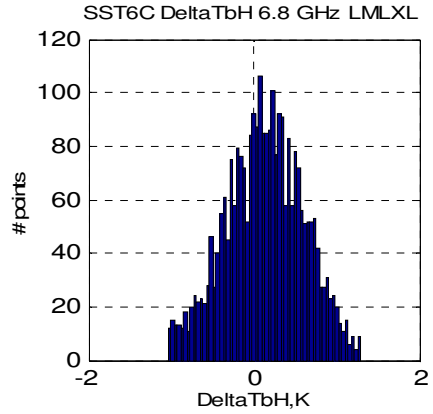
SST6C DeltaTbH 6.8 GHz LMLXL
#points
DeltaTbH,K

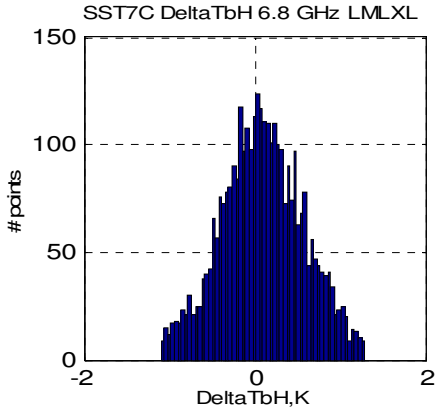
SST7C DeltaTbH 6.8 GHz LMLXL
#points
DeltaTbH,K

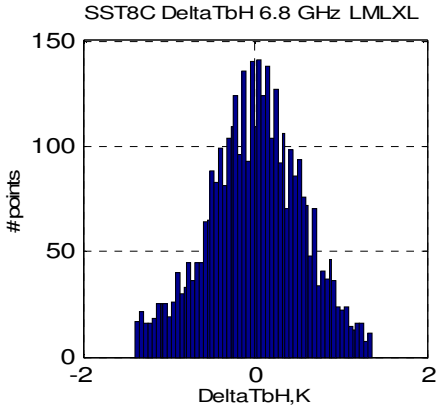
SST8C DeltaTbH 6.8 GHz LMLXL
#points
DeltaTbH,K

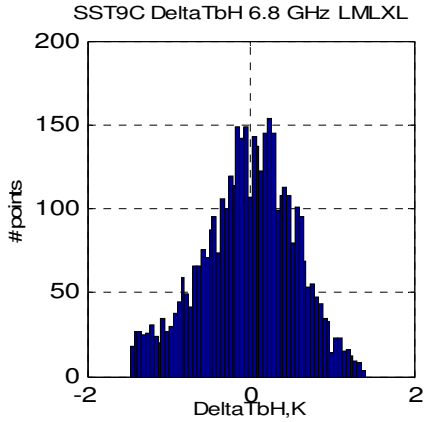
SST9C DeltaTbH 6.8 GHz LMLXL
#points
DeltaTbH,K

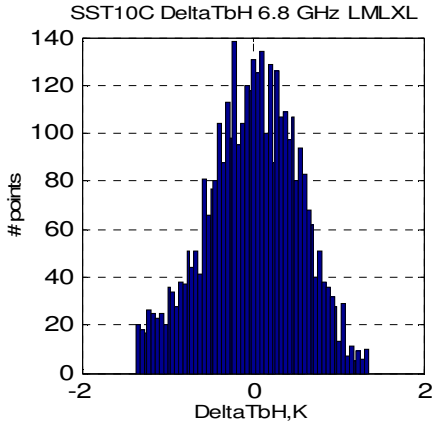
SST10C DeltaTbH 6.8 GHz LMLXL
#points
DeltaTbH,K

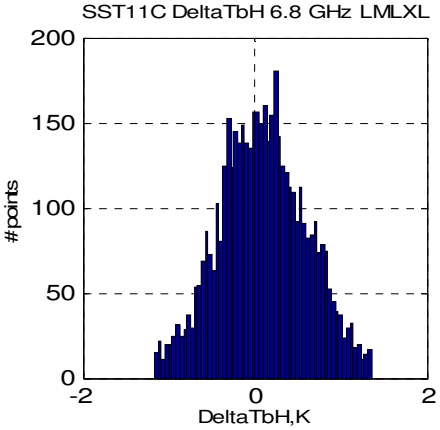
SST11C DeltaTbH 6.8 GHz LMLXL
#points
DeltaTbH,K

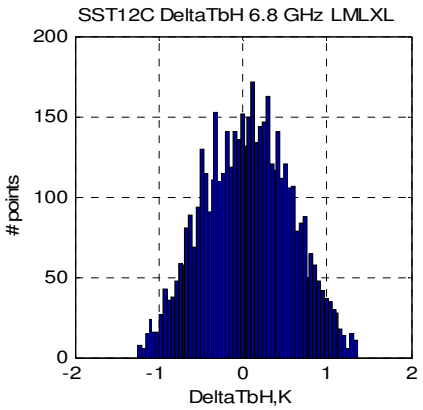
SST12C DeltaTbH 6.8 GHz LMLXL
points
DeltaTbH,K

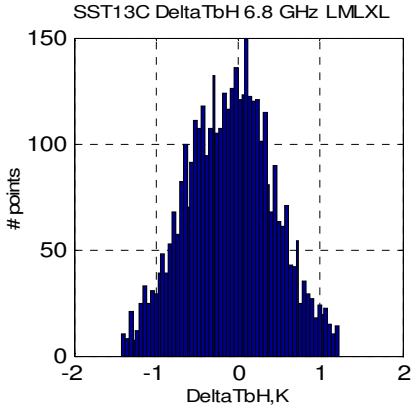
SST13C DeltaTbH 6.8 GHz LMLXL
points
DeltaTbH,K

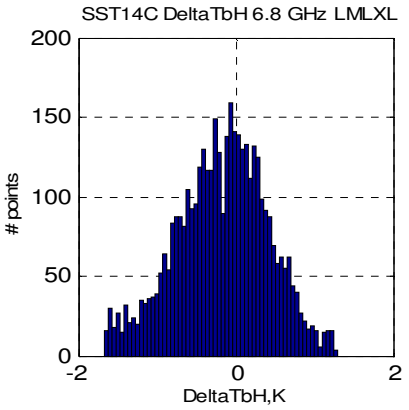
SST14C DeltaTbH 6.8 GHz LMLXL
points
DeltaTbH,K

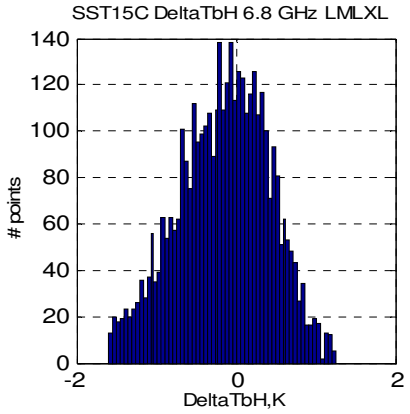
SST15C DeltaTbH 6.8 GHz LMLXL
points
DeltaTbH,K

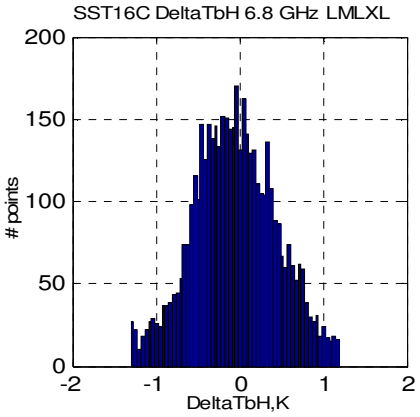
SST16C DeltaTbH 6.8 GHz LMLXL
points
DeltaTbH,K

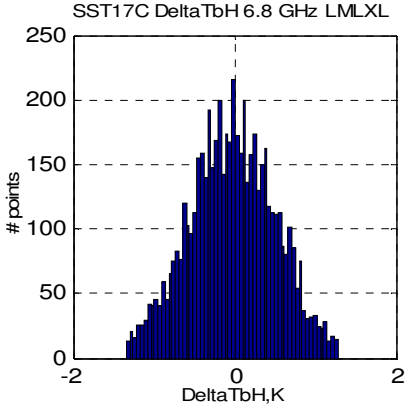
SST17C DeltaTbH 6.8 GHz LMLXL
points
DeltaTbH,K

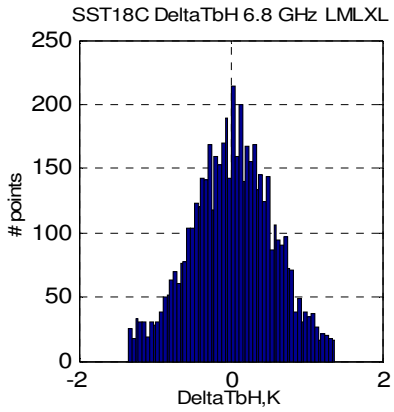
SST18C DeltaTbH 6.8 GHz LMLXL
points
DeltaTbH,K

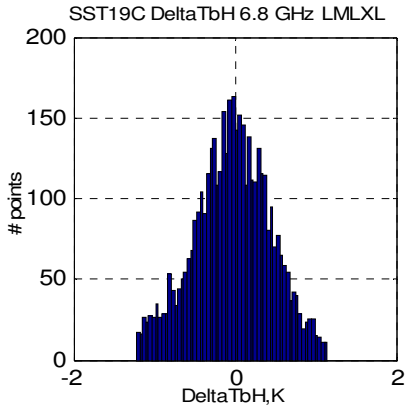
SST19C DeltaTbH 6.8 GHz LMLXL
points
DeltaTbH,K

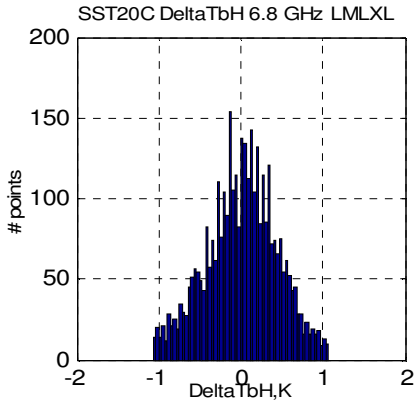
SST20C DeltaTbH 6.8 GHz LMLXL
points
DeltaTbH,K

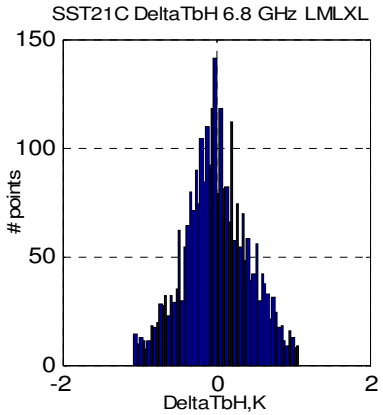
SST21C DeltaTbH 6.8 GHz LMLXL
points
DeltaTbH,K

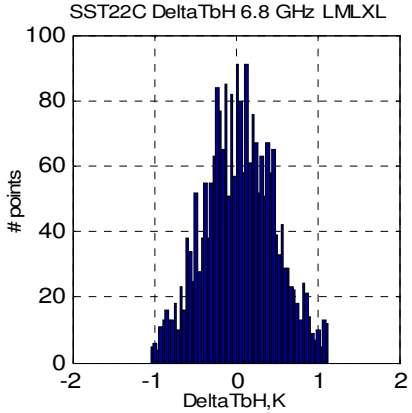
SST22C DeltaTbH 6.8 GHz LMLXL
points
DeltaTbH,K

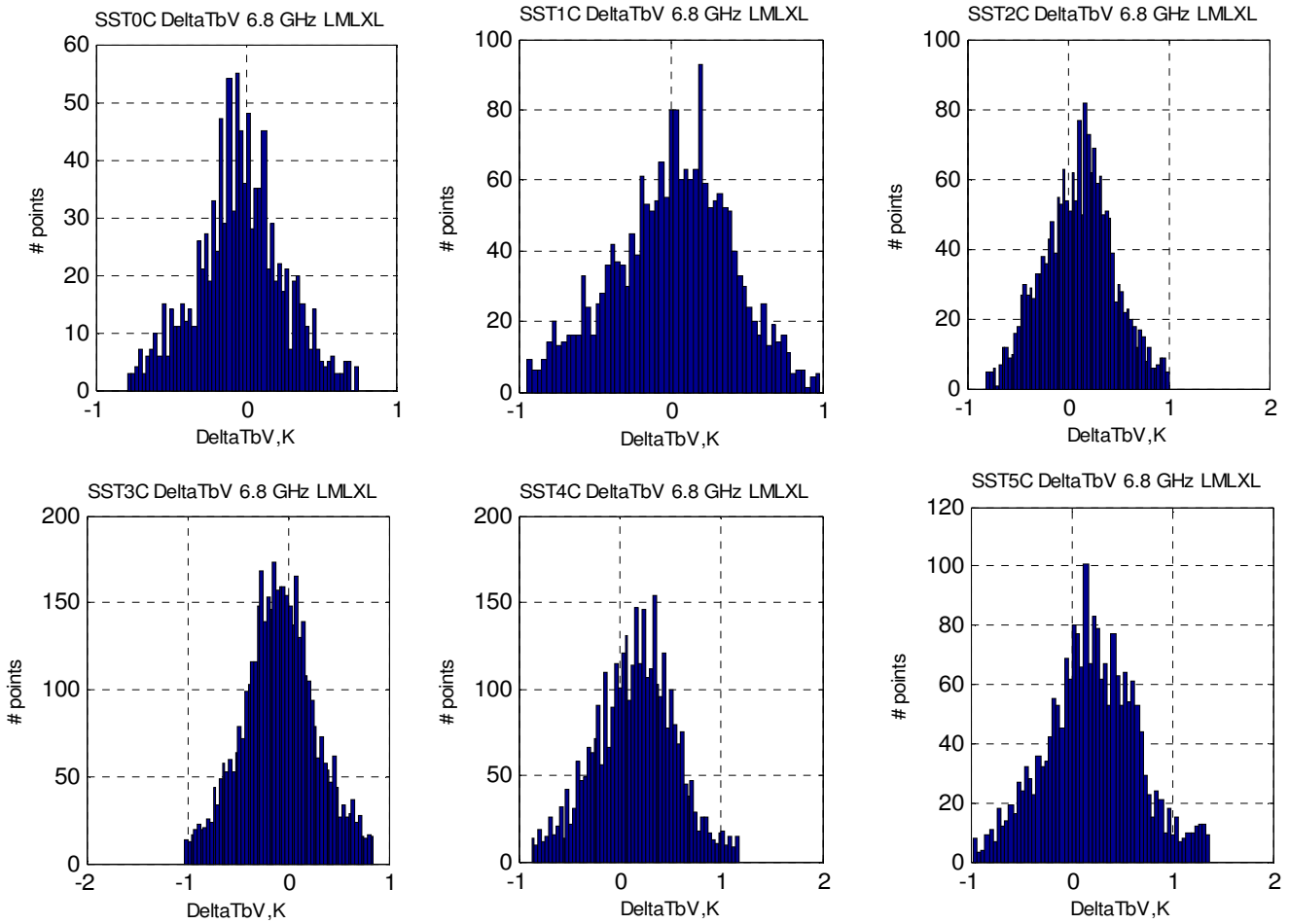
SST0C DeltaTbV 6.8 GHz LMLXL
points
DeltaTbV,K
SST1C DeltaTbV 6.8 GHz LMLXL
points
DeltaTbV,K
SST2C DeltaTbV 6.8 GHz LMLXL
points
DeltaTbV,K
SST3C DeltaTbV 6.8 GHz LMLXL
points
DeltaTbV,K
SST4C DeltaTbV 6.8 GHz LMLXL
points
DeltaTbV,K
SST5C DeltaTbV 6.8 GHz LMLXL
points
DeltaTbV,K

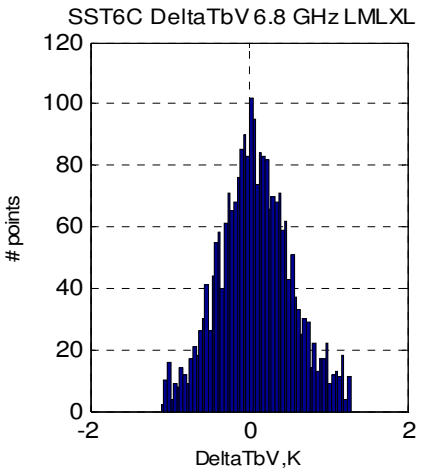
SST6C DeltaTbV 6.8 GHz LMLXL
points
DeltaTbV,K

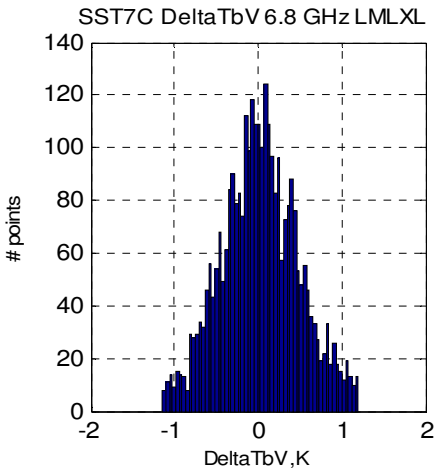
SST7C DeltaTbV 6.8 GHz LMLXL
points
DeltaTbV,K

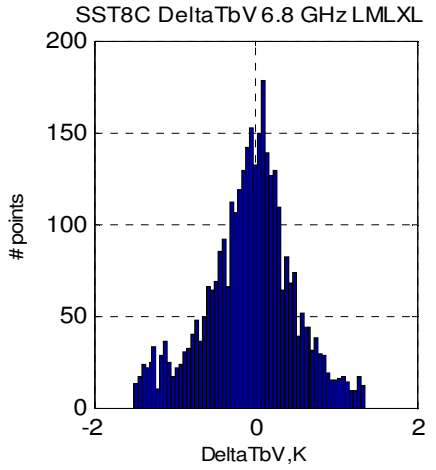
SST8C DeltaTbV 6.8 GHz LMLXL
points
DeltaTbV,K

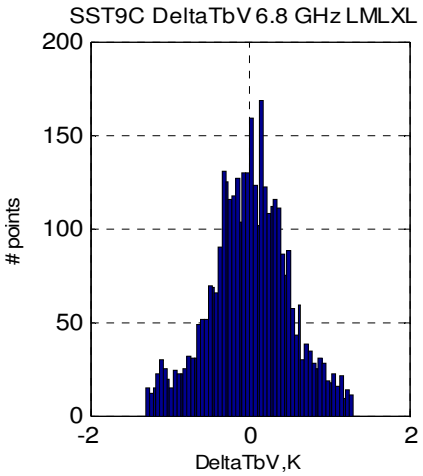
SST9C DeltaTbV 6.8 GHz LMLXL
points
DeltaTbV,K

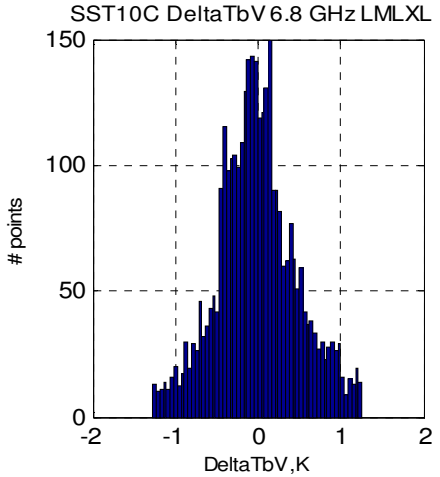
SST10C DeltaTbV 6.8 GHz LMLXL
points
DeltaTbV,K

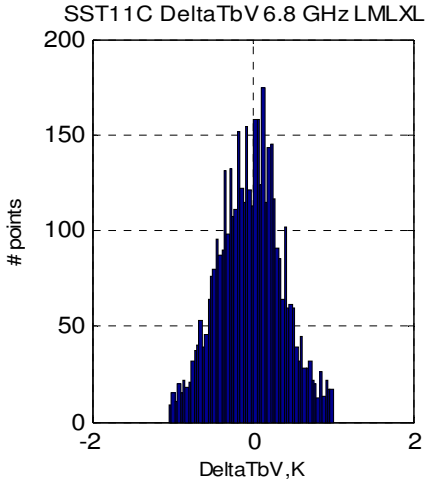
SST11C DeltaTbV 6.8 GHz LMLXL
points
DeltaTbV,K

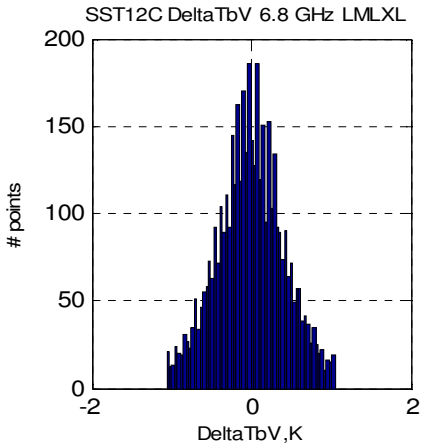
SST12C DeltaTbV 6.8 GHz LMLXL
points
DeltaTbV,K

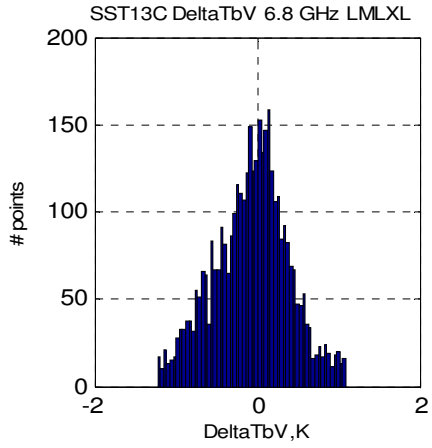
SST13C DeltaTbV 6.8 GHz LMLXL
points
DeltaTbV,K

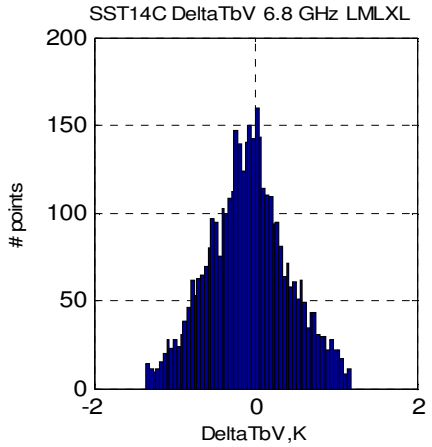
SST14C DeltaTbV 6.8 GHz LMLXL
points
DeltaTbV,K

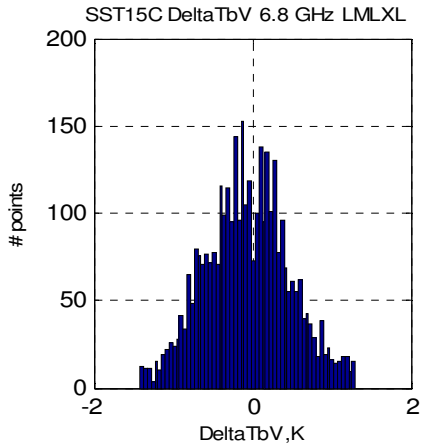
SST15C DeltaTbV 6.8 GHz LMLXL
points
DeltaTbV,K

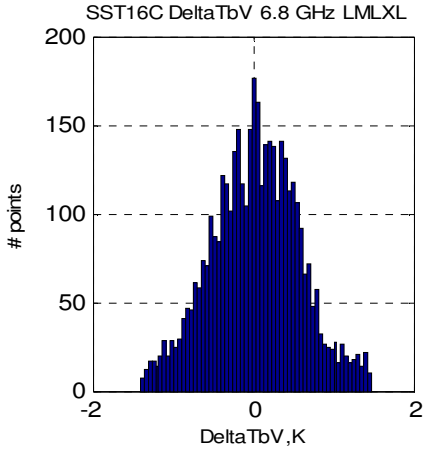
SST16C DeltaTbV 6.8 GHz LMLXL
points
DeltaTbV,K

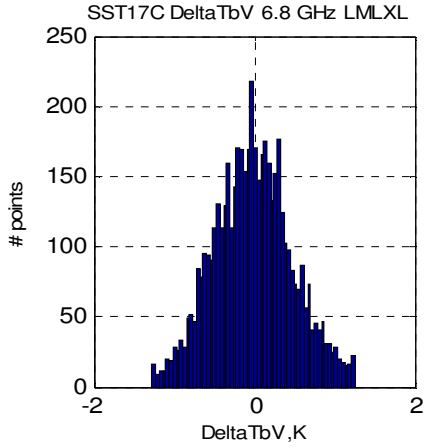
SST17C DeltaTbV 6.8 GHz LMLXL
points
DeltaTbV,K

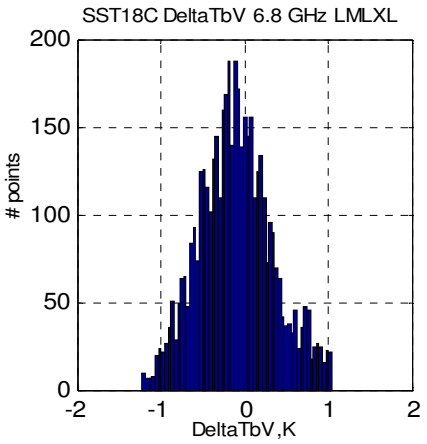
SST18C DeltaTbV 6.8 GHz LMLXL
points
DeltaTbV,K

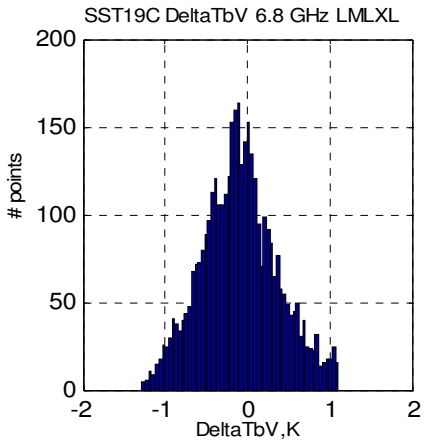
SST19C DeltaTbV 6.8 GHz LMLXL
points
DeltaTbV,K

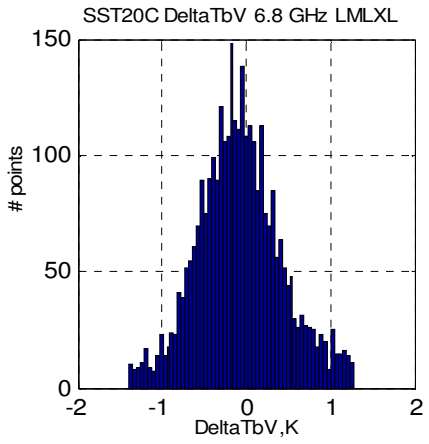
SST20C DeltaTbV 6.8 GHz LMLXL
points
DeltaTbV,K

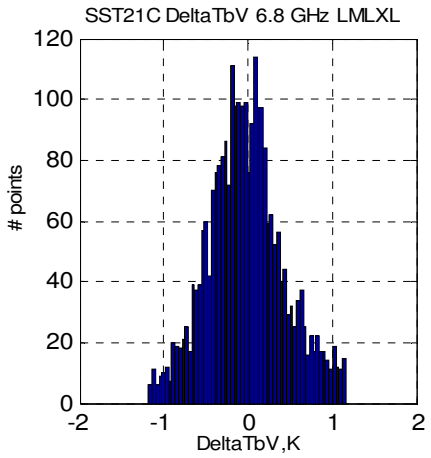
SST21C DeltaTbV 6.8 GHz LMLXL
points
DeltaTbV,K

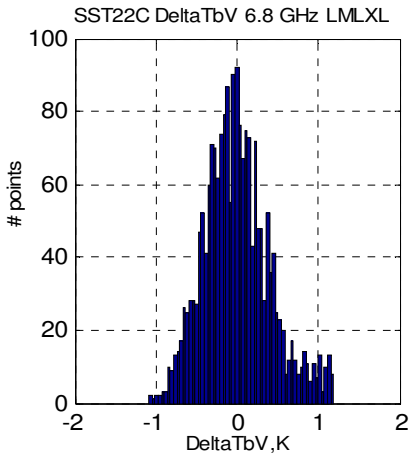
SST22C DeltaTbV 6.8 GHz LMLXL
points
DeltaTbV,K

6.8 GHZ Descending

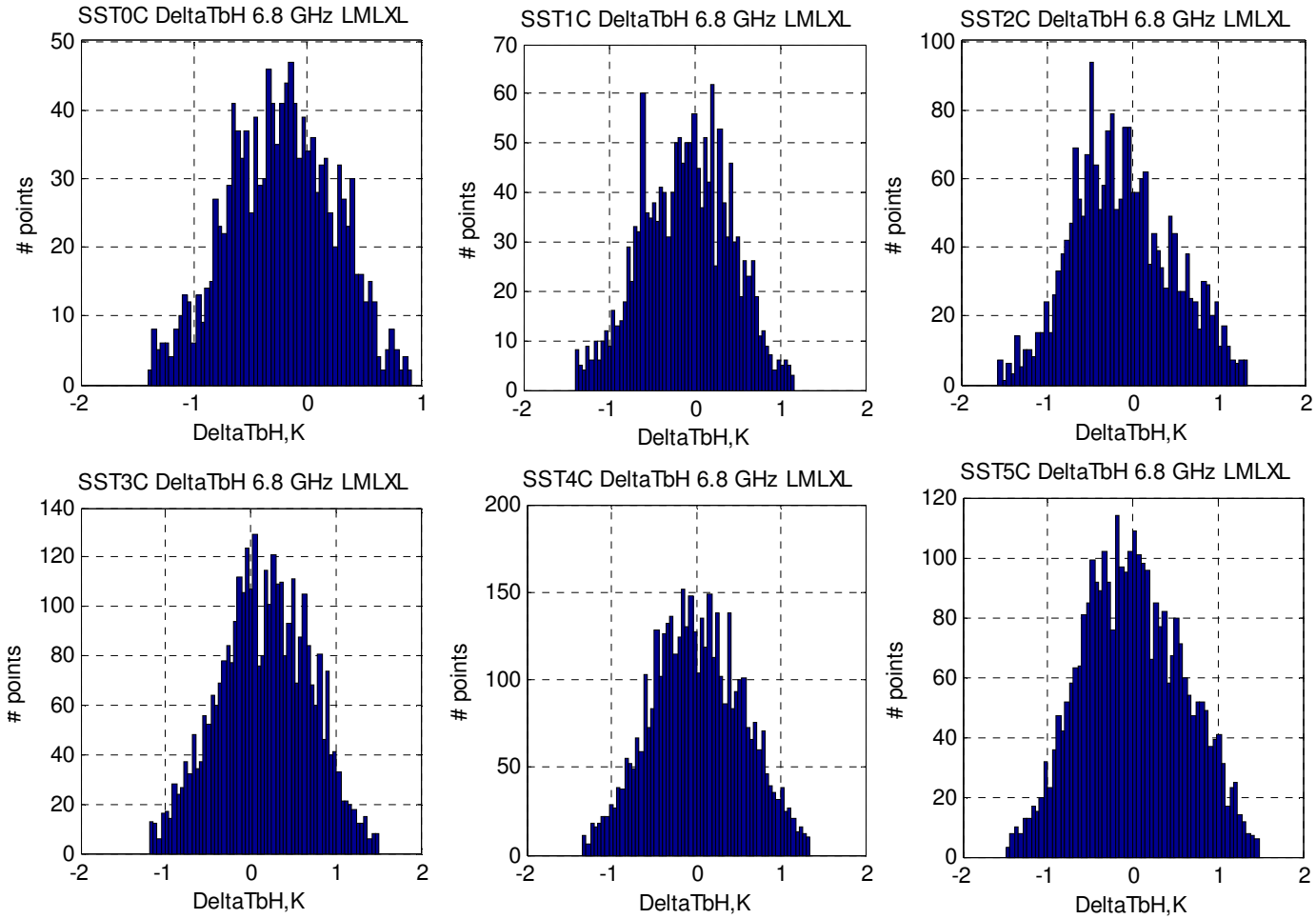
SST0C DeltaTbH 6.8 GHz LMLXL
points
DeltaTbH,K
SST1C DeltaTbH 6.8 GHz LMLXL
points
DeltaTbH,K
SST2C DeltaTbH 6.8 GHz LMLXL
points
DeltaTbH,K
SST3C DeltaTbH 6.8 GHz LMLXL
points
DeltaTbH,K
SST4C DeltaTbH 6.8 GHz LMLXL
points
DeltaTbH,K
SST5C DeltaTbH 6.8 GHz LMLXL
points
DeltaTbH,K

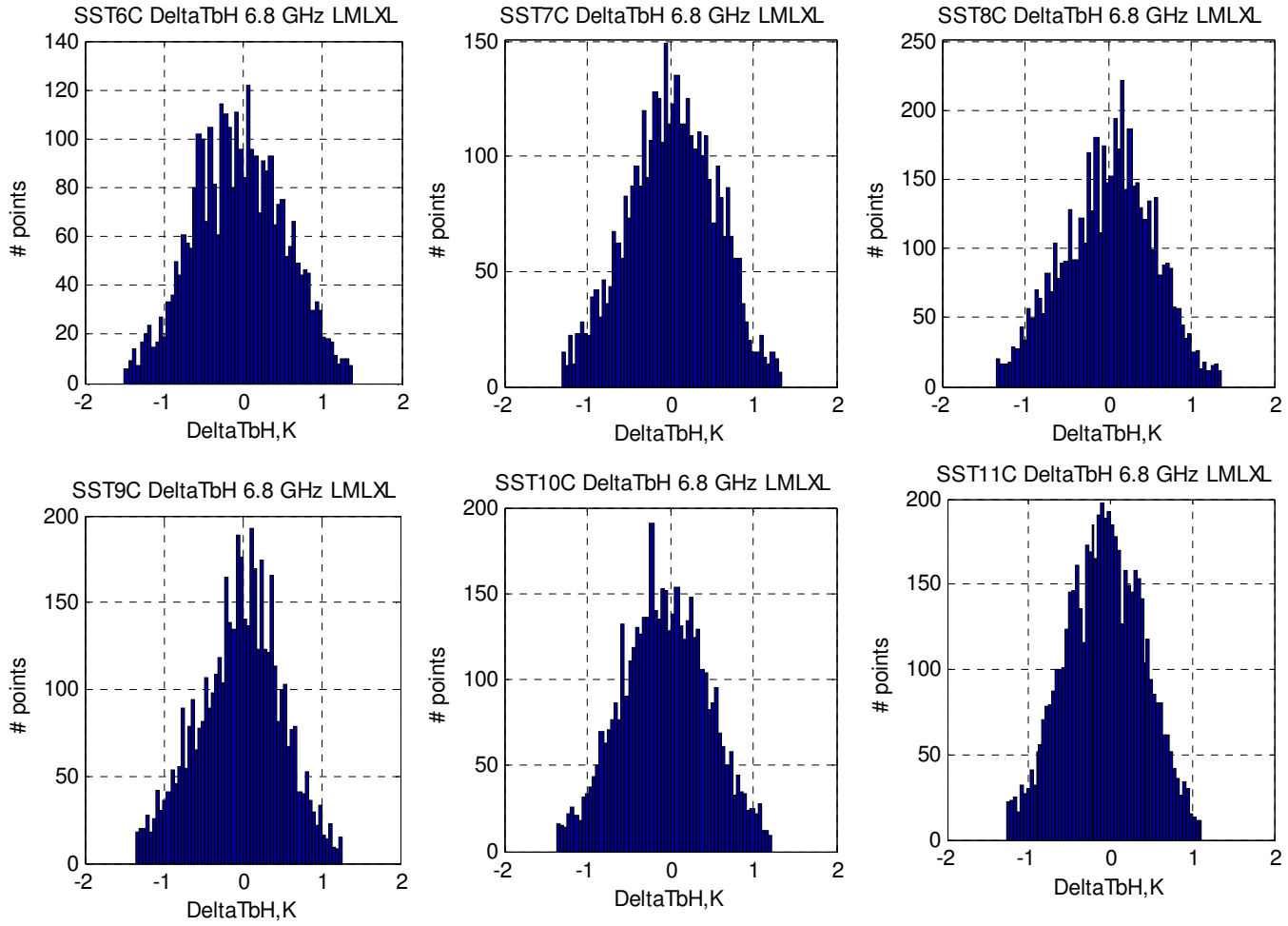
SST6C DeltaTbH 6.8 GHz LMLXL
SST7C DeltaTbH 6.8 GHz LMLXL
SST8C DeltaTbH 6.8 GHz LMLXL
SST9C DeltaTbH 6.8 GHz LMLXL
SST10C DeltaTbH 6.8 GHz LMLXL
SST11C DeltaTbH 6.8 GHz LMLXL
points
DeltaTbH,K

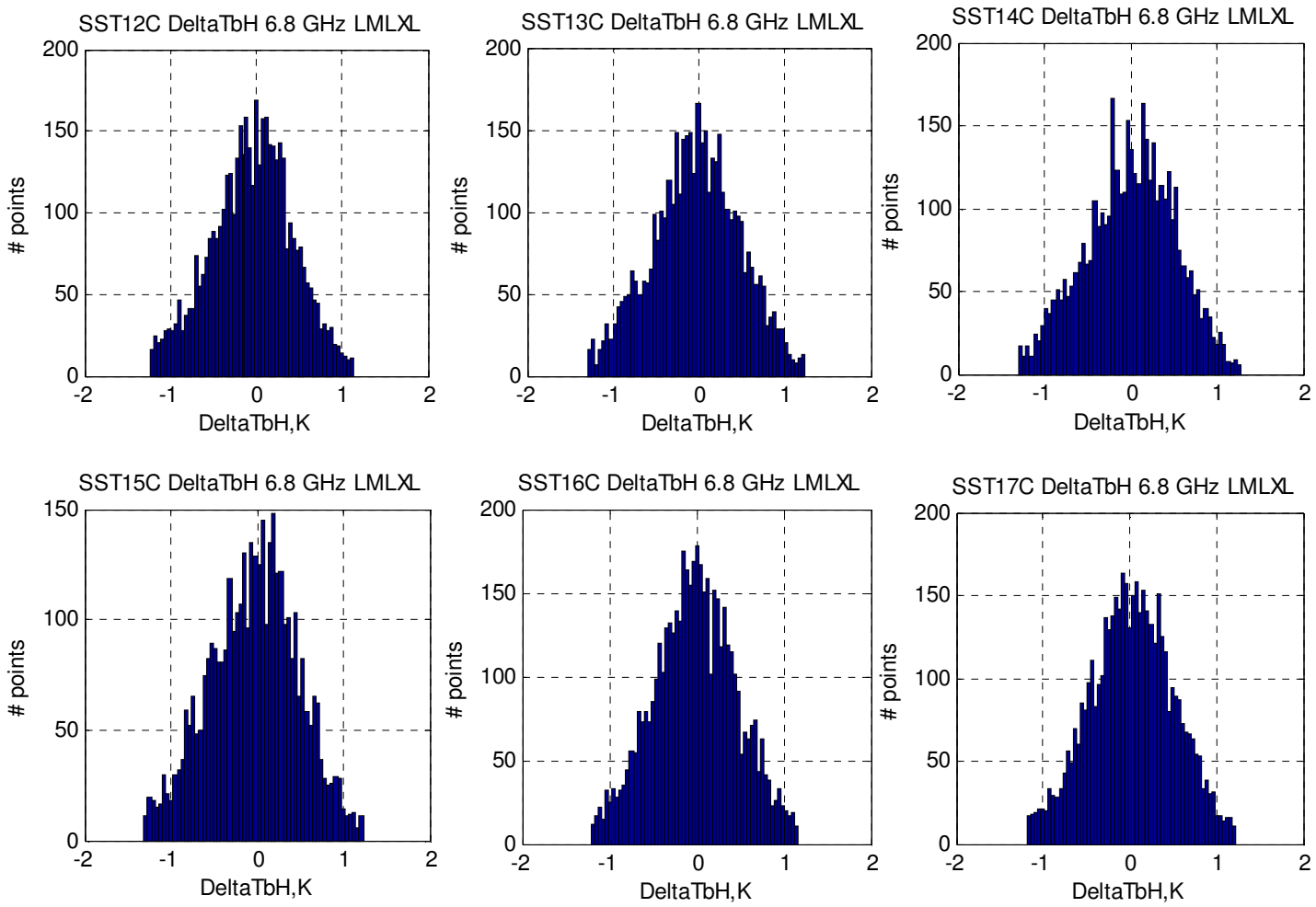
SST12C DeltaTbH 6.8 GHz LMLXL
SST13C DeltaTbH 6.8 GHz LMLXL
SST14C DeltaTbH 6.8 GHz LMLXL
SST15C DeltaTbH 6.8 GHz LMLXL
SST16C DeltaTbH 6.8 GHz LMLXL
SST17C DeltaTbH 6.8 GHz LMLXL
points
DeltaTbH,K

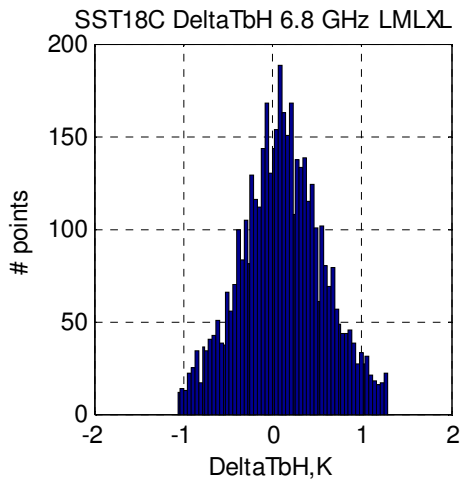
SST18C DeltaTbH 6.8 GHz LMLXL
points
DeltaTbH,K

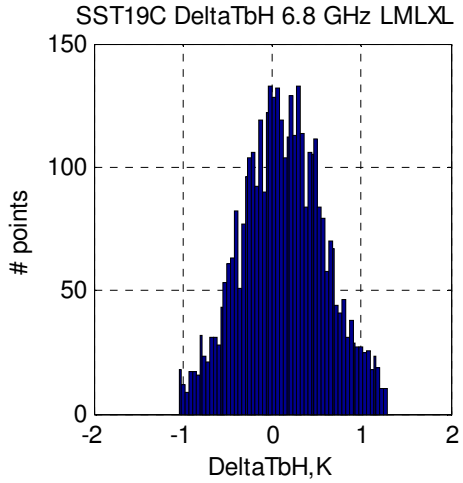
SST19C DeltaTbH 6.8 GHz LMLXL
points
DeltaTbH,K

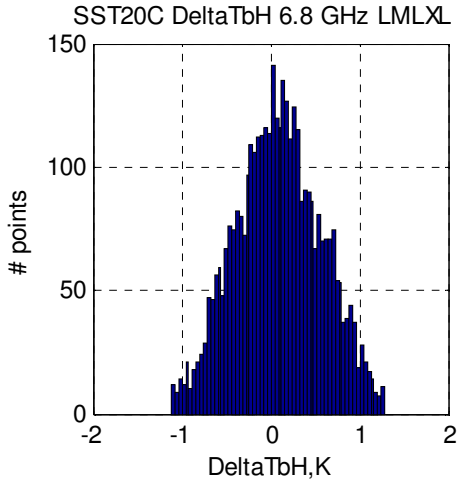
SST20C DeltaTbH 6.8 GHz LMLXL
points
DeltaTbH,K

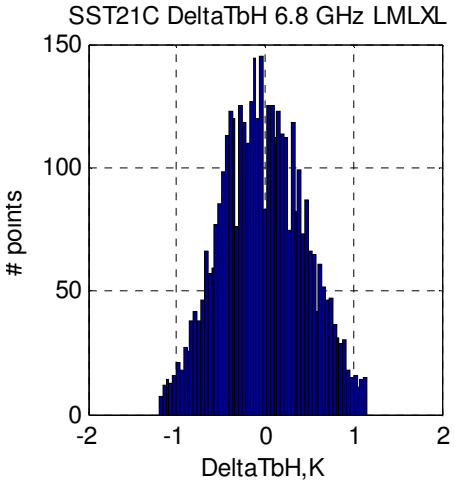
SST21C DeltaTbH 6.8 GHz LMLXL
points
DeltaTbH,K

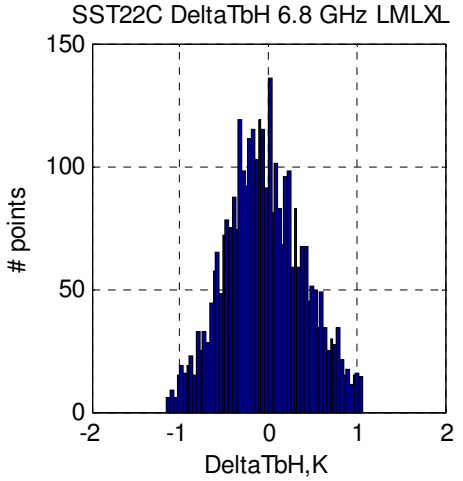
SST22C DeltaTbH 6.8 GHz LMLXL
points
DeltaTbH,K

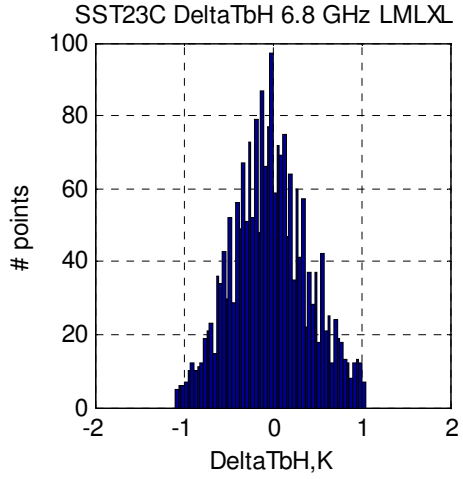
SST23C DeltaTbH 6.8 GHz LMLXL
points
DeltaTbH,K

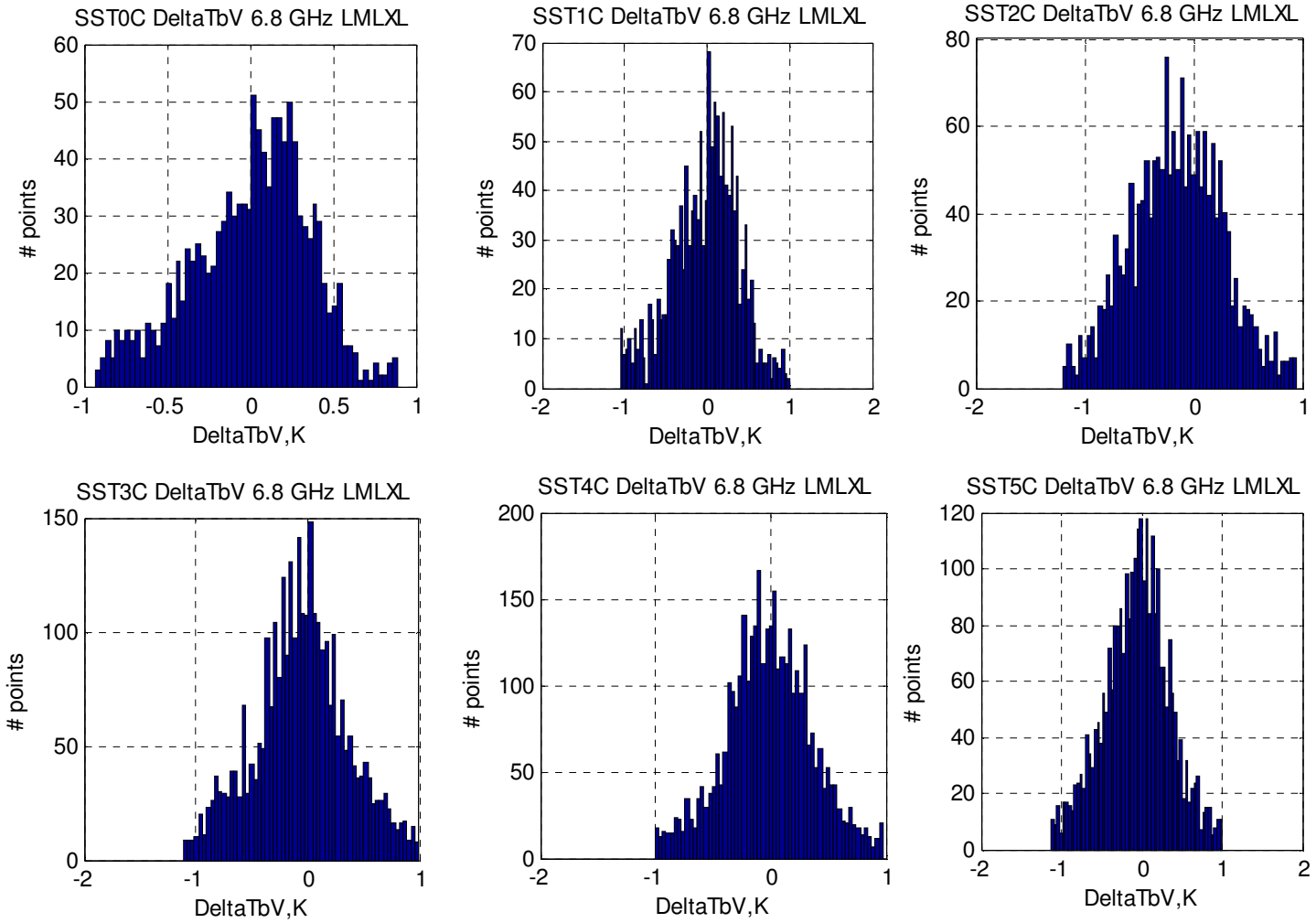
SST0C DeltaTbV 6.8 GHz LMLXL
points
DeltaTbV,K
SST1C DeltaTbV 6.8 GHz LMLXL
points
DeltaTbV,K
SST2C DeltaTbV 6.8 GHz LMLXL
points
DeltaTbV,K
SST3C DeltaTbV 6.8 GHz LMLXL
points
DeltaTbV,K
SST4C DeltaTbV 6.8 GHz LMLXL
points
DeltaTbV,K
SST5C DeltaTbV 6.8 GHz LMLXL
points
DeltaTbV,K

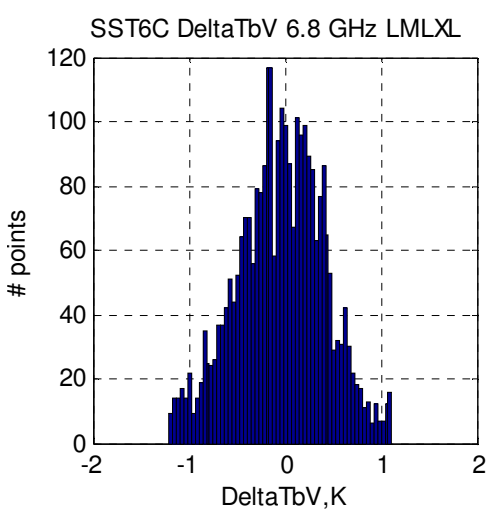
SST6C DeltaTbV 6.8 GHz LMLXL
points
DeltaTbV,K

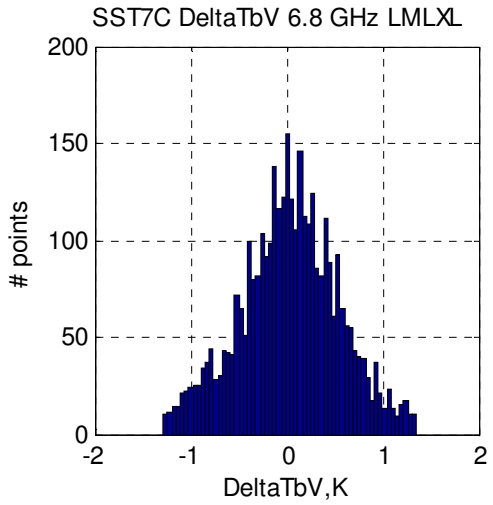
SST7C DeltaTbV 6.8 GHz LMLXL
points
DeltaTbV,K

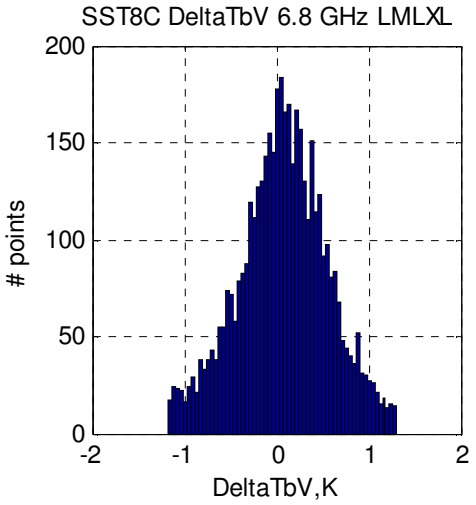
SST8C DeltaTbV 6.8 GHz LMLXL
points
DeltaTbV,K

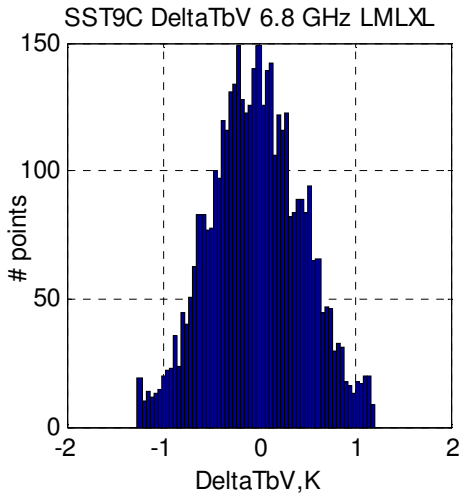
SST9C DeltaTbV 6.8 GHz LMLXL
points
DeltaTbV,K

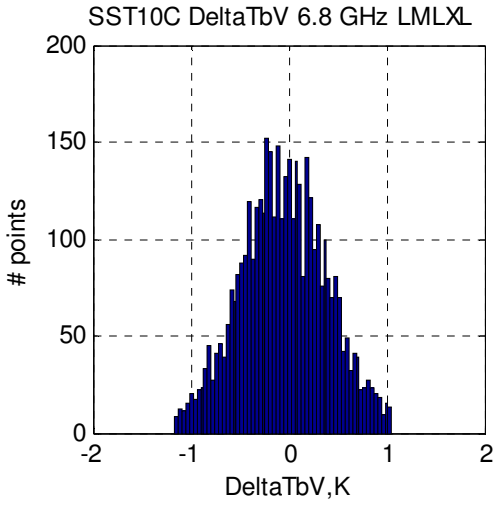
SST10C DeltaTbV 6.8 GHz LMLXL
points
DeltaTbV,K

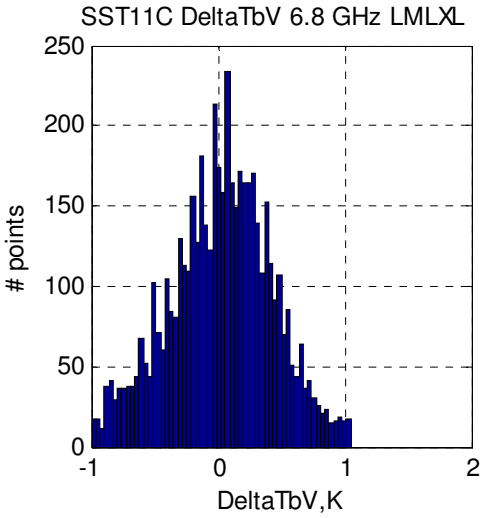
SST11C DeltaTbV 6.8 GHz LMLXL
points
DeltaTbV,K

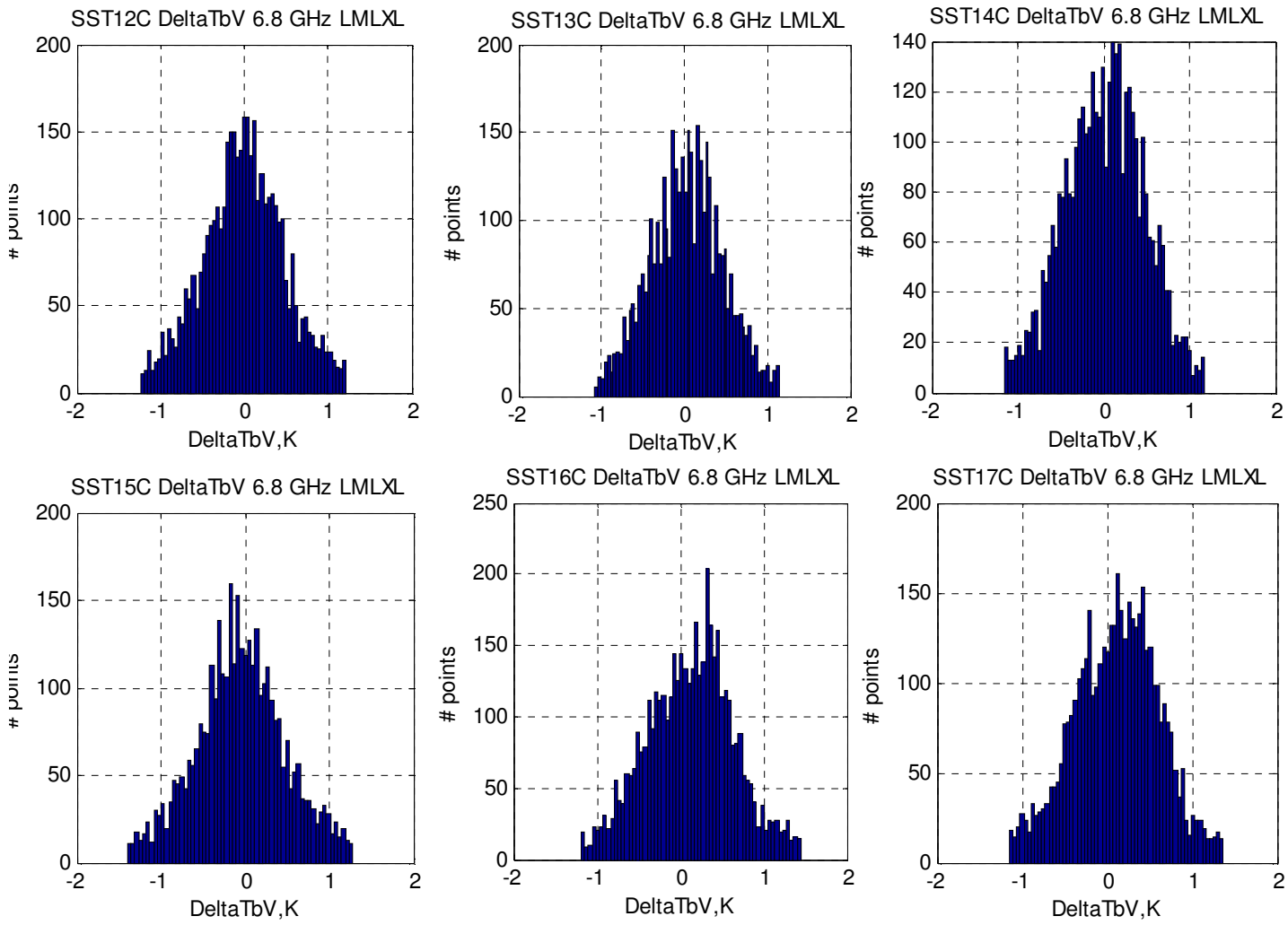
SST12C DeltaTbV 6.8 GHz LMLXL
SST13C DeltaTbV 6.8 GHz LMLXL
SST14C DeltaTbV 6.8 GHz LMLXL
SST15C DeltaTbV 6.8 GHz LMLXL
SST16C DeltaTbV 6.8 GHz LMLXL
SST17C DeltaTbV 6.8 GHz LMLXL
points
DeltaTbV,K

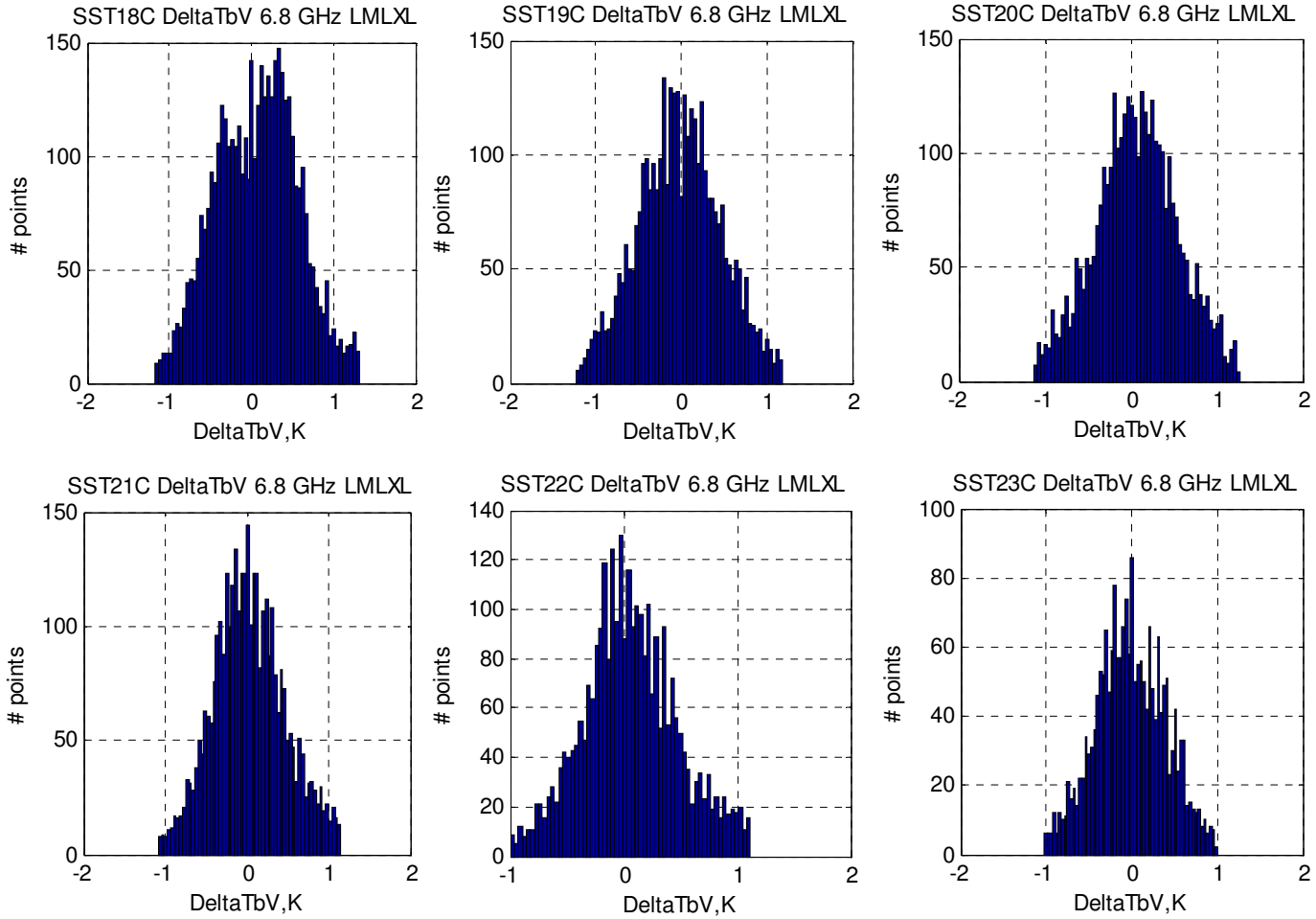
SST18C DeltaTbV 6.8 GHz LMLXL
SST19C DeltaTbV 6.8 GHz LMLXL
SST20C DeltaTbV 6.8 GHz LMLXL
SST21C DeltaTbV 6.8 GHz LMLXL
SST22C DeltaTbV 6.8 GHz LMLXL
SST23C DeltaTbV 6.8 GHz LMLXL
points
DeltaTbV,K

10.7 GHZ Ascending

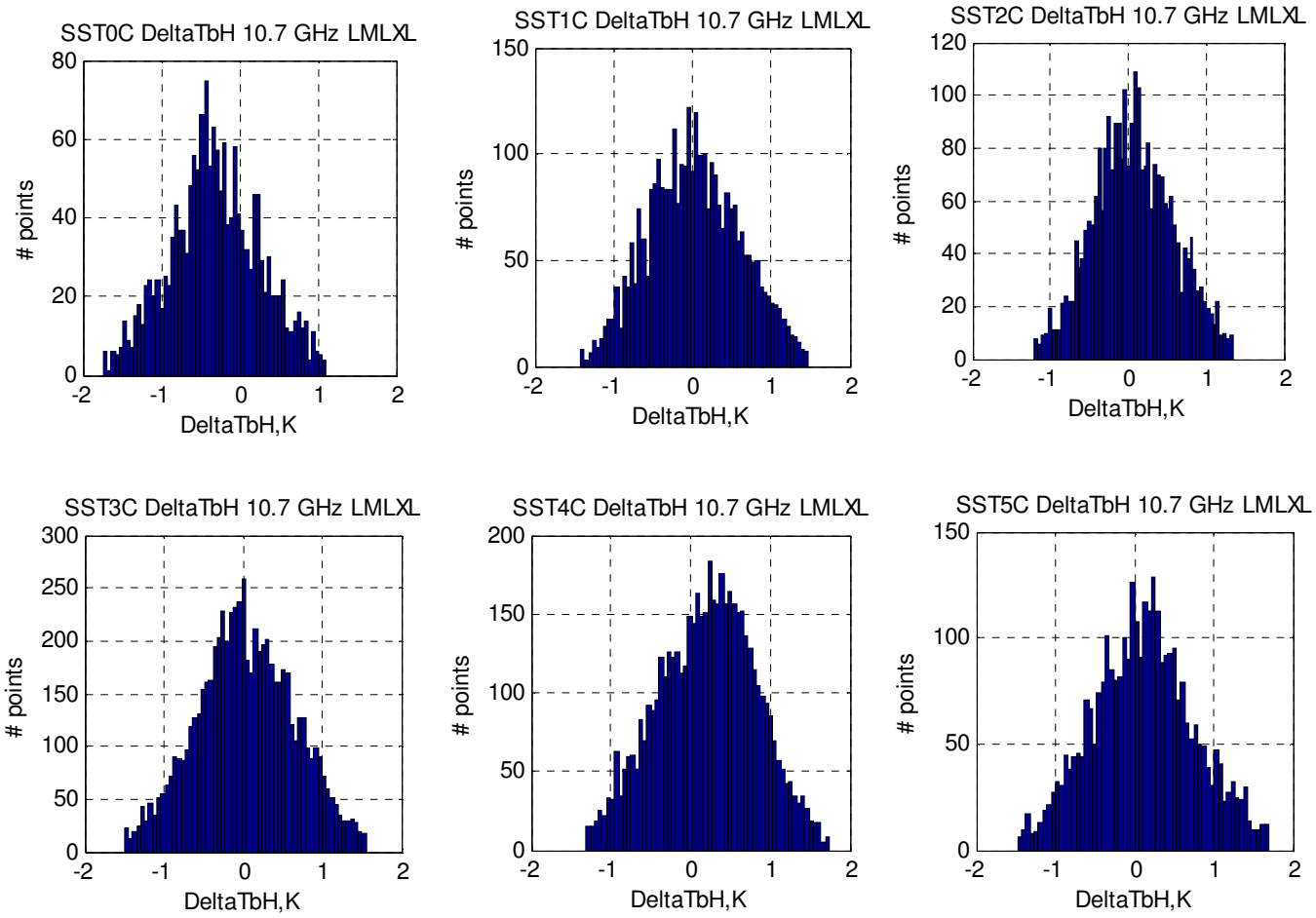
SST0C DeltaTbH 10.7 GHz LMLXL
points
DeltaTbH,K
SST1C DeltaTbH 10.7 GHz LMLXL
points
DeltaTbH,K
SST2C DeltaTbH 10.7 GHz LMLXL
points
DeltaTbH,K
SST3C DeltaTbH 10.7 GHz LMLXL
points
DeltaTbH,K
SST4C DeltaTbH 10.7 GHz LMLXL
points
DeltaTbH,K
SST5C DeltaTbH 10.7 GHz LMLXL
points
DeltaTbH,K

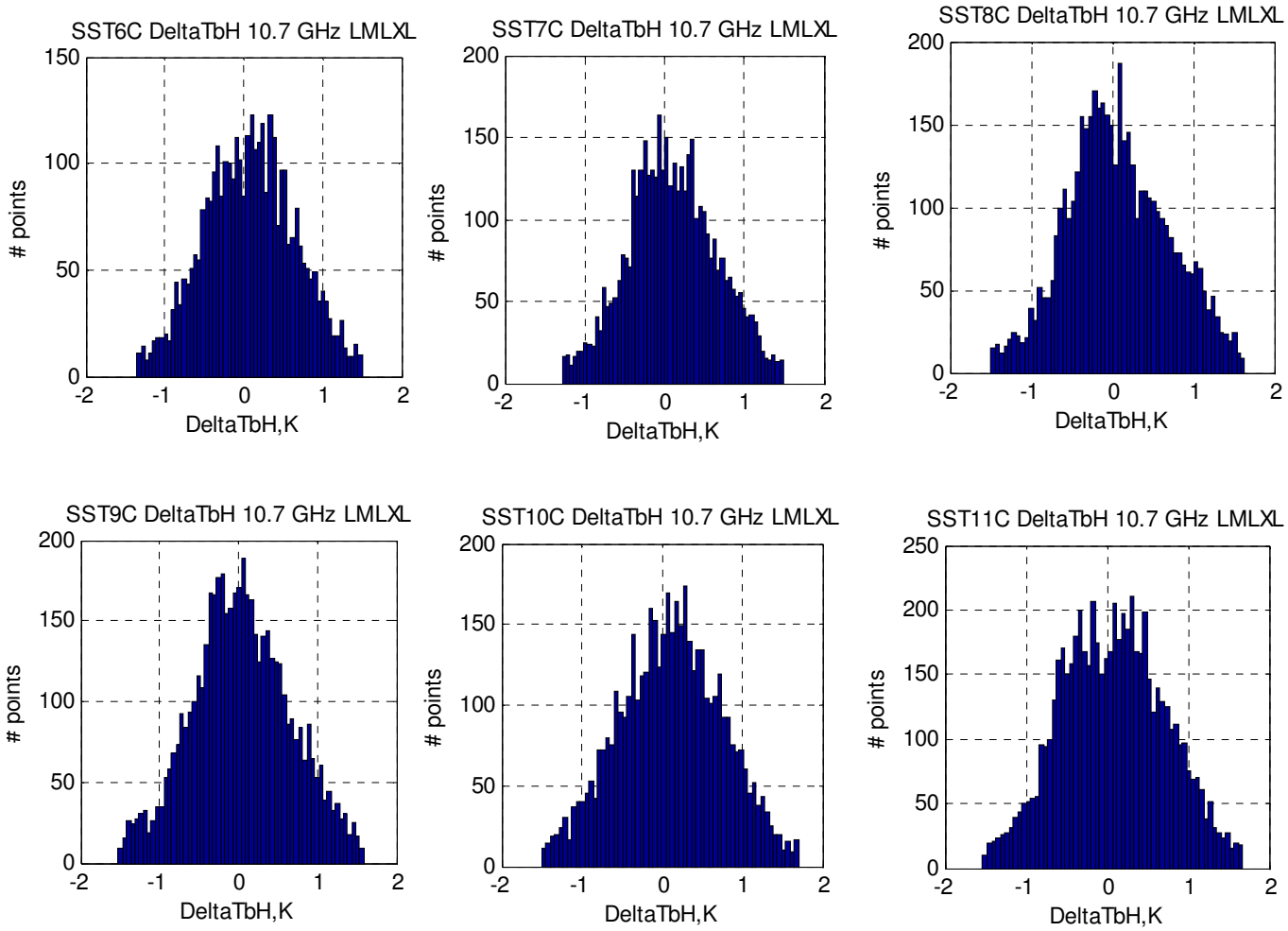
SST6C DeltaTbH 10.7 GHz LMLXL
SST7C DeltaTbH 10.7 GHz LMLXL
SST8C DeltaTbH 10.7 GHz LMLXL
SST9C DeltaTbH 10.7 GHz LMLXL
SST10C DeltaTbH 10.7 GHz LMLXL
SST11C DeltaTbH 10.7 GHz LMLXL
points
DeltaTbH,K

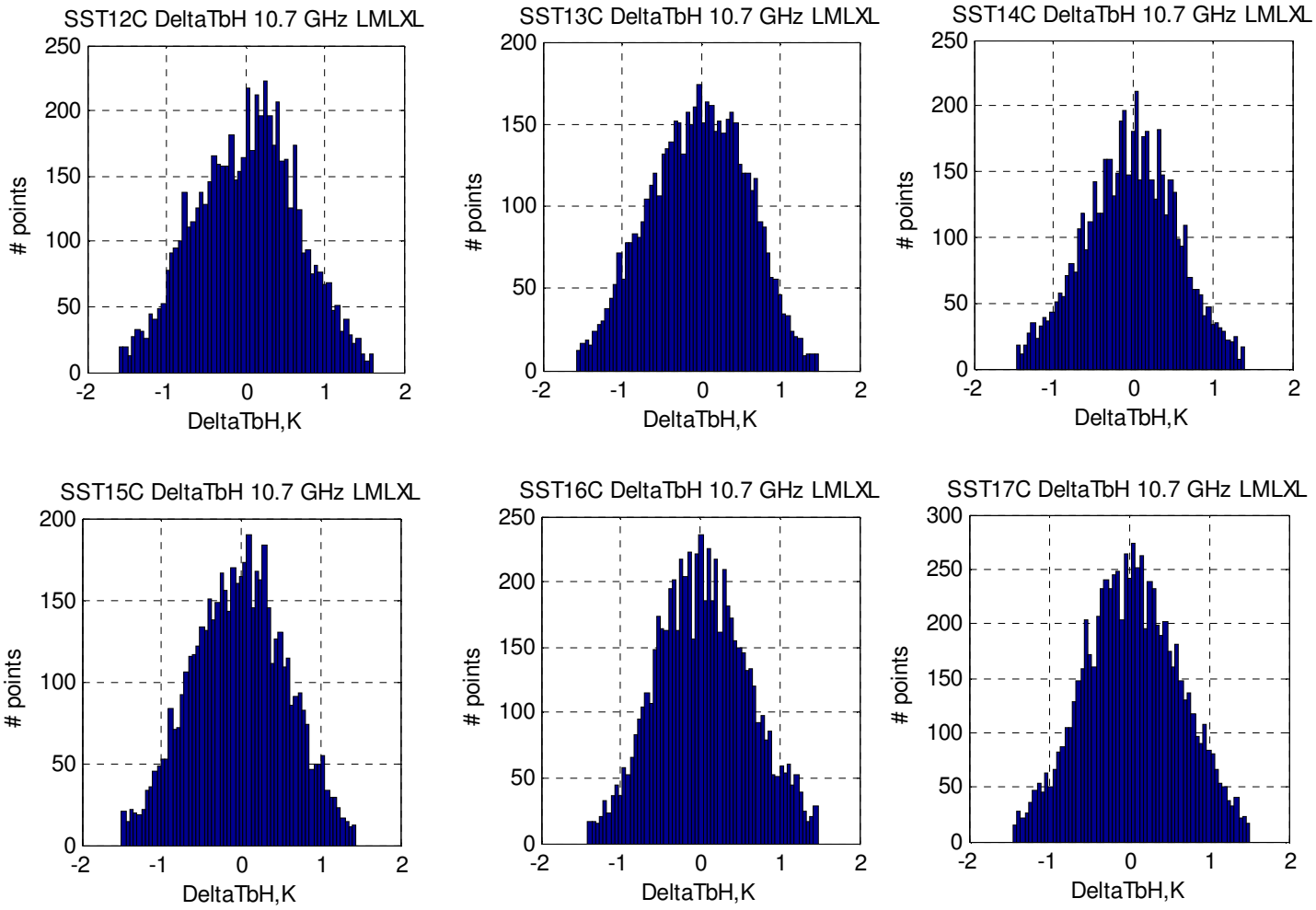
SST12C DeltaTbH 10.7 GHz LMLXL
SST13C DeltaTbH 10.7 GHz LMLXL
SST14C DeltaTbH 10.7 GHz LMLXL
SST15C DeltaTbH 10.7 GHz LMLXL
SST16C DeltaTbH 10.7 GHz LMLXL
SST17C DeltaTbH 10.7 GHz LMLXL
points
DeltaTbH,K

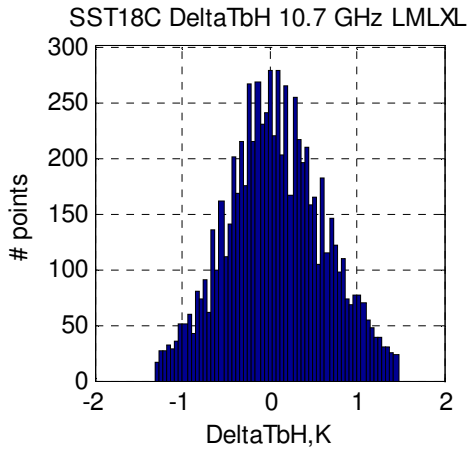
SST18C DeltaTbH 10.7 GHz LMLXL
points
DeltaTbH,K

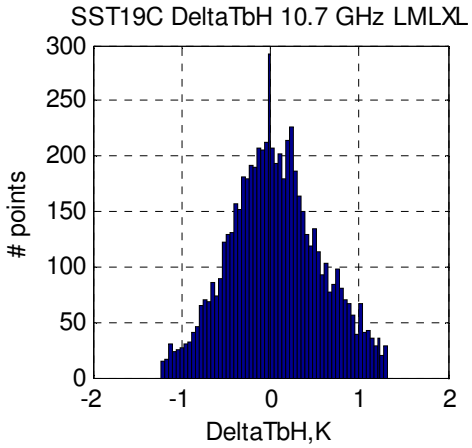
SST19C DeltaTbH 10.7 GHz LMLXL
points
DeltaTbH,K

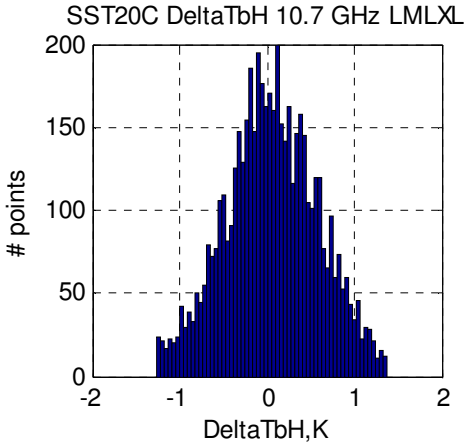
SST20C DeltaTbH 10.7 GHz LMLXL
points
DeltaTbH,K

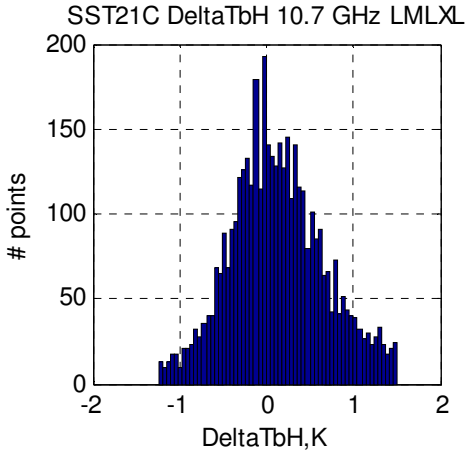
SST21C DeltaTbH 10.7 GHz LMLXL
points
DeltaTbH,K

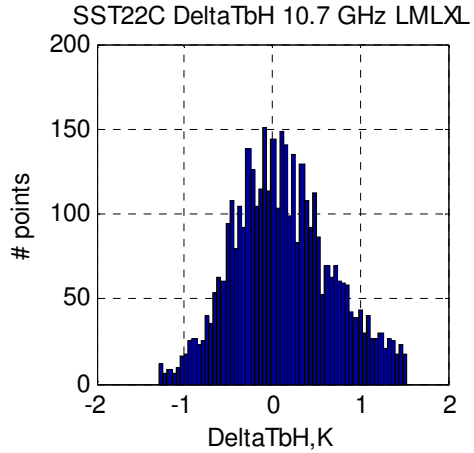
SST22C DeltaTbH 10.7 GHz LMLXL
points
DeltaTbH,K

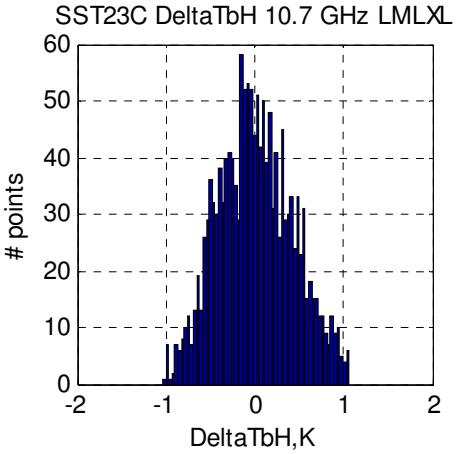
SST23C DeltaTbH 10.7 GHz LMLXL
points
DeltaTbH,K

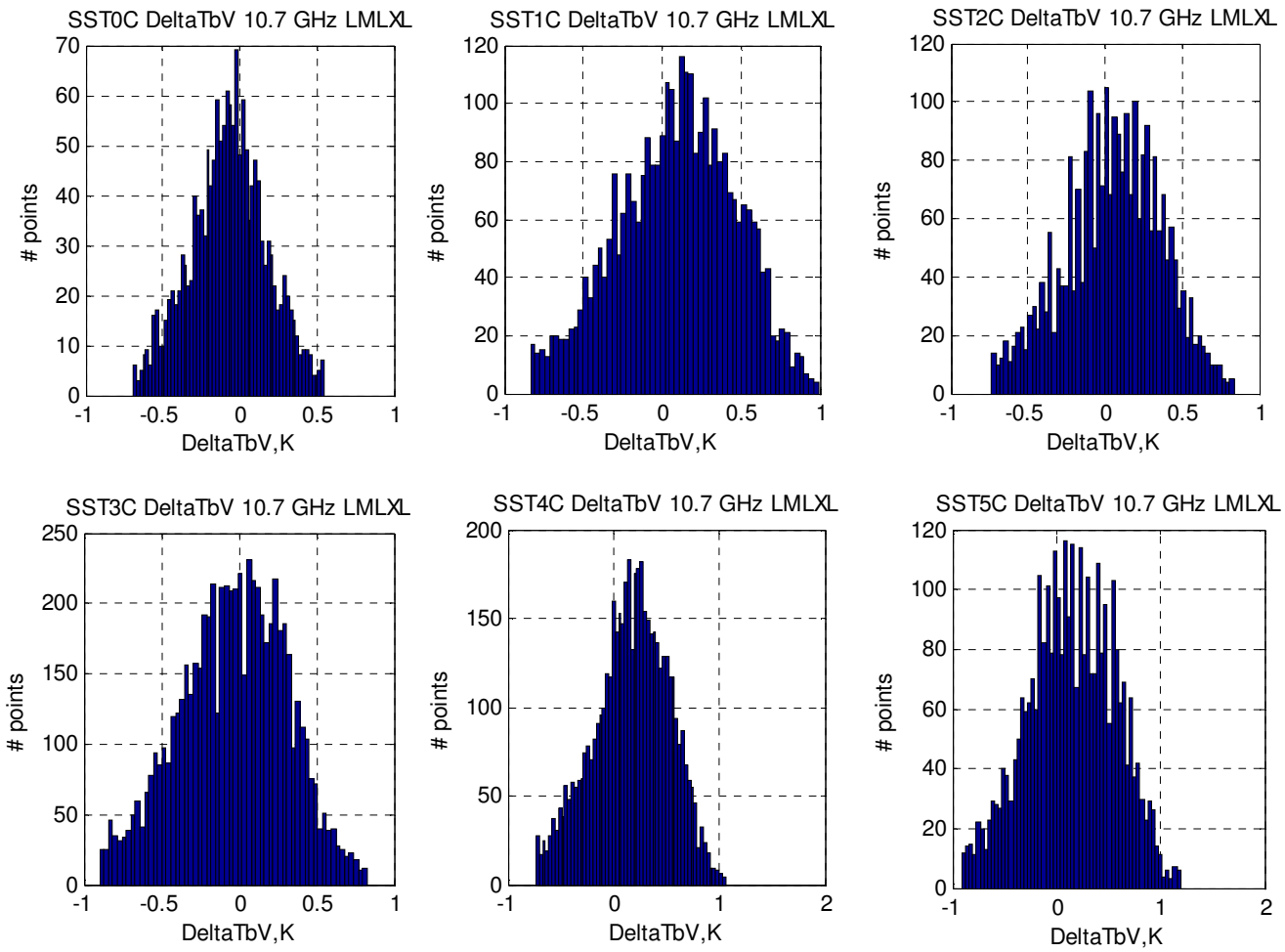
SST0C DeltaTbV 10.7 GHz LMLXL
SST1C DeltaTbV 10.7 GHz LMLXL
SST2C DeltaTbV 10.7 GHz LMLXL
SST3C DeltaTbV 10.7 GHz LMLXL
SST4C DeltaTbV 10.7 GHz LMLXL
SST5C DeltaTbV 10.7 GHz LMLXL
points
DeltaTbV,K

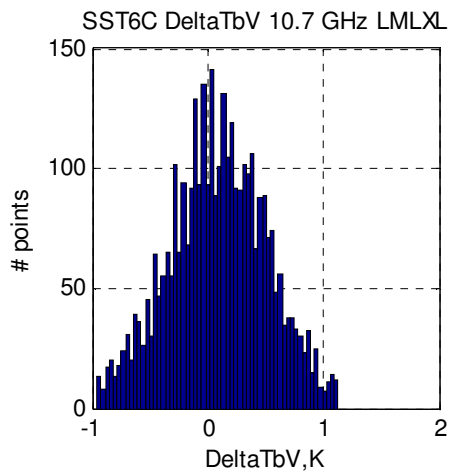
SST6C DeltaTbV 10.7 GHz LMLXL
points
DeltaTbV,K

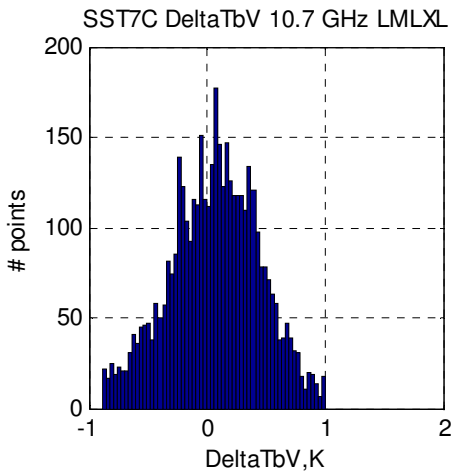
SST7C DeltaTbV 10.7 GHz LMLXL
points
DeltaTbV,K

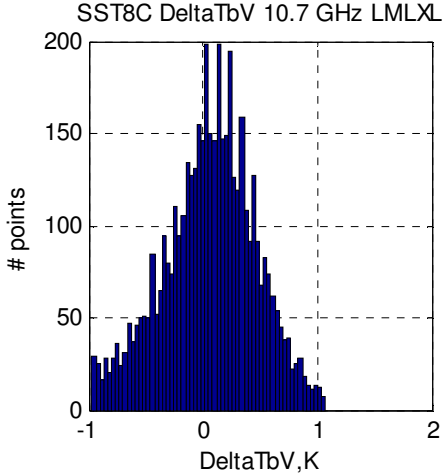
SST8C DeltaTbV 10.7 GHz LMLXL
points
DeltaTbV,K

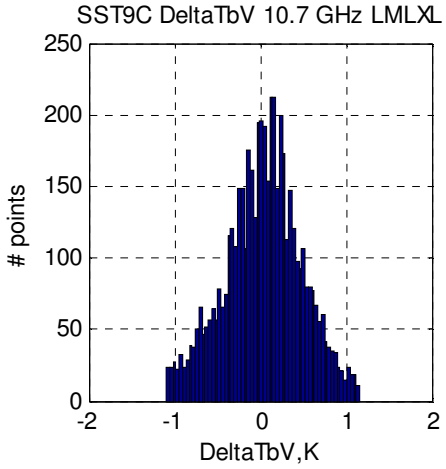
SST9C DeltaTbV 10.7 GHz LMLXL
points
DeltaTbV,K

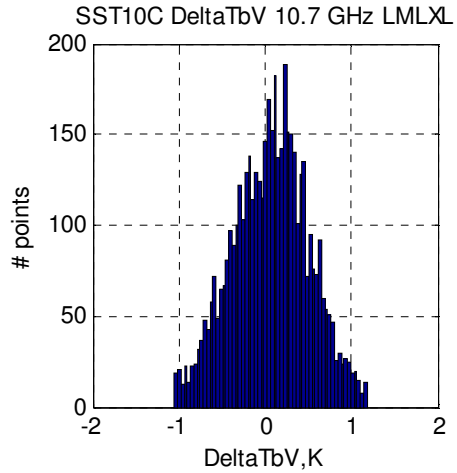
SST10C DeltaTbV 10.7 GHz LMLXL
points
DeltaTbV,K

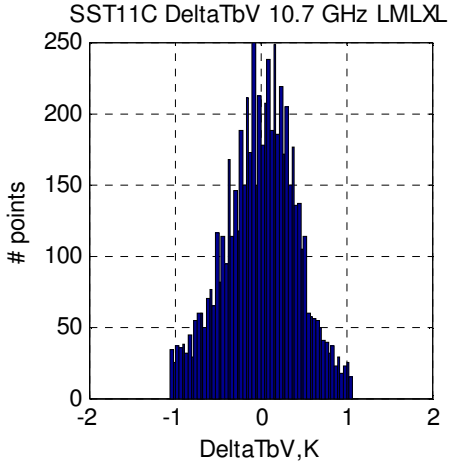
SST11C DeltaTbV 10.7 GHz LMLXL
points
DeltaTbV,K

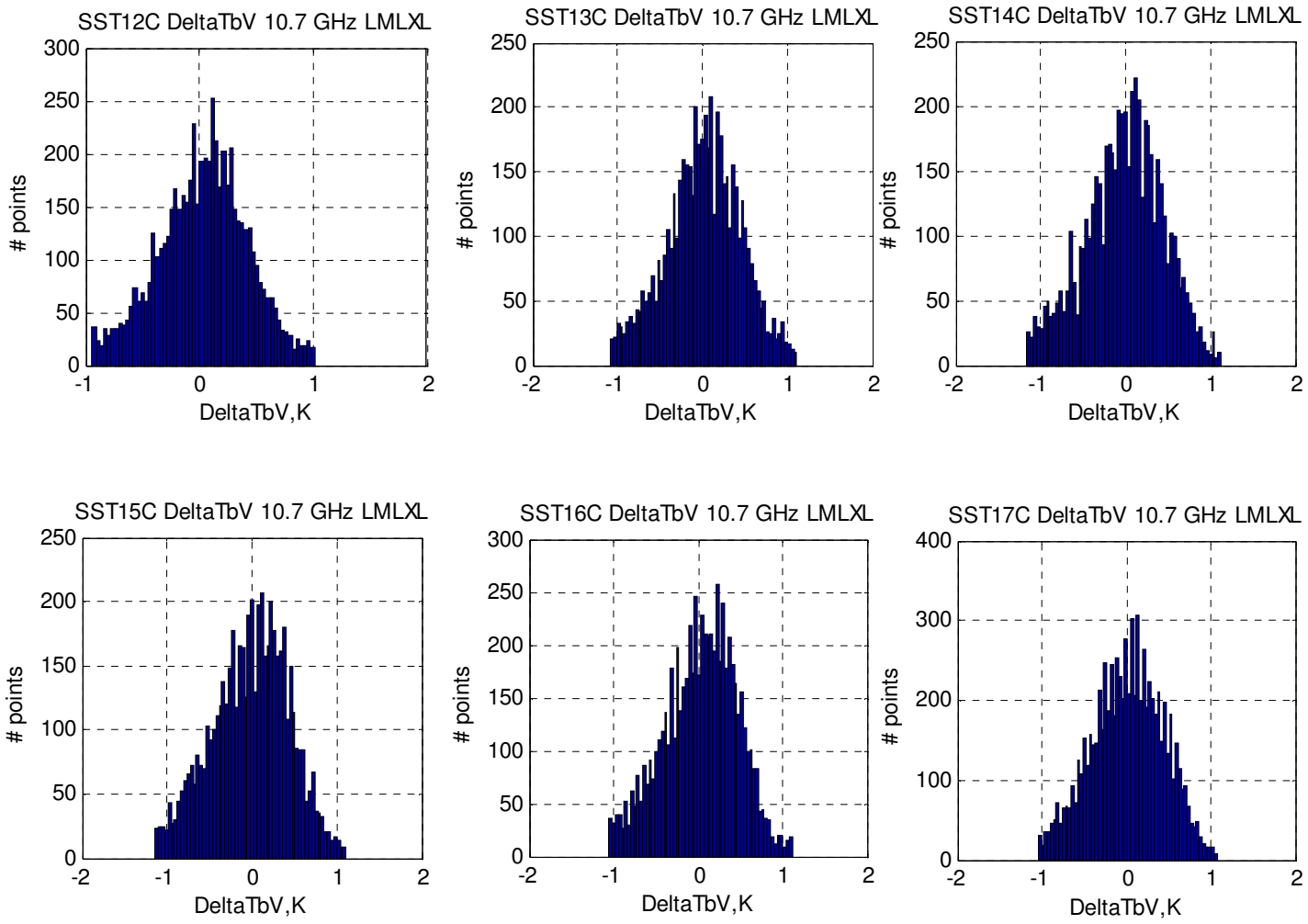
SST12C DeltaTbV 10.7 GHz LMLXL
SST13C DeltaTbV 10.7 GHz LMLXL
SST14C DeltaTbV 10.7 GHz LMLXL
SST15C DeltaTbV 10.7 GHz LMLXL
SST16C DeltaTbV 10.7 GHz LMLXL
SST17C DeltaTbV 10.7 GHz LMLXL
points
DeltaTbV,K

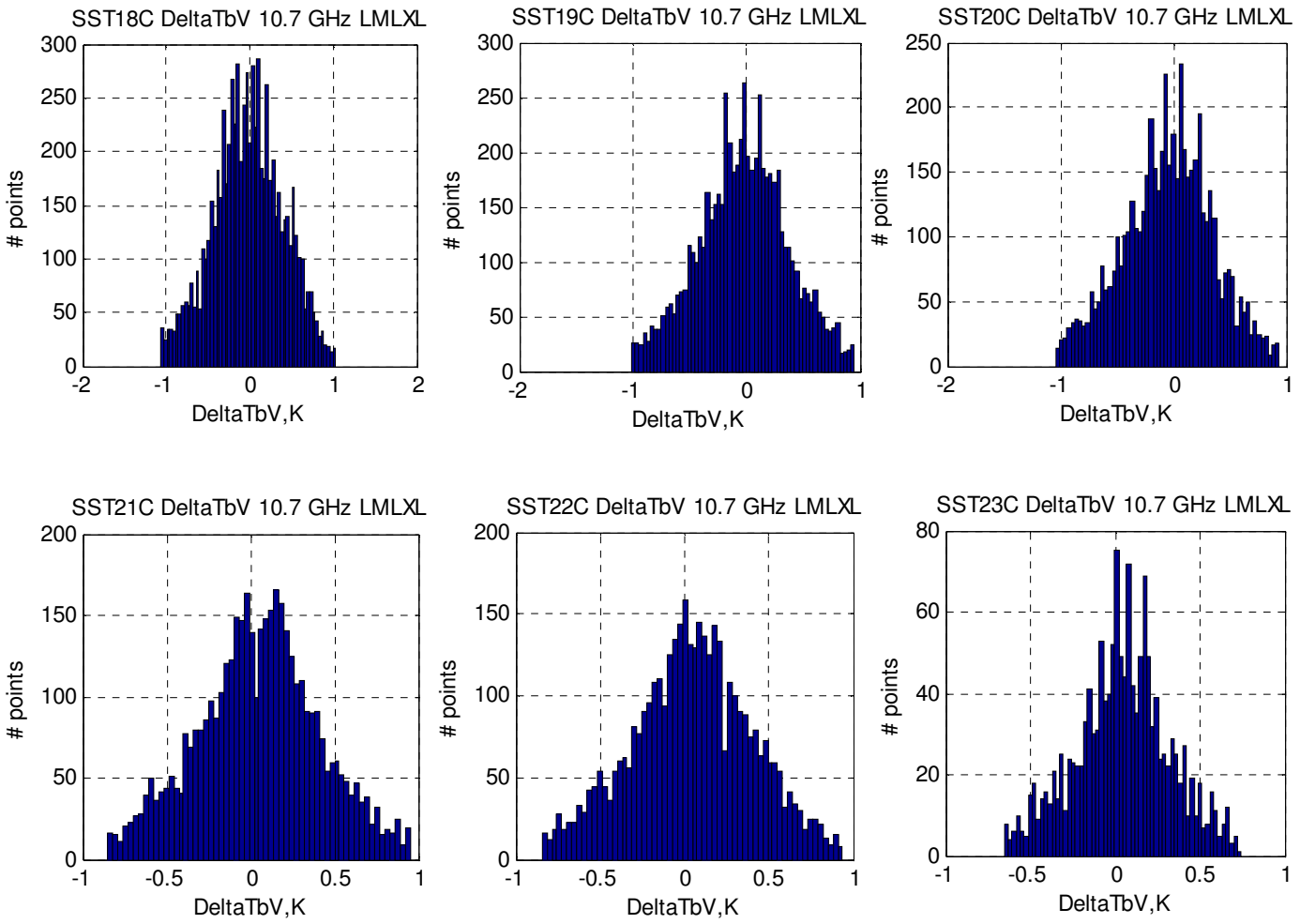
SST18C DeltaTbV 10.7 GHz LMLXL
SST19C DeltaTbV 10.7 GHz LMLXL
SST20C DeltaTbV 10.7 GHz LMLXL
SST21C DeltaTbV 10.7 GHz LMLXL
SST22C DeltaTbV 10.7 GHz LMLXL
SST23C DeltaTbV 10.7 GHz LMLXL
points
DeltaTbV,K

10.7 GHZ Descending

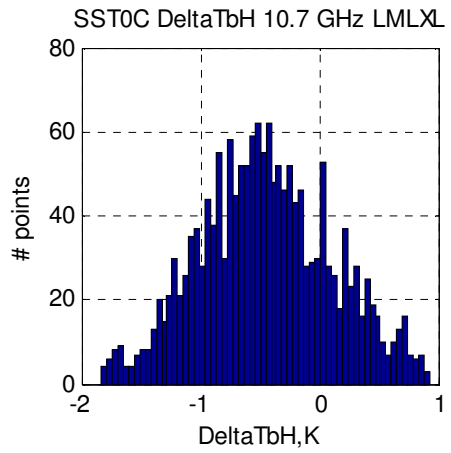
SST0C DeltaTbH 10.7 GHz LMLXL
points
DeltaTbH,K

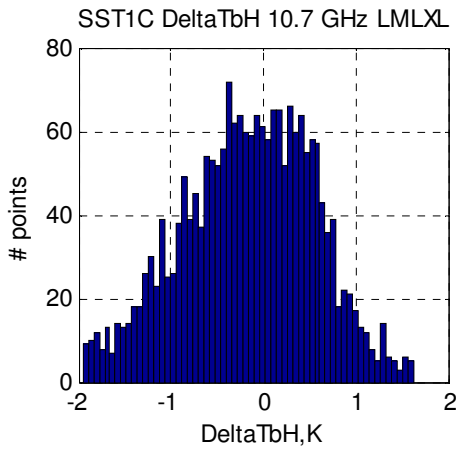
SST1C DeltaTbH 10.7 GHz LMLXL
points
DeltaTbH,K

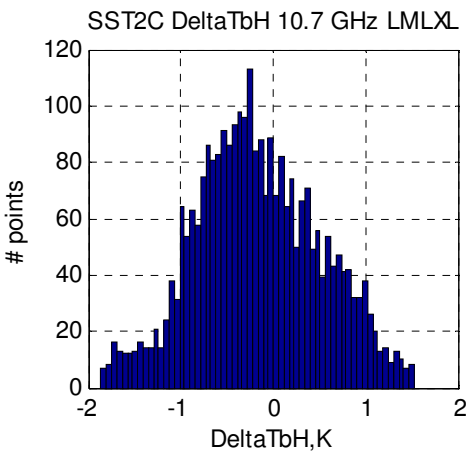
SST2C DeltaTbH 10.7 GHz LMLXL
points
DeltaTbH,K

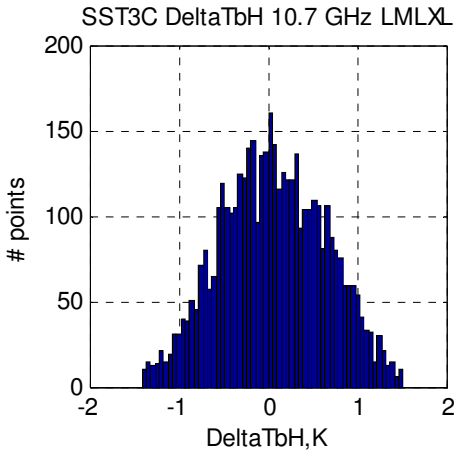
SST3C DeltaTbH 10.7 GHz LMLXL
points
DeltaTbH,K

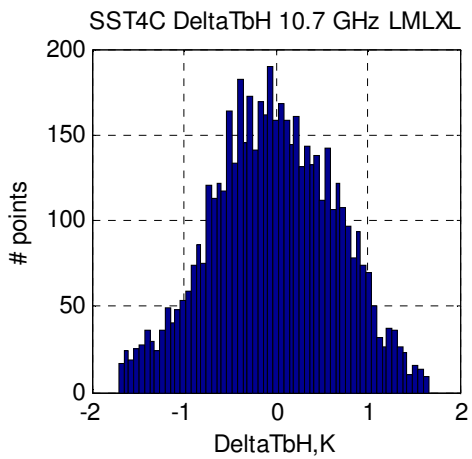
SST4C DeltaTbH 10.7 GHz LMLXL
points
DeltaTbH,K

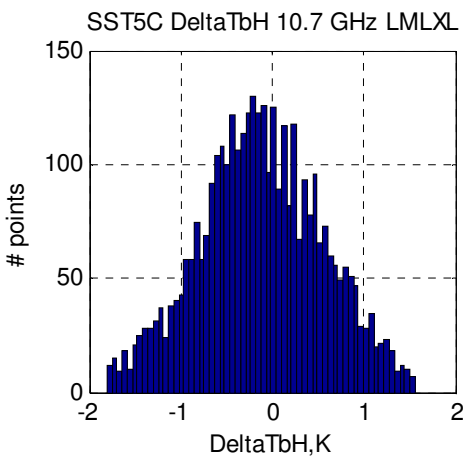
SST5C DeltaTbH 10.7 GHz LMLXL
points
DeltaTbH,K

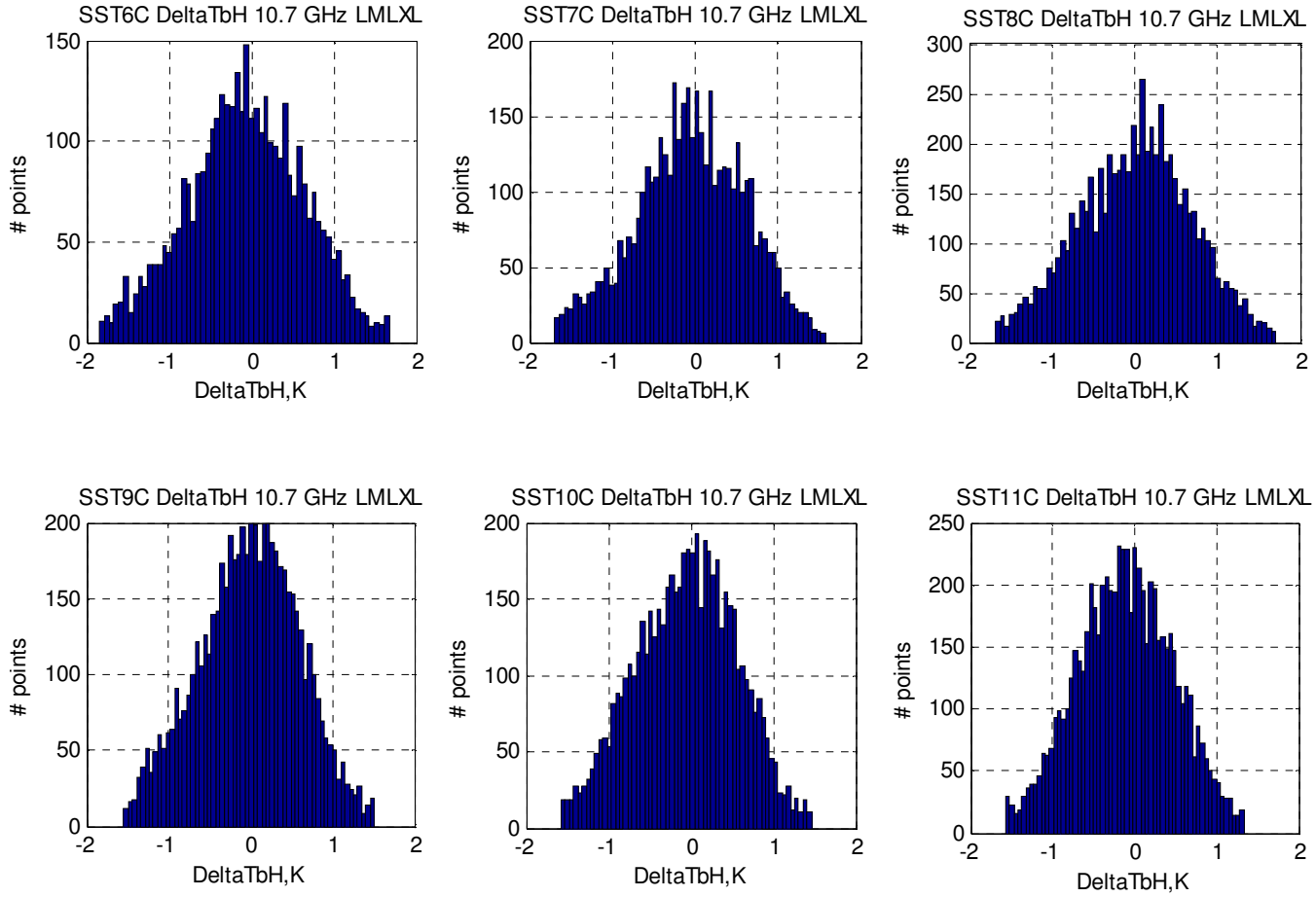
SST6C DeltaTbH 10.7 GHz LMLXL
SST7C DeltaTbH 10.7 GHz LMLXL
SST8C DeltaTbH 10.7 GHz LMLXL
SST9C DeltaTbH 10.7 GHz LMLXL
SST10C DeltaTbH 10.7 GHz LMLXL
SST11C DeltaTbH 10.7 GHz LMLXL
points
DeltaTbH,K

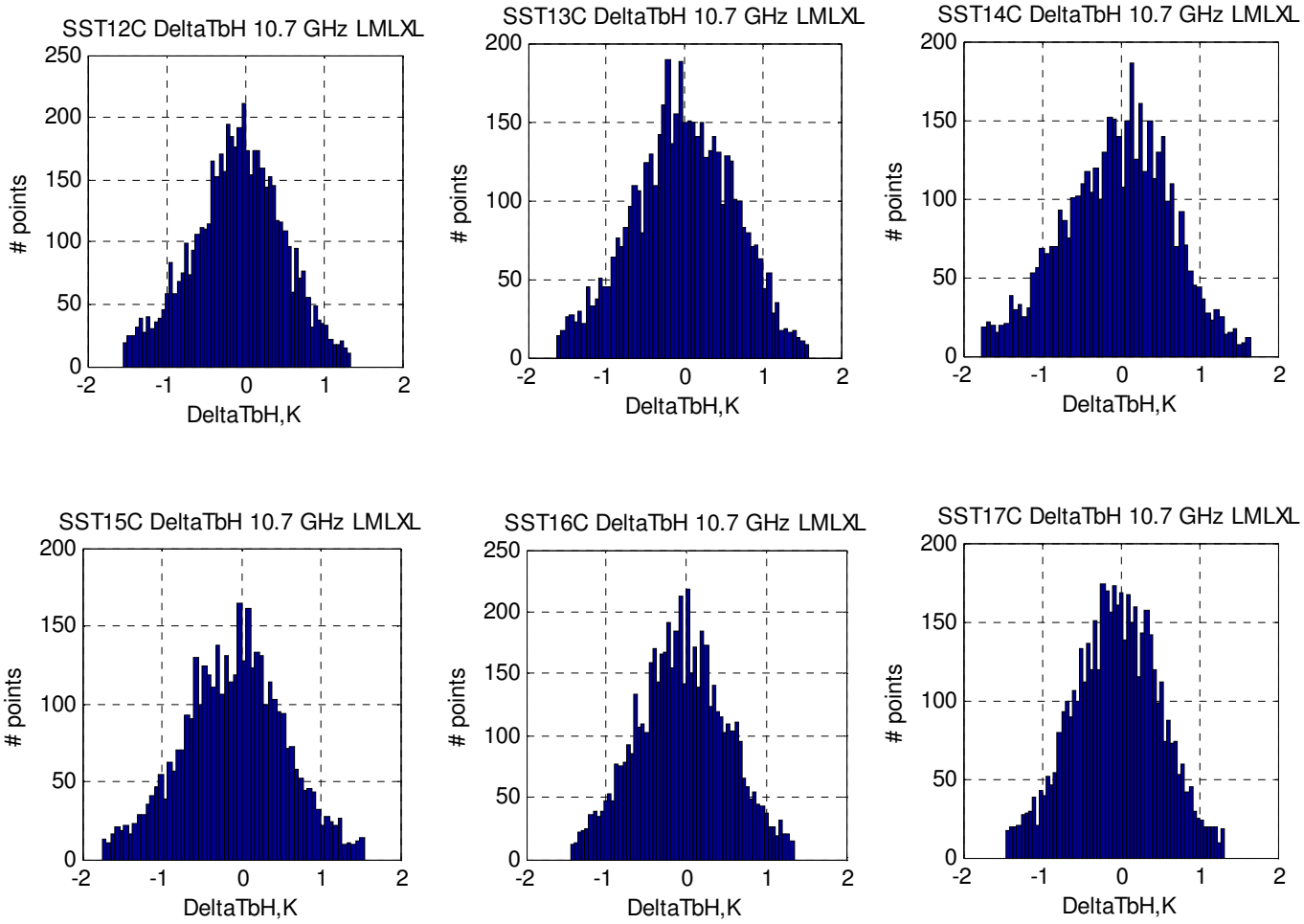
SST12C DeltaTbH 10.7 GHz LMLXL
SST13C DeltaTbH 10.7 GHz LMLXL
SST14C DeltaTbH 10.7 GHz LMLXL
SST15C DeltaTbH 10.7 GHz LMLXL
SST16C DeltaTbH 10.7 GHz LMLXL
SST17C DeltaTbH 10.7 GHz LMLXL
points
DeltaTbH,K

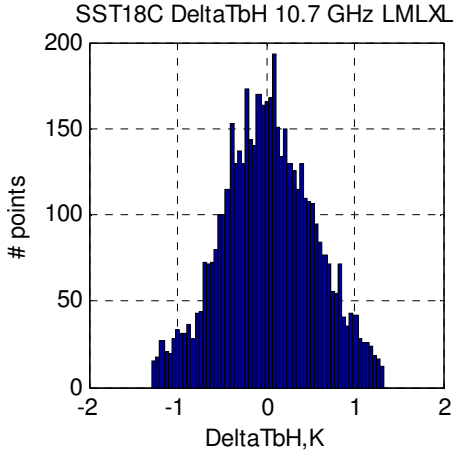
SST18C DeltaTbH 10.7 GHz LMLXL
points
DeltaTbH,K

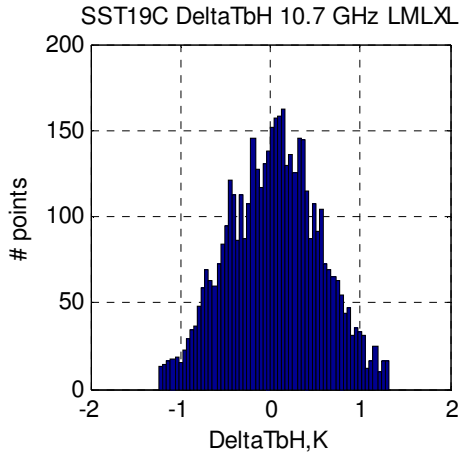
SST19C DeltaTbH 10.7 GHz LMLXL
points
DeltaTbH,K

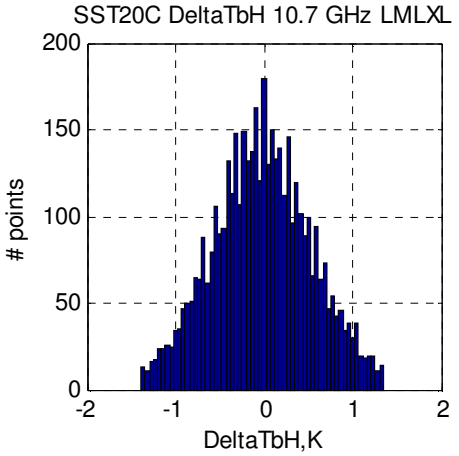
SST20C DeltaTbH 10.7 GHz LMLXL
points
DeltaTbH,K

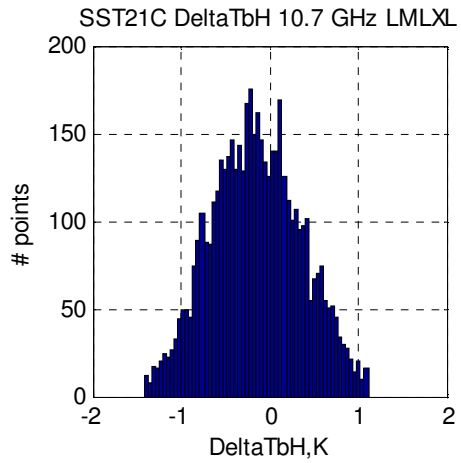
SST21C DeltaTbH 10.7 GHz LMLXL
points
DeltaTbH,K

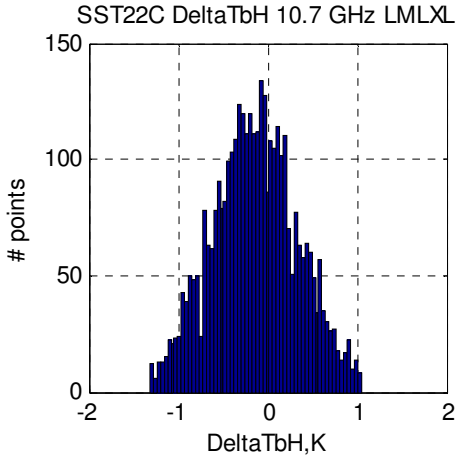
SST22C DeltaTbH 10.7 GHz LMLXL
points
DeltaTbH,K

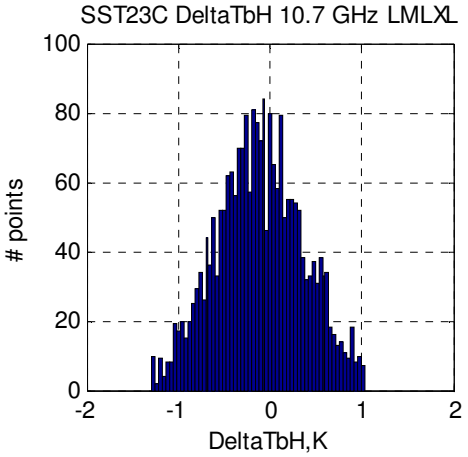
SST23C DeltaTbH 10.7 GHz LMLXL
points
DeltaTbH,K

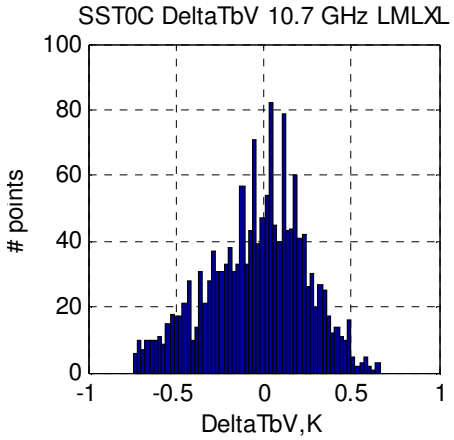
SST0C DeltaTbV 10.7 GHz LMLXL
points
DeltaTbV,K

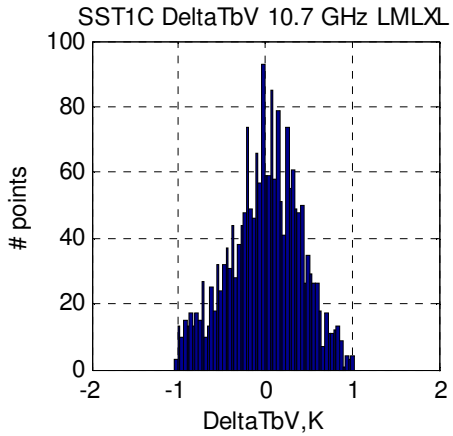
SST1C DeltaTbV 10.7 GHz LMLXL
points
DeltaTbV,K

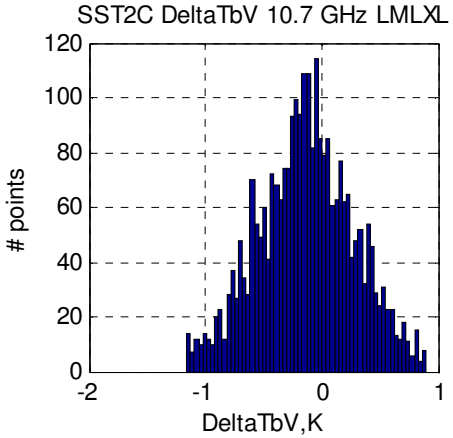
SST2C DeltaTbV 10.7 GHz LMLXL
points
DeltaTbV,K

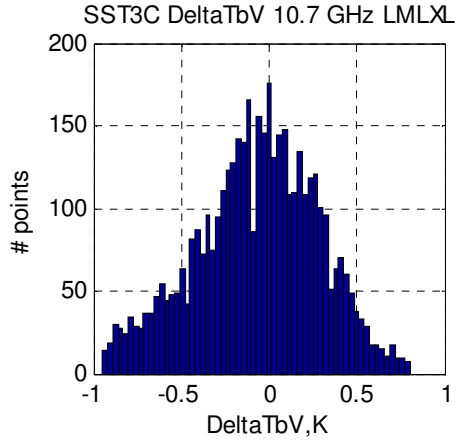
SST3C DeltaTbV 10.7 GHz LMLXL
points
DeltaTbV,K

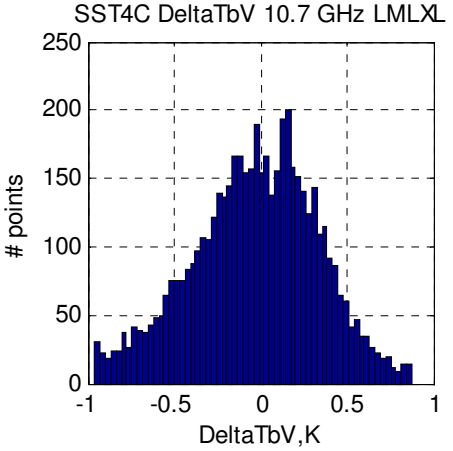
SST4C DeltaTbV 10.7 GHz LMLXL
points
DeltaTbV,K

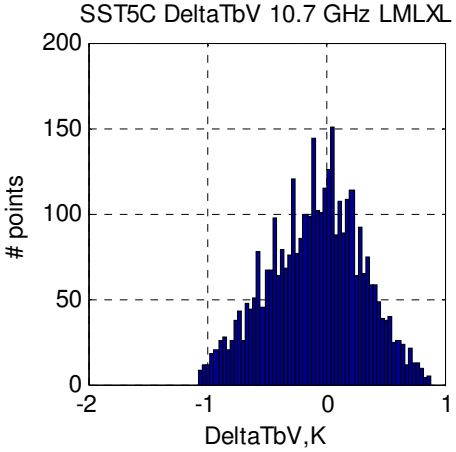
SST5C DeltaTbV 10.7 GHz LMLXL
points
DeltaTbV,K

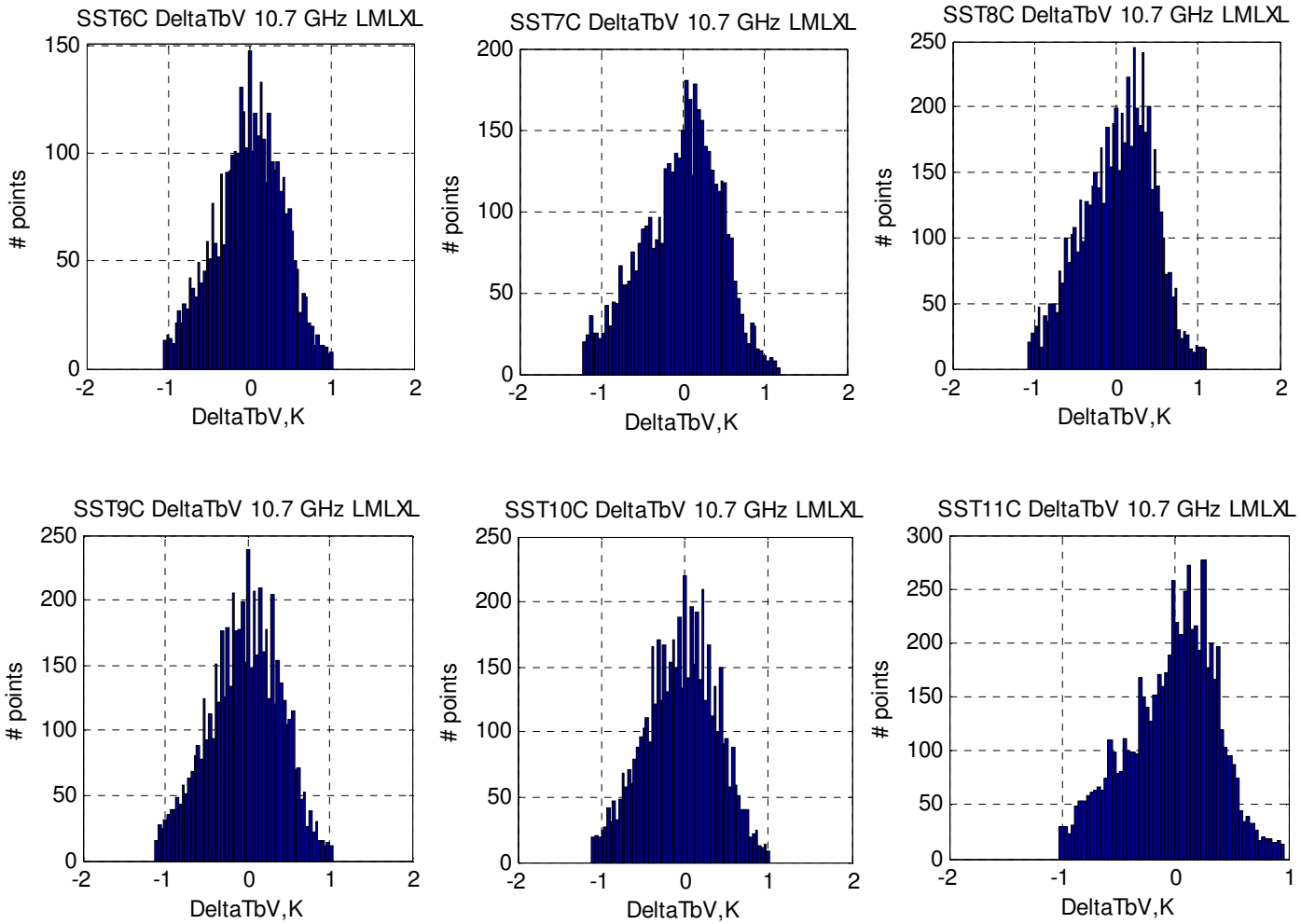
SST6C DeltaTbV 10.7 GHz LMLXL
SST7C DeltaTbV 10.7 GHz LMLXL
SST8C DeltaTbV 10.7 GHz LMLXL
SST9C DeltaTbV 10.7 GHz LMLXL
SST10C DeltaTbV 10.7 GHz LMLXL
SST11C DeltaTbV 10.7 GHz LMLXL
points
DeltaTbV,K

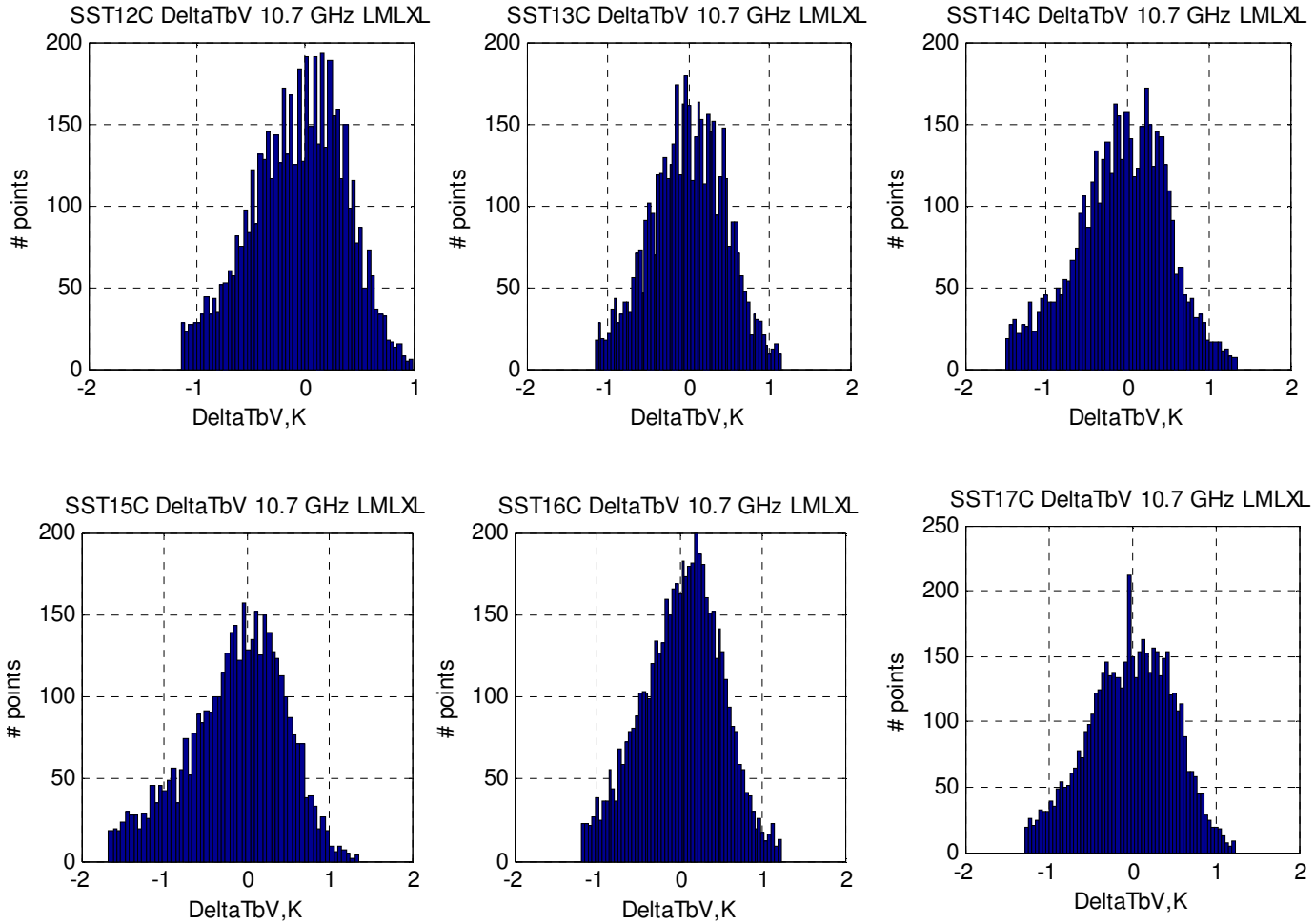
SST12C DeltaTbV 10.7 GHz LMLXL
SST13C DeltaTbV 10.7 GHz LMLXL
SST14C DeltaTbV 10.7 GHz LMLXL
SST15C DeltaTbV 10.7 GHz LMLXL
SST16C DeltaTbV 10.7 GHz LMLXL
SST17C DeltaTbV 10.7 GHz LMLXL
points
DeltaTbV,K

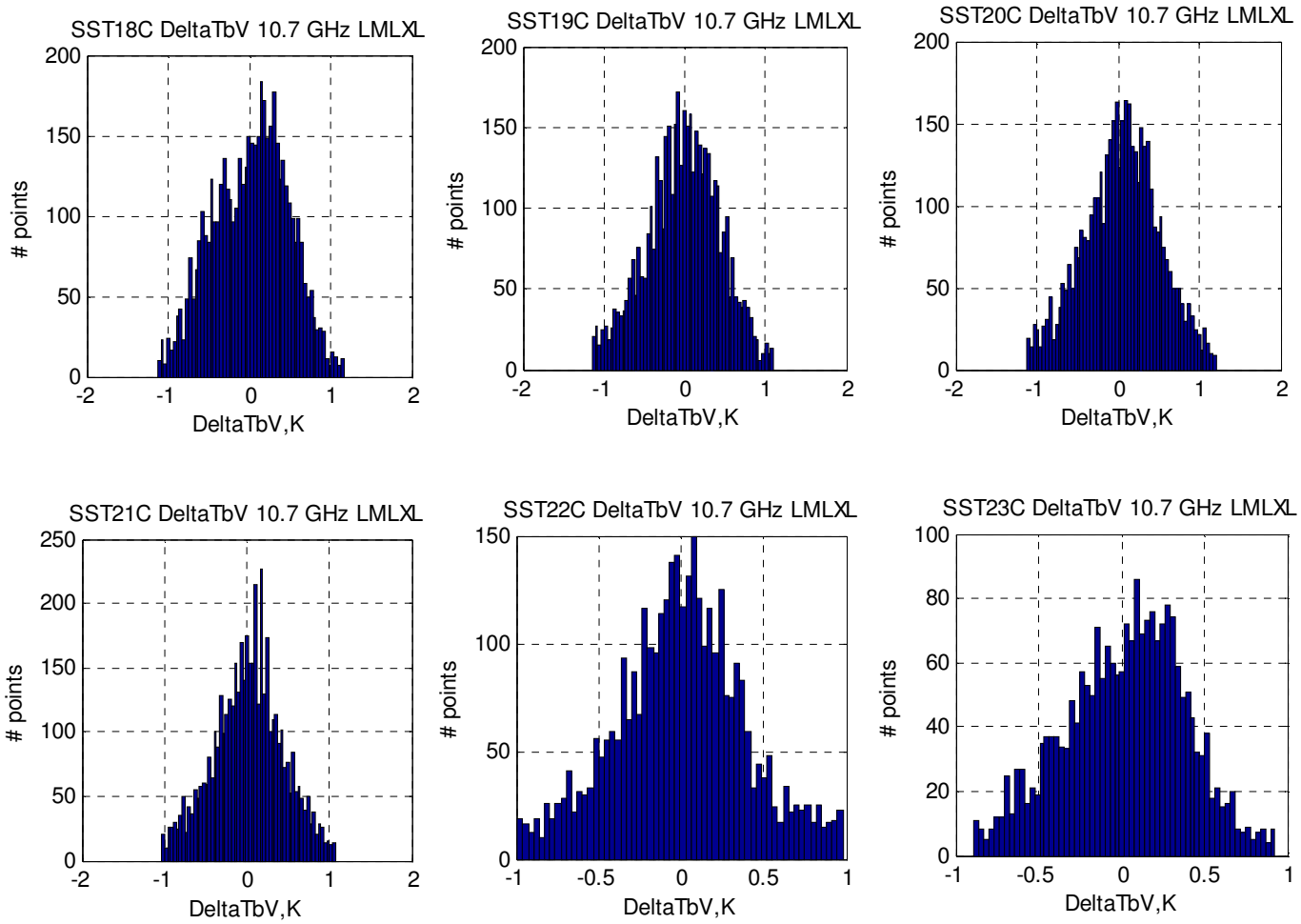
SST18C DeltaTbV 10.7 GHz LMLXL
SST19C DeltaTbV 10.7 GHz LMLXL
SST20C DeltaTbV 10.7 GHz LMLXL
SST21C DeltaTbV 10.7 GHz LMLXL
SST22C DeltaTbV 10.7 GHz LMLXL
SST23C DeltaTbV 10.7 GHz LMLXL
points
DeltaTbV,K

18.7 GHZ Ascending

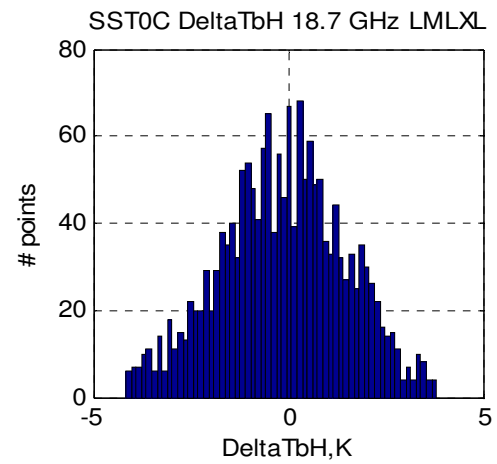
SST0C DeltaTbH 18.7 GHz LMLXL
points
DeltaTbH,K

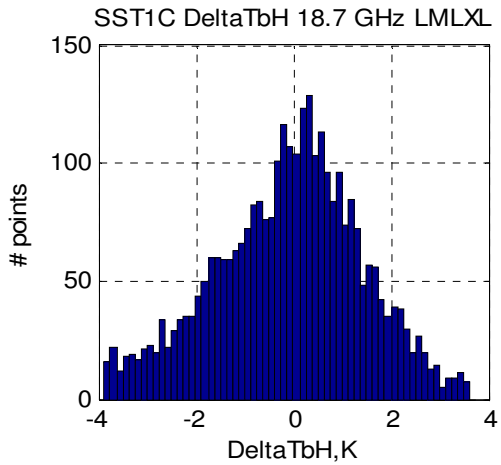
SST1C DeltaTbH 18.7 GHz LMLXL
points
DeltaTbH,K

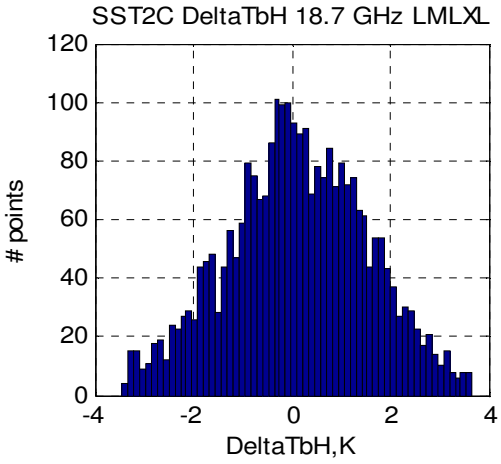
SST2C DeltaTbH 18.7 GHz LMLXL
points
DeltaTbH,K

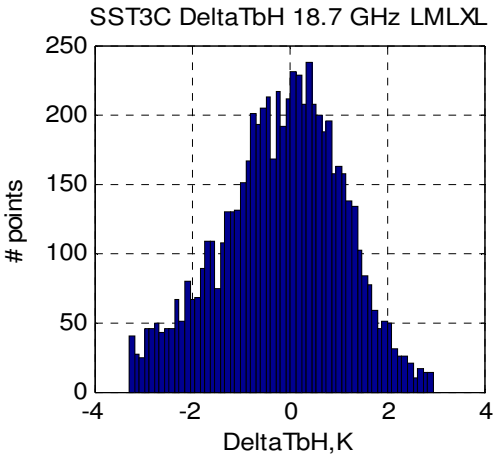
SST3C DeltaTbH 18.7 GHz LMLXL
points
DeltaTbH,K

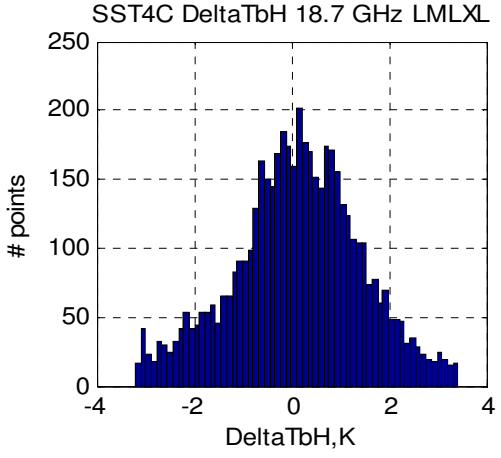
SST4C DeltaTbH 18.7 GHz LMLXL
points
DeltaTbH,K

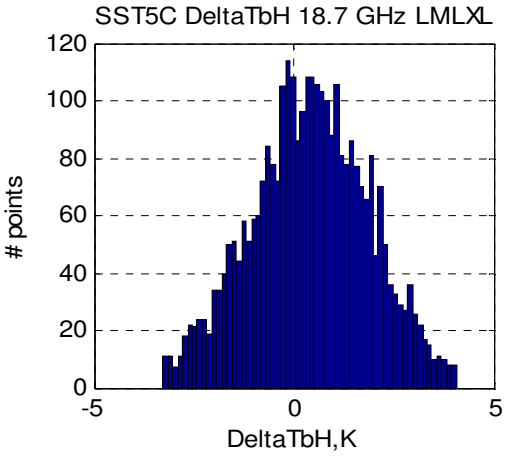
SST5C DeltaTbH 18.7 GHz LMLXL
points
DeltaTbH,K

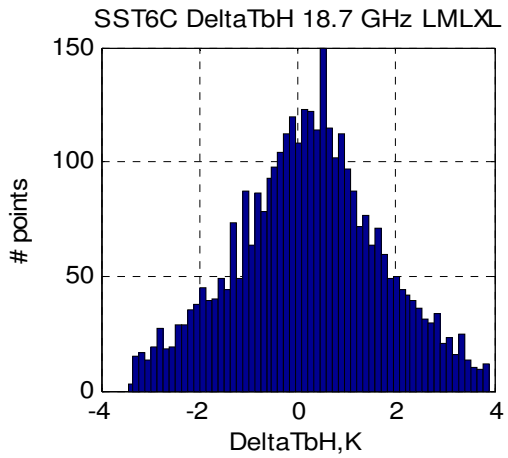
SST6C DeltaTbH 18.7 GHz LMLXL
points
DeltaTbH,K
0
50
100
150
-4
-2
0
2
4

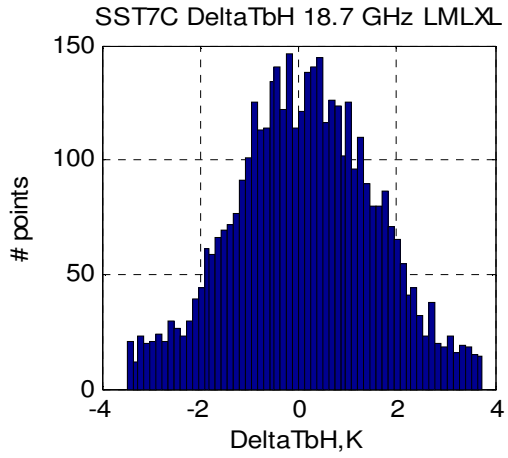
SST7C DeltaTbH 18.7 GHz LMLXL
points
DeltaTbH,K
0
50
100
150
-4
-2
0
2
4

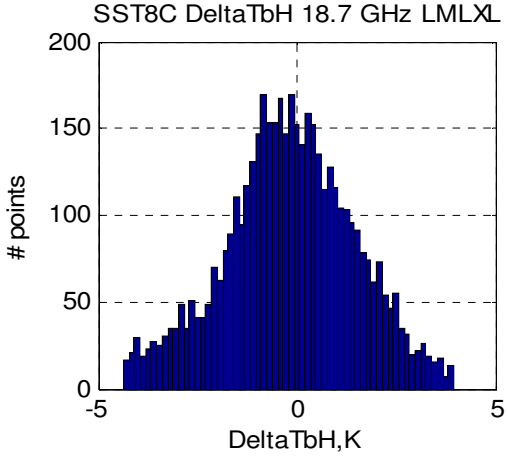
SST8C DeltaTbH 18.7 GHz LMLXL
points
DeltaTbH,K
0
50
100
150
200
-5
0
5

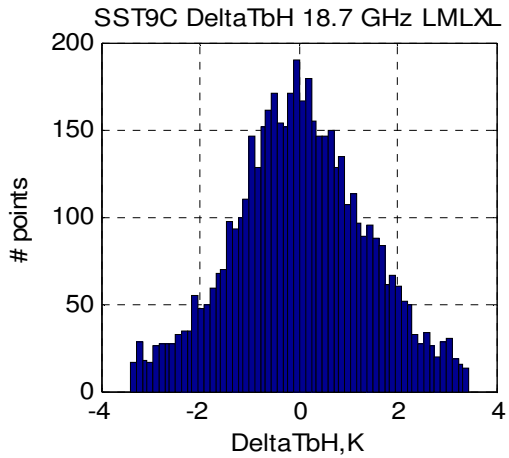
SST9C DeltaTbH 18.7 GHz LMLXL
points
DeltaTbH,K
0
50
100
150
200
-4
-2
0
2
4

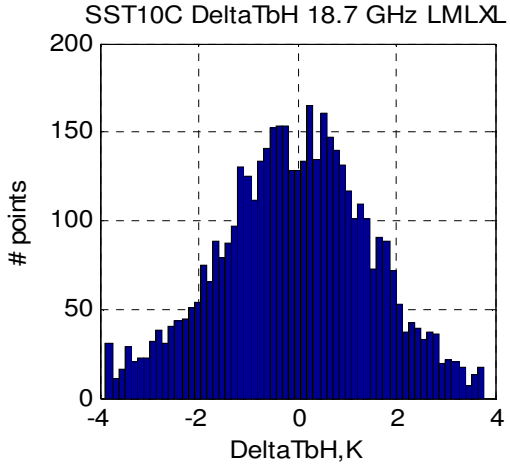
SST10C DeltaTbH 18.7 GHz LMLXL
points
DeltaTbH,K
0
50
100
150
200
-4
-2
0
2
4

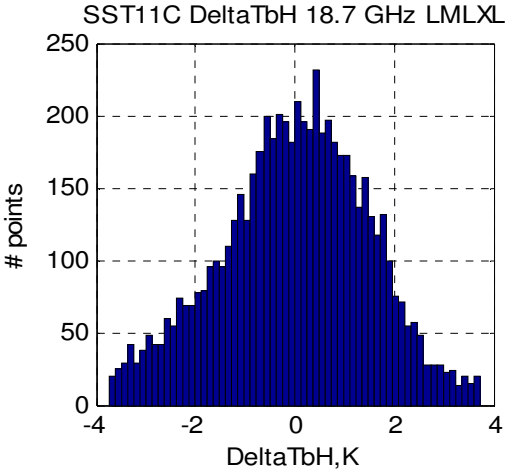
SST11C DeltaTbH 18.7 GHz LMLXL
points
DeltaTbH,K
0
50
100
150
200
250
-4
-2
0
2
4

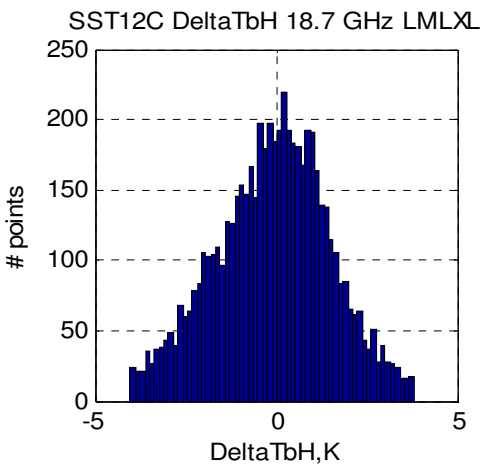
SST12C DeltaTbH 18.7 GHz LMLXL
points
DeltaTbH,K

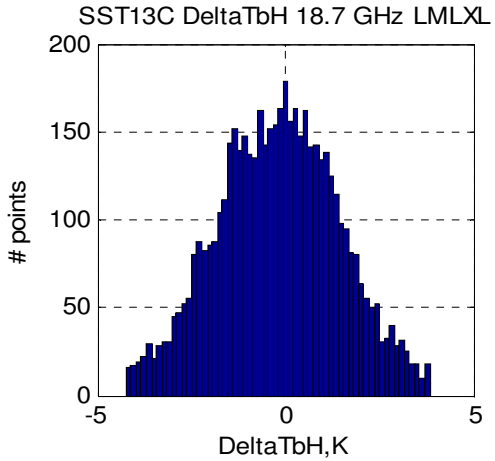
SST13C DeltaTbH 18.7 GHz LMLXL
points
DeltaTbH,K

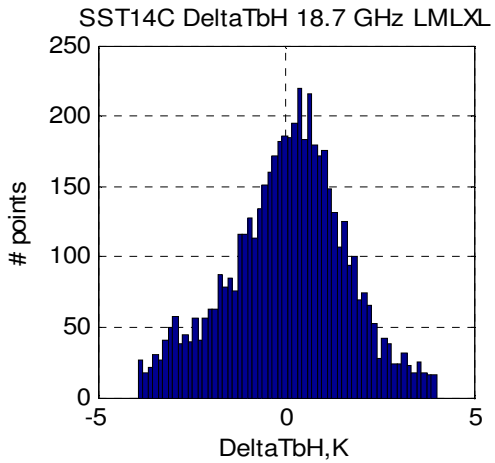
SST14C DeltaTbH 18.7 GHz LMLXL
points
DeltaTbH,K

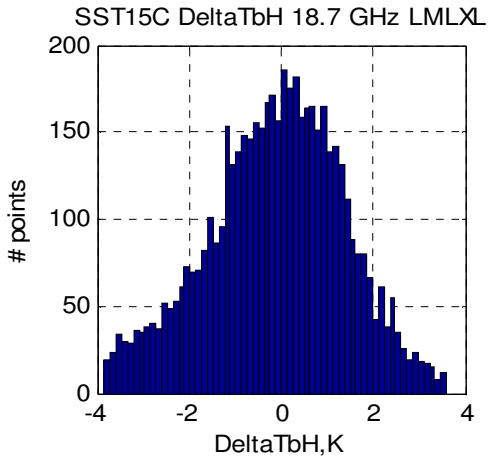
SST15C DeltaTbH 18.7 GHz LMLXL
points
DeltaTbH,K

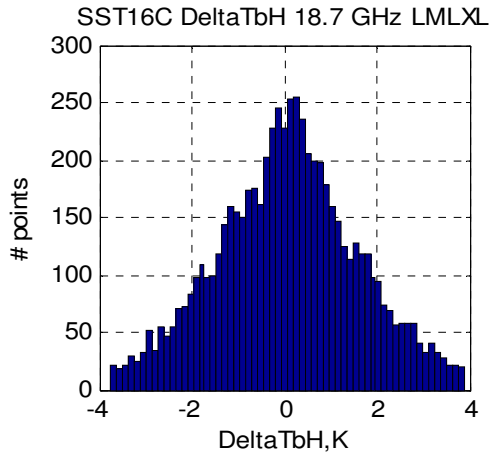
SST16C DeltaTbH 18.7 GHz LMLXL
points
DeltaTbH,K

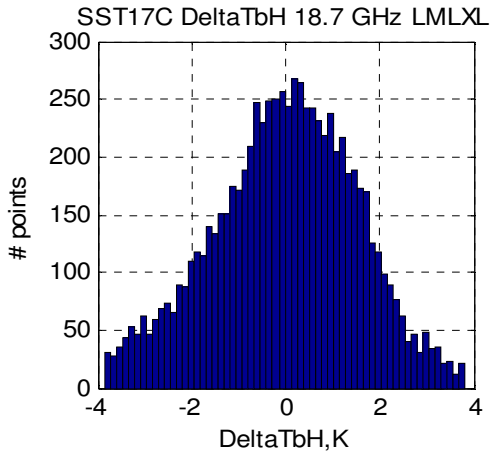
SST17C DeltaTbH 18.7 GHz LMLXL
points
DeltaTbH,K

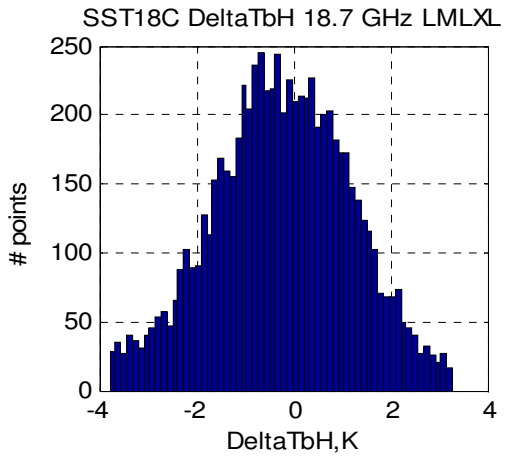
SST18C DeltaTbH 18.7 GHz LMLXL
points
DeltaTbH,K

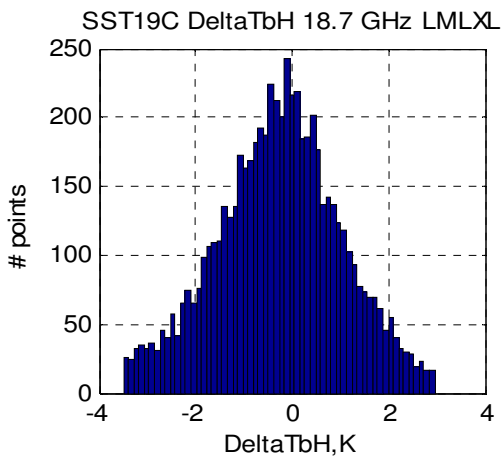
SST19C DeltaTbH 18.7 GHz LMLXL
points
DeltaTbH,K

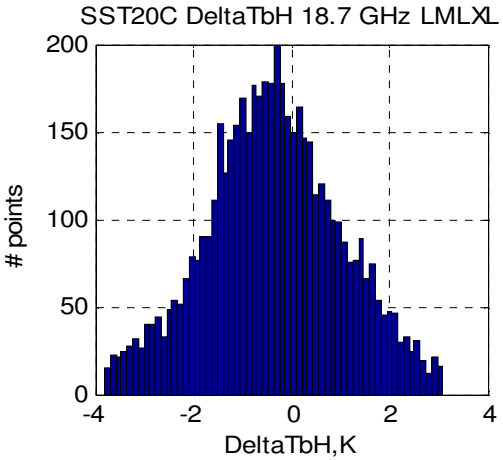
SST20C DeltaTbH 18.7 GHz LMLXL
points
DeltaTbH,K

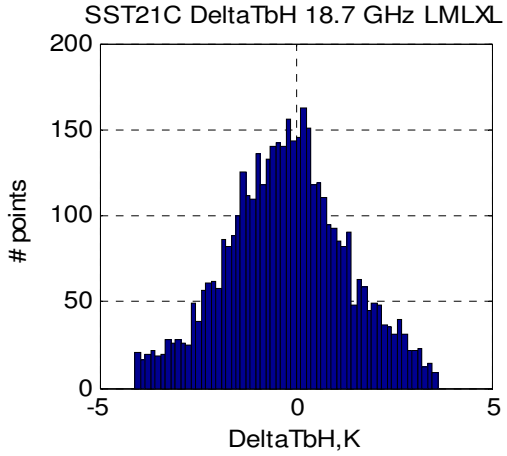
SST21C DeltaTbH 18.7 GHz LMLXL
points
DeltaTbH,K

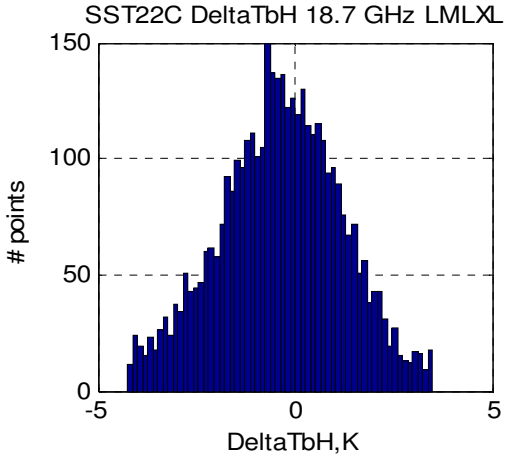
SST22C DeltaTbH 18.7 GHz LMLXL
points
DeltaTbH,K

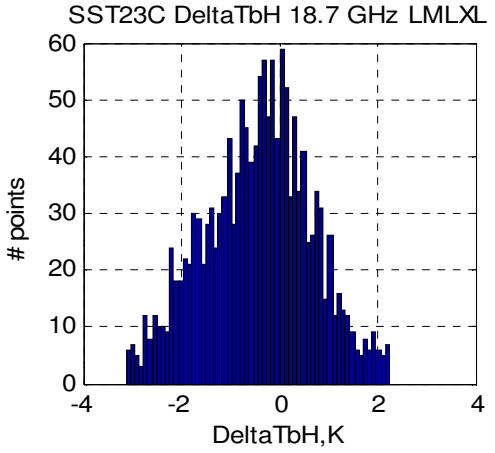
SST23C DeltaTbH 18.7 GHz LMLXL
points
DeltaTbH,K

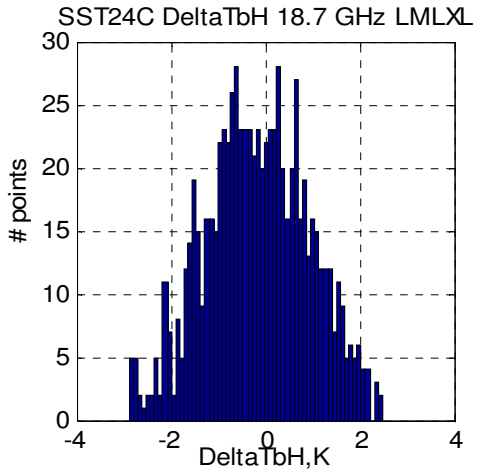
SST24C DeltaTbH 18.7 GHz LMLXL
points
DeltaTbH,K
0
5
10
15
20
25
30
-4
-2
0
2
4

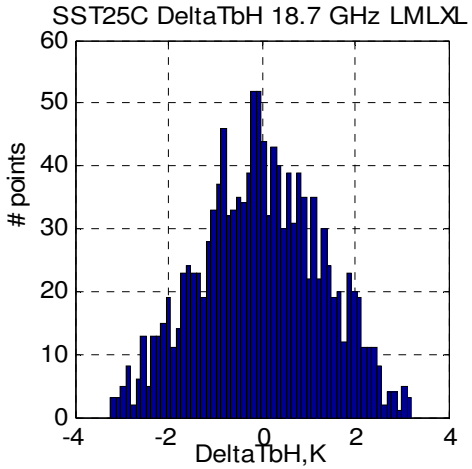
SST25C DeltaTbH 18.7 GHz LMLXL
points
DeltaTbH,K
0
10
20
30
40
50
60
-4
-2
0
2
4

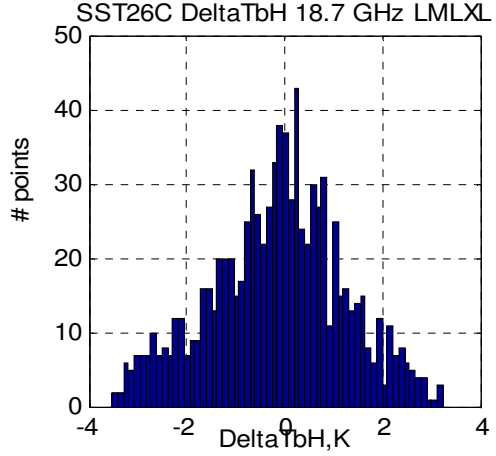
SST26C DeltaTbH 18.7 GHz LMLXL
points
DeltaTbH,K
0
10
20
30
40
50
-4
-2
0
2
4

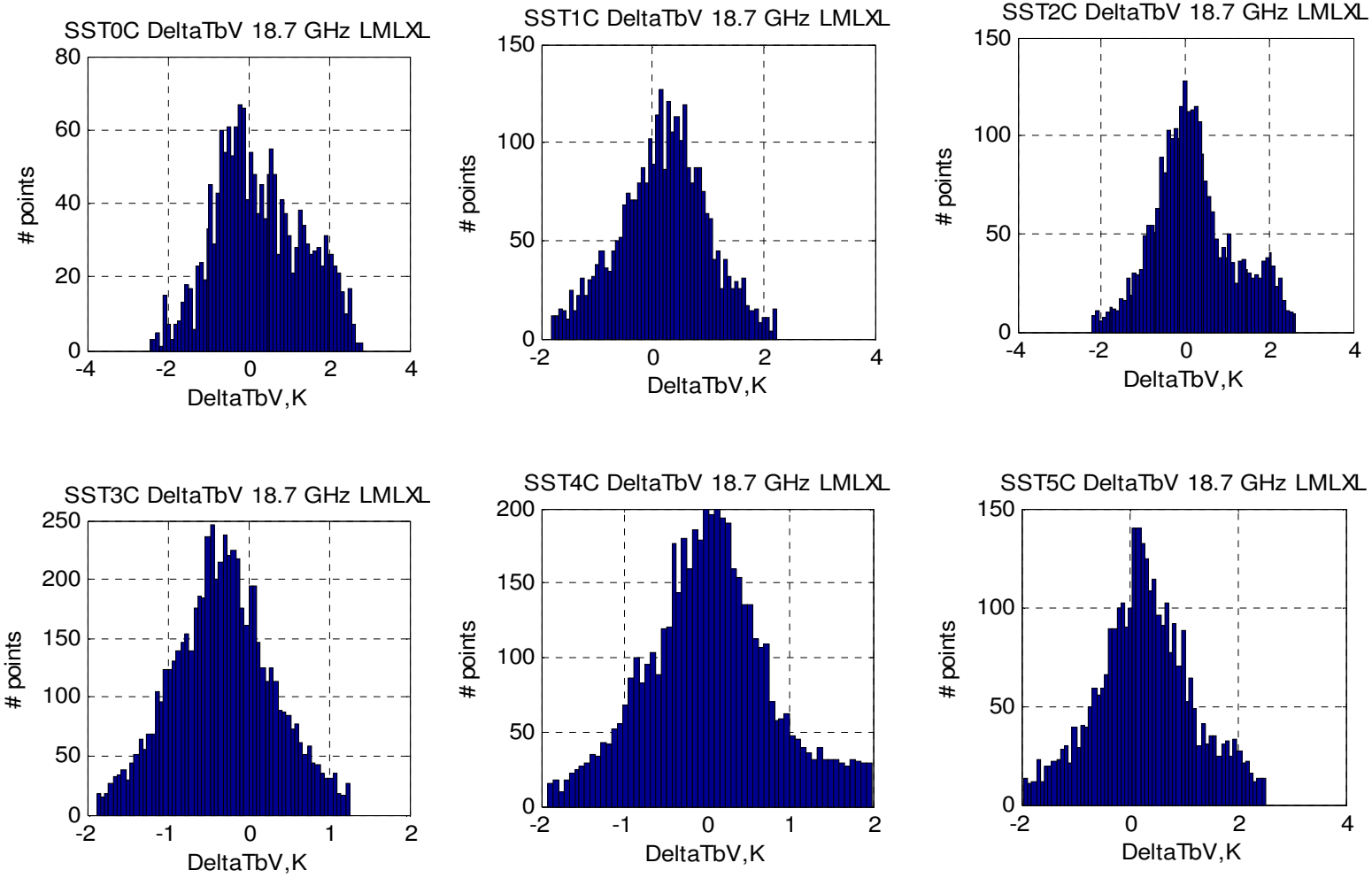
SST0C DeltaTbV 18.7 GHz LMLXL
points
DeltaTbV,K
SST1C DeltaTbV 18.7 GHz LMLXL
points
DeltaTbV,K
SST2C DeltaTbV 18.7 GHz LMLXL
points
DeltaTbV,K
SST3C DeltaTbV 18.7 GHz LMLXL
points
DeltaTbV,K
SST4C DeltaTbV 18.7 GHz LMLXL
points
DeltaTbV,K
SST5C DeltaTbV 18.7 GHz LMLXL
points
DeltaTbV,K

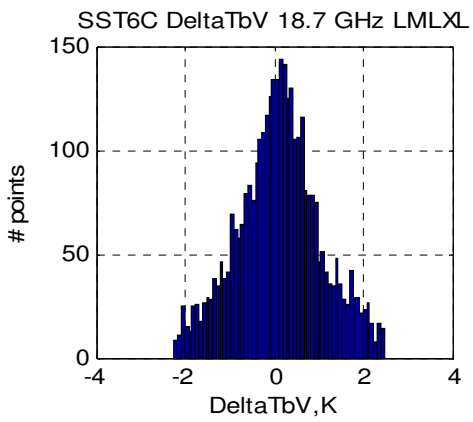
SST6C DeltaTbV 18.7 GHz LMLXL
points
DeltaTbV,K

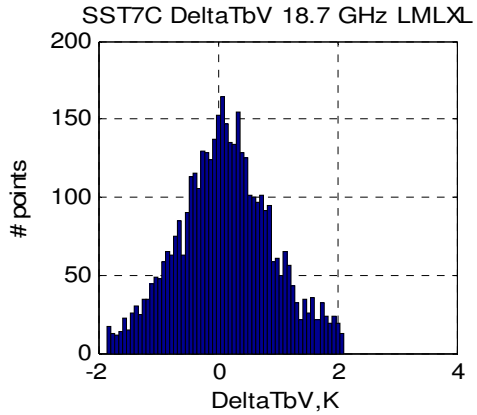
SST7C DeltaTbV 18.7 GHz LMLXL
points
DeltaTbV,K

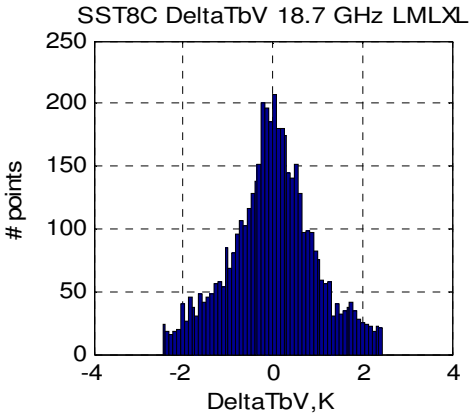
SST8C DeltaTbV 18.7 GHz LMLXL
points
DeltaTbV,K

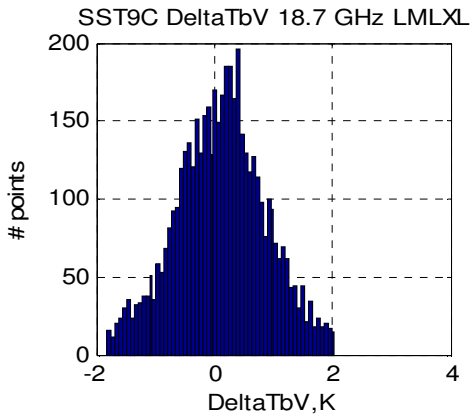
SST9C DeltaTbV 18.7 GHz LMLXL
points
DeltaTbV,K

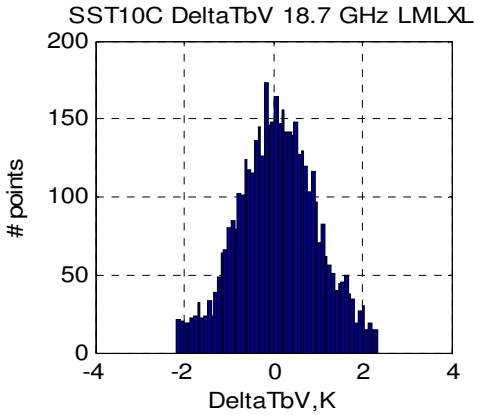
SST10C DeltaTbV 18.7 GHz LMLXL
points
DeltaTbV,K

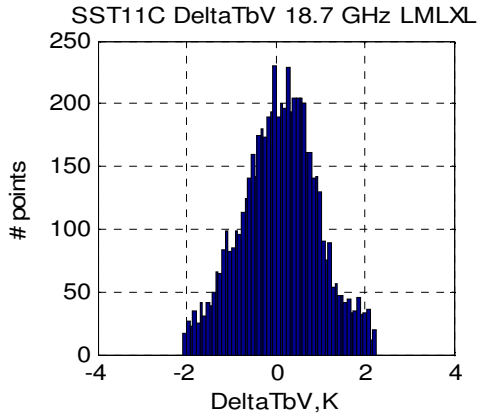
SST11C DeltaTbV 18.7 GHz LMLXL
points
DeltaTbV,K

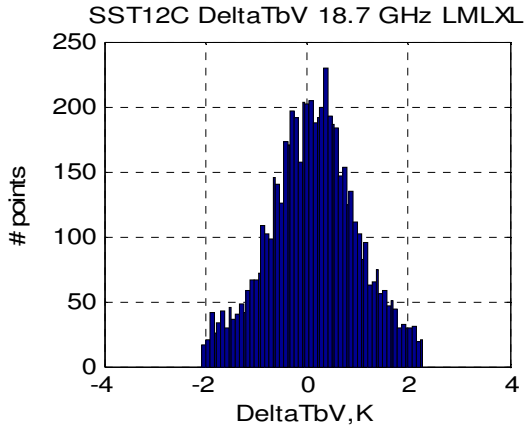
SST12C DeltaTbV 18.7 GHz LMLXL
points
DeltaTbV,K

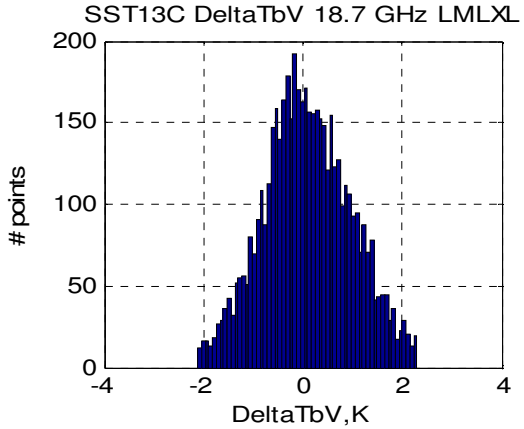
SST13C DeltaTbV 18.7 GHz LMLXL
points
DeltaTbV,K

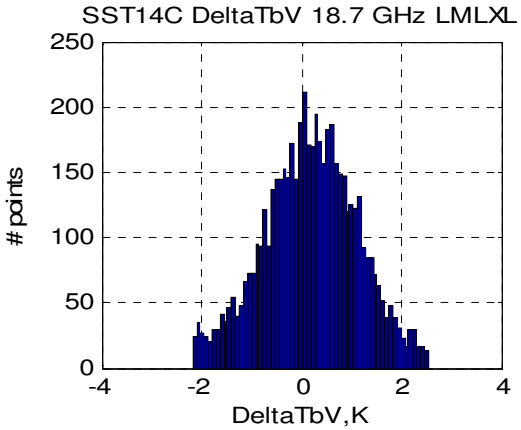
SST14C DeltaTbV 18.7 GHz LMLXL
points
DeltaTbV,K

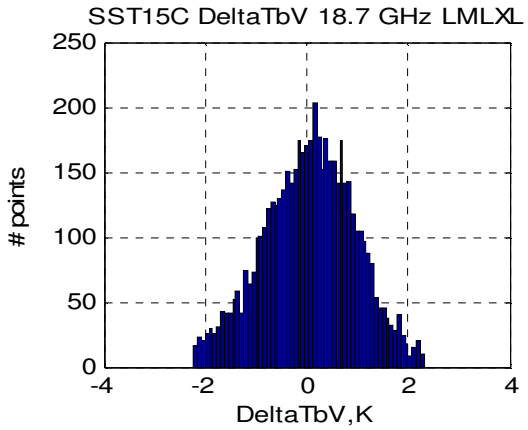
SST15C DeltaTbV 18.7 GHz LMLXL
points
DeltaTbV,K

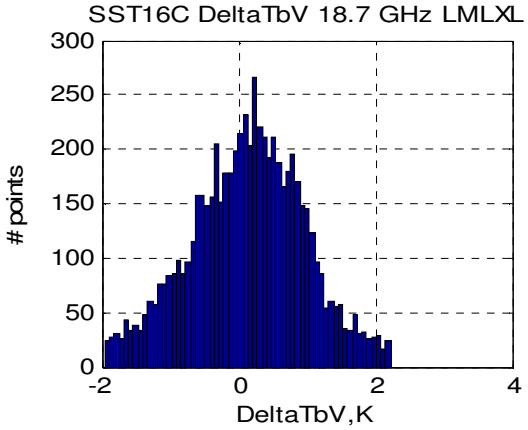
SST16C DeltaTbV 18.7 GHz LMLXL
points
DeltaTbV,K

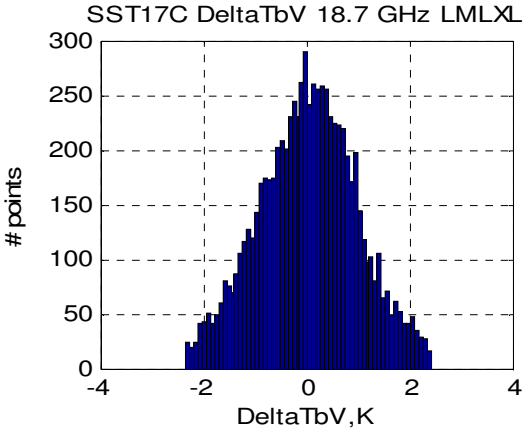
SST17C DeltaTbV 18.7 GHz LMLXL
points
DeltaTbV,K

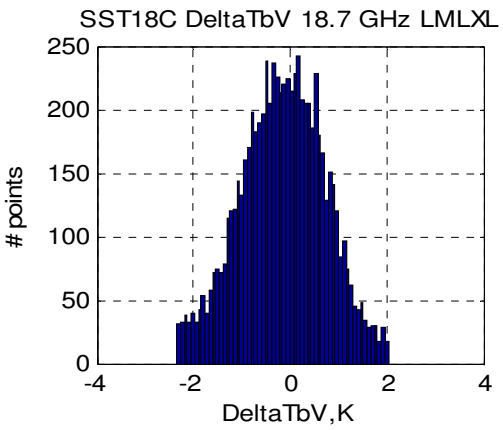
SST18C DeltaTbV 18.7 GHz LMLXL
points
DeltaTbV,K

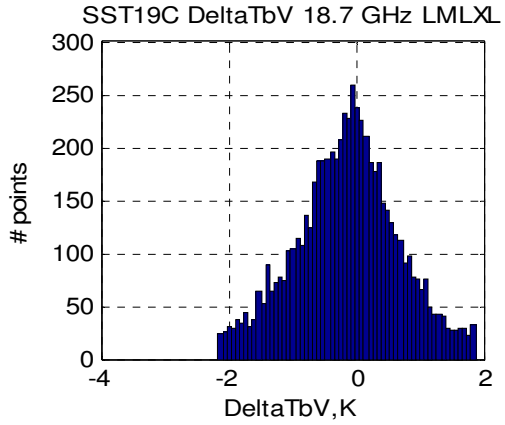
SST19C DeltaTbV 18.7 GHz LMLXL
points
DeltaTbV,K

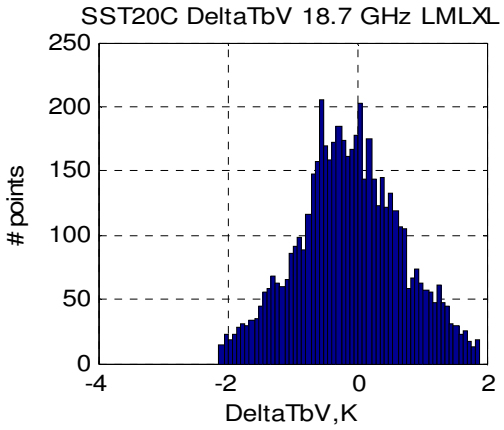
SST20C DeltaTbV 18.7 GHz LMLXL
points
DeltaTbV,K

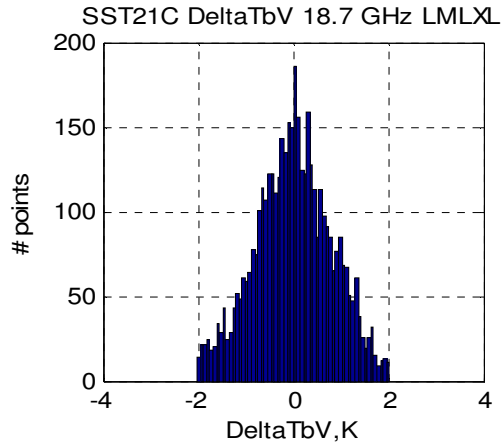
SST21C DeltaTbV 18.7 GHz LMLXL
points
DeltaTbV,K

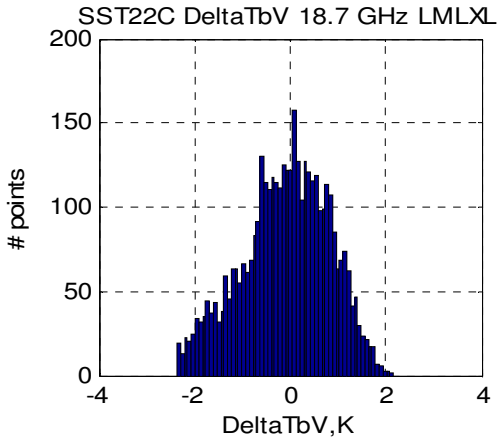
SST22C DeltaTbV 18.7 GHz LMLXL
points
DeltaTbV,K

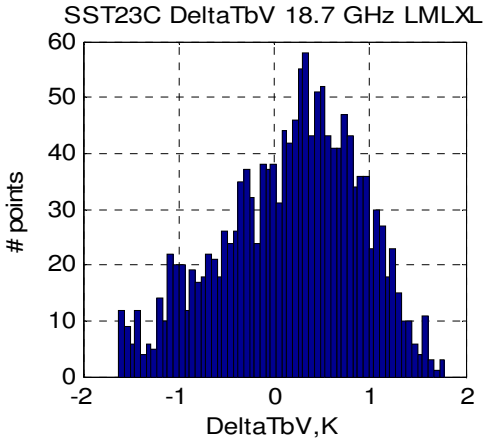
SST23C DeltaTbV 18.7 GHz LMLXL
points
DeltaTbV,K

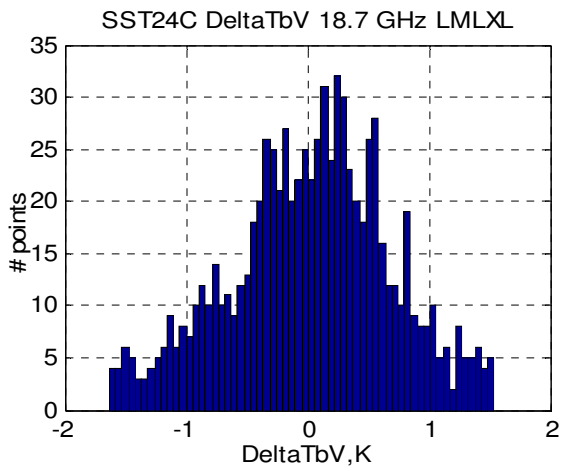
SST24C DeltaTbV 18.7 GHz LMLXL
points
DeltaTbV,K
0
5
10
15
20
25
30
35
-2
-1
0
1
2

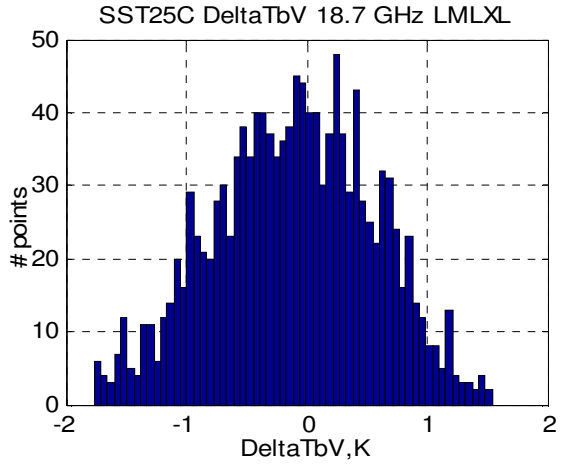
SST25C DeltaTbV 18.7 GHz LMLXL
points
DeltaTbV,K
0
10
20
30
40
50
-2
-1
0
1
2

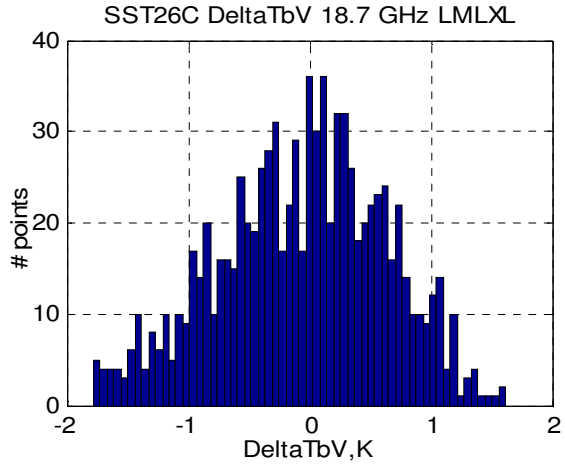
SST26C DeltaTbV 18.7 GHz LMLXL
points
DeltaTbV,K
0
10
20
30
40
-2
-1
0
1
2

18.7 GHZ Descending

At the 18.7 GHz, the following horizontal and vertical descending deltaTb bins with respect to SST were used to generate the polyfit coefficients values for the emissivity correction factor.

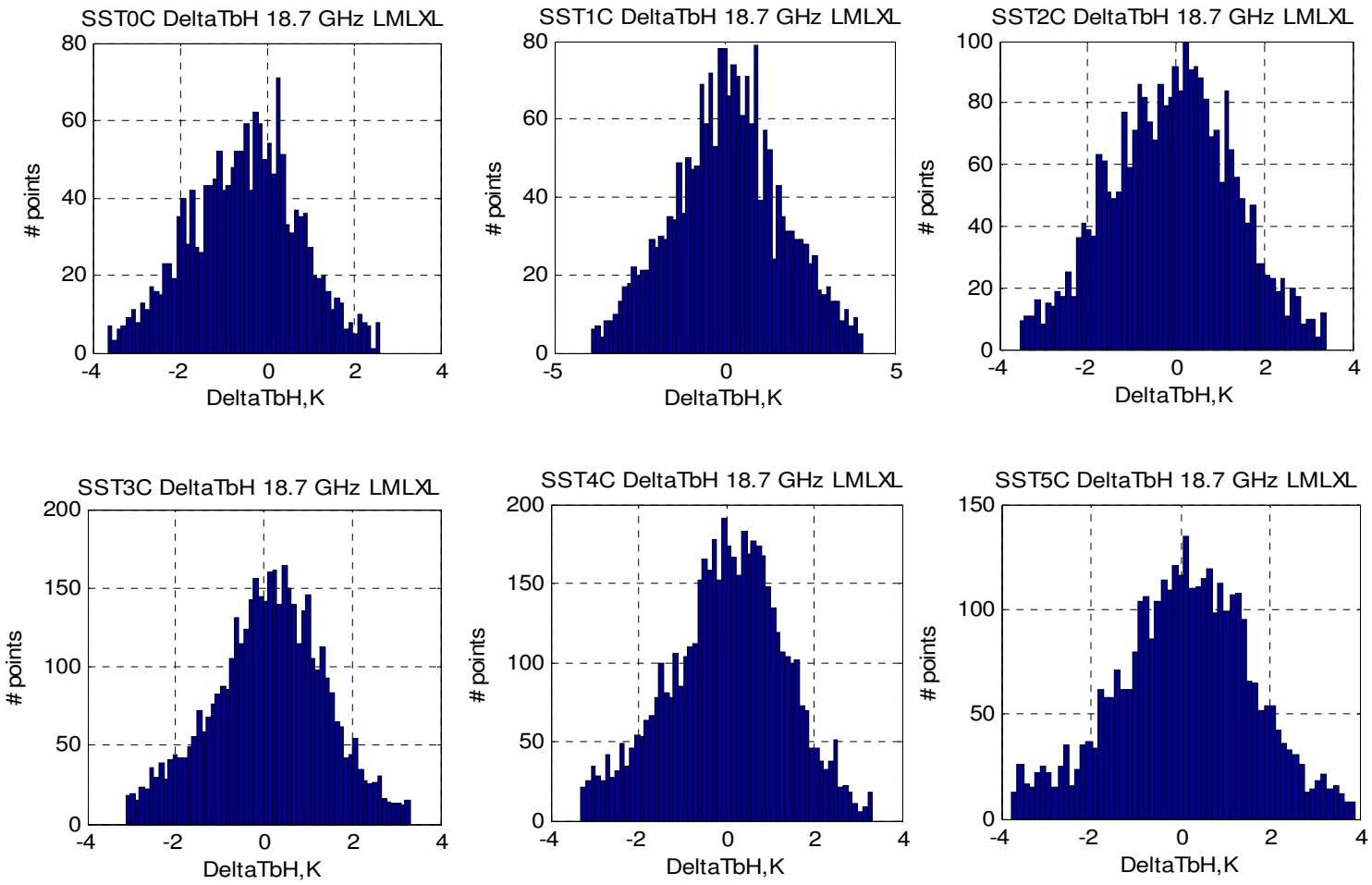
SST0C DeltaTbH 18.7 GHz LMLXL
SST1C DeltaTbH 18.7 GHz LMLXL
SST2C DeltaTbH 18.7 GHz LMLXL
SST3C DeltaTbH 18.7 GHz LMLXL
SST4C DeltaTbH 18.7 GHz LMLXL
SST5C DeltaTbH 18.7 GHz LMLXL
points
DeltaTbH,K

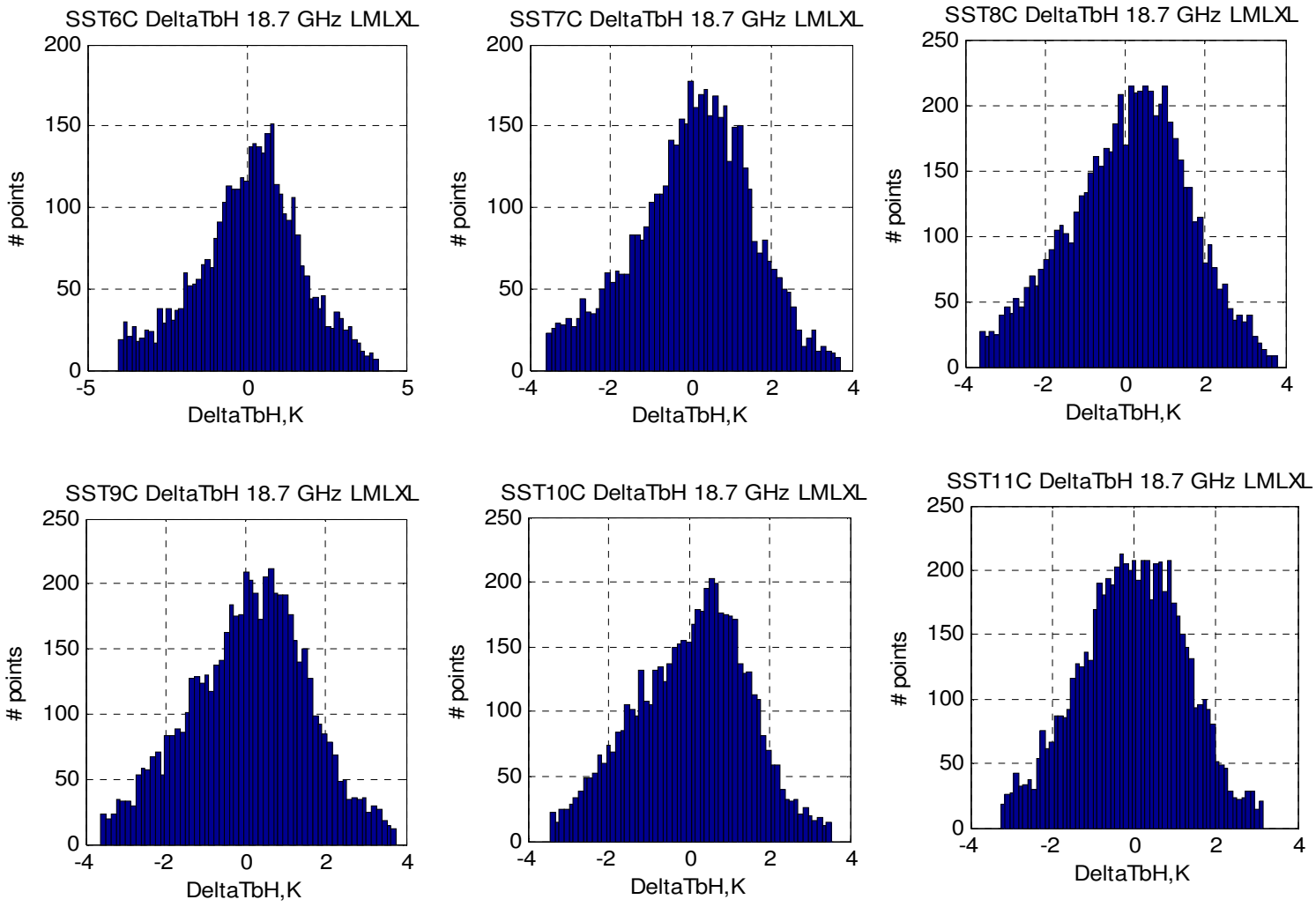
SST6C DeltaTbH 18.7 GHz LMLXL
SST7C DeltaTbH 18.7 GHz LMLXL
SST8C DeltaTbH 18.7 GHz LMLXL
SST9C DeltaTbH 18.7 GHz LMLXL
SST10C DeltaTbH 18.7 GHz LMLXL
SST11C DeltaTbH 18.7 GHz LMLXL
points
DeltaTbH,K

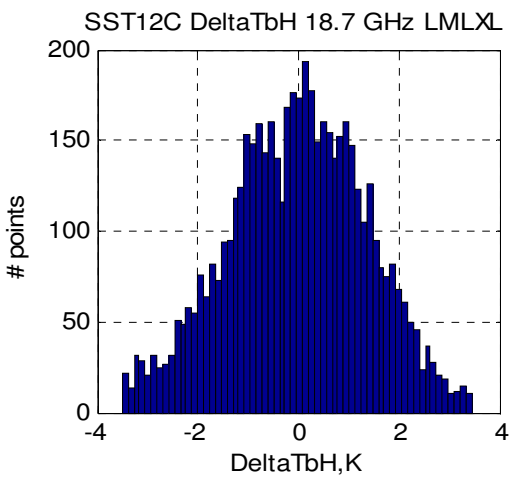
SST12C DeltaTbH 18.7 GHz LMLXL
points
DeltaTbH,K

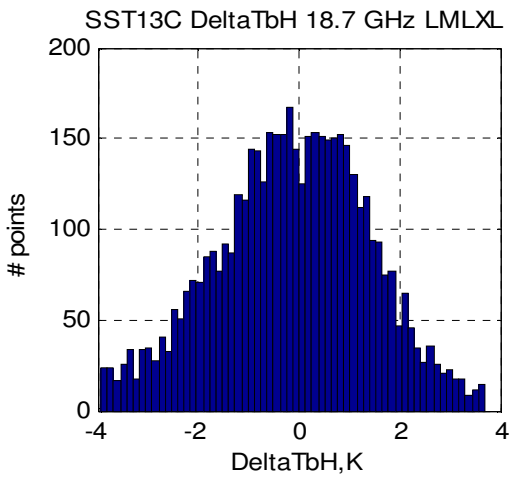
SST13C DeltaTbH 18.7 GHz LMLXL
points
DeltaTbH,K

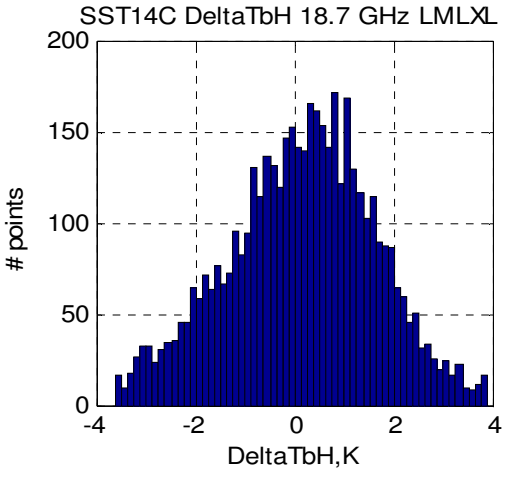
SST14C DeltaTbH 18.7 GHz LMLXL
points
DeltaTbH,K

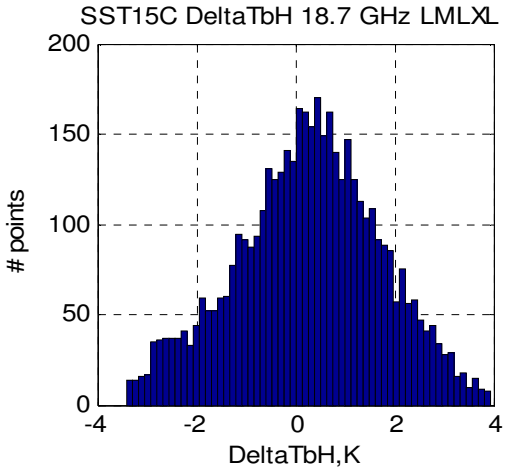
SST15C DeltaTbH 18.7 GHz LMLXL
points
DeltaTbH,K

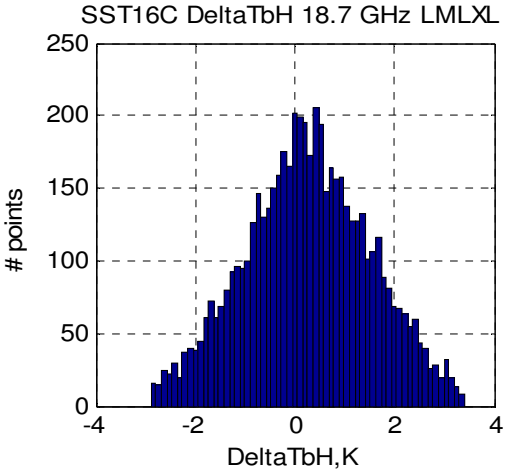
SST16C DeltaTbH 18.7 GHz LMLXL
points
DeltaTbH,K

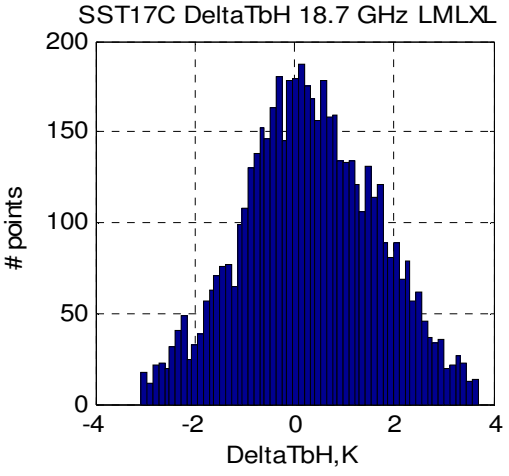
SST17C DeltaTbH 18.7 GHz LMLXL
points
DeltaTbH,K

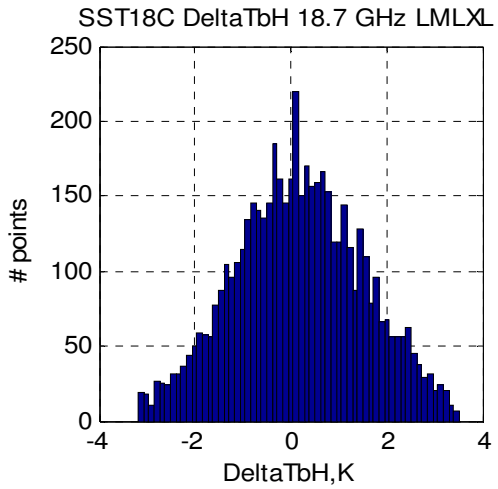
SST18C DeltaTbH 18.7 GHz LMLXL
points
DeltaTbH,K

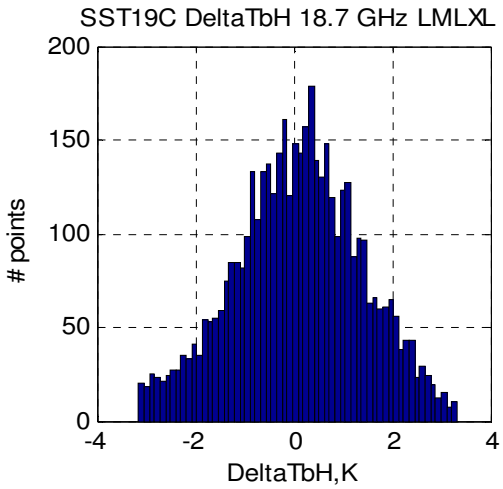
SST19C DeltaTbH 18.7 GHz LMLXL
points
DeltaTbH,K

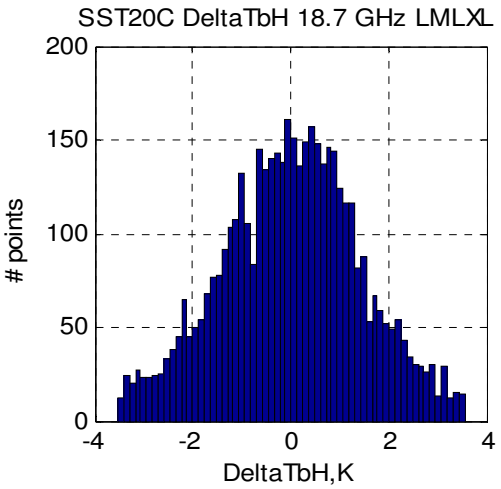
SST20C DeltaTbH 18.7 GHz LMLXL
points
DeltaTbH,K

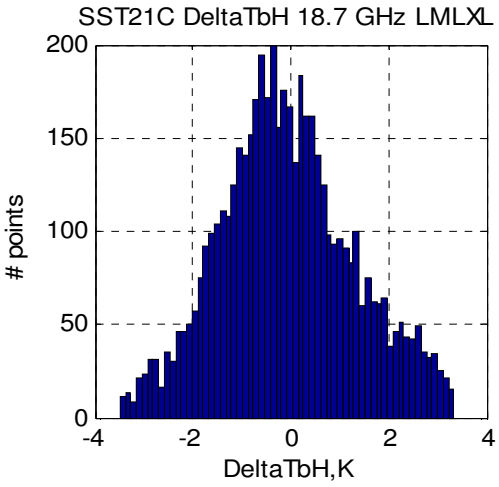
SST21C DeltaTbH 18.7 GHz LMLXL
points
DeltaTbH,K

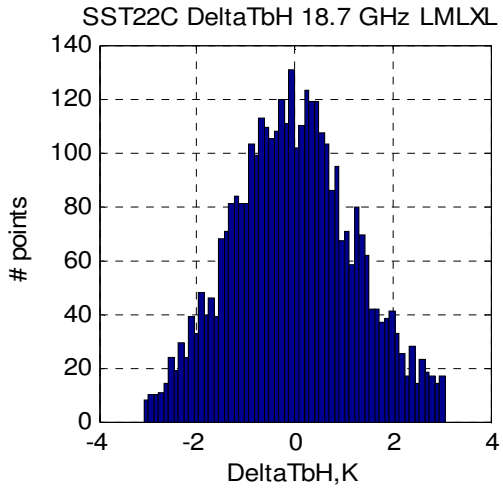
SST22C DeltaTbH 18.7 GHz LMLXL
points
DeltaTbH,K

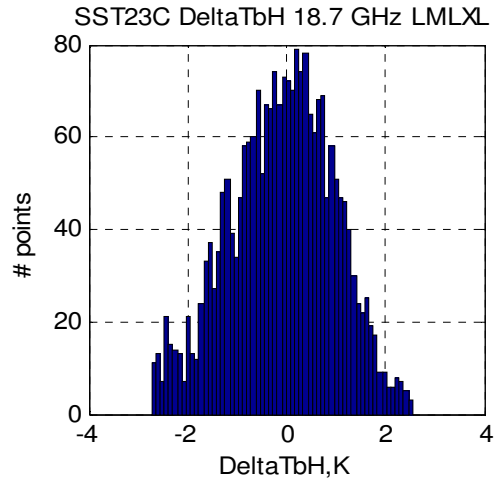
SST23C DeltaTbH 18.7 GHz LMLXL
points
DeltaTbH,K

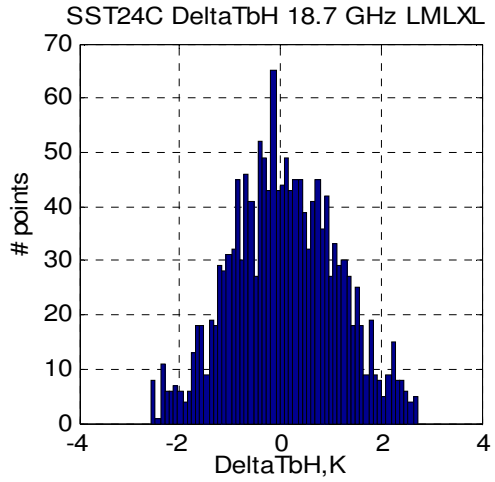
SST24C DeltaTbH 18.7 GHz LMLXL
points
DeltaTbH,K
0
10
20
30
40
50
60
70
-4
-2
0
2
4

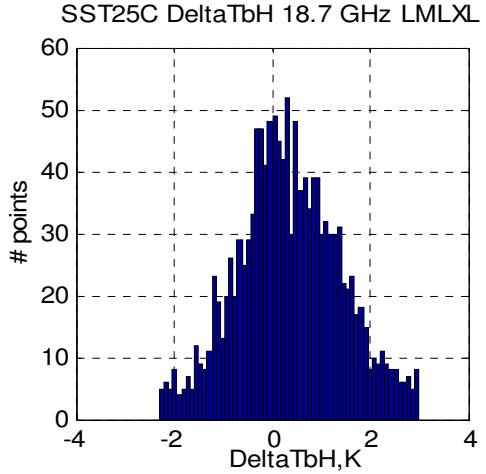
SST25C DeltaTbH 18.7 GHz LMLXL
points
DeltaTbH,K
0
10
20
30
40
50
60
-4
-2
0
2
4

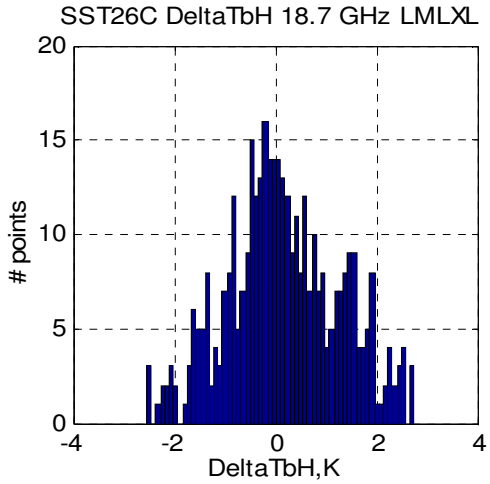
SST26C DeltaTbH 18.7 GHz LMLXL
points
DeltaTbH,K
0
5
10
15
20
-4
-2
0
2
4

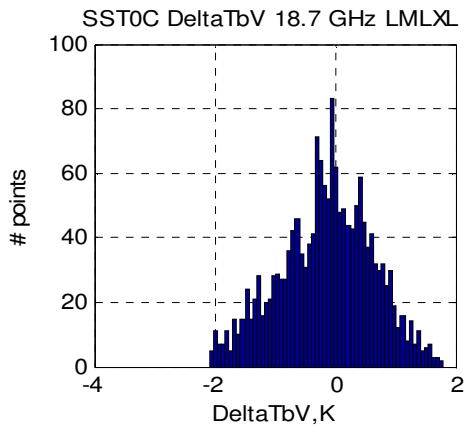
SST0C DeltaTbV 18.7 GHz LMLXL
points
DeltaTbV,K

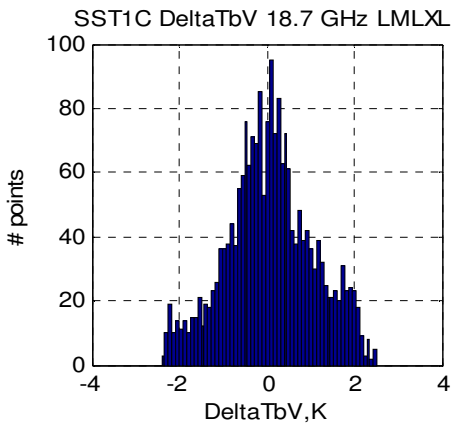
SST1C DeltaTbV 18.7 GHz LMLXL
points
DeltaTbV,K

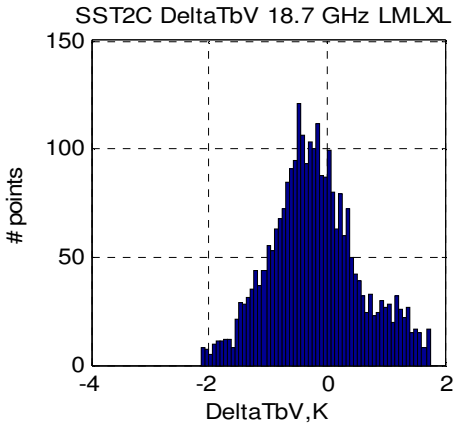
SST2C DeltaTbV 18.7 GHz LMLXL
points
DeltaTbV,K

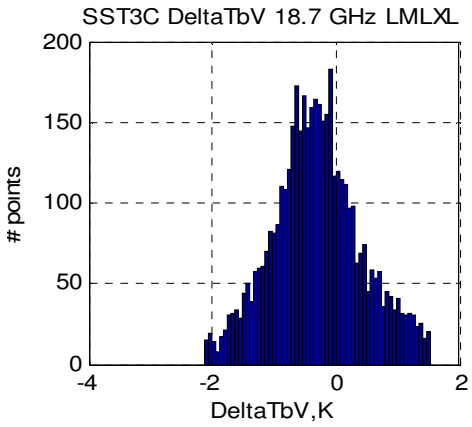
SST3C DeltaTbV 18.7 GHz LMLXL
points
DeltaTbV,K

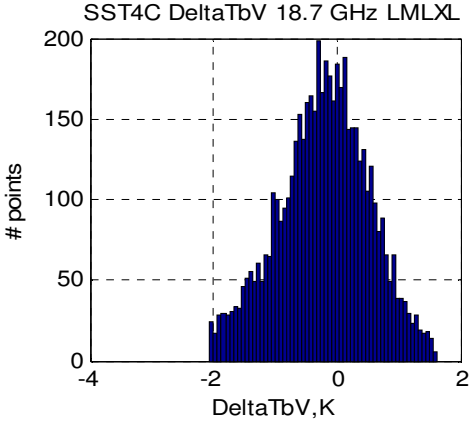
SST4C DeltaTbV 18.7 GHz LMLXL
points
DeltaTbV,K

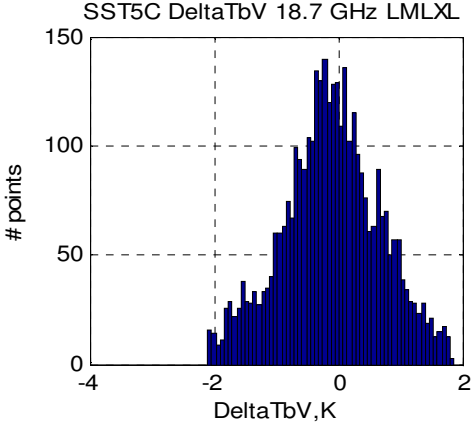
SST5C DeltaTbV 18.7 GHz LMLXL
points
DeltaTbV,K

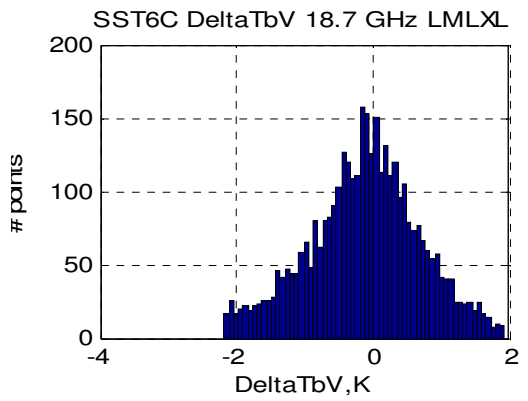
SST6C DeltaTbV 18.7 GHz LMLXL
points
DeltaTbV,K

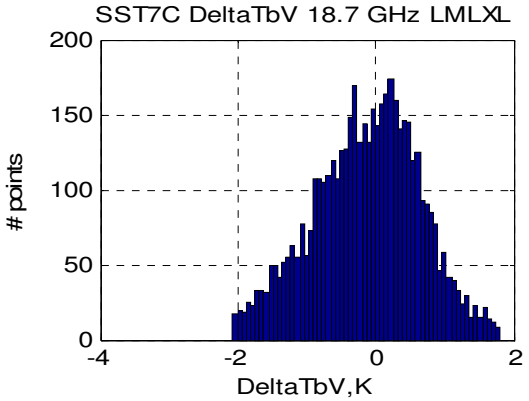
SST7C DeltaTbV 18.7 GHz LMLXL
points
DeltaTbV,K

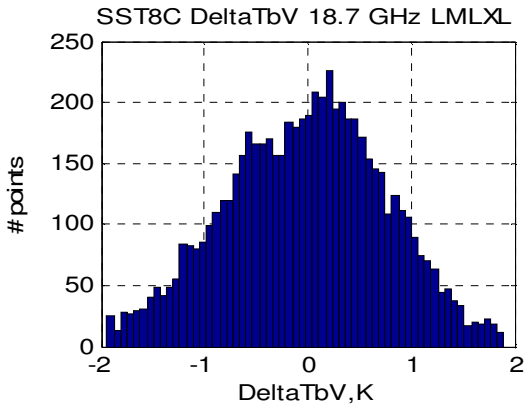
SST8C DeltaTbV 18.7 GHz LMLXL
points
DeltaTbV,K

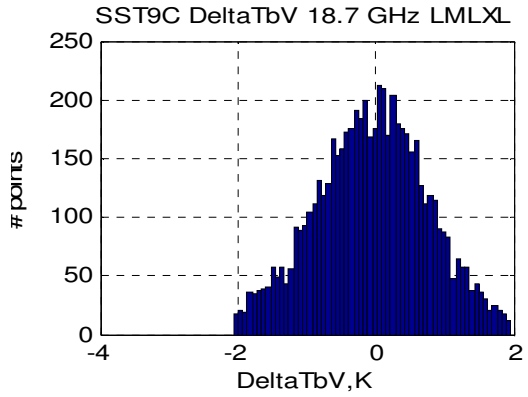
SST9C DeltaTbV 18.7 GHz LMLXL
points
DeltaTbV,K

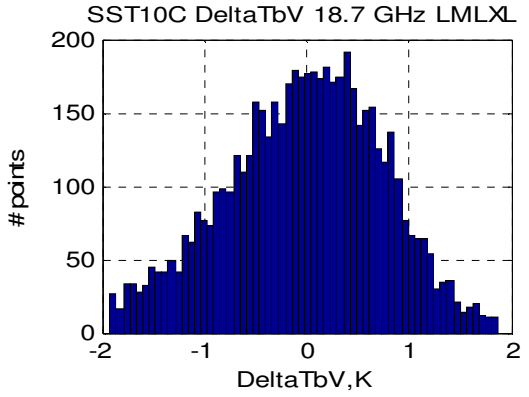
SST10C DeltaTbV 18.7 GHz LMLXL
points
DeltaTbV,K

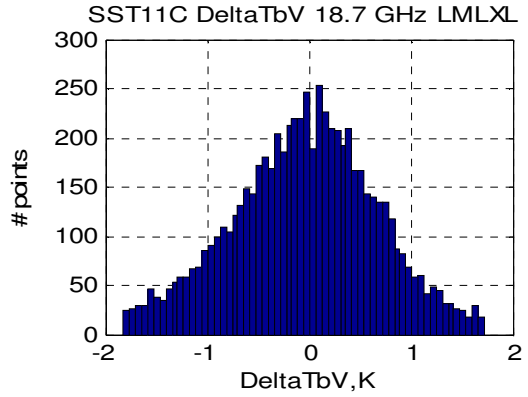
SST11C DeltaTbV 18.7 GHz LMLXL
points
DeltaTbV,K

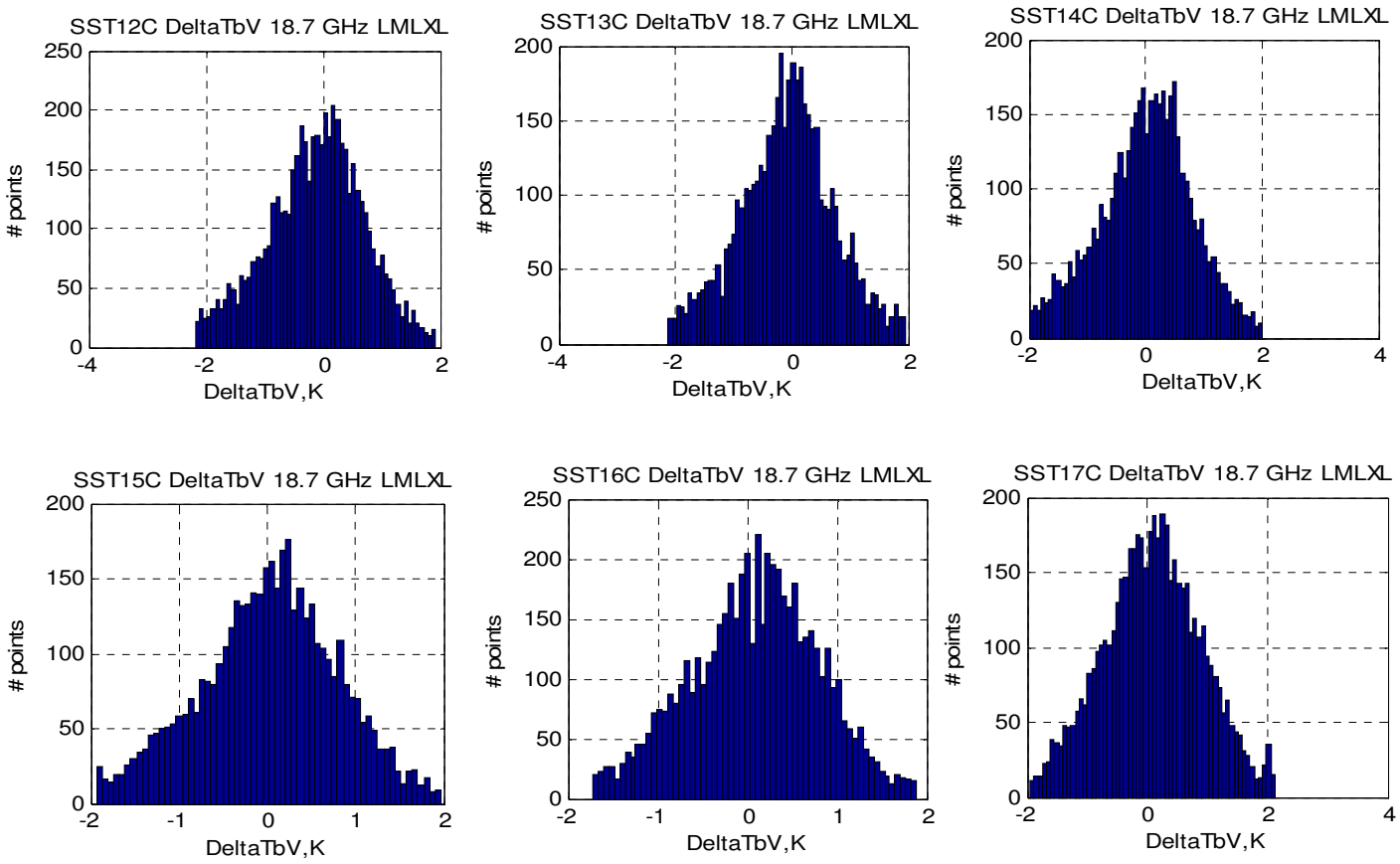
SST12C DeltaTbV 18.7 GHz LMLXL
SST13C DeltaTbV 18.7 GHz LMLXL
SST14C DeltaTbV 18.7 GHz LMLXL
SST15C DeltaTbV 18.7 GHz LMLXL
SST16C DeltaTbV 18.7 GHz LMLXL
SST17C DeltaTbV 18.7 GHz LMLXL
points
DeltaTbV,K

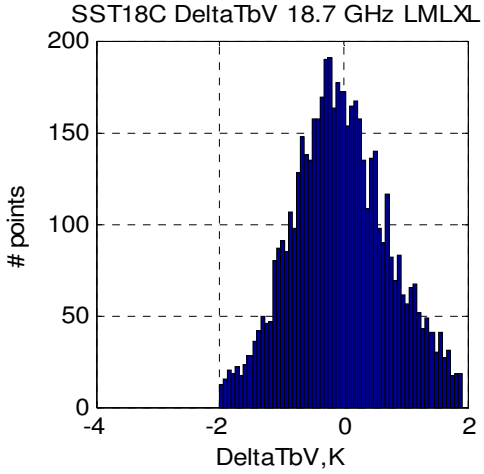
SST18C DeltaTbV 18.7 GHz LMLXL
points
DeltaTbV,K

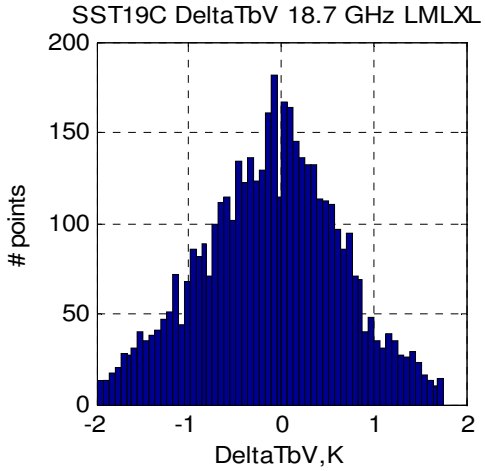
SST19C DeltaTbV 18.7 GHz LMLXL
points
DeltaTbV,K

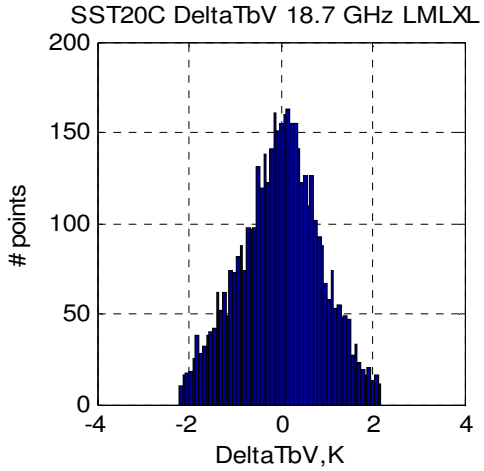
SST20C DeltaTbV 18.7 GHz LMLXL
points
DeltaTbV,K

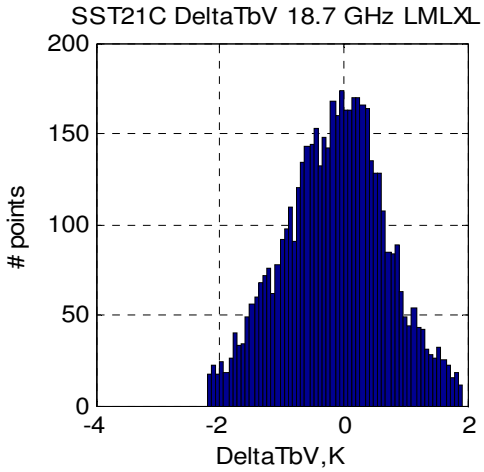
SST21C DeltaTbV 18.7 GHz LMLXL
points
DeltaTbV,K

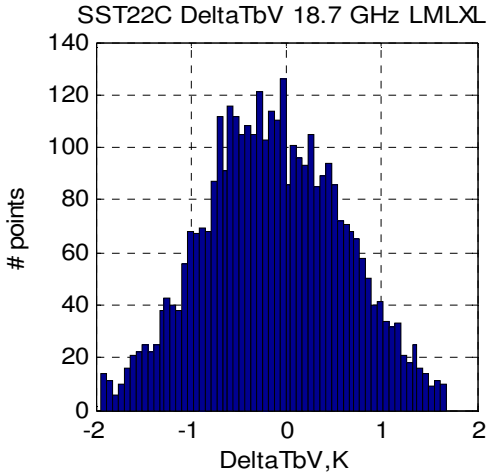
SST22C DeltaTbV 18.7 GHz LMLXL
points
DeltaTbV,K

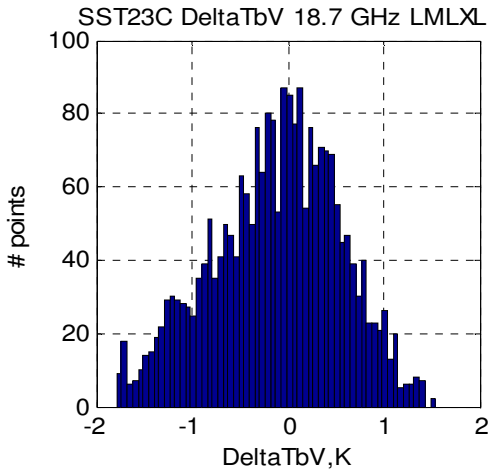
SST23C DeltaTbV 18.7 GHz LMLXL
points
DeltaTbV,K

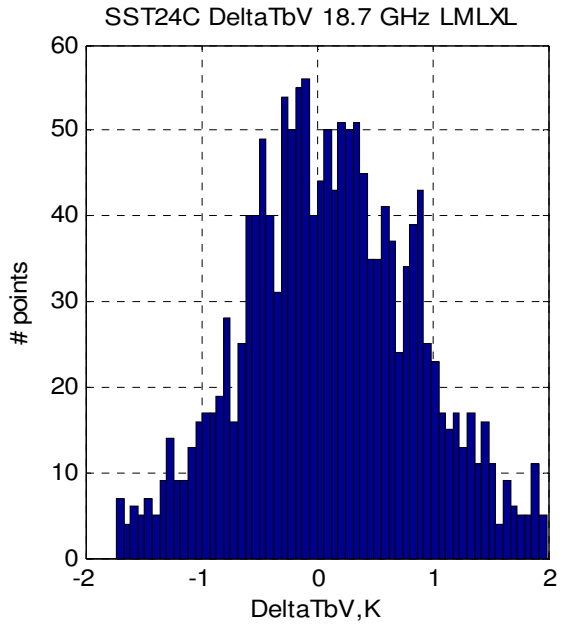
SST24C DeltaTbV 18.7 GHz LMLXL
points
DeltaTbV,K
0
10
20
30
40
50
60
-2
-1
0
1
2

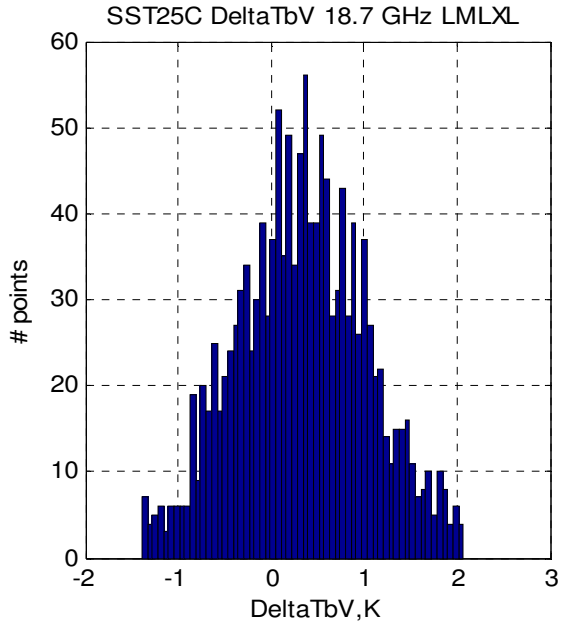
SST25C DeltaTbV 18.7 GHz LMLXL
points
DeltaTbV,K
0
10
20
30
40
50
60
-2
-1
0
1
2
3

37 GHz Ascending

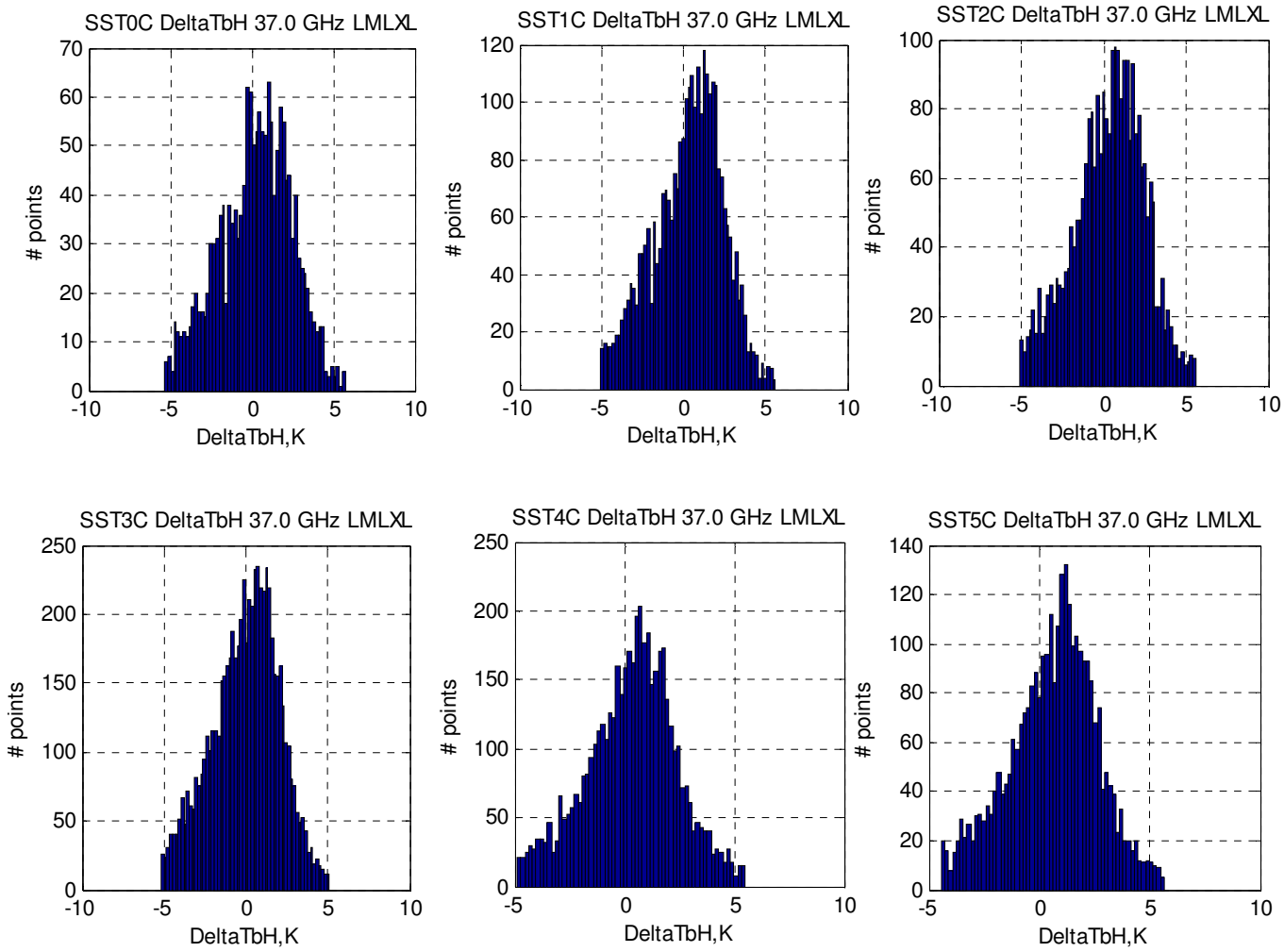
SST0C DeltaTbH 37.0 GHz LMLXL
SST1C DeltaTbH 37.0 GHz LMLXL
SST2C DeltaTbH 37.0 GHz LMLXL
SST3C DeltaTbH 37.0 GHz LMLXL
SST4C DeltaTbH 37.0 GHz LMLXL
SST5C DeltaTbH 37.0 GHz LMLXL
points
DeltaTbH,K

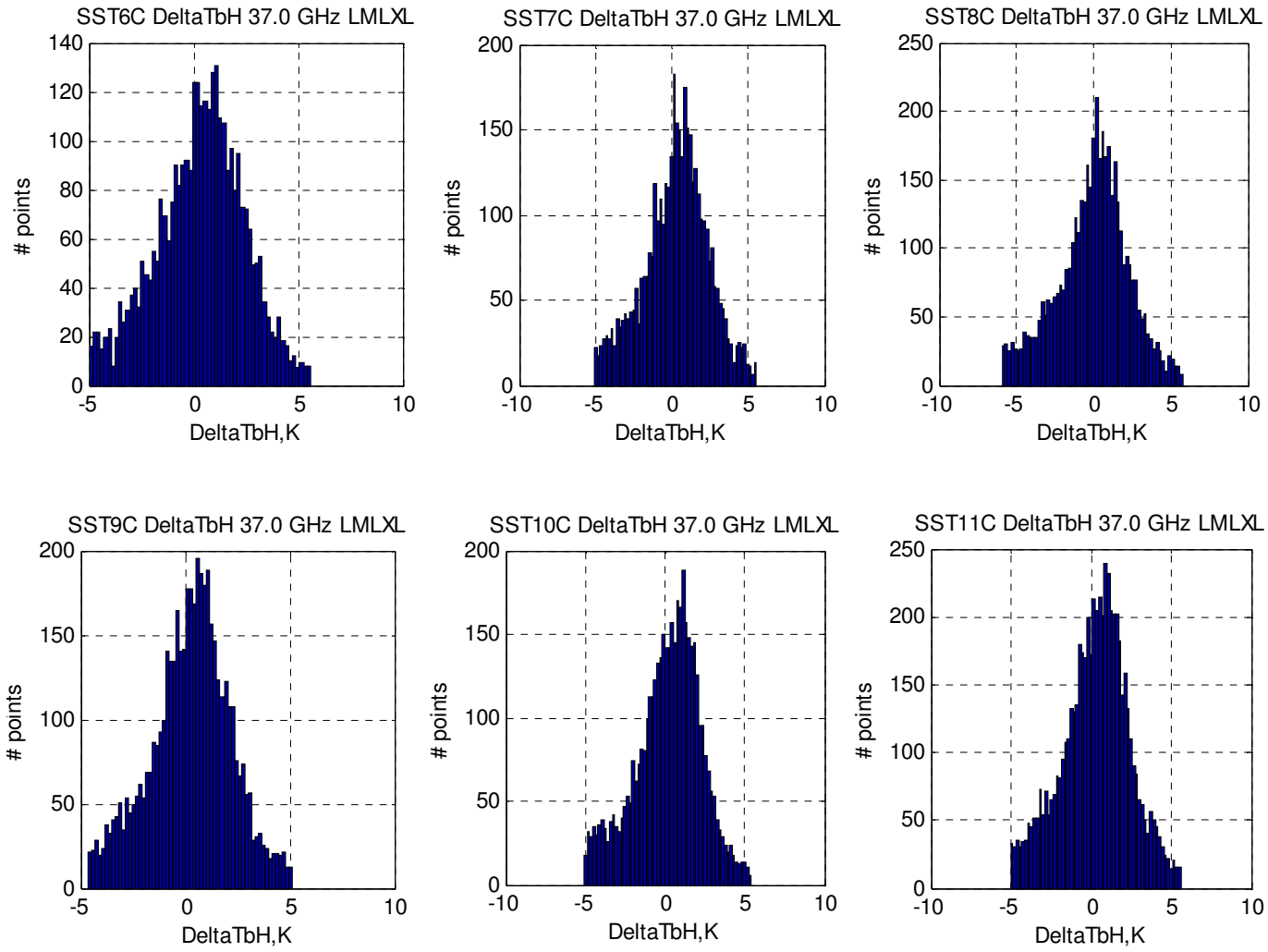
SST6C DeltaTbH 37.0 GHz LMLXL
points
DeltaTbH,K
SST7C DeltaTbH 37.0 GHz LMLXL
points
DeltaTbH,K
SST8C DeltaTbH 37.0 GHz LMLXL
points
DeltaTbH,K
SST9C DeltaTbH 37.0 GHz LMLXL
points
DeltaTbH,K
SST10C DeltaTbH 37.0 GHz LMLXL
points
DeltaTbH,K
SST11C DeltaTbH 37.0 GHz LMLXL
points
DeltaTbH,K

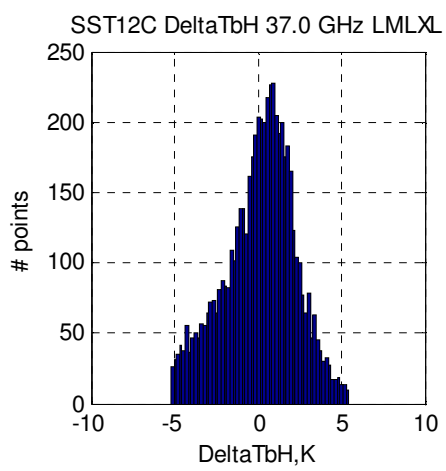
SST12C DeltaTbH 37.0 GHz LMLXL
points
DeltaTbH,K

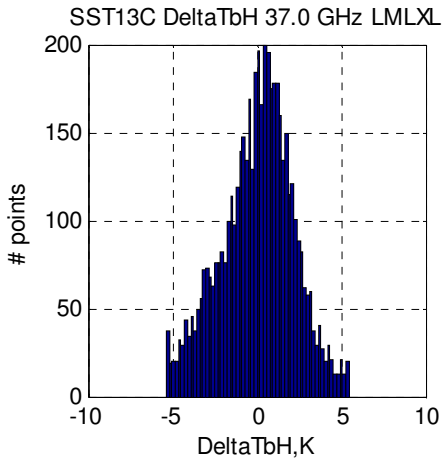
SST13C DeltaTbH 37.0 GHz LMLXL
points
DeltaTbH,K

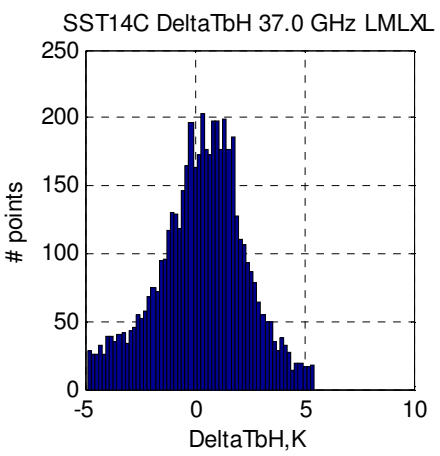
SST14C DeltaTbH 37.0 GHz LMLXL
points
DeltaTbH,K

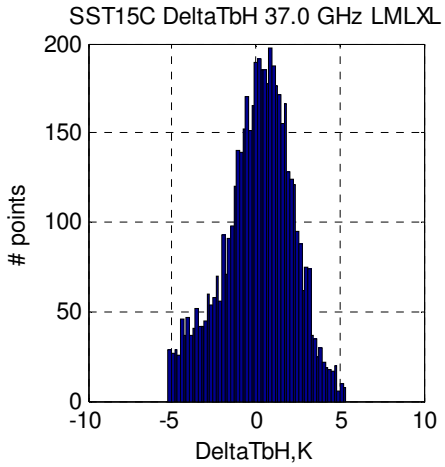
SST15C DeltaTbH 37.0 GHz LMLXL
points
DeltaTbH,K

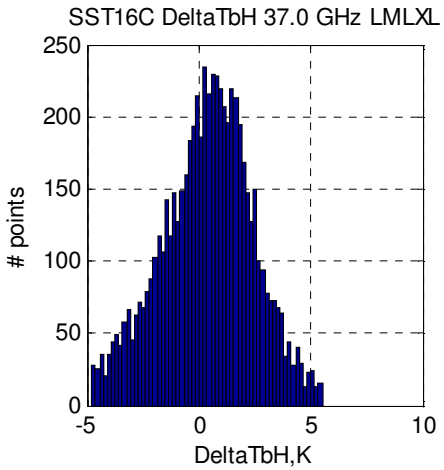
SST16C DeltaTbH 37.0 GHz LMLXL
points
DeltaTbH,K

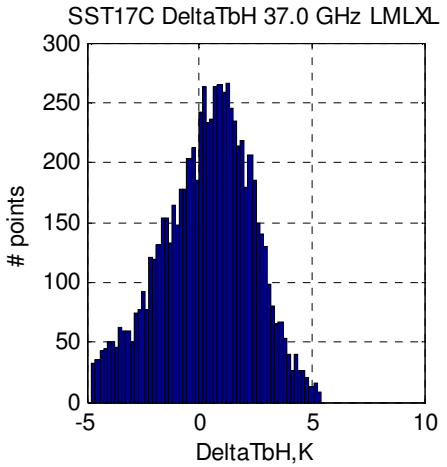
SST17C DeltaTbH 37.0 GHz LMLXL
points
DeltaTbH,K

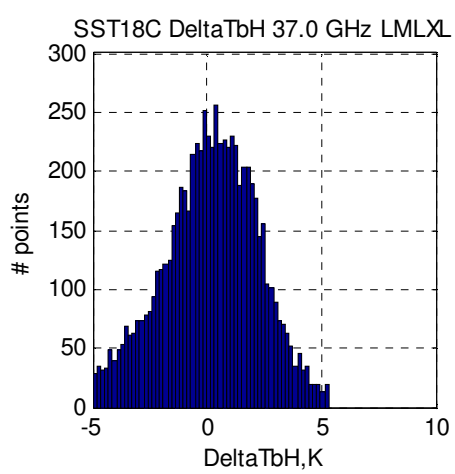
SST18C DeltaTbH 37.0 GHz LMLXL
points
DeltaTbH,K

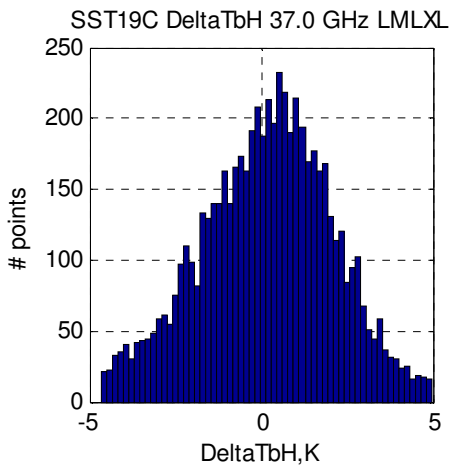
SST19C DeltaTbH 37.0 GHz LMLXL
points
DeltaTbH,K

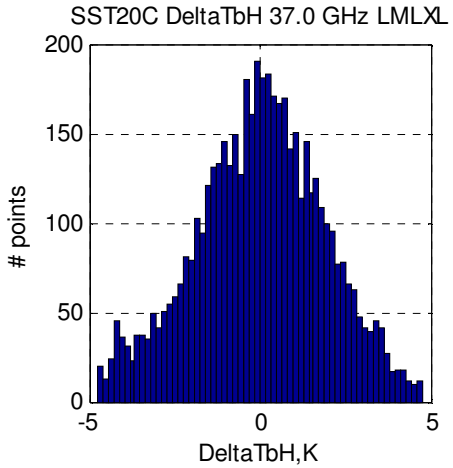
SST20C DeltaTbH 37.0 GHz LMLXL
points
DeltaTbH,K

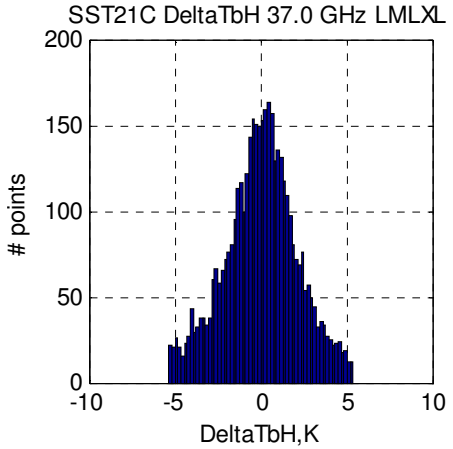
SST21C DeltaTbH 37.0 GHz LMLXL
points
DeltaTbH,K

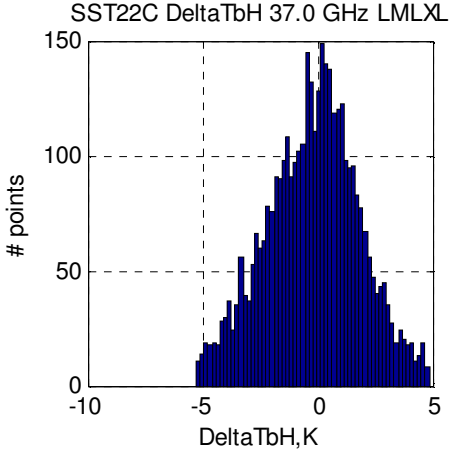
SST22C DeltaTbH 37.0 GHz LMLXL
points
DeltaTbH,K

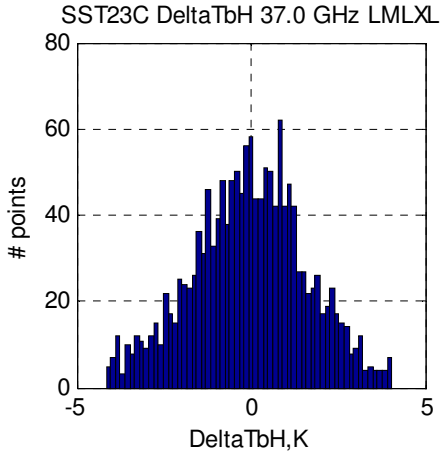
SST23C DeltaTbH 37.0 GHz LMLXL
points
DeltaTbH,K

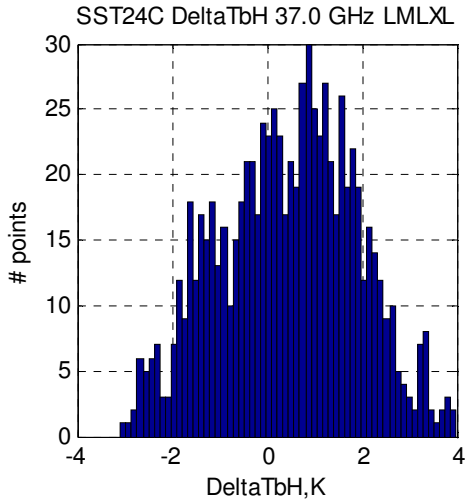
SST24C DeltaTbH 37.0 GHz LMLXL
points
DeltaTbH,K
30
25
20
15
10
5
0
-4
-2
0
2
4

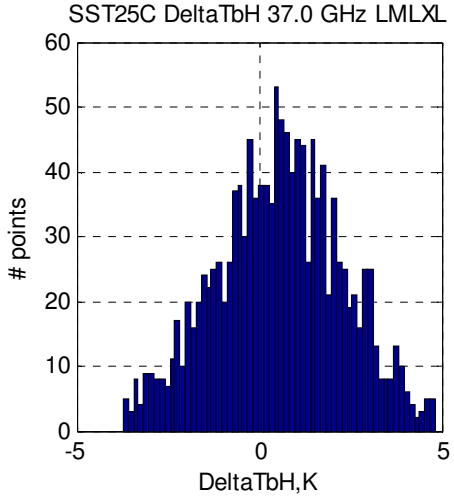
SST25C DeltaTbH 37.0 GHz LMLXL
points
DeltaTbH,K
60
50
40
30
20
10
0
-5
0
5

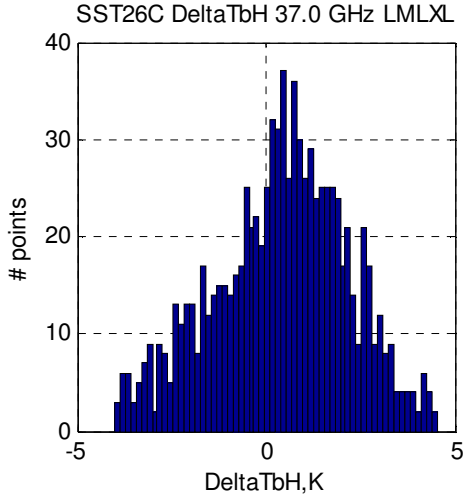
SST26C DeltaTbH 37.0 GHz LMLXL
points
DeltaTbH,K
40
30
20
10
0
-5
0
5

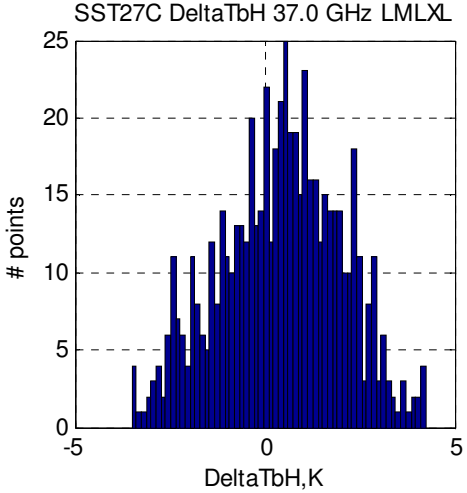
SST27C DeltaTbH 37.0 GHz LMLXL
points
DeltaTbH,K
25
20
15
10
5
0
-5
0
5

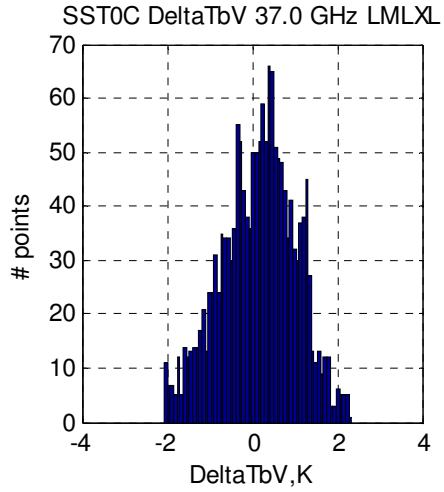
SST0C DeltaTbV 37.0 GHz LMLXL
points
DeltaTbV,K

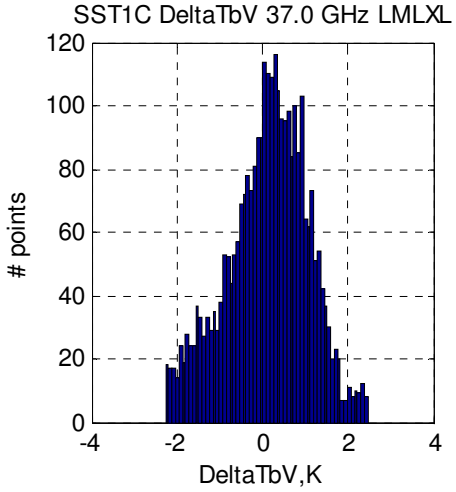
SST1C DeltaTbV 37.0 GHz LMLXL
points
DeltaTbV,K

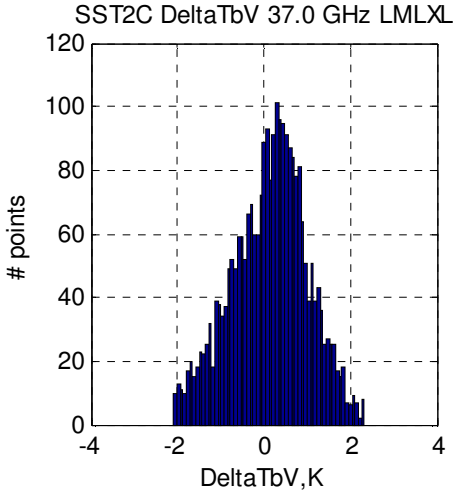
SST2C DeltaTbV 37.0 GHz LMLXL
points
DeltaTbV,K

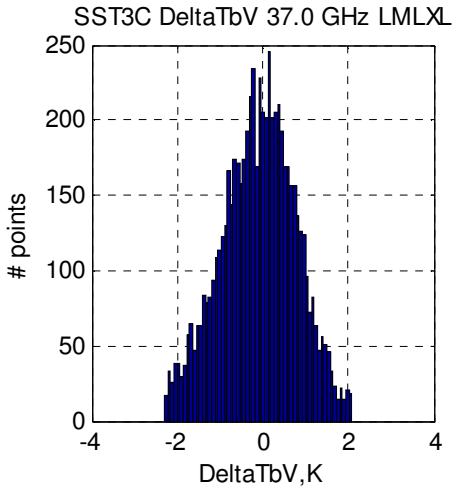
SST3C DeltaTbV 37.0 GHz LMLXL
points
DeltaTbV,K

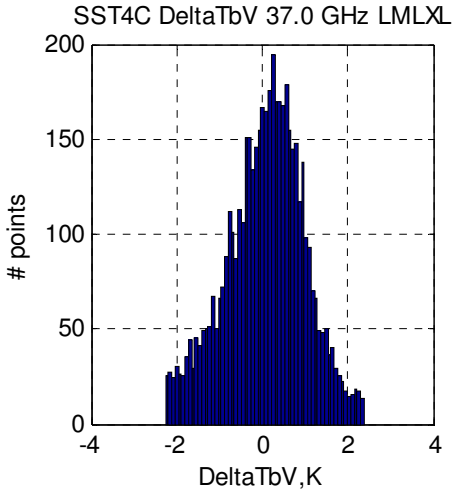
SST4C DeltaTbV 37.0 GHz LMLXL
points
DeltaTbV,K

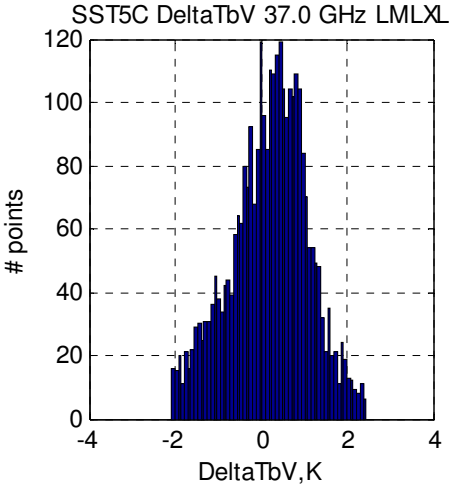
SST5C DeltaTbV 37.0 GHz LMLXL
points
DeltaTbV,K

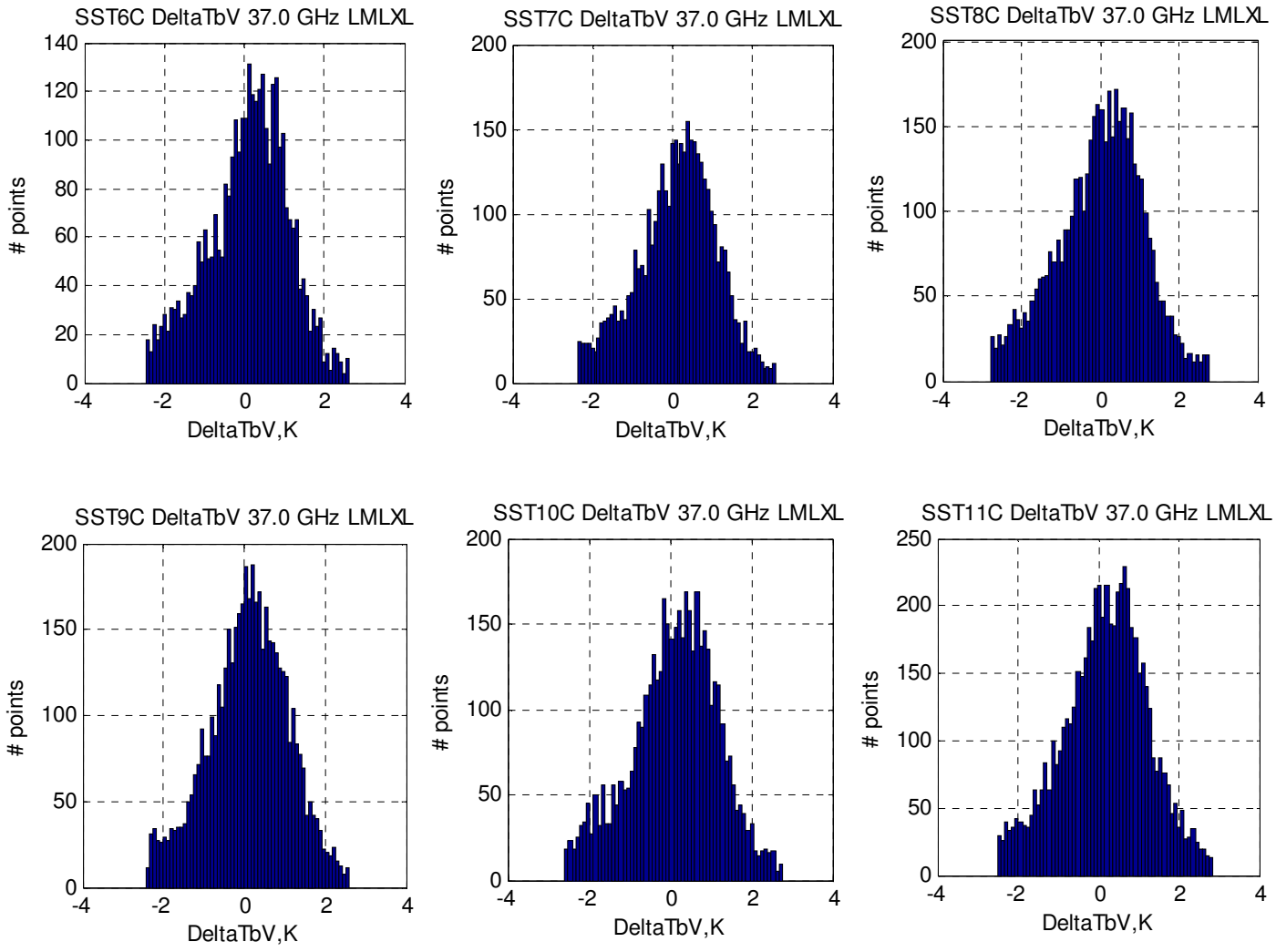
SST6C DeltaTbV 37.0 GHz LMLXL
SST7C DeltaTbV 37.0 GHz LMLXL
SST8C DeltaTbV 37.0 GHz LMLXL
SST9C DeltaTbV 37.0 GHz LMLXL
SST10C DeltaTbV 37.0 GHz LMLXL
SST11C DeltaTbV 37.0 GHz LMLXL
points
DeltaTbV,K

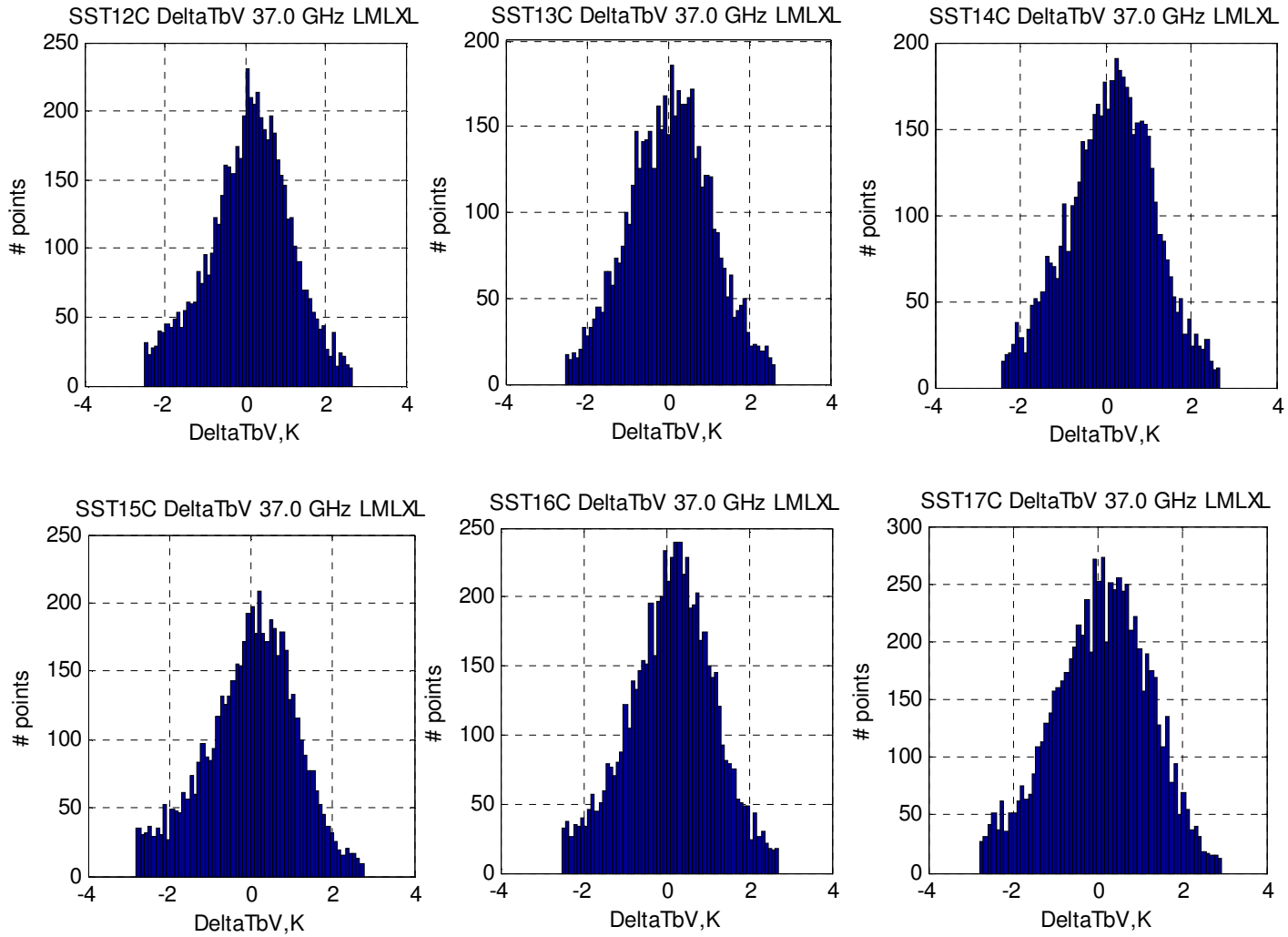
SST12C DeltaTbV 37.0 GHz LMLXL
SST13C DeltaTbV 37.0 GHz LMLXL
SST14C DeltaTbV 37.0 GHz LMLXL
SST15C DeltaTbV 37.0 GHz LMLXL
SST16C DeltaTbV 37.0 GHz LMLXL
SST17C DeltaTbV 37.0 GHz LMLXL
points
DeltaTbV,K

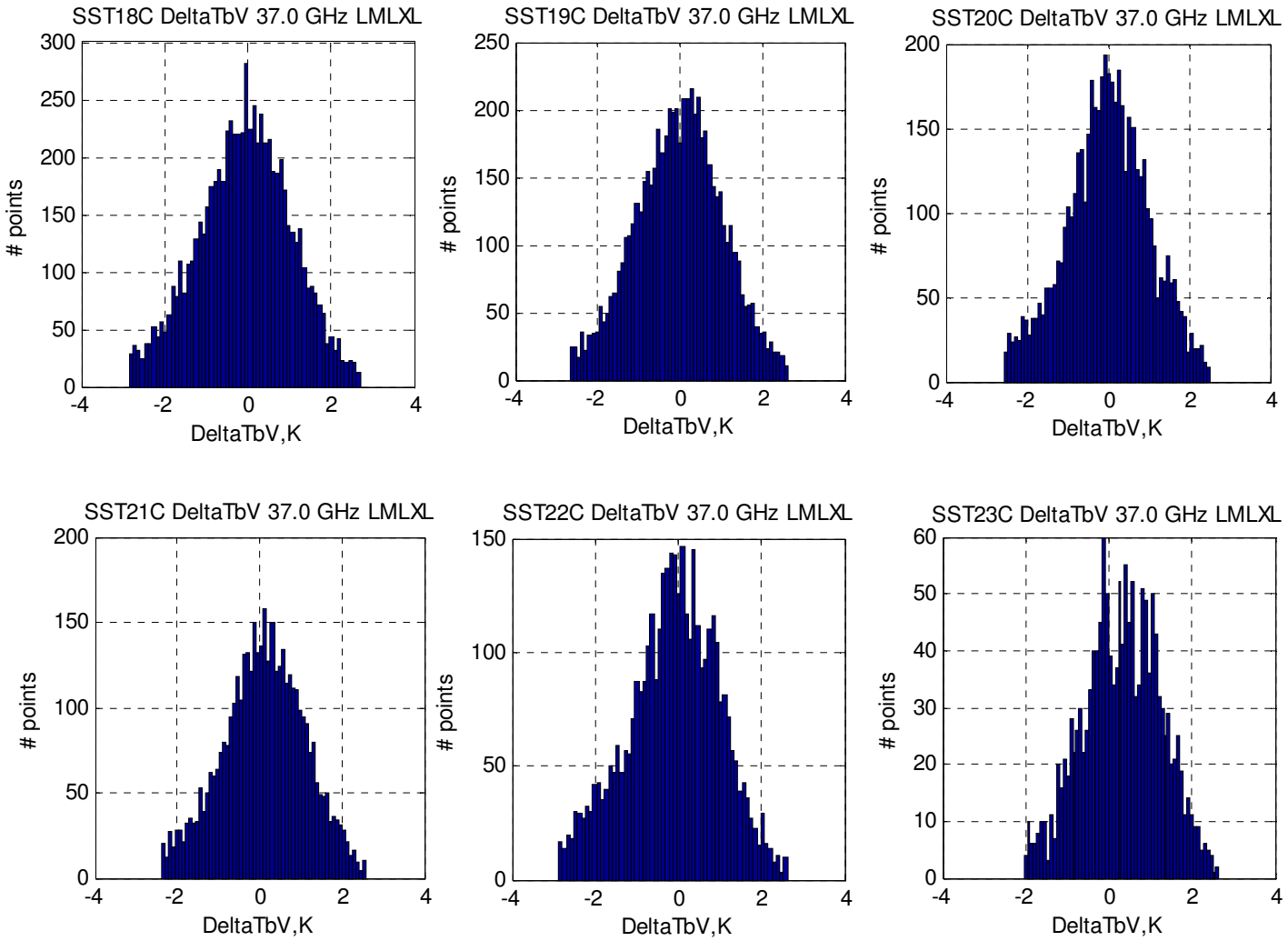
SST18C DeltaTbV 37.0 GHz LMLXL
points
DeltaTbV,K
SST19C DeltaTbV 37.0 GHz LMLXL
points
DeltaTbV,K
SST20C DeltaTbV 37.0 GHz LMLXL
points
DeltaTbV,K
SST21C DeltaTbV 37.0 GHz LMLXL
points
DeltaTbV,K
SST22C DeltaTbV 37.0 GHz LMLXL
points
DeltaTbV,K
SST23C DeltaTbV 37.0 GHz LMLXL
points
DeltaTbV,K

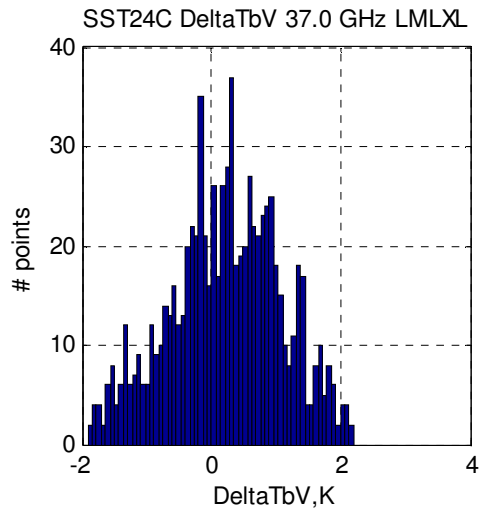
SST24C DeltaTbV 37.0 GHz LMLXL
points
DeltaTbV,K
0
10
20
30
40
-2
0
2
4

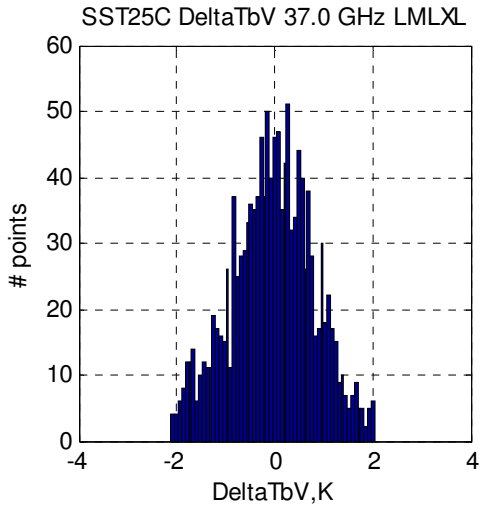
SST25C DeltaTbV 37.0 GHz LMLXL
points
DeltaTbV,K
0
10
20
30
40
50
60
-4
-2
0
2
4

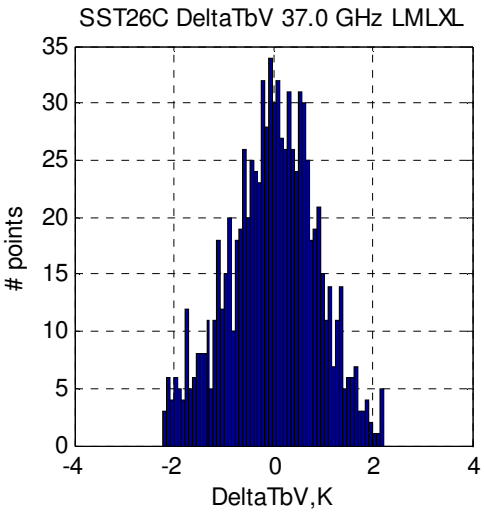
SST26C DeltaTbV 37.0 GHz LMLXL
points
DeltaTbV,K
0
5
10
15
20
25
30
35
-4
-2
0
2
4

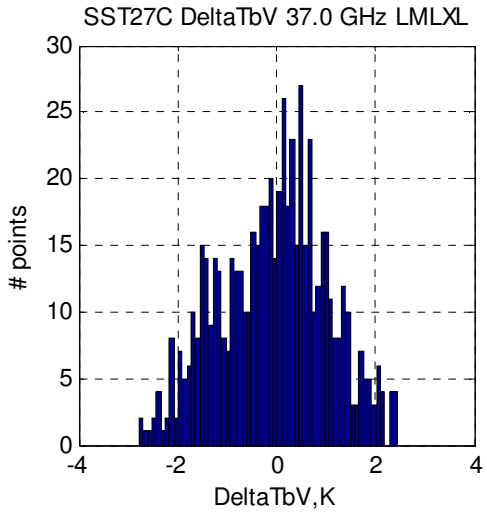
SST27C DeltaTbV 37.0 GHz LMLXL
points
DeltaTbV,K
0
5
10
15
20
25
30
-4
-2
0
2
4

37.0 GHz Descending

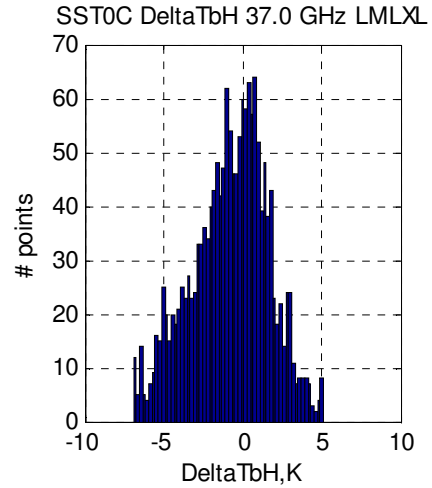
SST0C DeltaTbH 37.0 GHz LMLXL
points
DeltaTbH,K

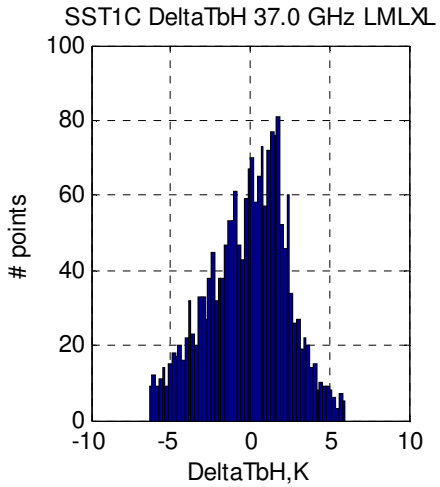
SST1C DeltaTbH 37.0 GHz LMLXL
points
DeltaTbH,K

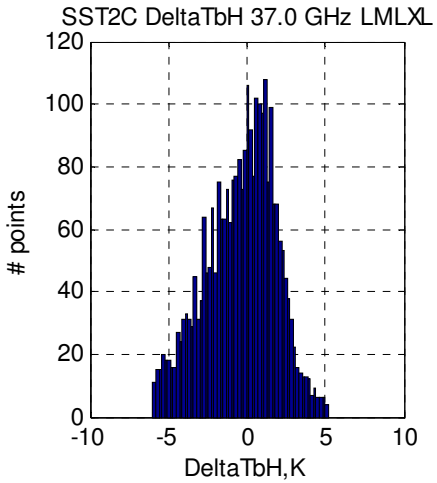
SST2C DeltaTbH 37.0 GHz LMLXL
points
DeltaTbH,K

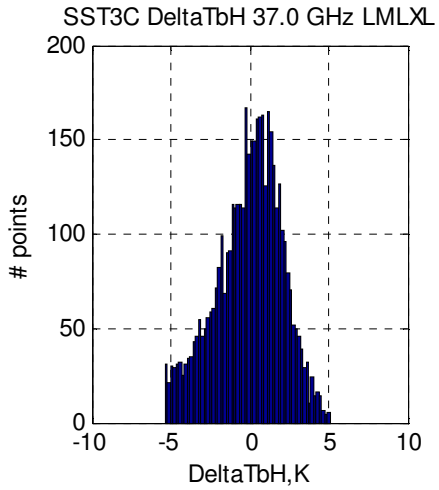
SST3C DeltaTbH 37.0 GHz LMLXL
points
DeltaTbH,K

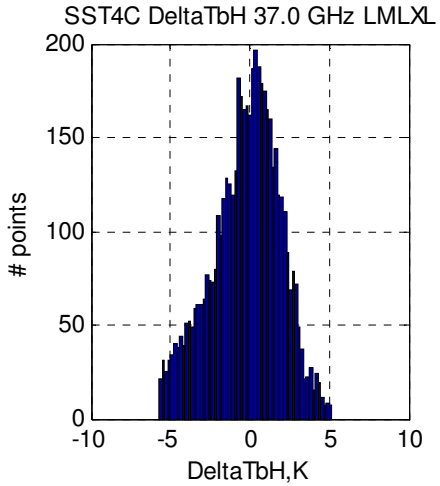
SST4C DeltaTbH 37.0 GHz LMLXL
points
DeltaTbH,K

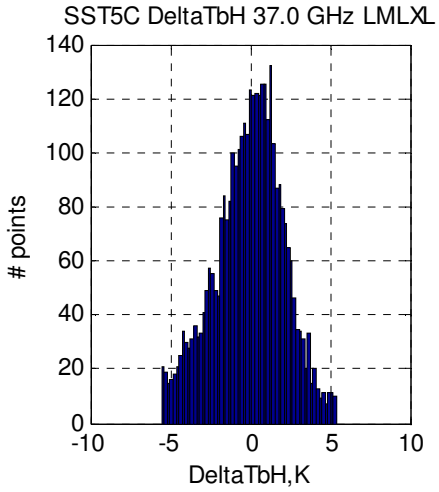
SST5C DeltaTbH 37.0 GHz LMLXL
points
DeltaTbH,K

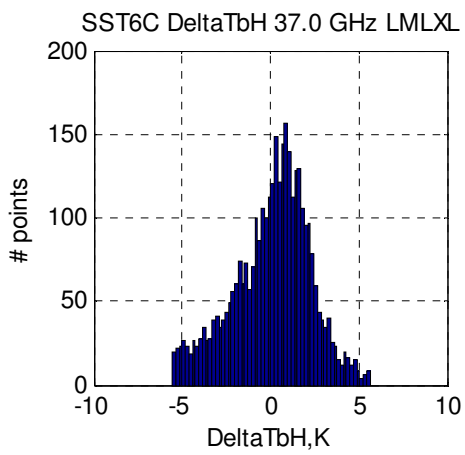
SST6C DeltaTbH 37.0 GHz LMLXL
points
DeltaTbH,K

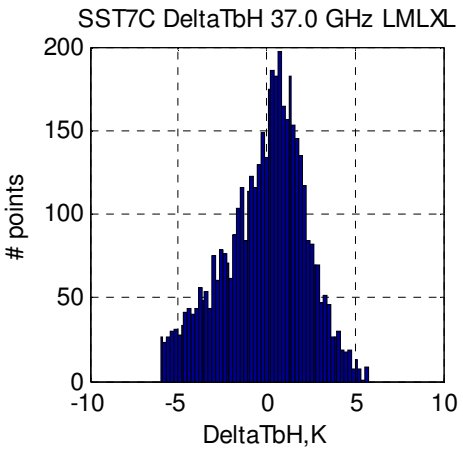
SST7C DeltaTbH 37.0 GHz LMLXL
points
DeltaTbH,K

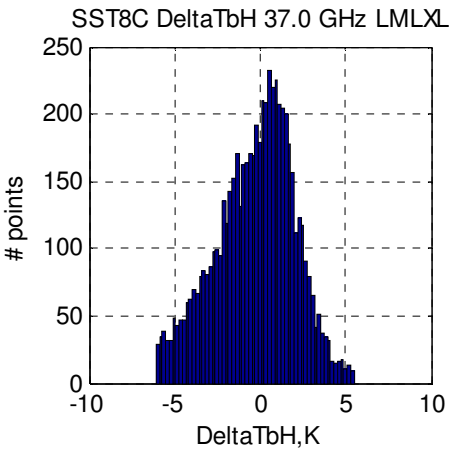
SST8C DeltaTbH 37.0 GHz LMLXL
points
DeltaTbH,K

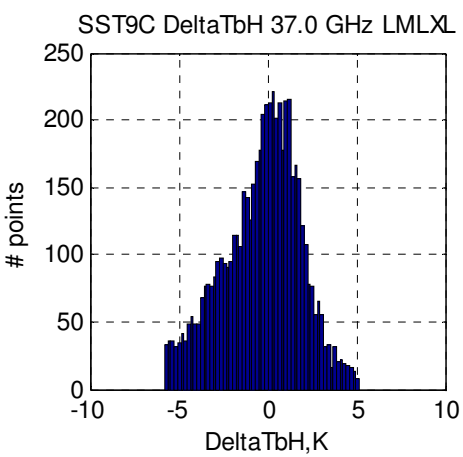
SST9C DeltaTbH 37.0 GHz LMLXL
points
DeltaTbH,K

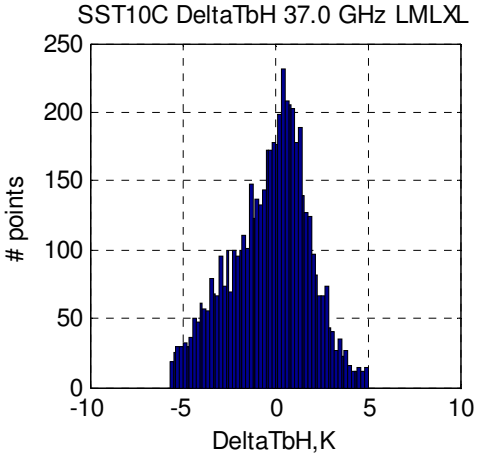
SST10C DeltaTbH 37.0 GHz LMLXL
points
DeltaTbH,K

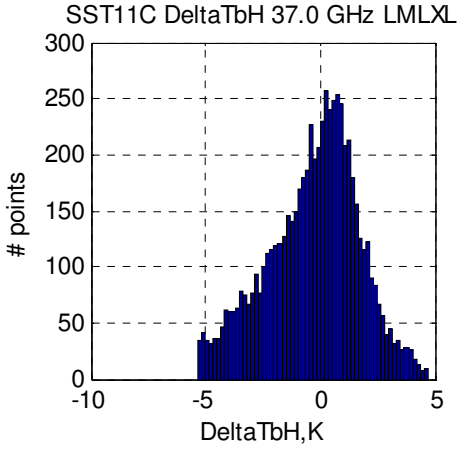
SST11C DeltaTbH 37.0 GHz LMLXL
points
DeltaTbH,K

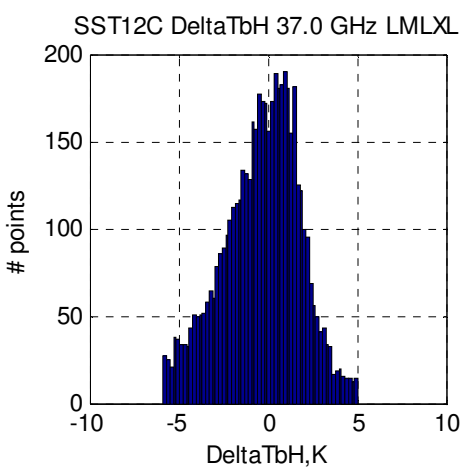
SST12C DeltaTbH 37.0 GHz LMLXL
points
DeltaTbH,K

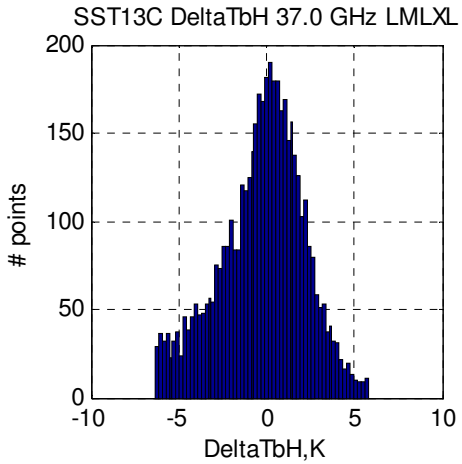
SST13C DeltaTbH 37.0 GHz LMLXL
points
DeltaTbH,K

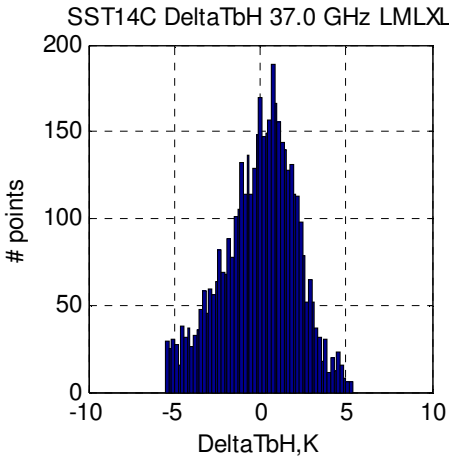
SST14C DeltaTbH 37.0 GHz LMLXL
points
DeltaTbH,K

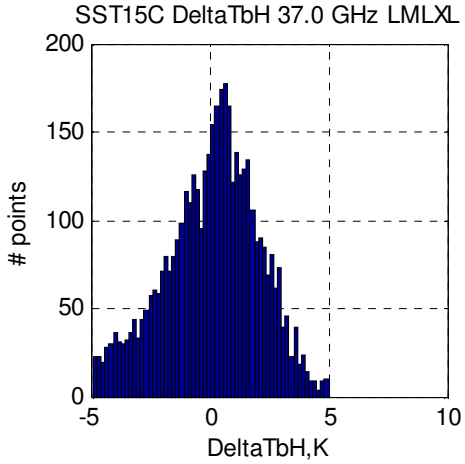
SST15C DeltaTbH 37.0 GHz LMLXL
points
DeltaTbH,K

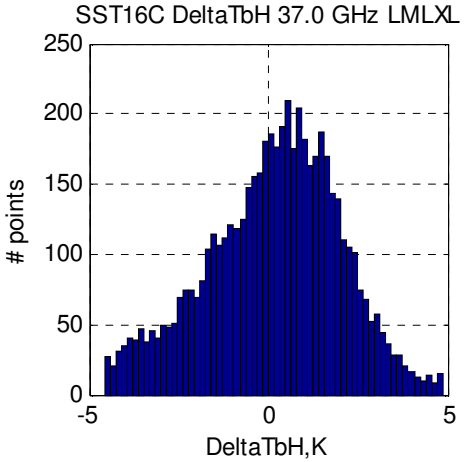
SST16C DeltaTbH 37.0 GHz LMLXL
points
DeltaTbH,K

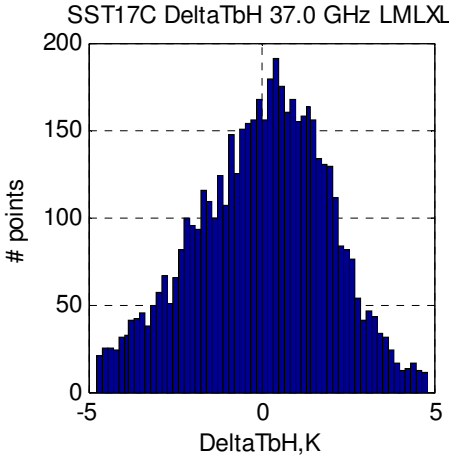
SST17C DeltaTbH 37.0 GHz LMLXL
points
DeltaTbH,K

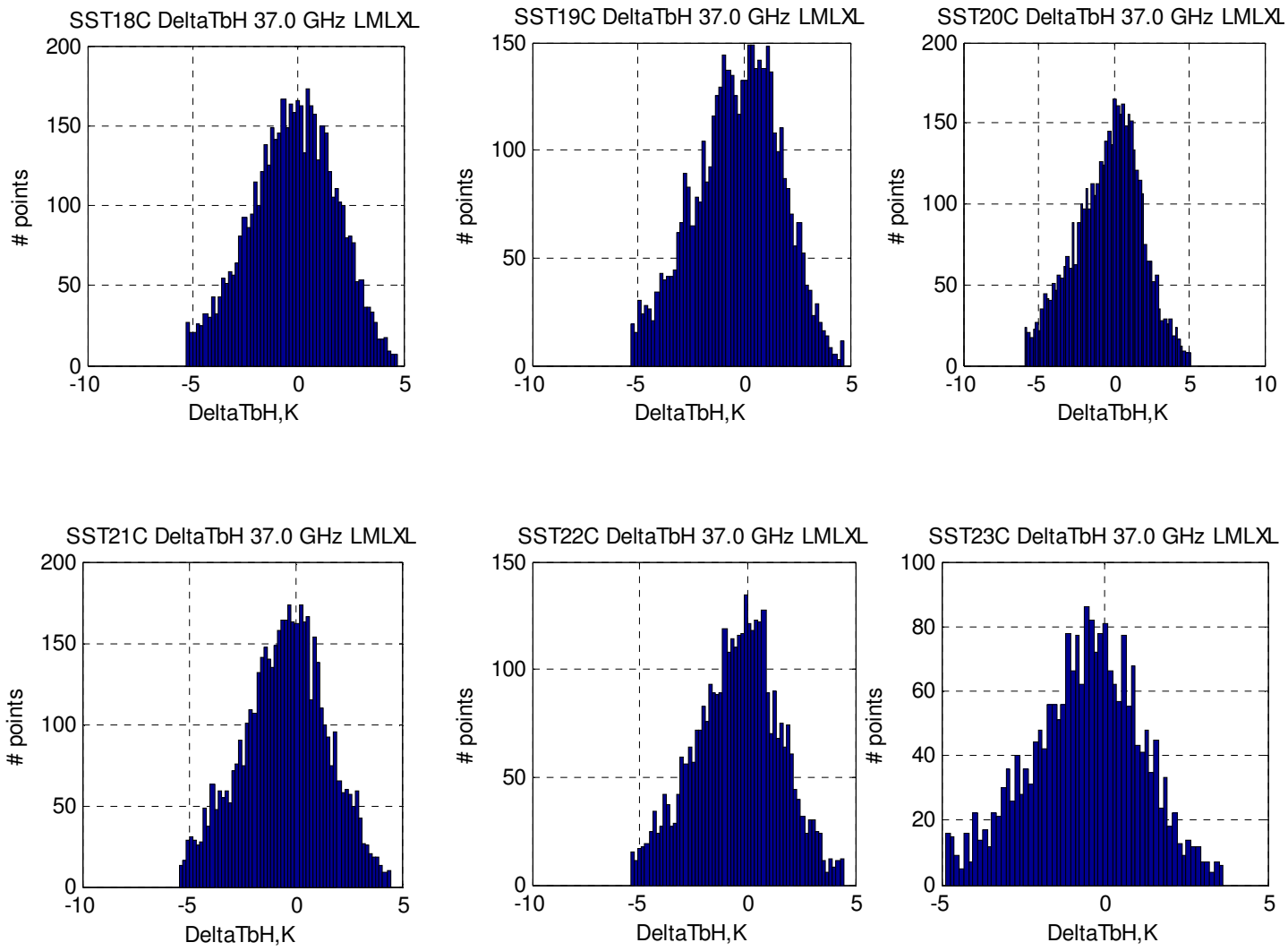
SST18C DeltaTbH 37.0 GHz LMLXL
points
DeltaTbH,K
SST19C DeltaTbH 37.0 GHz LMLXL
points
DeltaTbH,K
SST20C DeltaTbH 37.0 GHz LMLXL
points
DeltaTbH,K
SST21C DeltaTbH 37.0 GHz LMLXL
points
DeltaTbH,K
SST22C DeltaTbH 37.0 GHz LMLXL
points
DeltaTbH,K
SST23C DeltaTbH 37.0 GHz LMLXL
points
DeltaTbH,K

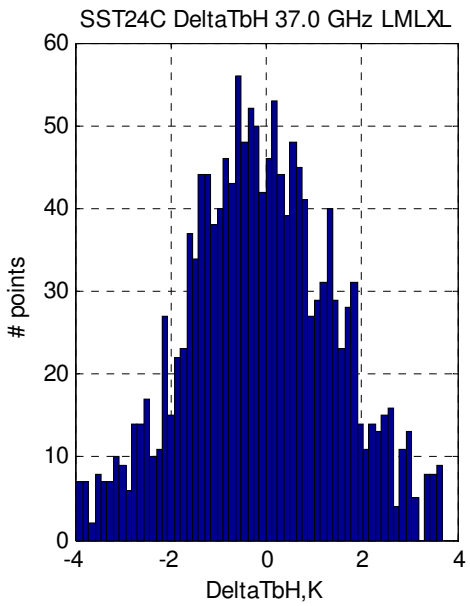
SST24C DeltaTbH 37.0 GHz LMLXL
points
DeltaTbH,K
0
10
20
30
40
50
60
-4
-2
0
2
4

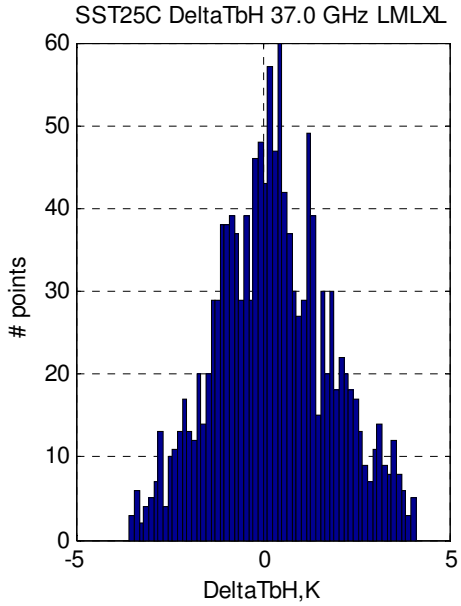
SST25C DeltaTbH 37.0 GHz LMLXL
points
DeltaTbH,K
0
10
20
30
40
50
60
-5
0
5

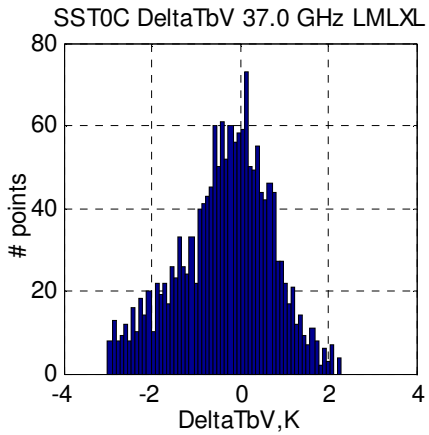
SST0C DeltaTbV 37.0 GHz LMLXL
points
DeltaTbV,K

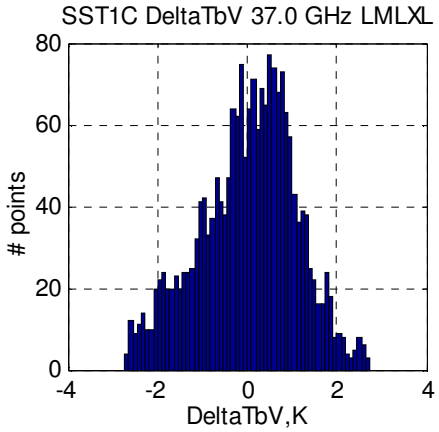
SST1C DeltaTbV 37.0 GHz LMLXL
points
DeltaTbV,K

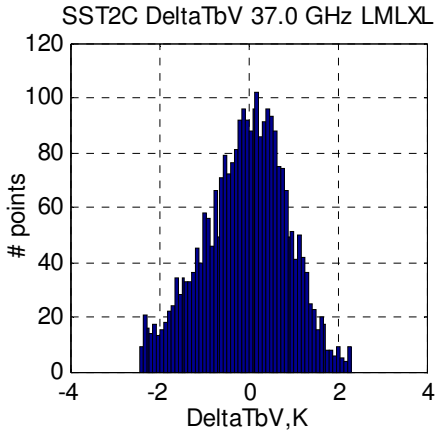
SST2C DeltaTbV 37.0 GHz LMLXL
points
DeltaTbV,K

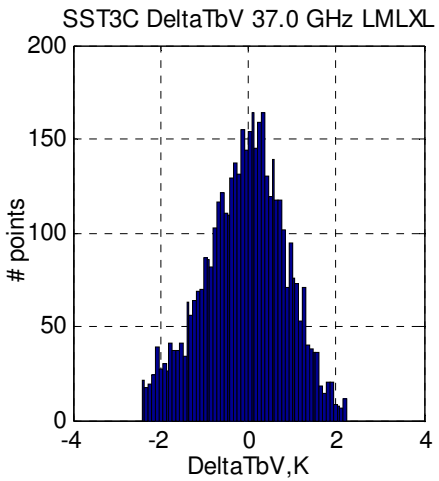
SST3C DeltaTbV 37.0 GHz LMLXL
points
DeltaTbV,K

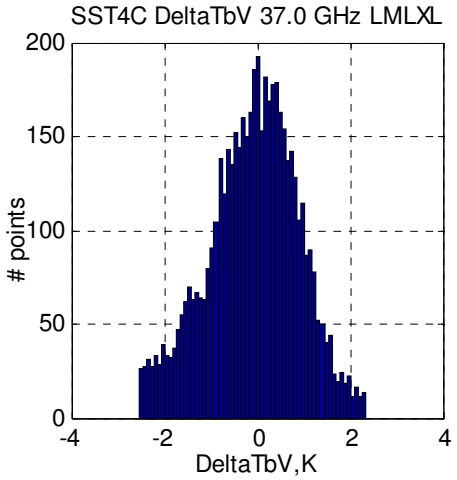
SST4C DeltaTbV 37.0 GHz LMLXL
points
DeltaTbV,K

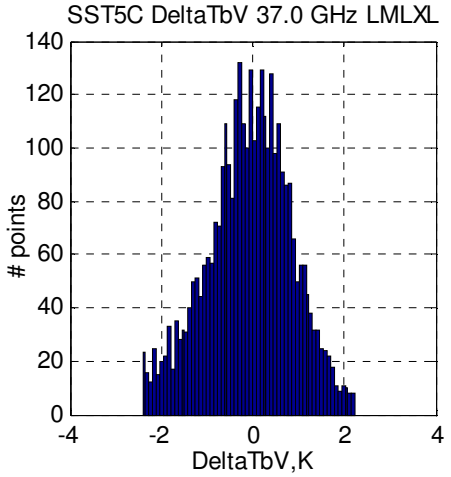
SST5C DeltaTbV 37.0 GHz LMLXL
points
DeltaTbV,K

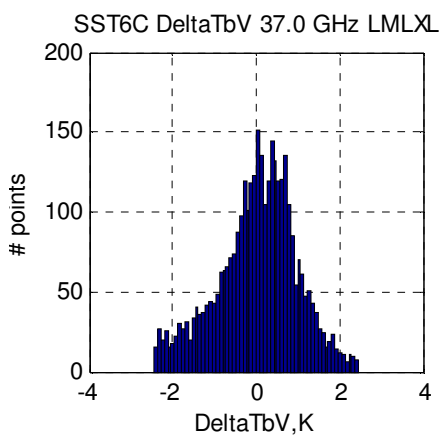
SST6C DeltaTbV 37.0 GHz LMLXL
points
DeltaTbV,K

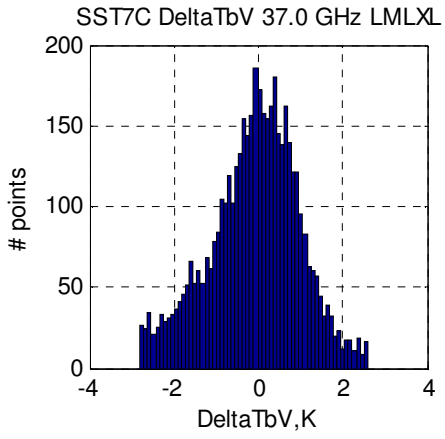
SST7C DeltaTbV 37.0 GHz LMLXL
points
DeltaTbV,K

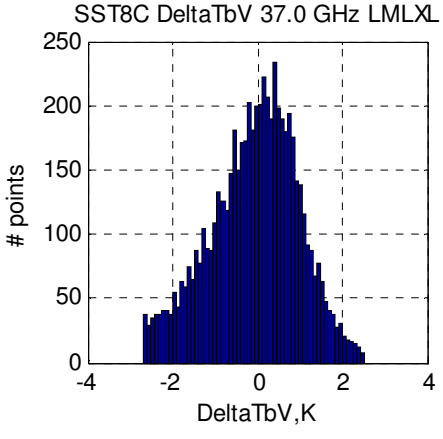
SST8C DeltaTbV 37.0 GHz LMLXL
points
DeltaTbV,K

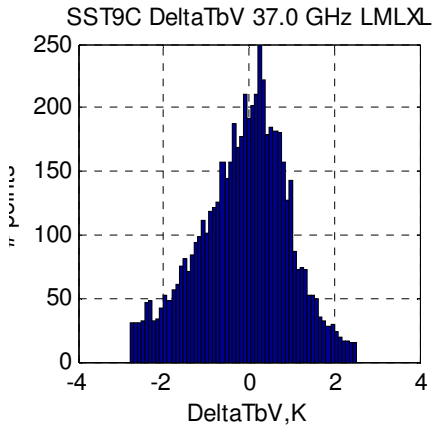
SST9C DeltaTbV 37.0 GHz LMLXL
DeltaTbV,K

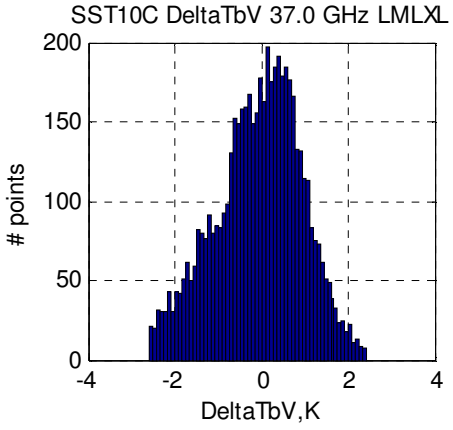
SST10C DeltaTbV 37.0 GHz LMLXL
points
DeltaTbV,K

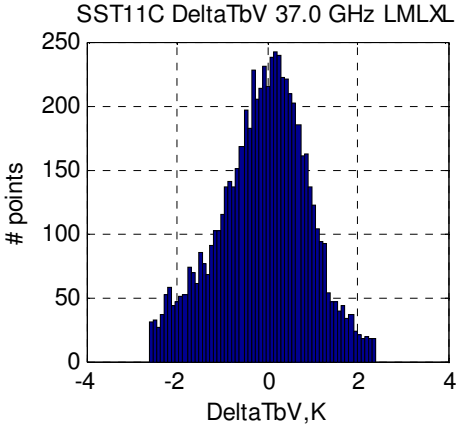
SST11C DeltaTbV 37.0 GHz LMLXL
points
DeltaTbV,K

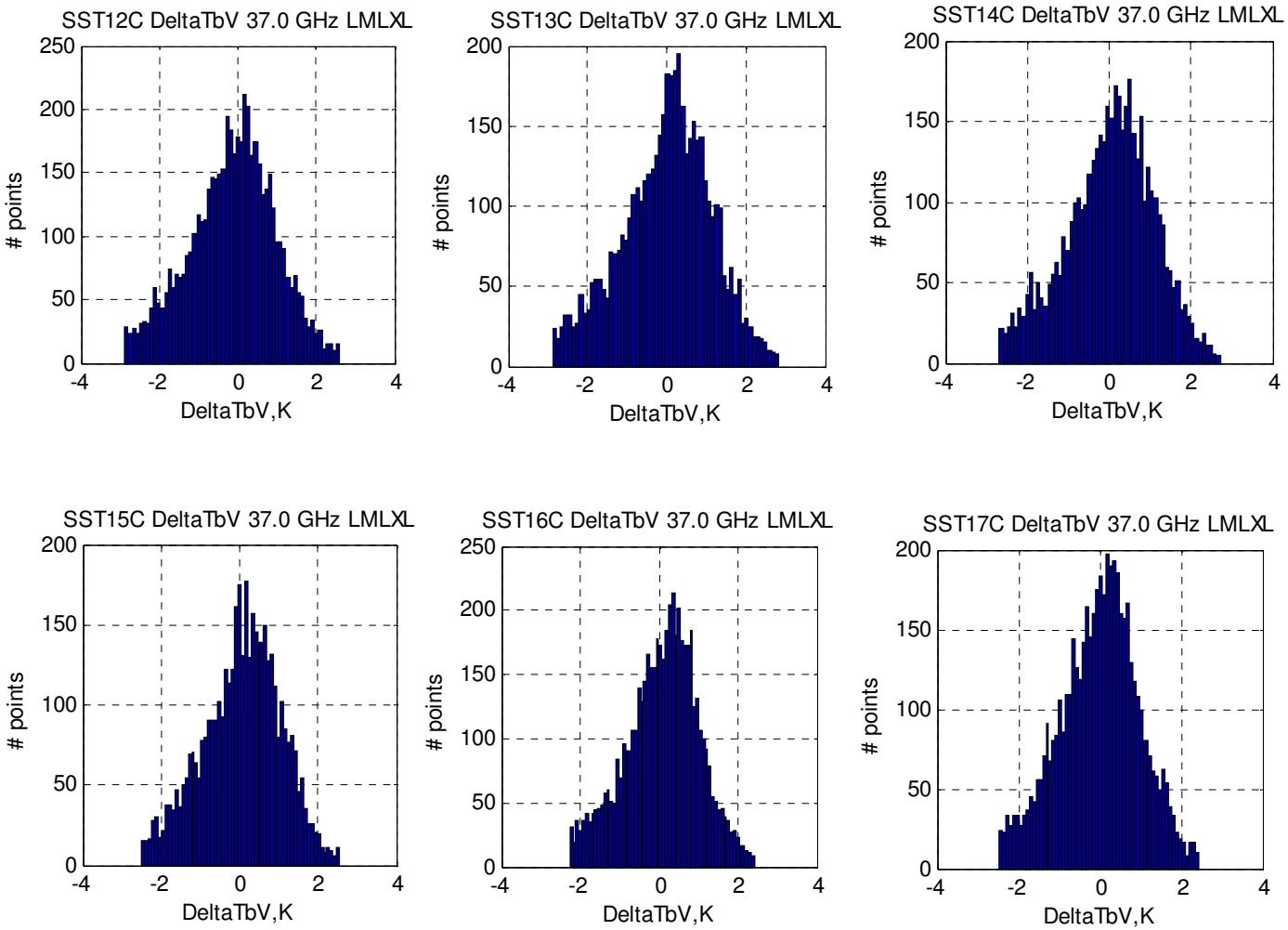
SST12C DeltaTbV 37.0 GHz LMLXL
SST13C DeltaTbV 37.0 GHz LMLXL
SST14C DeltaTbV 37.0 GHz LMLXL
SST15C DeltaTbV 37.0 GHz LMLXL
SST16C DeltaTbV 37.0 GHz LMLXL
SST17C DeltaTbV 37.0 GHz LMLXL
points
DeltaTbV,K

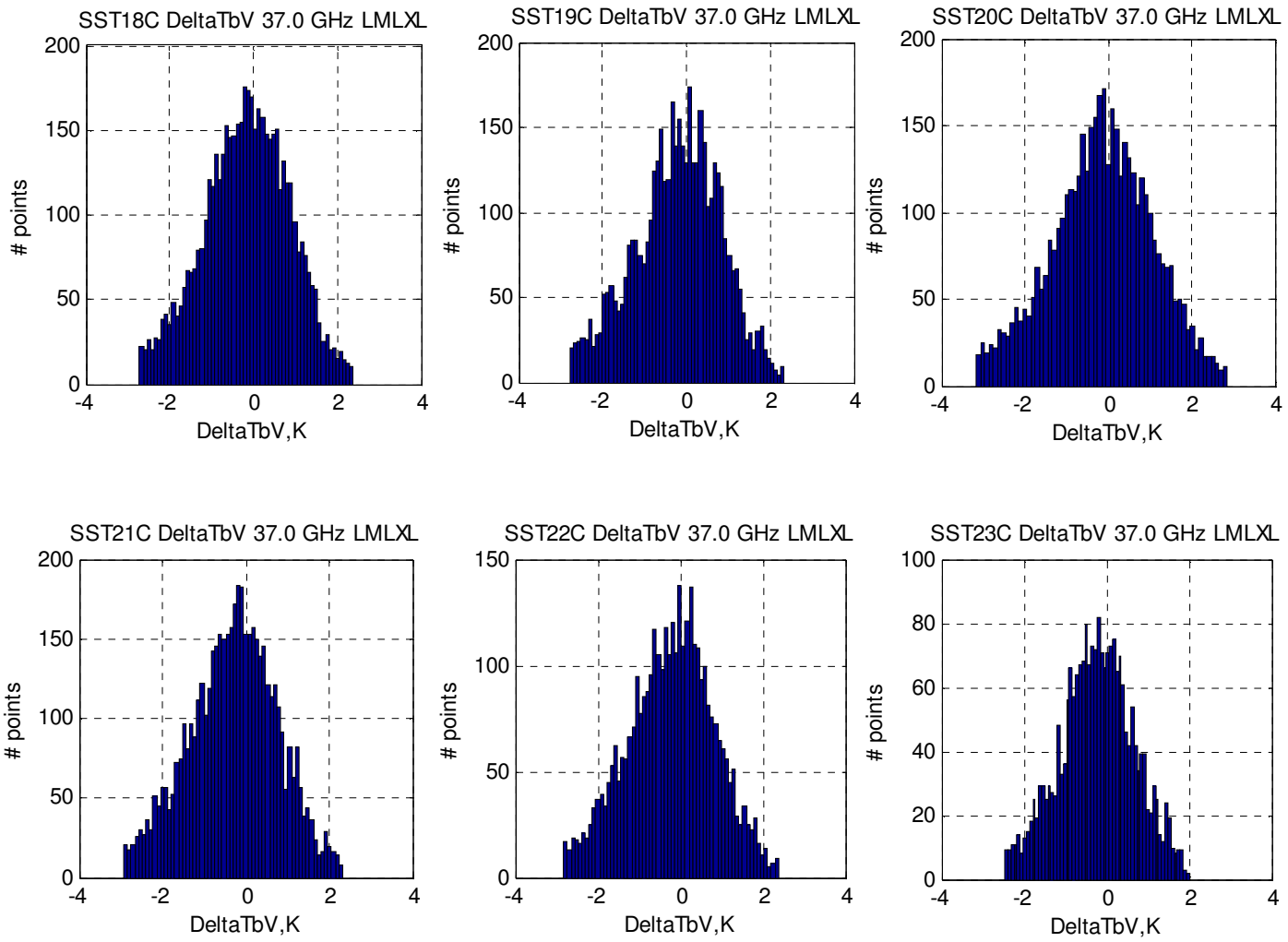
SST18C DeltaTbV 37.0 GHz LMLXL
SST19C DeltaTbV 37.0 GHz LMLXL
SST20C DeltaTbV 37.0 GHz LMLXL
SST21C DeltaTbV 37.0 GHz LMLXL
SST22C DeltaTbV 37.0 GHz LMLXL
SST23C DeltaTbV 37.0 GHz LMLXL
points
DeltaTbV,K

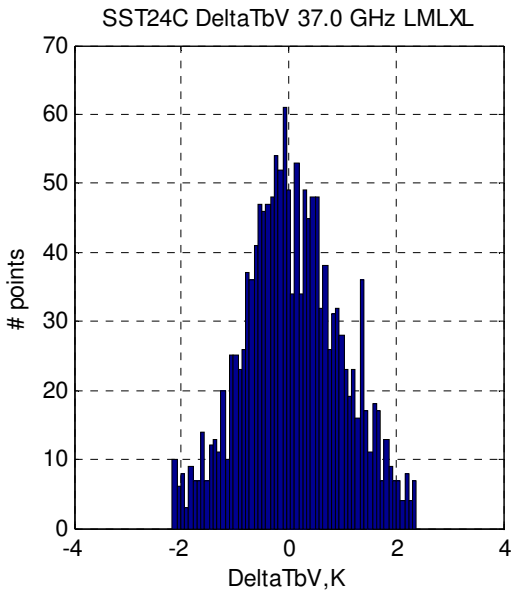
SST24C DeltaTbV 37.0 GHz LMLXL
points
DeltaTbV,K
70
60
50
40
30
20
10
0
-4
-2
0
2
4

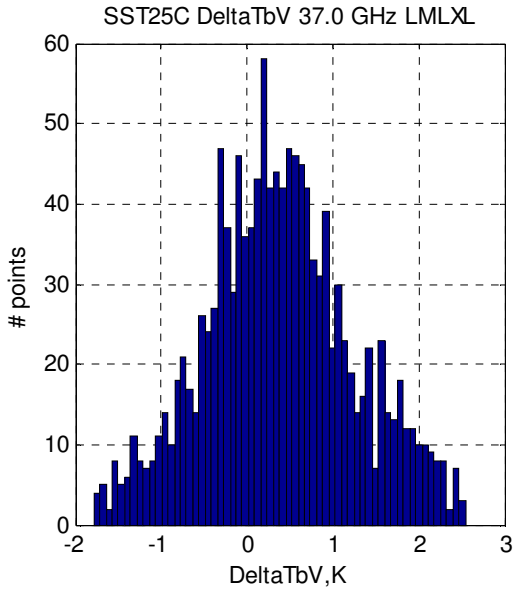
SST25C DeltaTbV 37.0 GHz LMLXL
points
DeltaTbV,K
60
50
40
30
20
10
0
-2
-1
0
1
2
3

LIST OF REFERENCES

1. Wisler, M. M. & Hollinger, J. P. (1977). *Estimation of Marine Environmental Parameters using Microwave Radiometric Remote Sensing Systems*. NRL Memo Rpt 3661, Naval Research Laboratory, Wash DC

2. Sun, Y. (2003). *Evaluation of a Microwave Radiative Transfer Model using Satellite Radiometer Observations*. Master's thesis, University of Central Florida

3. Elachi, C. (1987). *Introduction to the Physics and Techniques of Remote Sensing*. John Wiley & Sons, Inc., New York

4. Chen, H.S. (1985). *Space Remote Sensing: an Introduction*. Academic Press, Inc., Orlando, Fla

5. Ulaby, F.T., Moore R.K., & Fung A.K. (1981). *Microwave Remote Sensing: Active and Passive*, Microwave Remote Sensing Fundamentals and Radiometry. vol. 1, Artech House Inc., MA

6. Debye, P. (1929), *Polar Molecules*, Dover, New York.

7. Stogryn, A. (1971). Equations for Calculating the Dielectric Constant of Saline water. *IEEE Trans. Microwave theory Techn.*, MTT-19, pp. 733-736.

8. Klein, L. A., & Swift C. T. (1977). An Improved Model for the Dielectric Constant of Sea Water at Microwave Frequencies. *IEEE Trans. Antennas Propag.*, AP-25, pp.104-111.

9. Gross, E. P. (1955, January 15). Shape of Collision-Broadened Spectral Lines. *Phys. Rev.*, Vol. 97, pp. 395-403.

10. Meeks. M. L., & Lilley A. E. (1963) .The Microwave Spectrum of Oxygen in the Earth's Atmosphere. *J. Geophys. Res.*, 68, pp. 1683-1703.

11. Van Vleck, J. H., & Weisskopf V. F. (1945). On the Shape of Collision-Broadened Lines. *Rev. Mod. Phys.*, 17, pp. 227-236.

12. Hollinger, J.P., Peirce J.L., & Poe, G.A. (1990). SSM/I Instrument Evaluation. *IEEE Trans on Geosci Rem Sens 28(5)*, 781-790.

13. Gaiser, P.W.; St Germain, K.M.; Twarog, E.M. (2003, September 22-26). WindSat - Space Borne Remote Sensing of Ocean Surface Winds. *OCEANS 2003 Proc.*,Vol.1.

14. Jones, W. L., Park, J., Gaiser, P. W., and Wilheit, T. T. (2004, September 20-24). "Deep-Space Calibration of WindSat Radiometer". *Proc. IEEE TGARSS-04*, Anchorage, AK.

15. Twarog, E., Gaiser, P. W., Purdy, B., Jones, L., St Germain, K. & Poe, G. (2004, September 20-24) "WindSat Post-Launch Calibration". *Proc. IEEE TGARSS-04*, Anchorage AK.

16. Remote Sensing System, SSM/I data, Available on web site http://www.ssmi.com/ssmi/ssmi_browse.html

17. NCEP Reanalysis data, Available on website http://www.cdc.noaa.gov/cdc/data.ncep.reanalysis.html

18. Reynolds Sea Surface Temperature, Climate Diagnostics Center data, Available on website http://www.cdc.noaa.gov/cdc/data.reynolds_sst.html

19. NODC (Levitus) World Ocean Atlas 1998, NODC (Levitus) World Ocean Atlas Data 1998, Available on website http://www.cdc.noaa.gov/cdc/data.nodc.woa98.html

20. http://code8200.nrl.navy.mil/windsat.html

21. Imaoka, K.; Sezai, T.; Takeshima, T.; Kawanishi, T.; Shibata, A. (2002, June 24-28) Instrument characteristics and calibration of AMSR and AMSR-E, Geoscience and Remote Sensing Symposium, 2002. *IGARSS '02. 2002 IEEE International*, Volume: 1, pages: 18 - 20.